JOURNAL OF THE

Electrochemical Society

ol. 111, No. 10 October 1964

PRODUCTS YOU CAN TRUST
GRAPHITE PRODUCTS
GLC
DIVISION

GREAT LAKES CARBON CORPORATION

18 EAST 48th STREET, NEW YORK, N. Y. 10017 -- OFFICES IN PRINCIPAL CITIES

Report from

BELL LABORATORIES

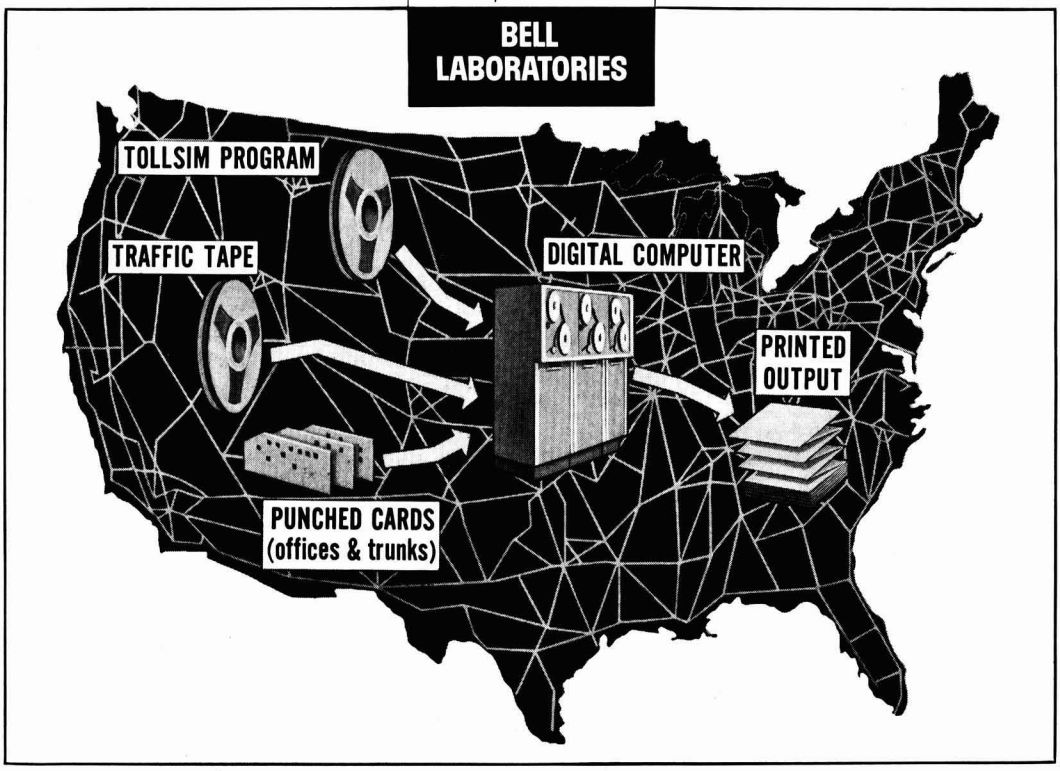

Many functions of the Bell System communications toll network are simulated by a digital computer using the TOLLSIM program along with a traffic tape and punched cards. The traffic tape, which may be used for a number of traffic studies, specifies times, originating and terminating points, numbers, and durations of simulated telephone calls. The punched cards specify characteristics of real or theoretical offices and trunks. The printed output, by recording and summarizing reattempts, abandoned calls, and other "real life" traffic data, both for the entire network and for its component parts, enables engineers to judge performance under various operating conditions. Many variations are possible. The effect of rearranging switching equipment in an office, for example, can be studied by using a different punched card for that office.

TRAFFIC ANALYSIS

Mathematics for good telephone service

At Bell Laboratories simulated telephone calls are placed through a computer programmed to represent the Bell System nationwide Direct Distance Dialing network. The computer program, known as TOLLSIM for "Toll Network Simulator," is one of many tools used by traffic specialists in studying how well traffic is handled by the network and how certain design changes might improve telephone service.

For example, a long-standing problem within the telephone industry is that of coping with heavy overload conditions during relatively short periods. These overloads can occur because of storms or other disasters that result in unusually heavy telephone calling. Such conditions also occur during the Christmas season and on Mother's Day.

In conjunction with earlier theoretical work, a TOLLSIM simulation indicated that, during overload conditions, a greater number of customers could be served if the pattern of automatic alternate routing of telephone calls were changed. The change involved making fewer attempts to route the calls over long, roundabout alternate routes when shorter direct trunks were busy. The results were then confirmed by field tests performed during the 1963 Christmas period.

This work is an example of the way Bell Laboratories people advance traffic theory and practical applications. The goal: to tailor facilities closely to the needs of telephone customers.

BELL TELEPHONE LABORATORIES... Research and Development Unit of the Bell System.

JOURNAL OF THE

OCTOBER 1964

EDITORIAL

TECHNICAL PAPERS

ELECTROCHEMICAL SOCIETY

VOL. 111 • NO. 10

Manuscripts submitted to the Journal should be sent, in triplicate, to the Editorial Office at 30 East 42 St., New York, N. Y., 10017. They should conform to the revised Instructions to Authors published on 251C-252C of this issue. Manuscripts so submitted become the property of The Electrochemical Society and may not be published elsewhere, in whole or in part, unless permission is requested of and granted by the Editor.

The Electrochemical Society does not maintain a supply of reprints of papers appearing in its Journal. A photoprint copy of any particular paper, however, may be obtained by corresponding direct with the Engineering Societies Library, 345 E. 47 St., New York, N. Y., 10017.

Inquiries re positive microfilm copies of volumes should be addressed to University Microfilms, Inc., 313 N. First St., Ann Arbor, Mich.

Walter J. Johnson, Inc., 111 Fifth Ave., New York, N. Y., 10003, have reprint rights to out-of-print volumes of the Journal, and also have available for sale back volumes and single issues, with the exception of the current calendar year. Anyone interested in securing back copies should correspond direct with them.

Published monthly by The Electrochemical Society, Inc., at 215 Canal St., Manchester, N. H.; **Executive Offices, Editorial Office** and **Circulation Dept.**, and **Advertising Office** at 30 East 42 St., New York, N. Y., 10017, combining the JOURNAL and TRANSACTIONS OF THE ELECTROCHEMICAL SOCIETY. Statements and opinions given in articles and papers in the JOURNAL OF THE ELECTROCHEMICAL SOCIETY are those of the contributors, and The Electrochemical Society assumes no responsibility for them.

Claims for missing numbers will not be allowed if received more than 60 days from date of mailing plus time normally required for postal delivery of JOURNAL and claim. No claims allowed because of failure to notify the Circulation Dept., The Electrochemical Society, 30 East 42 St., New York, N. Y., 10017, of a change of address, or because copy is "missing from files." Subscription to members as part of membership service; subscription to nonmembers $24.00 plus $1.50 for postage outside U.S. and Canada. Single copies $1.70 to members, $2.25 to nonmembers.

Entered as second-class matter at the Post Office at Manchester N. H., under the act of August 24, 1912. Postage paid at Manchester, N. H.

Editorial

How Long to Publish

How long should it really take to publish a technical article in the JOURNAL? Let us assume that an author mails a short manuscript to the New York Office on October 1. It is sent to one or two reviewers, is accepted without change and is back in the Office by October 20. It is prepared for the printer and mailed to him on October 25, the monthly deadline. The author receives proof about November 25 and returns it to New York. It is returned to the printer on December 14 and appears in the finished JOURNAL on January 2, three months after the initial mailing.

This schedule is of course exceptional. The longer technical articles take much more time for review. Suppose that three copies of a manuscript are mailed to New York on October 1. By October 10 or 12 two copies will have reached the appropriate Divisional Editor, one copy the Technical Editor (that is, if the author makes plain which Division should review his manuscript). The Divisional Editor will take some time to consider the paper and choose reviewers. Let us say that he mails copies to two reviewers on October 22. The Reviewer has other things to do. In his spare time he will read the paper carefully, probably several times, making notes; he will look up references, make a trip to the library, try to find a half-forgotten article, consult a colleague, finally write his review. While some manuscripts can be returned very promptly, we had best allow four weeks for the two copies to get back to the Divisional Editor, making the date November 20.

In most cases the Divisional Editor will now send a copy to the author, asking him to make some changes, deletions, additions or clarification. The delay is now in the hands of the author; let us allow him three weeks, and allow two more weeks for the manuscripts with the review file and the recommendations to be sent to the Technical Editor. Let us assume that everything is in order and there is no delay at this point. The manuscript is returned to the Managing Editor in New York and is too late to meet the deadline for the March JOURNAL (December 22).

No matter, the article could not be published in the March issue anyway. The JOURNAL budget has been increased year by year, but has never quite kept pace with the increasing number of manuscripts received and accepted. Our hypothetical article will be sent to the printer on February 25 and will appear in the May JOURNAL, seven months after the author first mailed it to New York.

An obvious way to speed up publication is to eliminate the two month backlog of accepted manuscripts. The page charge will provide more funds next year, and means of reducing expenses and allocating other funds are being investigated. If manuscripts can be pushed to the printer at the first monthly deadline after acceptance many of them can be published in five months, with some luck even in four. Additional correspondence with the author or delay at various points in the review process could, however, increase the time to six, seven, eight months. We are proud of our review process and do not want to abbreviate it to save time, at the expense of letting quality suffer.

As for a secretary who neglects manuscripts or correspondence, or a member of the editorial and review staff who doesn't find the time, we can only apologize and try to make changes. All staff members are asked to return manuscripts at once if they cannot be given prompt attention. In this work it is no disgrace for anyone to call for help; it is a part of the service to the JOURNAL.

—CVK

WHAT MAKES A STACKPOLE ANODE BETTER?

Rigid processing control. At Stackpole, close supervision of mixing, baking, graphitizing and impregnating produces a product of the highest quality and uniformity.

For instance, Stackpole's oil treating process impregnates the anode for keeps. Bleeding during operation is cut to a minimum. This means fewer diaphragm changes for you . . . longer cell life, lower maintenance costs.

Stackpole GraphAnodes® can be designed with any feature you need, such as holes, slots or bevels. Careful planing of all anode surfaces insures perfect cell alignment for maximum efficiency and life.

Let us tell you more about the difference in GraphAnodes, write: Stackpole Carbon Company, Carbon Division, St. Marys, Pa. Phone: 814-834-1521 TWX: 814-826-4808.

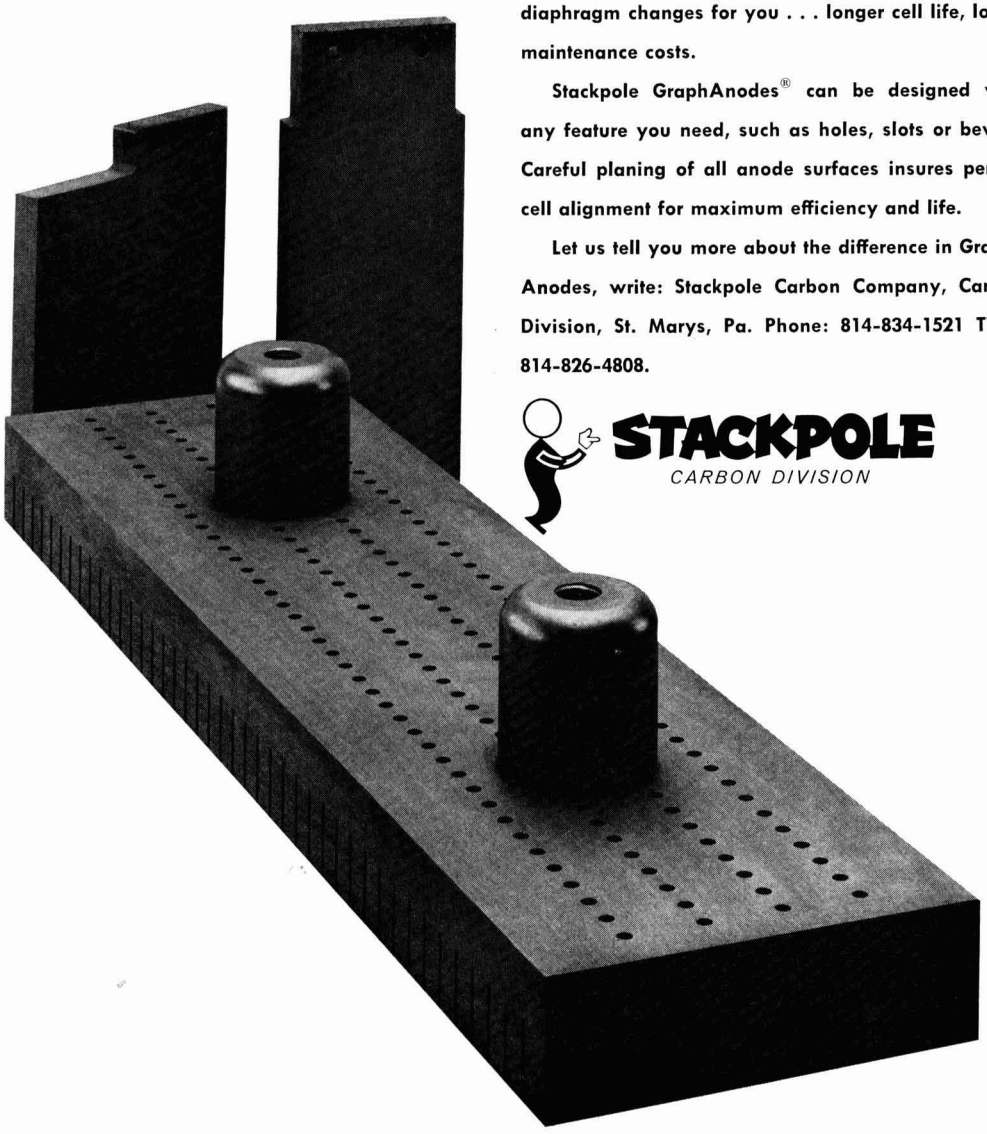

STACKPOLE
CARBON DIVISION

Monographs of The Electrochemical Society

ECS Series

The following are books developed and sponsored by The Electrochemical Society and published by John Wiley & Sons, Inc., 605 Third Ave., New York 17, N. Y. Members of The Electrochemical Society can receive a 33 1/3% discount by ordering volumes from Society Headquarters, 30 East 42 St., New York, N. Y., 10017. Book and invoice will be mailed by John Wiley & Sons. Nonmembers (including subscribers) should order direct from Wiley.

Corrosion Handbook. Edited by Herbert H. Uhlig. Published 1948, 1188 pages, **$16.00**

Modern Electroplating, Second Edition. Edited by Frederick A. Lowenheim. Published 1963, 769 pages, **$16.00.**

Abstracts of the Literature on Semiconducting and Luminescent Materials and Their Applications. Compiled by Battelle Memorial Institute.

Vol. I, 1953 Issue—published 1955, 169 pages, **$5.00** (soft cover); **Vol. II, 1954 Issue**—published 1955, 200 pages, **$5.00** (soft cover); **Vol. III, 1955 Issue**—Edited by E. Paskell; published 1957, 322 pages, **$10.00** (hard cover); **Vol. IV, 1956 Issue**—Edited by E. Paskell, published 1959, 456 pages, **$12.00** (hard cover); **Vol. V, 1957 Issue**—Edited by C. S. Peet; published 1960, 449 pages, **$12.00** (hard cover); **Vol. VI, 1958 Issue**—Edited by J. J. Bulloff and C. S. Peet; published 1961, 528 pages, **$14.00** (hard cover); **Vol. VII, 1959 Issue**—Edited by J. J. Bulloff and C. S. Peet; published 1962, 728 pages, **$20.00 (hard cover).**

Electrochemistry in Biology and Medicine. Edited by Theodore Shedlovsky. Published 1955, 369 pages, **$11.50**

Vapor Plating (The Formation of Metallic and Refractory Coatings by Vapor Deposition), by C. F. Powell, I. E. Campbell, and B. W. Gonser. Published 1955, 158 pages, **$6.00**

High-Temperature Technology (Materials, Methods, and Measurements). Edited by I. E. Campbell. Published 1956, 526 pages, **$15.00** (Out of print; new edition in course of preparation)

Stress Corrosion Cracking and Embrittlement. Edited by W. D. Robertson. Published 1956, 202 pages, **$7.50**

Arcs in Inert Atmospheres and Vacuum. Edited by W. E. Kuhn. Published 1956, 188 pages, **$7.50**
(Papers Presented at the Symposium on Arcs in Inert Atmospheres and Vacuum of the Electrothermics and Metallurgy Division of The Electrochemical Society, April 30 and May 1, 1956, San Francisco, Calif.)

Technology of Columbium (Niobium). Edited by B. W. Gonser and E. M. Sherwood. Published 1958, 120 pages, **$7.00**
(Papers Presented at the Symposium on Columbium—Niobium of the Electrothermics and Metallurgy Division of The Electrochemical Society, May 15 and 16, 1957, Washington, D. C.)

The Structure of Electrolytic Solutions. Edited by Walter J. Hamer. Published 1959, 441 pages, **$18.50**
(Based on a Symposium held in Washington, D. C., in May 1957, sponsored by The Electrochemical Society, New York, and The National Science Foundation, Washington, D. C.)

Mechanical Properties of Intermetallic Compounds. Edited by J. H. Westbrook. Published 1959, 435 pages, **$9.50**
(A Symposium, Sponsored by the Electrothermics and Metallurgy Division of The Electrochemical Society, May 4, 5, and 6, 1959, Philadelphia, Pa.)

The Surface Chemistry of Metals and Semiconductors. Edited by Harry C. Gatos, with the assistance of J. W. Faust, Jr., and W. J. La Fleur. Published 1960, 526 pages, **$12.50**
[Proceedings of an International Symposium Sponsored Jointly by the Office of Naval Research and The Electrochemical Society, Inc. (Corrosion and Electronics Divisions), October 19, 20, and 21, 1959, Columbus, Ohio]

Transactions of the Symposium on Electrode Processes. Edited by Ernest Yeager. Published 1961, 374 pages, **$20.00** (The papers and discussions of the Symposium on Electrode Processes, sponsored jointly by the U. S. Air Force, Office of Scientific Research, and The Electrochemical Society, Inc., Philadelphia, Pa., May 1959).

Iodide Metals and Metal Iodides, by Robert F. Rolsten. Published 1961, 441 pages, **$17.50**
Ultrafine Particles, Editor-in-Chief—William E. Kuhn. Published 1963, 561 pages, **$15.00.**

Other ECS Publications

Vacuum Metallurgy, third printing, 1958. Edited by J. M. Blocher, Jr.; 216 pages; **$5.00,** less a 20% discount to ECS members only. Available from Electrochemical Society Headquarters, 30 East 42 St., New York 17, N. Y. (Papers Presented at the Vacuum Metallurgy Symposium of the Electrothermics and Metallurgy Division of The Electrochemical Society held in Boston, Mass., October 6 and 7, 1954)

Rhenium, Edited by B. W. Gonser. Published by Elsevier Publishing Co., 1962. 225 pages; **$11.00.** (Papers Presented at the Symposium on Rhenium of the Electrothermics and Metallurgy Division of The Electrochemical Society, May 3 and 4, 1960, Chicago, Ill.) ECS Members can obtain a 30% discount by sending their orders direct to Society Headquarters, 30 East 42 St., New York 17, N. Y. Remittance, made payable to American Elsevier Publishing Co., 52 Vanderbilt Ave., New York 17, N. Y. should accompany the order. Nonmembers must order direct from the publisher.

Iron Ore Reduction, Edited by R. R. Rogers. Published by Pergamon Press Ltd., New York and London, 1962. 359 pages; **$12.50.** (Proceedings of a Symposium of the Electrothermics and Metallurgy Division of The Electrochemical Society, held in Chicago, Ill., May 3-5, 1960) Send all orders to The Macmillan Co., 60 Fifth Ave., New York, N. Y.

Electrochemical Chlorination of n-Dodecane

F. N. Ruehlen, G. B. Wills, and H. M. Fox

Research Division, Phillips Petroleum Company, Bartlesville, Oklahoma

ABSTRACT

Dodecane was efficiently chlorinated at a porous carbon anode in an electrolytic cell containing a 20% hydrochloric acid electrolyte. The dodecane flowed continuously through the porous anode, and chlorinated products were continuously withdrawn. Voltametric studies on small-scale electrodes indicated that the reaction mechanism involves chlorine evolution followed by a chlorination reaction which takes place in a thin film adhering to the electrode. The distribution of products, *i.e.*, the ratio of monochlorododecanes to dichlorododecanes produced were correlated on the basis of a calculated statistical distribution assuming a free radical mechanism. The pronounced deviations from this statistical distribution at low current densities are explained on the basis of a competing reaction which involves the diffusion of free radical inhibitors into the reaction film.

Monochlorination of paraffin hydrocarbons is a growing route to olefins, alcohols, amines, amides, nitriles, alkyl benzenes, and many other alkyl products. Chlorine is substituted for hydrogen by direct action of chlorine in either light-activated or thermally activated reactions. This study considers still another technique, electrochemical chlorination. A specific objective of the study was to determine if n-dodecane can be continuously and efficiently monochlorinated at the anode of an electrolytic cell containing an aqueous hydrochloric acid electrolyte.

The experimental work was directed primarily toward two aspects of the problem: (i) determination of the effect of cell operating characteristics on products, specifically in respect to reduction of polychlorides, and (ii) understanding the mechanism of the reactions. Most of the work was conducted in a chlorination cell which was equipped to provide dodecane continuously at the surface of a porous carbon anode and to skim products and unreacted dodecane continuously from the cell. Voltametric studies were also made using small cells and specially constructed electrodes.

Experimental

Chlorination cell.—The anode of the chlorination cell (Fig. 1) was a porous carbon cylinder with one end closed and the open end tapped to receive a ¼-in. Teflon pipe nipple. This nipple served as the hydrocarbon feed entry as well as a support for the anode. The anode was 3.7 cm long with an outside diameter of 2.5 cm and a wall thickness of 0.7 cm. A coating of porcelain cement restricted the working surface to the vertical perimeter below the end of the Teflon nipple. Electrical connection to the anode was made by means of a copper wire extending downward through the hydrocarbon feed tube.

Hydrocarbon feed to the cell was monitored by a small flow meter, but the actual quantities of dodecane fed were determined from volume changes in a calibrated feed cylinder. The hydrocarbon feed was purged with nitrogen to expel dissolved oxygen. The electrolyte was 20% hydrochloric acid and fresh acid was introduced continuously to the cell at a rate of 60 to 100 ml/hr depending on the current density. Current densities in the range 15 to 180 ma/cm^2 were used, and the cell temperature was maintained between 93° and 102°C. The cell terminal voltage ranged from 1.5 to about 2.0v depending on current density and dodecane feed rate. Samples were collected for analysis after several hours of operation at constant current and hydrocarbon feed rate. These samples were analyzed for mono- and dichlorododecanes by gas- liquid chromatography.

National Carbon Grade 60 (NC-60) porous carbon was used as anode material. This carbon is reported to have a void volume of about 0.2 cm^3/g in pores ranging from 10 to 60μ in diameter. Phillips pure-grade dodecane was the feed.

Voltametric cells.—Graphite-paste electrodes similar to those described by Adams (1) were constructed for the voltametric studies. The conductive pastes were prepared by mixing either dodecanes or unreactive binders with fine graphite powder. Holders were prepared from glass tubing. The lead wire extended through the glass tubing and was immersed in the paste which was packed in the end of the tubing. The electrode surface was the exposed area at the end of the tubing. Carbon or platinum counter electrodes were used. Reference electrodes were either saturated calomel or silver-silver chloride electrodes. The electrode potential was increased linearly with time relative to a reference electrode by a potentiostat based on operational amplifiers. Similar potentiostats are described in detail elsewhere (2). The cell current as a function of anode-to-reference voltage was plotted

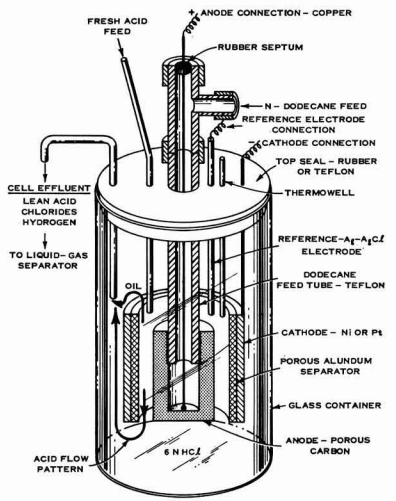

Fig. 1. Chlorination cell

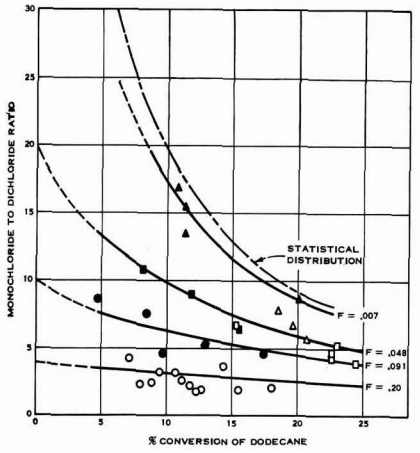

Fig. 2. Effect of current density and conversion on product distribution; current density, ma/cm²: ○, 17; ●, 50; □, 67; ■, 90; △, 120; ▲, 70-180 with peroxide additive.

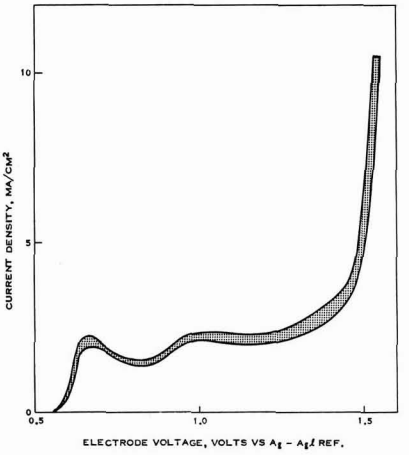

Fig. 3. Anodic voltage scans of several paste electrodes in 20% HCl containing 4 g/l potassium iodide; sweep rate, 0.32 v/min; *temperature*, 25°C; *substrate*, No. 38 Atcheson graphite; *binders*: 36.5 w/o dodecane, 58.8 w/o carbon tetrachloride, 62.5 w/o trichlorobromo-methane.

by an x-y recorder with a 2-sec pen and a 4½-sec chart. The voltage axis may also be considered a time axis by virtue of the linear sweep voltage.

Except as indicated the electrolyte was a 20% solution of hydrochloric acid. Some of the voltametric traces on paste electrodes were obtained in electrolyte containing 4 g/liter of potassium iodide. Consequently, oxidation peaks corresponding to the formation of iodine and iodine monochloride were noted in addition to the final upswing associated with chlorine evolution (Fig. 3). The purpose of this multiple oxidation was to show that different electrodes were comparable. It was found that paste electrodes varied in the chloride oxidation potential depending on the ratio of binder to substrate, the type of substrate, or even the mechanics of forming the electrodes. By demonstrating identical response to other reactions than the chloride oxidation confirmed that the analysis was not affected by compositional and mechanical variations in the electrodes.

Results and Discussion

Product distribution.—Products recovered in the continuous chlorination of dodecane were monochlorododecanes, dichlorododecanes, and higher chlorododecanes. One of the objectives of the product studies was to maximize the yield of monochlorododecane, which was considered to be the most important product from a commercial standpoint. Conversions were limited in this study to about 25% to minimize the yield of dichloro- and higher chlorododecanes. At conversions of 25% and less, the yield of higher chlorododecanes (primarily trichlorododecanes) was negligible. Therefore, the trichlorododecanes and higher are omitted from further discussion.

The product distribution obtained on dodecane chlorination is summarized by Fig. 2. This figure shows the monochloride-to-dichloride ratio as a function of dodecane conversion. It gives, in effect, selectivity to the two major products *vs.* conversion as affected by current density. At the highest current densities evaluated, the yields of monochlorododecane approached a calculated statistical distribution. This calculation assumed a simple model in which chlorine is evolved at the electrode and then substituted for hydrogen on the dodecane on a strictly statistical basis. For such a model the product composition is dependent only on conversion and the ratios of the rate constants for the various species present. Here, these ratios were taken to be equal to the ratio of hydrogen atoms in the respective species. Thus the ratio of reactivity of dodecane to monochlorododecane was taken to be 26/25. To a very good approximation the expected ratio of monochlorododecane to dichlorododecane can be related to extent of conversion as follows

$$R_1/R_2 = -(52 + \mathrm{Ln}\, X)/25\, \mathrm{Ln} X \qquad [1]$$

where R_1 is moles of monochlorododecane/mole of dodecane feed, R_2 moles of dichlorododecane/mole of dodecane feed, and X moles of unreacted dodecane/mole of dodecane feed.

The curve labeled "statistical distribution" on Fig. 2 is a graphical representation of Eq. [1]. Under favorable conditions this ratio was closely approached but in no case was the curve exceeded. The lines drawn through the experimental points on Fig. 2 were calculated from the statistical distribution on the assumption that a certain fraction, F, of the reacting dodecane molecules converted directly to dichlorododecanes by an alternate nonradical reaction mechanism.

The pronounced dependence of the product distribution on current density is thought to be a result of inhibition of the postulated radical mechanism by transport of trace amounts of free radical inhibitors from the bulk electrolyte into the reaction zone. At high current densities this inhibition effect could be overwhelmed by the increased chlorine concentration in the reaction zone. This reasoning also explains the beneficial effect of the benzoyl peroxide, which decomposes to produce radicals that could scavenge the inhibitors and, thus give much the same effect as an increase in current density. Another observation that substantiates the foregoing was the observed change in current efficiency and selectivity to monochlorododecanes that takes place during the first two or three hours of operation with a new anode. During this initial period there was a steady and significant improvement in current efficiency and selectivity to monochlorododecanes. It is postulated that a fresh carbon anode contains adsorbed oxygen or other impurities which consume chlorine or otherwise inhibit the formation of free radicals. Once these impurities were consumed, the electrodes were operated for several days with no change in performance. Current efficiencies were in the range of 80 to 100% and were substantially independent of current density, dodecane feed rate, and conversion level. The appearance of the surface of an anode was usually changed after it was used for chlorination, and the extent of the change appeared to depend on the cur-

rent-density history of the electrode. Extensive change in appearance was not observed except at current densities much beyond those reported.

Electrode reaction mechanism.—The results in Fig. 3 show that the reaction of chlorine and dodecane does not lead to significant electrode depolarization. Dodecane and fully halogenated binders gave equivalent traces. Similar results were obtained with a small NC-60 porous carbon electrode at several temperatures in the range of 25°-95°C. For example at a current density of 5 ma/cm^2 an electrode saturated with dodecane gave the same voltage as a similar electrode completely free of dodecane. In light of these findings, it seems reasonable to conclude that the chlorination of dodecane does not take place on the electrode surface to any significant extent at least at current densities in excess of 5 ma/cm^2.

Properties of the dodecane film on the anode and the dependence of these properties on feed rate, density differences, electrode geometry, and viscosity were not investigated by direct experiment. It is believed that under the conditions evaluated the dodecane film was continuous. Likewise, reaction rates were not directly studied. However, the rates were sufficiently fast to give essentially complete utilization of the evolved chlorine.

Conclusions

1. Utilizing a cell such as described, normal dodecane is continuously and efficiently chlorinated to dodecane monochlorides. Under favorable conditions, the product distribution approaches but never exceeds a calculated statistical distribution.

2. Approach to the statistical distribution is favored by high current density or free radical promoters in the feed.

3. There is no significant depolarization due to presence of dodecane on the anode.

4. The mechanism of the reaction is believed to be chlorine evolution followed by liquid-phase chlorination reaction, which is essentially complete before the dodecane breaks away from the anode.

Manuscript received Oct. 17, 1963.

Any discussion of this paper will appear in a Discussion Section to be published in the June 1965 JOURNAL.

REFERENCES

1. C. Olson and R. N. Adams, *Anal. Chim. Acta*, **22**, 582 (1960).
2. G. L. Booman, *Anal. Chem.*, **31**, 10 (1959).

New Methods of Obtaining Fuel Cell Electrodes

I. Aluminum-Nickel Mixed Powder Hydrogen Electrode

A. R. Despić, D. M. Drazić, C. B. Petrović, and V. Lj. Vujčić

Faculty of Technology, University of Beograd, and the Institute for Chemistry, Technology, and Metallurgy, Beograd, Yugoslavia

ABSTRACT

A new method of obtaining Raney nickel hydrogen electrodes was evaluated, in which the electrodes were made by pressing aluminum-nickel powder mixture, followed by simultaneous sintering of Ni skeleton and alloying of the surface layer of the formed Ni skeleton with aluminum present in its pores. The best results were obtained with a mixture of 10% (by weight) Al and 90% Ni, followed by sintering and alloying at 660°C for ½ hr. Such electrodes, with slopes of the anodic polarization curves of 0.8-1 cm^2 v/amp, and limiting current densities of *ca.* 250 ma/cm^2 were similar to those made of Ni and Raney-Ni powder of the same quality, according to the method of Justi. Microscopic investigation revealed that during the heating reaction between Ni and Al took place yielding Ni_2Al_3, which is electrochemically the most active type of Raney nickel alloy. In the case of double layer electrodes, made by this method, the extent of the active layer did not substantially influence the electrochemical characteristics of the electrodes down to 0.5 mm thickness. The major advantages of this type of electrode lie in the simplicity of their preparation as well as in their mechanical strength.

Catalytic activity, or sufficiently high working current density of a hydrogen fuel cell electrode at low polarization, can be achieved in two ways. One is that of impregnation of the inactive porous bodies [*e.g.*, made of porous carbon (1) or sintered Ni or Fe powders (2)] by an active component exhibiting a catalytic influence on the electrochemical reaction at the electrode (*e.g.*, platinum). The other way is that of mixing an electrochemically active component in the form of powder (*e.g.*, Raney nickel) with an inactive powder (*e.g.*, nickel), and then pressing and sintering this powder mixture into an active hydrogen electrode (3). In the latter case the role of the inactive component is to form a sufficiently strong metal skeleton, in the pores of which the particles of active Raney nickel alloy are situated. The particles of the Raney alloy themselves are not able to give sufficiently strong mechanical structure to the electrode.

The impregnation method has two major disadvantages. The first one is the high price of the catalytically active materials used in it (Pt, Pd, etc.) while the second one is the sensitivity of these catalysts to poisoning by very small amounts of impurities which can be present in the hydrogen used. Therefore, the danger of poisoning the electrodes implies the use of adequately purified hydrogen, increasing the cost of the fuel.

The Raney-type electrodes are known not to have both of the disadvantages mentioned above. How-

ever, the process of their preparation is considerably more involved, comprising the preparation of the Raney alloy, its disintegration into a powder of uniform particle size, mixing of Raney alloy powder with the corresponding Ni powder, pressing and sintering of this mixture into a compact body to be activated, and finally rendering the electrode active.

The purpose of this communication is to estimate the value of the ideas developed by Petrović, Despić, Jancić, and Drazić (4) that an active hydrogen electrode may be obtained by the formation of the Raney alloy at the pore-walls inside the inactive Ni porous body by the reaction of the surface layer of Ni with Al brought into the pores by a suitable method. This work is concerned with the investigation of the Raney nickel electrodes obtained by pressing and heating a mixture of aluminum and nickel powders. This process yielded simultaneous sintering of Ni particles and formation of Raney nickel by the reaction between Ni and Al.

Experimental

Two kinds of electrodes were used. For the first set of experiments the electrodes were made of a mixture of carbonyl nickel powder (Mond Nickel Co. nonfractionated Grade A) and an aluminum powder (Carlo Erba, with grain size ranging between 1 and 90μ). The percentage of Al in the mixture was varied between 0 and 15% (by weight). Such a mixture was homogenized manually in a porcelain mortar (homogenization in a mechanical homogenizer was inefficient because of the large difference in specific gravities of Ni and Al). An amount of this mixture was put into a die and pressed with a force of 50 tons to form a disk shaped electrode 40 mm in diameter and 1 mm thick.

In the second set of experiments double layer electrodes were made of the same shape as were the previous ones, but with a varying thickness of the active (coarse) layer (0.2-0.5 mm). Coarse layers were made of the same Ni-Al powder mixture with 10% Al, as used above. The fine layers were made of pure Ni powder (4-5μ grain size) and were 0.25 mm thick.

The sintering of such pressings was done at temperatures between 600° and 700°C, in an atmosphere of purified and dried hydrogen for ½ hr. The removal of oxygen from technical hydrogen was done with Deoxo equipment after which the gas was dried in a column with NaOH pellets. In the process of sintering, the double layer electrodes showed a tendency to bend because of different shrinking properties of the fine and coarse layers. This difficulty was overcome by applying an appropriate holder in which the electrodes were sintered while under slight pressure.

After cooling, the electrodes were placed into 6*N* KOH solution warmed to 80°C, in order to dissolve Al from the formed Raney alloy, so as to obtain the active form of the electrode. When hydrogen bubbles stopped evolving, the electrodes were taken out of the solution and were mounted in a special holder, enabling contact between one side of the electrode and hydrogen gas under a pressure of several atmospheres, as well as contact of the other side with 6N KOH solution (warmed to 60°C). The whole assembly was gas tight.

Prior to electrochemical investigations, an additional electrochemical activation was done in the usual manner by means of anodic polarization (3).

The investigation of electrochemical behavior of the electrodes was done in a thermostated cell in 6*N* KOH at 60°C by observing anodic polarization at varying current density. The electrode potentials were measured against a Hg/HgO reference electrode dipped into the same solution. All the values of the electrode potentials quoted below refer to the normal hydrogen scale, taking the potential of the mentioned reference electrode as + 0.057v (5). The ohmic

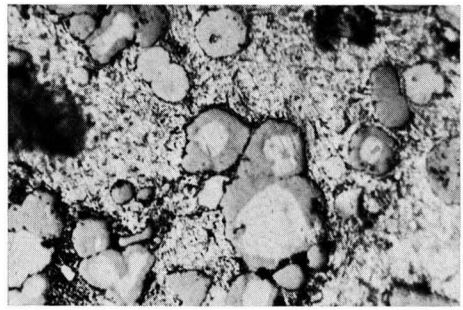

Fig. 1. Photomicrograph of Al-Ni mixture sintered at 680°C. Bright surfaces, Ni; gray surfaces, Ni_2Al_3; background, Al powder. Magnification 750X.

voltage drops between the tip of the Luggin capillary and the electrode were evaluated by means of the galvanostatic oscillographic method and it was found that even for the highest current densities they were less than 10 mv. Hence, in the subsequent course of measurements they were neglected.

The mechanical properties of the electrodes were examined by determining the bending strength of 10 mm wide strips cut out of the electrodes according to the standard method.

Results and Discussion

At the outset of this work there was little doubt that both alloying between Al and Ni powders and sintering of nickel particles could be achieved as separate processes (7). However, in order to get an electrochemically active and mechanically strong porous nickel electrode it was essential that under a given set of conditions sintering be effected before alloying took place to any noticeable extent.

In the course of preliminary studies a microscopic investigation was undertaken and a typical picture obtained is shown in Fig. 1 for a sample pressed and sintered at 680°C. This revealed that on one hand nickel particles could be joined together prior to their reaction with aluminum, and on the other hand that considerable alloying had taken place resulting in bluish-gray zones of newly formed phase at the surface of nickel particles. The new phase was found to be Ni_2Al_3 (6), which according to Justi *et al.* (4) is catalytically the most active type of Raney nickel alloy.

The effect of alloying of Al and Ni on the catalytic activity of electrodes can be seen from the results of the following experiments.

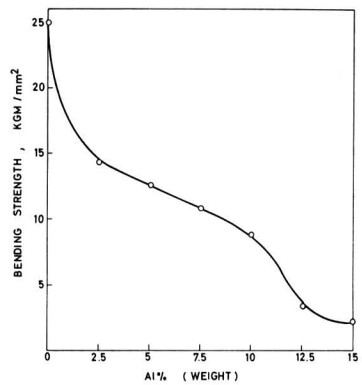

Fig. 2. Dependence of bending strength of sintered electrodes on percentage of Al.

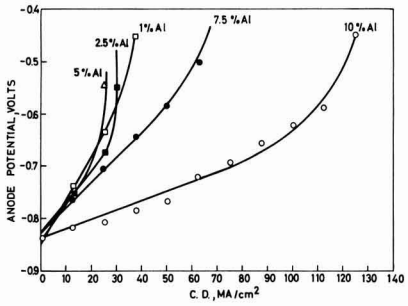

Fig. 3. Plots of electrode potential *vs.* current density for electrodes with varying Al content. m-the slopes of straight parts of the curves in cm^2 (volt/amp).

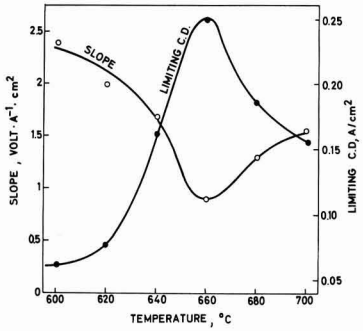

Fig. 4. Mean values of the slopes and limiting current densities as functions of the sintering temperature.

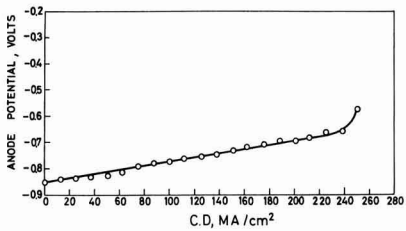

Fig. 5. Typical anodic polarization curve for an electrode sintered at 660°C. Pressure of H_2-2 atm.

In the set of experiments with a varying ratio of Al and Ni in the mixture the intention was to find the optimal content of Al, giving both good electrochemical characteristics and sufficient mechanical strength to sustain the pressure of the gas. Therefore the electrodes with various quantities of Al from 0 to 15%, sintered at 640°C, were first examined, both mechanically and electrochemically. The results of the mechanical tests are given in Fig. 2, in which the bending strength is plotted as a function of aluminum content. The bending strength of such electrodes was always lower than that of those made of pure Ni powder. However, up to 10% of Al, it was sufficiently high to give mechanically strong electrodes. Further increase in Al content resulted in a sharp decrease of the bending strength, and the electrodes made of such powder compositions were of no practical use in electrochemical examinations.

The results marking 10% as a critical content of Al can be considered as a support to the view that the aluminum particles, being relatively soft, deform under the applied force during pressing and fill the free space between the Ni particles. One can calculate that in order to fill with Al an ideal free space remaining between close packed Ni spheres of uniform diameter, irrespective of the sphere size, 15% of Al would be required. Taking into account that the Ni powder used in these experiments was a polydisperse system with grain sizes ranging from 1 to 40μ, it is obvious that smaller spheres of Ni could fill the pores in the same way as Al. This results in a smaller quantity of Al being necessary to fill the real free space between the adjoining Ni particles.

The results of the electrochemical investigations of the electrodes with various contents of Al are presented in Fig. 3. The slope (m, [cm^2 v/amp]) of the straight part of the polarization curve and the limiting current density were taken as criteria of the electrode quality. It can be seen that the increase in the Al content of the powder mixture resulted in increasingly better electrochemical properties of the obtained electrodes, *i.e.*, decreased the value of the slope and increased the limiting current density.

Since the sintering process is competitive to the process of formation of the Raney alloy, sintering temperature was expected to have an influence on the properties of the electrodes. The effect of temperature on mechanical properties of electrodes is presented in Table I, for electrodes with 10% Al content. The increase of the sintering temperature resulted in an increase of the bending strength, probably because of a more pronounced sintering between the Ni particles giving a more compact Ni skeleton.

Table I. Effect of sintering temperature on the bending strength

Temperature	640°	660°	680°	700°
Bending strength, kg/mm^2	9.9	10.3	11.0	13.2

The effect of temperature on electrochemical properties is presented in Fig. 4. The graphs represent the dependence of the slopes and the limiting current densities of the tested electrodes on temperature. Each point represents a mean value of 1-3 electrodes. Under the given experimental conditions it appears that *ca.* 660°C was the most appropriate temperature for obtaining optimal electrochemical behavior of the electrodes. A graph representing a typical current-potential relation for one of the electrodes sintered at 660° is given in Fig. 5.

It was also observed that the optimal sintering temperature depends on the quality of the hydrogen purification. With hydrogen deoxygenated in a column filled with Pd asbestos heated at 300°C, dried in silica-gel columns and with the final traces of humidity removed by a trap dipped into liquid air, the electrodes sintered at 660° showed the effects of oversintering. They were mechanically stronger but their electrochemical behavior was worse.

The effect of thickness of the active layer of the double layer electrodes on their electrochemical behavior has been studied on the electrodes sintered at 640°. The thickness of the coarse (active) layer has been varied between 0.2 and 0.5 mm. The current-potential dependences for these electrodes are presented in Fig. 6, together with the corresponding graph for a 1 mm thick single layer electrode. These data indicate that the thickness of the active layer has a profound influence on the electrochemical properties below 0.5 mm, while above that it does not have any marked influence, the results being similar to those for 1 mm thick electrodes. One should point out here that similar results were obtained in this Institute earlier with 3 mm thick electrodes (5) made of the same Ni powder and a separately prepared Raney alloy according to the method used by Justi *et al.* (3).

Since both Ni and Al powders used in these experiments had wide spectra of grain sizes, homogeneous porosity has not been achieved in our experiments, although this is known to be an important factor in

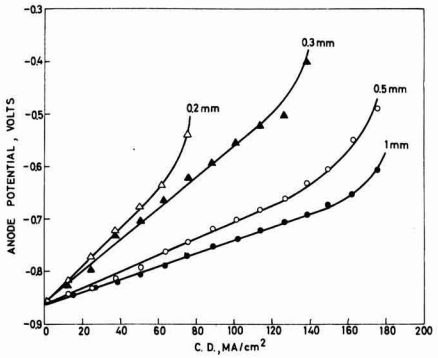

Fig. 6. Effect of thickness of the active layer of double layer electrodes on the polarization curves.

obtaining highly active hydrogen electrodes. It can be expected that by carefully selecting proper particle sizes of Ni and Al powders one should be able to obtain much better electrochemical properties of the electrodes made according to the given method.

Manuscript received Jan. 22, 1964.

Any discussion of this paper will appear in a Discussion Section to be published in the June 1965 JOURNAL.

REFERENCES

1. K. Kordesch, "Fuel Cells," G. Young, Editor, p. 11, Reinhold Publishing Co., New York (1960).
2. *Chem. and Eng. News*, **41**, No 38, 60 (1963).
3. E. Justi and A. Winsel, "Kalte Verbrennung," F. Stein. Wiesbaden (1962).
4. C. B. Petrović, A. R. Despić, M. Dj. Jancić, and D. M. Drazić, Method of obtaining fuel cell electrodes by reacting in situ a metal powder mixture forming Raney alloy. Yug. pat. appl.
5. Fuel cell research team, Project Report. Institute for Chemistry, Technology, and Metallurgy. Beograd, 1962.
6. M. Z. Malcev, T. A. Barsunova, and F. A. Borin, "Metallografya cvetnih metallov i splavov," Metalurgizdat, Moscow, 1960.
7. T. Yamanaka, *Repts. Sci. Research Inst. (Japan)*, **31**, 58 (1955).

The Role of Antimony in Positive Plate Behavior in the Lead-Acid Cell

Jeanne Burbank

United States Naval Research Laboratory, Washington, D. C.

ABSTRACT

Antimonial and antimony-free lead-acid cells of similar construction were examined together in a shallow cycle routine. The presence of antimony in the positive grid alloy caused depolarization of the plate in the float condition. It did not affect the discharge potential of the plate. The positive plate active material became progressively softer in the antimony-free cells which failed after short test duration. The antimonial cell maintained its capacity and the active material remained firm. The active material of both successful and failing positive plates was examined by electron microscopy and x-ray diffraction. The active material in the antimonial cell contained many complex prismatic crystals, whereas the antimony-free cell was characterized by nondescript nodular masses. The active material in the antimonial cell contained a large amount of α PbO_2 while the antimony-free positive contained very little of this polymorph. Because both kinds of cell were pasted and formed by the same manufacturer with the same paste formulation, it is concluded that the difference in paste morphology and composition is caused by the presence of antimony in the positive grid. It is also concluded that success or failure in float cycle tests is determined by the morphology of the positive paste.

The lead acid cell normally is fabricated with grids of lead alloyed with 5-12% antimony. This antimony has long been known to affect cell behavior in several ways, but the benefits resulting from its use have outweighed its deleterious effects, and today only special purpose cells are manufactured without antimony. The antimonial alloys are easier to cast than the antimony-free metals, lower casting temperatures are required, better castings are the rule because molds are readily filled by the melt, and the strength of the alloy makes it possible to handle and fabricate the castings immediately. In addition, antimony minimizes grid growth by distributing the corrosion attack across the body of the grains, relieving attack at the grain boundaries. All these factors combine to promote continuation of the use of antimony in the lead acid cell.

The hydrogen overvoltage on antimony is lower than on lead, and this causes spontaneous self-discharge of the negative plate. As antimony accumulates on the negative plate during operation of the cell, the efficiency of charge decreases because of the low hydrogen overvoltage on the antimony, and increasing portions of the charging current are wasted in generation of hydrogen gas. It is possible to scour the negative plate of antimony by overcharging, when it is driven off as stibine, but stibine is a poisonous gas, and charging in confined spaces may present a health hazard.

It has been shown that antimony is leached from the positive grid during charge of the battery and radioactive isotopes have been used to trace the migration of antimony in the cell. Antimony does accumulate to some extent in the positive active ma-

terial, and self-discharge of this plate has been investigated; however, the effect of antimony on the positive plate of the lead acid cell is not usually considered detrimental. Nevertheless, antimony initially in the positive will eventually find its way to the negative and cause the major deleterious side reaction, interference with charging of the plate.

In some recent studies with antimony-free lead-calcium cells, it has been shown that in certain cells the positives were failing through rapid softening of the positive active material which resulted in 80-90% loss in ampere-hour capacity. These studies showed that the positive active material of the failing cells was made up of nondescript nodular particles of PbO_2, whereas successful antimony-free lead-calcium cells contained prismatic crystalline particles. The difference in performance of these positive plates was attributed to this difference in morphology of the PbO_2 (1-18).

The paste used in fabricating the failing lead-calcium cells was the same as normally used in the manufacturer's production of antimonial cells, and these, in turn, were performing satisfactorily in normal service. Therefore, the studies with the antimony-free lead-calcium cells that failed by softening of the positive paste presented a unique opportunity to study the effects of antimony on cell behavior because it was possible to obtain the same paste in an antimonial grid and thus directly compare antimonial and antimony-free cells, identical in all respects except for the positive grid alloy.

Experimental

The plates used in this investigation were all obtained from a single manufacturer, and the only difference between them was that one positive grid was a standard antimonial lead alloy, whereas the other grids were lead calcium alloy. The pasting and forming were carried out by the manufacturer under reputedly identical conditions, and the positives were "formed but not charged" when the cells were assembled for this study. Lead calcium alloy negative plates were used in all cells.

Four small cells were assembled, each having one positive and two negative plates, with standard glass mat retainers and microporous rubber separators. Two sets of two cells each were run in series. The power supply, controller, and auxiliary electrode circuit of the battery analyzer of Work and Wales (19) were used to test the cells. A mercury, mercurous sulfate reference electrode in each cell was used to measure plate potentials, with the plate and cell voltage and the current monitored continuously.

The cells were assembled in plastic cell cases and filled with 1.200 sp gr H_2SO_4. Charging was carried out according to the manufacturer's standard instructions. Following the initial charge, the specific gravity was adjusted to 1.250-1.260.

The cells, which were all positive-plate limited, were given several cycles to develop capacity and then placed on the float cycle routine known to produce rapid failure in the lead-calcium cells (17, 18). These tests are summarized in Table I.

During the tests, the positive plates were inspected visually at intervals, and before and after the tests the positive active material was examined by electron microscopy. For the electron microscopic examination, samples of the paste were extracted with saturated ammonium acetate solution to remove any divalent lead compounds present. Drops of the slurry of extracted material were gently touched to the surface of distilled water in a 10-in. crystallizing dish. The particles floated out across the surface and were picked up on parlodion covered specimen screens of the electron microscope. After drying, the particles were replicated with evaporated carbon (20).

Following replication, the parlodion supporting films were removed by solution in acetone. The PbO_2 was dissolved in dilute HNO_3 containing H_2O_2, and the carbon replica was rinsed by floating on water. After air drying, the replicas were photographed in the electron microscope, model RCA EMU-2B.

The active materials from both kinds of positive plate were examined by x-ray diffraction using a General Electric XRD-5 X-Ray unit and copper radiation. The pastes were examined before and after the float cycle tests.

Table I. Summary of tests and results

Capacity cycle No.	Charge, amp-hr	Number of float cycles	Discharge capacity, amp-hr	
Calcium cells 1 & 2			Cell 1	Cell 2
1	—	—	>8.47	8.47
2	10.57	10	>8.37	8.37
3	8.05	7	>7.65	7.65
4	7.53	9	>7.15	7.15
5	7.25	5	>7.13	7.13
6	7.25	7	4.73	6.23
Calcium cell 3				
7	—	—	8.00	
8	8.40	8	6.30	
9	7.36	9	6.27	
10	7.92	14	5.03	
11	8.37	12	3.56	
12	3.69	9	1.53	
13	4.53	9	0.80	
Antimonial cell				
14	—	—	8.00	
15	8.40	8	7.60	
16	9.17	9	7.60	
17	7.92	14	7.50	
18	8.37	12	7.40	
19	7.36	9	7.40	
20	7.70	9	7.30	

Notes: Each capacity cycle in this series of tests comprised a constant voltage charge followed by a series of shallow daily float cycles for 5 to 14 days with continuous float at 2.24v per cell during the intervals. Capacity discharges were given every two weeks with constant voltage recharge at 2.24v.

In capacity cycles 2, 11, and 13 the cells were given constant current overcharges. Capacity cycles 1, 7, and 14 show the initial cell capacities prior to the start of the tests.

Each float cycle in the tests of calcium cells 1 and 2 comprised a discharge of 1 amp-hr at 2 amp, and recharge by float with interim float. One float cycle was given each work day until the next succeeding capacity discharge. Calcium cell 3 and the antimonial cell were in series for these tests, and cell 3 was used as control for float and the constant voltage charges. The effect of antimony on the cell and plate voltages could be followed by direct comparison with the antimony-free calcium cell. When required, these two cells were separated and handled individually; for example, for capacity discharges 8 to 13 and 15 to 20, it was necessary to run the capacity discharges and recharges individually.

At capacity cycles 6 and 13 the positive plates of the calcium cells were soft and mushy, whereas at capacity cycle 20 the antimonial cell positive was firm and in good condition.

Results and Discussion

Table I shows the capacities obtained from the cells, and also indicates that the antimony-free cells with lead-calcium alloy grids failed after relatively short test duration. The 90% fall in cell capacities, curve B, Fig. 1, illustrates a typical failure of these antimony-free cells. Failure was due to the positive plate in every case.

In contrast to this, the capacity of the antimonial cell, curve A, Fig. 1, changed hardly at all despite

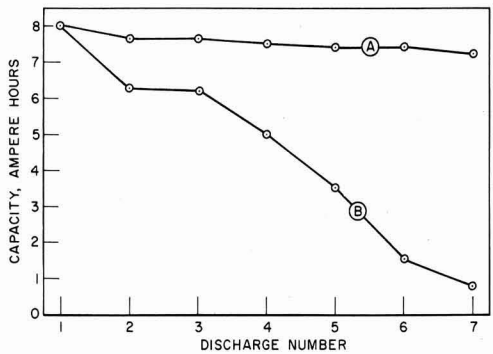

Fig. 1. Change in cell capacity in shallow cycle test. Curve A, antimonial cell; curve B, lead calcium cell.

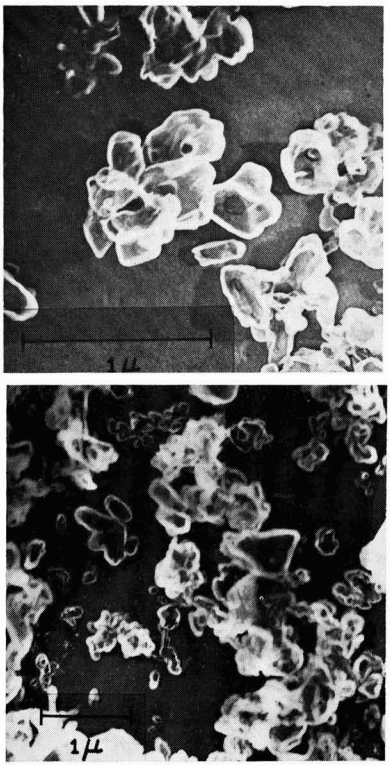

Fig. 2. Typical examples of nondescript nodular PbO_2 particles. These particles were taken from lead calcium cells that consistently failed in float installations and in float cycle tests. See also ref. (17), (18), (31).

the fact that it did not receive the overcharge normally used to maintain antimonial cells. This satisfactory behavior of the antimonial cell was not unexpected in light of earlier work (22).

It had not been known with certainty whether the identical paste would stand up in an antimonial cell in a similar test, but the results of the tests reported here show that the same paste in an antimonial cell did not fail as rapidly as in the lead-calcium cells, and it gave no indication of incipient failure at the time the tests were terminated.

When the cells were opened for inspection, the calcium positives were very messy to handle: PbO_2 smeared readily over glass mats, paper towels, and glass rods used as probes, and enough washed off to discolor the electrolyte heavily. In contrast, the antimonial positives were much cleaner, the glass mats were white and clear, some PbO_2 wiped off on paper towels used to handle the wet plates and the glass probes, but not enough floated away to cause even a noticeable discoloration of the electrolyte. To be sure, the wet working positive plate of any lead cell is softer than the same plate dried, and PbO_2 can usually be smeared from the surface; however, the totally mushy condition of the failing calcium positive is

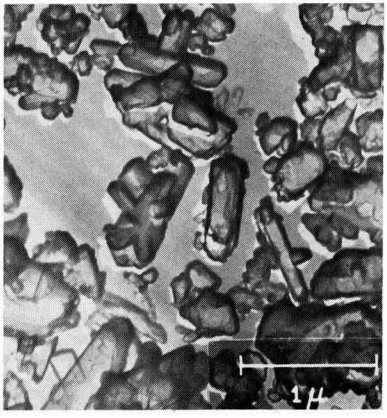

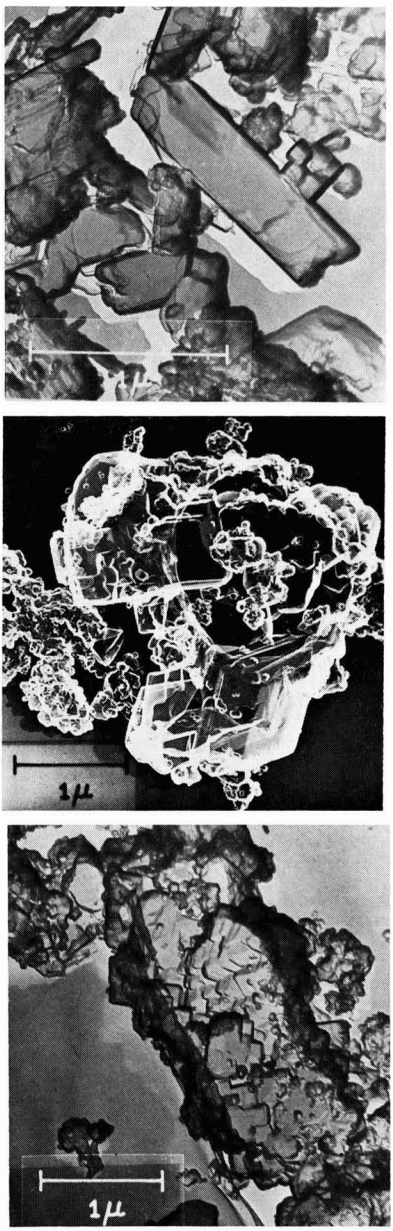

Fig. 3. (left and above) Typical examples of prismatic PbO_2 particles from lead antimony positive plates. The positive plate containing particles such as shown here was successful in the shallow cycle test, in normal service life, and cycle life test, and maintained its firm texture and capacity. See also Fig. 6, ref. (31).

much more pronounced, and the softening proceeds through the thickness of the plate until the entire active mass may be washed out with a stream of water (17, 18).

The sole difference between the positives in these cells was the presence of antimony in the grid metal. It is concluded that the presence of antimony in the grid inhibited or prevented the softening of the paste and the resulting loss in capacity.

In this work with the antimonial and calcium cells, the calcium cell was used for voltage control in order to determine the electrochemical effects of the antimony. The well-known depolarization of the negative plate, in itself, prevents an antimonial negative from controlling float as the negative does in antimony-free cells (7, 16, 18, 21, 23, 24). The presence of antimony in the positive grid caused 20-70 mv depolarization in overcharge at constant current. However, the positive plate voltages relative to the mercury, mercurous sulfate reference electrode of both the antimonial and calcium cells were identical during charge and discharge, and no electrochemical effect of the antimony was observed when the cell was in either of these conditions.

Electron micrographs of the positive active material showed that, in the failing lead-calcium cells, the individual particles were nondescript globules both before and after failure (17,18) and some typical examples are shown in Fig. 2. In contrast to this, the same positive paste from the antimonial cell was found to contain large amounts of prismatic material and some typical electron micrographs are shown in Fig. 3. It is concluded that the presence of antimony has affected the morphology of the PbO_2 particles formed in the paste. The electron micrographs indicate that the prismatic material takes the form of extensive complex clusters that appear to be multiple twins or parallel growths. It is believed that these crystalline formations impart mechanical stability to the positive active material. This prismatic morphology observed by electron microscopy is believed to be required in order to maintain the firm texture of the positive plates in the lead cell.

On the basis of these results, it is concluded that the antimony exerts the direct and beneficial influence of causing prismatic PbO_2 formation in the positive active material. The mechanism of this action remains to be studied; however, it appears likely that preferential adsorption of a soluble antimony species on the growing surface of the PbO_2 crystal may control the morphology. Antimony forms the ions SbO_2^+ and SbO_3^- at positive plate potentials (25). X-ray diffraction showed that metallic antimony itself becomes passivated by a heavy layer of Sb_2O_5 at this potential when anodized in H_2SO_4 solution, but this oxide is rather soluble, and the determinative influence of soluble species on electrodeposits is well known (26). The work described here indicates that the presence of antimony in the grid metal influences the morphological development of electrochemically formed PbO_2 in the positive plate of the lead acid cell, but the precise mechanism of this action remains to be clarified.

In nonantimonial cells where a prismatic PbO_2 morphology was previously observed by electron microscopy (16, 18), it was accompanied by a sponge-like network of harder material, visible in the magnification range of the optical microscope (27); however, in the antimonial and nonantimonial positive plates used in this work, no such network was visible in the formed plate when examined optically prior to testing, and none was present in the nonantimonial plate at the conclusion of the tests (28). The intricate shapes of the submicroscopic crystals in the antimonial positive, Fig. 3, suggest that it may be possible for them to form an interlocking network, but, of course, this would not be observable by optical means.

X-ray diffraction examination of the positive active materials showed that the paste from the antimonial cell contained appreciable amounts of both α and β PbO_2, whereas the paste from the lead-calcium cell contained a very large preponderance of β PbO_2 and only a very small amount of α PbO_2. At the conclusion of the tests, the amount of α PbO_2 in both types of plate had decreased, but a considerable amount was still present in the antimonial positive. Simultaneously, the amount of β PbO_2 had increased in both plates.

It is concluded from this study that antimony in the grid metal acts to promote the deposition of α PbO_2 in the active material during plate formation, possibly by the same mechanism as cobalt ion (26).

Variations in the α PbO_2 content of positive pastes have been studied, and, in SAE overcharge tests, it extends the life of the plates (29, 30). It has also been suggested that there may be a relation between α PbO_2 and positive paste retention in the lead acid cell (27). The presence of a large amount of α PbO_2 in the antimonial active material and the performance of the antimonial cell in the tests reported here lend some credence to this speculation.

Conclusions

On the basis of the results of this study, it is concluded that the beneficial effects of having antimony in the positive grid are: (*a*) development of significant amounts of α PbO_2 during plate formation, (*b*) retention of a firm paste texture and cell capacity in shallow cycle tests, and (*c*) prismatic crystallization of the PbO_2 particles making up the paste. Without antimony, only a small amount of α PbO_2 was present initially, the paste softened and lost capacity in the shallow cycle tests, and the paste contained few, if any, prismatic crystals. These conclusions are in agreement with those of earlier studies that showed that success or failure in float cycle tests was related to the morphology and texture of the positive paste (16-18).

Manuscript received March 26, 1964.

Any discussion of this paper will appear in a Discussion Section to be published in the June 1965 JOURNAL.

REFERENCES

1. G. W. Vinal, "Storage Batteries," 4th ed., John Wiley & Sons, Inc., New York (1955).
2. L. Jumau, *Eclairage electrique*, **16**, 133 (1898).
3. Strasser and Gahl, *Z. Elektrochem.*, **7**, 11 (1900).
4. J. T. Crennel and A. G. Milligan, *Trans. Faraday Soc.*, **27**, 103 (1931).
5. G. W. Vinal, D. N. Craig, and C. L. Snyder, *Bur. Standards J. Research*, **10**, 795 (1933).
6. H. E. Haring and K. G. Compton, *Trans. Electrochem. Soc.*, **68**, 283 (1935).
7. H. E. Haring and U. B. Thomas, *ibid.*, **68**, 293 (1935).
8. J. W. R. Byfield, *ibid.*, **79**, 259 (1941).
9. A. C. Zachlin, *ibid.*, **82**, 365 (1942).
10. A. C. Zachlin, *ibid.*, **92**, 259 (1947).
11. J. J. Lander, *This Journal*, **99**, 339 (1952).
12. J. J. Lander, *ibid.*, **99**, 467 (1952).
13. J. B. Burbank and A. C. Simon, *ibid.*, **100**, 11 (1953).
14. W. Herrmann and G. H. Proepstl, *Z. Elektrochem.*, **61**, 1154 (1957).
15. W. Herrmann, W. Ilge, and G. H. Proepstl, "The Migration of Antimony in the Grid of a Lead Storage Cell Studied Using a Radioactive Tracer Method" in "United Nations Peaceful Uses of Atomic Energy," Proceedings of the Second International Conference, Geneva, September 1958, p. 272, Pergamon Press, New York (1959).
16. J. Burbank and C. P. Wales, "The Lead Calcium Battery, Part 2. Small Portable Cells," Naval Research Lab. Report 5770, May 2, 1962.
17. J. Burbank and C. P. Wales, "The Lead Calcium Battery, Part 3. Submarine Cells," Naval Research Lab. Report 5773, May 29, 1962.
18. J. Burbank, "Positive Plate Characteristics in the Floating Lead-Calcium Cell" in "Batteries," Proceedings of the 3rd International Symposium,

Bournemouth, October 1962, p. 43, D. H. Collins, Editor, Pergamon Press, New York (1963).
19. G. W. Work and C. P. Wales, *This Journal*, **104**, 67 (1956).
20. D. E. Bradley, *J. Appl. Phys.* **27**, 1399 (1956).
21. J. Burbank and C. P. Wales, "The Lead Calcium Battery, Part 1, Introduction and Background," Naval Research Lab. Report 5693, Nov. 22, 1961.
22. J. J. Lander, "Life Tests of Thin Plate Lead Acid Cells under Cycle, Stand, and Float Routine," Naval Research Lab. Memorandum Report 556, January 1956.
23. U. B. Thomas, F. T. Forster, and H. E. Haring, *Trans. Electrochem. Soc.*, **92**, 313 (1947).
24. R. C. Shair, *AIEE Trans.*, Pt. II (Applications and Industry) **79**, 1 (1960).
25. M. Pourbaix, *et al.*, "Atlas D'Equilibres Electrochemiques," p. 524 ff. Gautier-Villars & Co., Paris (1963).
26. I. I. Astakhov, I. G. Kiseleva, and B. N. Kabanov, *Doklady Akad. Nauk USSR*, **126**, 1041 (1959).
27. A. C. Simon and E. L. Jones, *This Journal*, **109**, 760 (1962).
28. A. C. Simon, Private communication.
29. V. H. Dodson, *This Journal*, **108**, 401 (1961).
30. V. H. Dodson, *ibid.*, **108**, 406 (1961).
31. J. Burbank, *ibid.*, **111**, 765 (1964).

Corrosion of Steels and Nickel Alloys in Superheated Steam

W. E. Ruther and S. Greenberg

Metallurgy Division, Argonne National Laboratory, Argonne, Illinois

ABSTRACT

The corrosion behavior of the 18-8 stainless steels and some nickel alloys in superheated steam was found to be dependent on the surface preparation. Those treatments which left a severely cold worked surface resulted in reduced corrosion attack in subsequent exposure to steam as compared with annealed metal surfaces. The corrosion rate of electropolished annealed type 304 stainless steel in oxygenated (30 ppm) steam rose rapidly as the temperature increased from 540° to 650°C. At 600° and 650° the measured rate decreased with increasing time during 80 day static tests. The corrosion appeared more linear with time in dynamic tests at 650°C (~7 mg/dm^2-day). In these tests there appeared to be no effect of velocity (30-91 m/sec) or oxygen and hydrogen content on the corrosion rate. Flaking and loss of the outer corrosion coating was severe in the dynamic tests. The corrosion rate of type 406 was too small to be precisely measured in all of the tests, static and dynamic, in which it was simultaneously exposed with type 304. A coating equivalent to about 2 x 10^{-4} cm metal penetration was formed on the initial exposure of 406. No flaking of the outer coating was evident in 80 day tests. The corrosion attack of the 400 series steels in static oxygenated steam went down with increasing chromium content, particularly above about 13 w/o Cr. Both type 430 (16 w/o Cr) and 446 (25 w/o Cr) exhibited greater short term corrosion resistance than type 304 to 650°C, 42 kg/cm^2 steam. The nickel based alloys, particularly Inconel 625, were also more corrosion resistant than type 304 in short static and dynamic tests in 650°C, 42 kg/cm^2, superheated steam.

The cycle efficiency of a boiling water nuclear electric power plant can usually be improved substantially by incorporating a nuclear steam superheater before the turbogenerator. Special environmental conditions are encountered in such a superheater as compared with typical fossil fuel installations. For example, oxygen concentrations of 20-30 ppm and stoichiometric amounts of hydrogen might be expected in steam passing through the intense radiation field. The requirement for thin protective fuel element cladding (to reduce neutron losses) introduces serious corrosion penetration problems.

Spalaris and co-workers (1) have reviewed the available nonnuclear steam corrosion literature. They concluded that much of the data, typically obtained from weight gains and/or scale thickness, did not permit calculation of precise corrosion rates. Furthermore, these data were obtained in steam of very low oxygen content since that is the normal operating condition for nonnuclear boilers.

Recently, several of the laboratories associated with nuclear power plant design have been re-evaluating commercial alloys in simulated reactor steam environments in static autoclaves and dynamic test facilities (2, 3). Much of the effort has been concentrated on corrosion cracking since the serious nature of that problem became apparent in early in-reactor experiments (4). While it was not the intent to minimize the potential cracking hazards, this laboratory chose initially to study other variables. The effects of steam temperature, pressure, oxygen and hydrogen content, and velocity on the general corrosion rate were investigated. Since the work was performed in support of a specific reactor superheater, the major fraction of the data involved the design temperature and pressure for that reactor (650°C, 42 kg/cm^2)[1]. For the same reason first 304 and later 406 stainless steel received particular attention.

Experimental

The static testing of corrosion coupons was performed in constantly refreshed type 347 stainless steel autoclave systems of about 1.5 liter capacity. Deionized, distilled water was vacuum degassed in storage carboys and then charged with the desired gas. A flow of about 5 ml/min of this water was pumped into the high-pressure system. A boiler and superheater preheated the stream prior to its entering the

[1] One kg/cm^2 equals 14.2 psi.

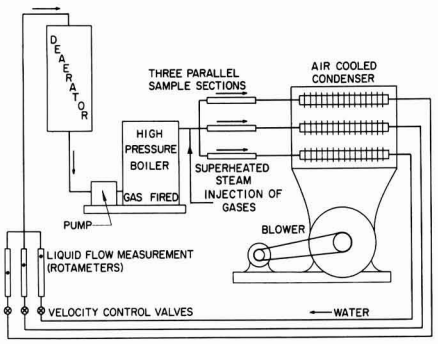

Fig. 1. Schematic diagram of dynamic test facility. Maximum test conditions: 650°C; 1000 psi; 300 ft/sec.

test autoclave. The outgoing steam was condensed in an air cooler, and the condensed water left the system via a back pressure regulator. Care was taken to provide open space around each specimen in the autoclave sufficient to prevent local depletion of oxygen in the slowly moving steam.

The high velocity testing was accomplished in a recirculating system shown schematically in Fig. 1. Type 318 stainless steel tubing and type 316 Swagelok fittings were used in the high-temperature section. Condensate water flow rates were converted to steam flows through the use of steam tables. Although 270 kg/hr of deionized distilled water were converted to steam and condensed, the steam channels were necessarily small to permit corrosion studies at velocities up to 91 m/sec past the specimens. Dimensions of the flat samples were 5 x 1.2 x 0.16 cm. Oxygen and hydrogen were introduced directly in the steam through high-pressure gas rotameters. The oxygen content of the condensate was determined using an Industrial Instruments oxygen analyzer. This analyzer depends on the specific reaction between thallium metal and dissolved oxygen in deionized water. The amount of reaction, hence the dissolved oxygen content, is measured by the conductivity of the effluent solution of thallium hydroxide.

Except as specifically noted, the specimens were corrosion tested in the annealed condition. The General Electric Company supplied the Rene' 41 alloy and the International Nickel Company supplied the other nickel alloys used in this investigation. Chemical compositions are given in Table I.

Electropolishing of all of the alloys was accomplished in a 12.5% phosphoric acid, 65% sulfuric acid, 22.5% water (per cent by volume of the concentrated acids) bath at 85°C. Current densities (0.3-0.6 amp/cm^2) were varied from one alloy to another to obtain good polishing. The bath was not too satisfactory for 403 and 410 steels due to acid attack, and Rene' 41 did not polish as brilliantly as did most of the other alloys. In one instance a 10% perchloric acid, 90% acetic acid mixture was used on the 300 series stainless steels.

Surface preparations, other than electropolishing, consisted of acid etching (dilute nitric-hydrofluoric acid mixture), grinding (metallographic wheels—Durite paper), grit blasting (50μ SiO_2 particles), and machining.

Since an unknown portion of the corrosion coating was lost to the test environment, weight gains could not be used to determine the average corrosion rate. A rather lengthy, but effective, defilming process was evolved. First the sample was made the cathode at about 0.3 amp/cm^2 in 1 w/o (weight per cent) dibasic ammonium citrate solution at about 85°C. The current was alternately applied and interrupted for 30 sec intervals by an automatic timer. After about 15 min in this bath, the outer layer of the corrosion coating could be brushed off. The inner layer was removed by a defilming process developed at the Knolls Atomic Power Laboratory (5). This consisted of 2 hr in gently boiling alkaline permanganate solution (20 w/o NaOH, 3 w/o $KMnO_4$), a hot rinse, and 2 hr in 20 w/o dibasic ammonium citrate solution. The samples were brushed at the conclusion of this treatment with a nylon hand brush to remove the loosely adherent smut. A second run through the last two solutions was necessary in the case of some stubborn films. Blank losses for this defilming technique were very low compared with the typical amounts of total corrosion for the 300 series stainless steels (*i.e.*, 0.02 mg/cm^2 for 304) and the nickel alloys. While the blank losses were higher for the ferritic steels, the process was still satisfactory for 406 and 446.

Data and Results

Surface preparation effects.—In the initial steam corrosion experiments a wide range of total attack was noted for type 304 and 347 samples obtained from different sources. Some specimens acquired only a thin colored temper film during an exposure which resulted in heavy corrosion product coatings on other coupons of the same nominal composition. In one case the machined edges of a sample corroded much less than the as-received faces of the same specimen. It was obvious that these large surface effects had to be investigated before meaningful corrosion rates could be measured.

In the first series of experiments only two types of sample preparation were tested for a number of different alloys. The oxygen content of the superheated steam was varied with the results shown in Table II.

The surface effect was much more pronounced in the case of low oxygen content steam and was noted for all the alloys except Inconel 625 and Rene'41.

Table I. Chemical compositions of alloys

Alloy	Percentage by weight										
	Al	Cr	C	Fe	Mo	Mn	Ni	P	Si	S	Other
304		18.2	0.07	R		1.68	8.76	0.026	0.85	0.01	
316		17.5	0.05	R	2.50	1.62	13.45	0.025	0.49	0.021	0.20 Cu
321		18.0	0.04	R	0.30	1.38	9.62	0.019	0.88	0.013	0.53 Ti
347		18.6	0.078	R		1.82	10.8	0.028	0.82	0.010	(Cb + Ta) 0.90
403		12.3	0.12	R		0.46		0.015	0.27	0.013	
405[1]	0.2	12.5	0.08	R							
406	4.48	13.1	0.11	R		0.44	0.36	0.019	0.46	0.007	
410		12.5	0.13	R		0.44		0.013	0.25	0.009	
410 (E2)		11.6	0.03	R					0.5		0.50 Ti
430		16.3	0.08	R		0.40		0.021	0.50	0.011	
446		24.7	0.09	R		0.62		0.023	0.35	0.010	
Incoloy 800		20.0	0.04	45.2		0.85	33.0		0.40	0.007	0.41 Cu
Inconel 600		16.3	0.04	7.24		0.17	75.9		0.29	0.007	
625	0.17	22.0	0.03	1.86	8.75	0.12	62.3		0.25	0.007	[(Cb + Ta) 4.24, Ti] 0.23
X750	0.74	15.13	0.04	6.87		0.45	72.5		0.25	0.007	(Cb + Ta) 0.98, Ti 2.62
Rene' 41	1.52	19.05	0.07	0.3	9.83		R		0.05	0.005	3.21 Ti 10.95 Co

R—Remainder. [1] Nominal analysis.

Table II. Corrosion in static refreshed superheated steam at 650°C, 42 kg/cm² (600 psig)

Alloy	Defilmed metal loss, mg/cm²			
	0.03 ppm Oxygen		30 ppm Oxygen	
	Wet ground	Electro-polished	Wet ground	Electro-polished
304	0.15	6.96	6.63	7.45
316	0.15	11.7	1.74	9.16
321	0.16	9.10	0.34	9.04
347	0.16	10.2	3.87	11.2
Inconel 600	0.45	3.21	0.22	0.44
Inconel 625	0.11	0.12	0.10	0.16
Inconel X750	0.25	1.96	0.19	0.20
Incoloy 800	0.13	4.67	0.21	8.30
GE Rene' 41	0.13	0.20	0.14	0.15

7.0 Days exposure, 3-hr start-up.

Table III. Corrosion of type 304 stainless steel in 650°C, 42 kg/cm² steam

Surface preparation	Defilmed metal loss, mg/cm²	
	30 ppm O_2	0.2 ppm O_2
Grit blast (50μ SiO_2)	2.3	1.0
Machined	3.6	0.06
Wet grind 80 grit	8.4	0.45
Wet grind 240 grit	13.8	0.25
Wet grind 600 grit	11.8	0.72
Mechanically polished (Linde B)	11.5	15.6
Electropolished	8.0	13.1
Acid pickled	12.8	14.2

Tested 7.0 days, 3-hr start-up.

Other stainless steel samples were electropolished in a perchloric-acetic bath and corrosion tested with those prepared in the usual phosphoric-sulfuric solution. The same corrosion behavior was observed for both sets of samples, indicating that the poor corrosion resistance was characteristic of the polished surface and was not due to a residual phosphate or sulfate film.

Investigating other surface preparations for type 304, it was observed (Table III) that essentially strain-free surfaces resulted in a maximum metal loss during the one week corrosion test. Again, this was particularly noticeable in the results from the experiments with lower oxygen concentration.

Two further series of experiments were performed to test this tentative conclusion. In the first, samples were vacuum annealed after preparing them in several ways which had previously resulted in low metal loss values on exposure to steam. The result of annealing in each case was to increase the corrosion loss significantly (Table IV).

Since a cold worked disturbed layer apparently provided improved corrosion resistance, a second series of experiments was performed with 304 sheet that had been cold rolled 50%. The sheet became ferromagnetic as a result of the rolling. For this material the metal loss (Table V) values on corrosion were lower than for the original sheet for all surface preparations, although some differences were still noted. Presumably, increased cold working would tend to further reduce the differences.

Table IV. Effect of annealing on the corrosion of type 304 stainless steel in steam[1]

Surface preparation	Defilmed metal loss, mg/cm²
Grit blast (50μ SiO_2)	1.0
Grit blast + anneal[2]	9.2
Wet ground (80 grit)	0.45
Wet ground + anneal	10.0

[1] 7.0 days, 650°C; 42 kg/cm²; 0.2 ppm O_2.
[2] Annealed 5 min, 1100°C, vacuum.

Table V. Effect of cold work on the corrosion of type 304 stainless steel in steam at 650°C, 42 kg/cm²

Surface preparation	Defilmed metal loss, mg/cm²	
	30 ppm O_2	0.2 ppm O_2
As-received before cold rolling	10.1	10.1
As cold rolled (CR)	1.4	0.16
CR + wet ground	0.79	0.05
CR + acid pickled	2.9	4.0
CR + electropolished	3.7	1.3

Tested 7.0 days, 3-hr start-up.

Those specimens in Table II with low metal losses had thin temper films after their corrosion exposure. Those samples with large metal losses were covered with a heavy dark coating. Microscopic examination of the corrosion interface of the latter on 304 indicated two layers of corrosion product of about equal thickness (Fig. 2). The attack on the metal was not uniform, and numerous pockets of oxide were noted deeper than the average penetration. It was interesting to note that the grain boundaries and the adjacent metal were more resistant than the central portion of the grains (Fig. 3).

In oxygenated steam much of the outer oxide layer had spalled off the electropolished specimens, leaving a brilliant black surface similar in smoothness to the original electropolished surface. Wet ground specimens in the same test did not spall appreciably, but a microsection of the metal-oxide interface on 304 was similar to that of the electropolished specimen. Spalling of the outer oxide coating was not thoroughly investigated, but it was related to thickness, mechanical keying with the inner coating and was triggered by temperature changes in these low velocity tests.

Tests for periods of several days indicated that even in oxygenated steam, the wet ground specimens passed through a temper film stage. This film subsequently broke down and the corrosion increased. This two-step process caused a considerable variation in the amount of metal corroded in one week. If the thin temper film broke down early in the test, the metal corroded value was high. If the particular sample retained the temper film during most of the exposure, the amount of metal loss was much lower. Samples exposed in the electropolished condition suffered this variability in metal loss values to a less extent.

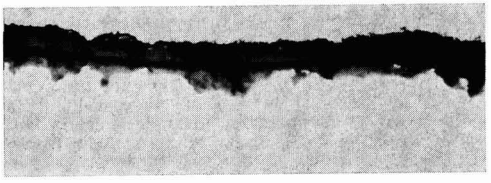

Fig. 2. Two layered structure of corrosion film on type 304; 7 days; 650°C; 42 kg/cm²; 0.03 ppm O_2. Top layer, mounting foil; center layer, oxide; bottom layer, stainless steel. Magnification 320X.

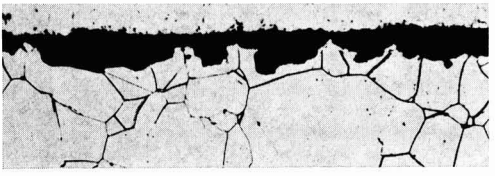

Fig. 3. Grain center attack of type 304 stainless steel; 7 days; 650°C; 42 kg/cm²; 30 ppm O_2. Top layer, mounting foil; center layer, oxide; bottom layer, stainless steel. Magnification 320X.

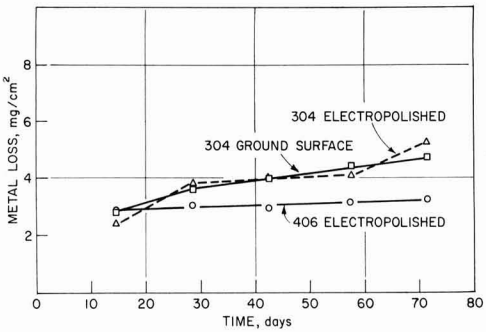

Fig. 4. Corrosion of stainless steels in static oxygenated steam, 600°C; 42 kg/cm².

The microstructures of the corrosion interface of wet ground specimens after temper film breakdown was similar to that of initially electropolished specimens. This suggested that the corrosion observed on the electropolished surfaces represented the intrinsic corrosion resistance of the alloys. If the correct interpretation has been made, the improved corrosion resistance noted for worked surfaces would represent a temporary effect. For this reason the electropolished surface preparation was chosen for measuring the corrosion rates of the various alloys. However, as will be shown later, the improvement in corrosion behavior for grit blasted surfaces has been observed to persist for relatively long periods of time.

Static corrosion testing.—Temperature.—Only two temperatures, 600° and 650°C, have been investigated in any detail. However, in a preliminary experiment, etched specimens of 304 and 347 were exposed to superheated steam (~0.2 ppm O_2) at 540°C for 374 days. The samples acquired a dulling tarnish film with isolated areas of gray film and rust colored spots. Metallographic examination after 117 days indicated carbide precipitation but no intergranular attack. Weight gains of only 0.2 mg/cm² for the type 304 and 0.1 mg/cm² for the type 347 were recorded at 374 days in this experiment. The combination of these data with the temper film observations indicated that the corrosion rate was quite low at this temperature.

At 600°C the corrosion data for 304 and 406 are presented in Fig. 4 for oxygenated steam (30 ppm) at 42 kg/cm². In this figure, as in subsequent ones, each point represents one defilmed specimen. Of the two specimen preparations tried, the grinding seemed to result in a somewhat more reproducible surface, judging from the relative smoothness of the corrosion curves. No significant difference in corrosion rate could be distinguished for the two preparation techniques under these test conditions.

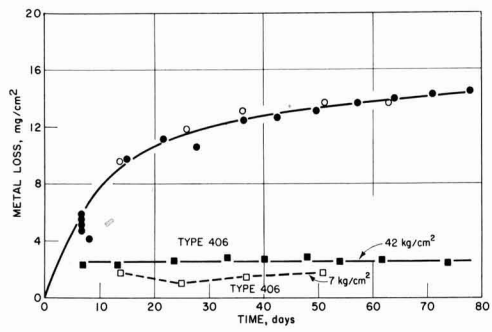

Fig. 5. Corrosion of electropolished stainless steels in oxygenated (30 ppm O_2) steam at 650°C. Type 304; ●, 42 kg/cm²; ○, 7 kg/cm².

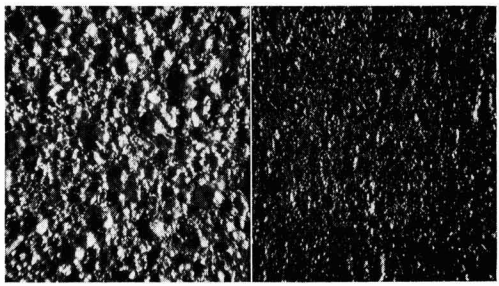

Fig. 6. Appearance of defilmed corroded samples, exposed at 650°C; 42 kg/cm²; 30 ppm O_2. Left, type 304 stainless steel, 87.9 days; right, type 406 stainless steel, 82.5 days. Magnification approximated 60X.

Type 406 steel samples were electropolished for testing in this environment. After the first exposure only very slight changes in metal loss values were obtained, almost within the normal defilming uncertainty. The average metal loss corresponded to a metal penetration of about 4×10^{-4} cm.

An unscheduled equipment shutdown at 58 days subjected the samples in one experiment to cool oxygenated water for about 20 hr. The previously smooth gray coating of type 304 was severely pitted by this low-temperature exposure while the 406 coating was not attacked. The pits noted on the 304 were rust colored and penetrated through the outer layer of corrosion coating and into the inner layer. When the samples were defilmed some slight evidence of the cold water pitting attack was noted on the underlying metal.

A corrosion rate measurement was also made at 650° (42 kg/cm²) using electropolished samples (Fig. 5). Both the total corrosion and the instantaneous corrosion rate (slope) for 304 were greater at this temperature than at 600°C for similar exposure times. Arbitrarily drawing a straight line through the longer exposure data for 304 resulted in a slope of ~5 mg/cm²-day (mdd).

Type 406 again corroded rapidly at the start with no measurable corrosion thereafter. Slightly less total corrosion was noted at this higher temperature. A sample exposed for 89 days was bent 180° around a 1 cm bar to check for embrittlement. None was evident in this simple test.

Defilmed samples of 304 acquired a deeply etched surface with increasing time (Fig. 6). Some of the pit bottoms were 0.006 cm below the average surface for the 88 day specimen. Type 406 alloy had a much smoother surface texture after defilming than did 304. No attempt was made to estimate the shallow pit depths on the specimen of 406 exposed 83 days.

Pressure.—Several steam pressures have been investigated at a temperature of 650°C. Early in the program two tests were performed in a tube furnace at atmospheric pressure. In the first, samples of the 300 series stainless steels were exposed to gently flowing dried oxygen (100 ml/min) at 650°C. The second test in this furnace used the same oxygen flow to which about 0.5 cc/min of water was added as steam. Data from these experiments are compared with a test at 42 kg/cm² total pressure (30 ppm O_2) in Table VI.

A comparison of the metal loss values for 1 atm wet oxygen and for 42 kg/cm² steam suggested only a small effect of pressure once adequate moisture was present. A surface preparation effect was noted even at 1 atm.

A longer experiment was performed in oxygenated (30 ppm) steam at 7 kg/cm², using electropolished samples of 304 and 406 (Fig. 5). The attack on 304 at 7 kg/cm² was quite similar to that obtained at 42 kg/cm². However, type 406 samples at the lower

Table VI. Effect of steam pressure on the corrosion of stainless steel

Sample, Preparation		Defilmed metal loss, mg/cm² 1 atm Dry O_2	1 atm Wet O_2	42 kg/cm² Steam (30 ppm O_2)
304	Wet ground	0.19	3.6	6.6
	Electropolished	0.16	5.9	7.5
321	Wet ground	0.27	1.2	1.8
	Electropolished	0.16	6.5	9.2
316	Wet ground	0.15	1.8	0.34
	Electropolished	—	6.6	9.0
347	Wet ground	0.24	2.3	3.9
	Electropolished	0.36	6.4	11.2

* 7 Days exposure.

Table VII. Corrosion of electropolished alloy specimens in 650°C, 42 kg/cm² (30 ppm O_2) steam

Alloy	Defilmed metal loss, mg/cm² 7 Days	14 Days
Incoloy 800	9.7	11.0
Type 403	13.5	a
405	18.9	23.9
410	11.4	a
410 (E_2)	14.8	16.0
430	5.0	5.1
446	0.34	0.42

a. Very heavy coating; could not be completely removed in defilming.

pressure were still partially covered with temper film at the end of the test. The partial covering accounts for the variation in metal loss from one specimen to another, since the area per cent coverage by the heavier gray coating was not the same for each sample. At 42 kg/cm², the 406 samples were completely coated with the heavier gray film after one week exposure.

Miscellaneous alloys.—During the course of the investigation a number of different alloys were tested in static autoclaves for relatively short periods of time. Some of these tests were presented in Table II to illustrate the effect of surface preparation. Results of other tests are shown in Table VII.

Type 446 was clearly the most resistant alloy tested during these relatively short exposures. Among these 400 series alloys the corrosion resistance increased greatly as the chromium content was increased from 12 to 25%.

Dynamic testing.—Steels.—Five week experiments were performed to determine the effect of velocity (30-91 meters/sec) and the oxygen content on the corrosion of types 304 and 406 steels at 650°C, 42 kg/cm². The two oxygen levels were 0.04-0.08 ppm and 30 ppm. As shown in Fig. 7 the data for the two experiments may be nearly superimposed, suggesting that oxygen content and velocity were not important variables in the range investigated. Comparison of Fig. 5 and 7 did show that the high velocity steam was more corrosive to type 304 than static steam. Type 406 did not show this dependence.

One additional longer test at the same temperature and pressure has been run with simultaneous gas addition of 30 ppm oxygen and 3.8 ppm hydrogen into the flowing steam. A test velocity of 61 m/sec was chosen. Again, (Fig. 8) varying the gas content of the steam had very little effect on the corrosion behavior of the electropolished specimens.

In this test, as in all of the other high velocity experiments, severe flaking of the outer corrosion coating occurred after only one week for the type 304 specimens (Fig. 9). As the test continued further loss was noted. For example, at 123 days a 304 specimen had lost an estimated 14 mg/cm² of corrosion coating, assuming a composition of Fe_3O_4. This was nearly half of the total coating produced. The same estimate performed for type 406 indicated that 95-98% of the coating was retained on the specimen at 123 days.

A smaller number of grit blasted samples were also tested. As might be expected from the results described earlier, the total metal losses were smaller (about half) for this surface preparation. The corrosion rate also appeared to be lower for these specimens.

Other alloys.—Five of the alloys frequently used for high-temperature applications were exposed to oxygenated (30 ppm) flowing steam at 650°C, 42 kg/cm². A test velocity of 61 m/sec was maintained past the electropolished specimens. Results are presented in Fig. 10. The earlier corrosion results of type 304 and 406 steel are included to establish reference levels. Of the five alloys tested, Inconel 600 and Inconel X750 were the poorest in corrosion resistance. The other three alloys (Inconel 625, Incoloy 800, and Rene' 41) all had metal losses less than type 406 at

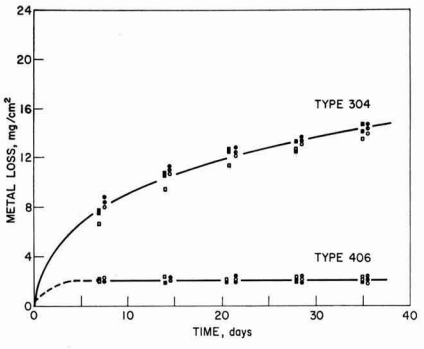

Fig. 7. Corrosion of stainless steel in flowing steam at 650°C; 42 kg/cm². Oxygen content, 0.05 ppm: Open circle, 30 meters/sec; solid circle, 61 meters/sec; circle with vertical line, 91 meters/sec. Oxygen content, 30 ppm: open box, 30 meters/sec; solid box, 61 meters/sec; box with vertical line, 91 meters/sec.

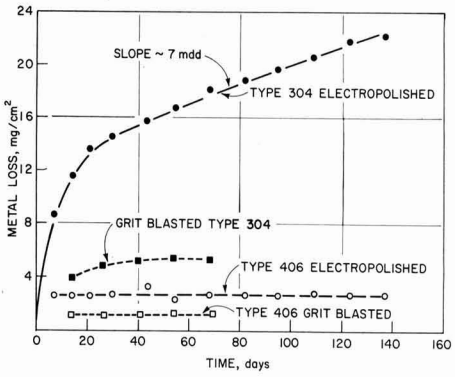

Fig 8. Corrosion of stainless steels in flowing steam. Temperature, 650°C; pressure, 42 kg/cm²; steam velocity, 61 meters/sec; oxygen, 30 ppm; hydrogen, 3.8 ppm.

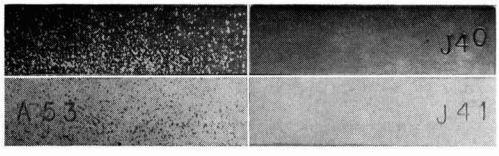

Fig. 9. Appearance of corrosion specimens after exposure to flowing steam at 650°C, 42 kg/cm²; oxygen and hydrogen added. Upper left, one-week exposure; upper right, one-week exposure; bottom left, two-week exposure; lower right, two-week exposure. Left, type 304 stainless steel; right, type 406 stainless steel.

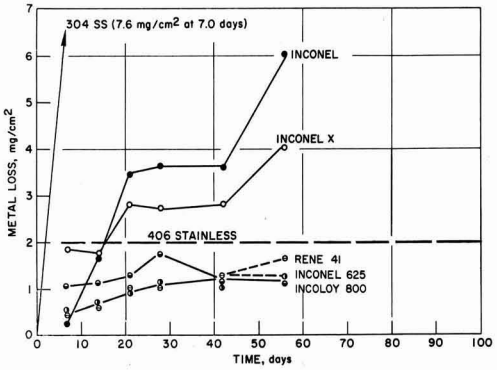

Fig. 10. Corrosion of nickel alloys in flowing steam; 650°C, 42 kg/cm², 61 meters/sec velocity, 30 ppm oxygen.

56 days, but with the possible exception of Incoloy 800, the metal losses were increasing with time.

Incoloy 800 had a low metal loss in this test, but in repeated static tests it exhibited a strong surface preparation effect and large metal losses. The static tests come to pressure and temperature much more slowly than the dynamic test (3 hr *vs.* about 5 min), suggesting that the method of starting the test may have played an important role in the corrosion behavior of this alloy.

Discussion

Surface.—The marked improvement in the corrosion resistance to deoxygenated steam of samples with machined surfaces had been previously noted (5) but was attributed to the removal of mill scale by the machining. In the current investigation the improvement could be reproduced on carefully cleaned surfaces and appeared to be a result of cold working the surface. It would appear likely that the oxide film formed on the cold worked metal differed in physical and electrical properties as well as in protective qualities from that formed on an annealed surface, but no extensive study was made.

It should be emphasized that the dependence of corrosion behavior on surface preparation varies from one environment to another and from one alloy to another. At temperatures of the order of 300°C in water, annealed or electropolished surfaces have been observed to corrode less rapidly than worked surfaces (7, 8) while at 400°C in steam the converse has been noted (8).

In oxygenated steam, the environment of particular interest in this study, the different surface preparations caused different corrosion behavior, but to a smaller extent than in steam of low oxygen content. Electropolishing was chosen as the primary surface preparation for the corrosion rate measurements. It appeared to represent most nearly the intrinsic corrosion resistance of the material as deduced from metallographic examinations of corroded samples. However, for many practical applications it would be advisable to reduce corrosion losses by using a final preparation which resulted in cold worked surfaces for the initial exposure.

Type 304.—The corrosion rate of type 304 in oxygenated steam rose rapidly as the temperature increased from 540° to 650°C. At 600° and 650°C the measured rate decreased with increasing time during the 80 day static tests. The rate was higher by a factor of about 1.5 in a dynamic test at 650°C. In rapid flow tests there appeared to be no effect of varying velocity or oxygen and hydrogen content on the corrosion rate. Flaking and loss of the outer corrosion coating was particularly severe in these dynamic tests. In a nuclear superheater these particles of oxide would be radioactive. Their deposition in the turbine and condenser would present a serious contamination problem.

Even if it were not susceptible to stress corrosion cracking, it would appear that type 304 is unsuitable at 650°C and higher for the thin wall nuclear fuel element cladding discussed earlier.

Type 406.—The corrosion rate of type 406 was too small to be precisely measured in all of the tests, static and dynamic, in which it was exposed simultaneously with type 304. It did, however, rapidly form a protective coating at the onset of the tests which amounted to an average metal penetration of about 2 to 4 x 10^{-4} cm. No flaking of the outer corrosion coating was noted in tests of over 100 days duration. No embrittlement due to the high temperature was detected in one simple bending test.

Since alloys of approximately the same chromium content as 406, but without aluminum, suffered considerably more corrosion attack, it was assumed that the aluminum content was responsible for the low corrosion rate of this alloy.

Miscellaneous alloys.—The corrosion of the 400 series steels in static oxygenated steam went down with increasing chromium content, particularly above about 13 w/o Cr. Both type 430 (16% Cr) and type 446 (25% Cr) exhibited short term corrosion attack lower than the 18-8 austenitic stainless steels at 650°C.

The high nickel alloys, particularly Inconel 625, were also more corrosion resistant than the 18-8 steels in short static and dynamic tests at 650°C. Inconel 600 and Inconel 750X were the poorest of the high nickel alloys in extended testing in high velocity steam. Rene' 41, a cobalt bearing alloy, had very satisfactory corrosion resistance. This alloy had been included in the study for general interest although its use in a nuclear reactor was not contemplated.

Type 406 steel appears to offer advantages in general corrosion resistance, lower cost and neutron capture cross section over most of the high nickel alloys tested, but is inferior in high temperature strength and in some fabrication aspects. It appears to be an interesting material for high temperature steam applications.

Acknowledgment

The authors gratefully acknowledge the technical assistance of Messrs. D. Dorman, R. Lee, and R. Schlueter in performing many of the experiments described. Work was performed under the auspices of the United States Atomic Energy Commission.

Manuscript received Jan. 13, 1964. This paper was presented at the New York Meeting, Sept. 29-Oct. 3, 1963.

Any discussion of this paper will appear in a Discussion Section to be published in the June 1965 JOURNAL.

REFERENCES

1. C. N. Spalaris, F. A. Comprelli, D. L. Douglass, and M. B. Reynolds, GEAP 3875, (1962).
2. H. J. Pessel, Proc. Nuclear Superheat Meeting No. 8, March 1963 (COO-267).
3. G. G. Gaul and W. L. Pearl, *Nuc. Sci. and Eng.*, **17**, 30 (1963).
4. C. N. Spalaris, R. F. Boyle, T. F. Evans, and E. L. Esch, GEAP 3796.
5. M. T. Jones, Reactor Technology Report No. 14, KAPL 2000-11 (1960).
6. R. C. Ulmer, H. A. Grabowski, and R. C. Patterson, *Trans. ASME*, **82**, (A) 264-271.
7. H. R. Copson and W. E. Berry, *Corrosion*, **18**, 21t (1962).
8. Societe d'Etudes, de Recherches et d'Applications pour l'Industrie; EURAEC 704 (1963).

Surface Oxidation of Gold Electrodes

S. B. Brummer and A. C. Makrides

Tyco Laboratories, Inc., Waltham, Massachusetts

ABSTRACT

The surface oxides formed on electropolished gold by potentiostatic anodization in the range 1.2-1.85v *vs.* H^+/H_2 have been studied by galvanostatic reduction at current densities between 10 and 1000 $\mu a/cm^2$. Molar perchlorate solutions of *p*H 0.06 to 2.8 were employed. The extent of oxide formation is determined by the potential of anodization; the charge increasing linearly with the potential of formation in the range of 1.45-1.8v. Cathodic chronopotentiograms show that reduction of the oxide occurs at a definite potential which depends on the cathodic current density. Current-potential curves, constructed from the chronopotentiograms, follow a Tafel relation with a slope of 41 mv. The electrochemical order of the reduction reaction is —1.4 with respect to *p*H. Ease of reduction of the oxide, as measured by its rate of reduction at a fixed potential at any given *p*H, decreases with increase of potential of formation of the oxide. A mechanism for reduction is suggested in which it is assumed that the reduction of an intermediate (Au^{II}) is the slow step in the over-all process.

The formation and reduction of surface oxides on metal electrodes are of major importance in determining the kinetics of basic electrochemical reactions, for example, of the reactions involving the O_2/H_2O couple. Of particular interest are noble metals, often used as oxygen electrodes, where the absence of dissolution reactions facilitates the interpretation of current-potential relations for surface oxidation. The present study deals mainly with the kinetics of reduction of surface oxides formed on gold, a metal which is unusual in its stability toward oxidation at low temperatures.

The oxidation of gold has not received as much attention as that of platinum and is not, at present, well characterized. A number of studies have been made using chronopotentiometry (1-7). Of particular interest is the work of Laitinen and Chao (1) who combined potentiostatic techniques with galvanostatic measurements and established the steady-state concentration of oxide as a function of potential. The final surface species is believed to be Au_2O_3 (perhaps hydrated) [*e.g.*, (7)], but there is disagreement concerning the presence (5) or absence (1, 4) of lower valent oxides. Although the surface coverage with oxidized species during galvanostatic oxidation has frequently been examined (2-8), apparently no attempt has been made to examine the kinetics of the reduction of the oxides of gold. In the present work, the kinetics of reduction of films formed potentiostatically have been studied over a range of *p*H.

Experimental

The principal experimental technique involved the potentiostatic oxidation of the electrode surface followed by reduction with constant current. Potential-time measurements were also made during anodic charging and during free decay from various surface oxidation conditions.

A three-compartment electrolytic cell constructed of Pyrex glass contained the working electrode in the central compartment and had sufficient volume to minimize concentration changes during an experiment. A Haber-Luggin capillary led to the reference electrode which was a platinized platinum cylinder immersed in a solution saturated with purified hydrogen. The counterelectrode was a roughened gold cylinder and was connected to the main compartment via a coarse fritted disk. All electrodes were mounted in such a way that only glass and Teflon came in contact with solution (9).

Gold electrodes, of "spectroscopically standardized" material (Johnson, Matthey and Co.), were in the form of cylinders of area ~0.8 cm^2. Immediately before use, the electrodes were electropolished in a cyanide bath (10) using a current density of ~6 amp/cm^2. The specimens were polished until they showed no evidence of surface marking when viewed under a low power microscope. They were then washed in chromic-sulfuric acid, triply distilled water, and finally with the test solution. The electrodes usually retained their luster at the completion of a series of oxidation experiments, and only rarely did polishing affect the measured roughness factor of the electrodes after the first couple of treatments. Geometric areas were estimated immediately after the experiments, using a micrometer. All results are given in terms of the geometric area of the electrodes.

Solutions were made up with triply distilled water (one from alkaline permanganate) and were molar with respect to ClO_4^-. Different acidities were obtained using appropriate quantities of $HClO_4$ (Baker Analyzed Reagent) and NaOH (Baker Analyzed Reagent). The *p*H was varied from 0.06 (*N* $HClO_4$) to 2.8. The working and counter electrode chambers were flushed with a continuous slow stream of N_2, which had first passed through traps packed with glass beads cooled in liquid N_2. Connections were made with Teflon tubing and all stockcocks, required to control the rate of gas flow, had Teflon barrels. The experimental results were not affected by stirring during the anodization or during the subsequent reduction of the film.

Potential control was maintained with a Wenking fast-rise potentiostat. Switching to a galvanostatic circuit was performed with a mercury-wetted relay (Western Electric 275C). Constant current was supplied by batteries in series with large resistances and was measured with a Greibach microammeter (type 510) to a precision of ½%. The potential during forced decay was measured on a Tektronix type 561A oscilloscope with a type 2A63 vertical amplifier and a type 2B67 time base.

Potentials could be read to 1 mv using a sensitive scale on the oscilloscope and a L&N potentiometer to back off most of the potential developed between the working and reference electrodes. Potential measure-

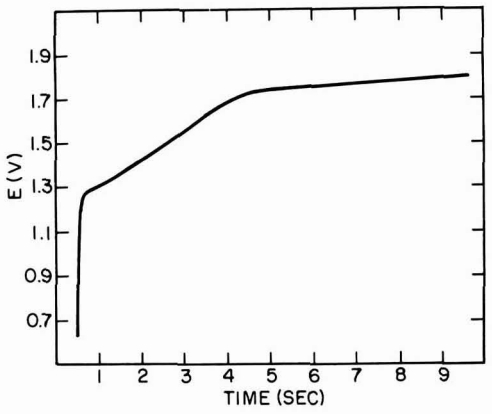

Fig. 1. Typical anodic chronopotentiogram in 1*N* $HClO_4$

ments during free decay were made with a L&N direct reading *p*H meter (input impedance $\sim 10^{12}\Omega$).

Reproducibility of charge with a given electrode during a run was usually ±2%, but between different experiments scatter up to ±5% was observed, probably because of differences in the surface roughness of the electrode. The reproducibility of the potential during reduction was usually within the precision of measurement (±1 mv) during a given experiment, and often was as good between different experiments. More usually, a variation of ±2 mv was observed between different experiments. All potentials are referred to the reversible H^+/H_2 potential in the same solution unless otherwise noted.

All observations were made at room temperature, 23° ± 2°C.

Results and Discussion

Anodic charging curves.—In Fig. 1, a typical charging curve is presented. It is seen that the potential rises steeply at first and then at about 1.28v, the exact value depending on the applied current density, a sharp break occurs. This is followed by a short region (20-30 mv) during which the potential rises quite slowly with time and then a much longer range (~1.3-1.75v) where the potential increases more rapidly with time. The potential becomes steady at about 1.8v and this, no doubt, corresponds to steady-state oxygen evolution. The anodic charge during the period from the first break to 1.8v is 630 $\mu C/cm^2$ which is somewhat less than the charge which is measured cathodically after potentiostatic pretreatment (for 5 min, see below) at 1.8v. However, the general shape of the charge *vs.* potential curves found from anodic curves is the same as that obtained by cathodic reduction after potentiostatic oxidation. The anodic charging curves are similar to those reported by Hickling (4), but differ in some respects from those reported by Laitinen and Chao (1). Hickling found that the total charge preceding oxygen evolution is equivalent to a monolayer of Au_2O_3 (perhaps hydrated). Our results and those of Laitinen and Chao (1) show that the amount of oxide on the surface increases smoothly with potential without any breaks corresponding to various stoichiometries. In particular, there are no arrests corresponding to the formation of Au^I or Au^{II} oxides.

Reduction curves.—Galvanostatic reduction curves of films formed potentiostatically at potentials ranging from 1.2 to 1.85v were determined at various cathodic current densities. Measurements were not extended above 1.85v to avoid permanent damage to the electrode (1) resulting in part, perhaps from extensive oxidation at the grain boundaries (11). A series of runs in which the time of anodization was varied showed that the charge obtained after 5 min

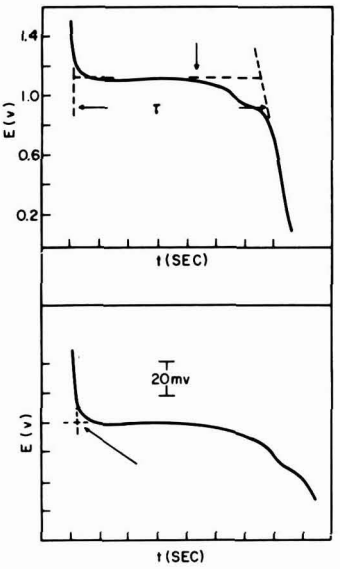

Fig. 2. Typical cathodic chronopotentiogram in 1*N* $HClO_4$ after 5 min of anodization at controlled potential. Arrow in upper figure indicates ~0.8 monolayer of O^{2-} remaining on surface. Arrow in lower figure indicates the potential corresponding to the reduction of the oxide.

and after 20 min of anodic oxidation differed by less than 0.5%. Since the reproducibility of the charge determinations was no better than this, all oxidations were carried out for 5 min.

In Fig. 2 are presented two typical cathodic chronopotentiograms. These were determined after the electrode had been oxidized potentiostatically at 1.55v for 5 min. It is seen that, in contrast to anodic curves, a clear and initially, well-defined arrest is observed corresponding to the onset of the reduction of the film. After a time, (indicated by the arrow in the top diagram in Fig. 2), corresponding to reduction to less than about 0.8 of a monolayer of adsorbed O^{2-}, the potential falls rapidly. Then, almost at the end of the arrest, a slight "kink" is observed. Eventually, the rate of change of potential corresponds to double layer charging, and this is followed by an arrest, not shown, where H_2 is evolved.

The method of calculating the transition time, τ, is indicated on the first curve of Fig. 2 and the method of estimating the potential of reduction is shown in the second, magnified, trace. If the reduction were commenced from less than about 1.45v, the arrest corresponding to the reduction of adsorbed oxygen was less distinct and the calculation of the charge, *q*, less exact. Also, it was no longer possible to determine with any precision the initial potential of reduction. If reduction were started from 1.65v or above, a slight (2-5 mv) overshoot (less positive values) of the potential was observed. In this case, the potential of reduction was estimated both at the overshoot and at the arrest. The latter, while perhaps more valid, was more difficult to estimate accurately, so that there was more scatter in the current-potential curves for reduction. The results reported related to the overshoot.

At *p*H of 1 and above, the charge is independent of the cathodic current density, which is expected if impurity effects are negligible (no effect of stirring) and if the dissolution rate of the film is also negligibly small. However, in more acid solutions the charge decreased linearly with increase in τ (Fig. 3). The equivalent rate of loss of charge is about 3 $\mu a/cm^2$ at *p*H 0.06. This zero order decay is suggestive of a

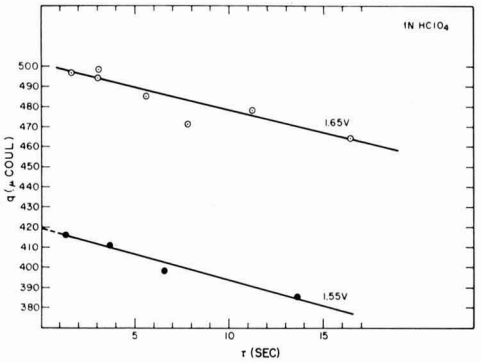

Fig. 3. Variation of the cathodic charge with time of reduction in 1*N* $HClO_4$.

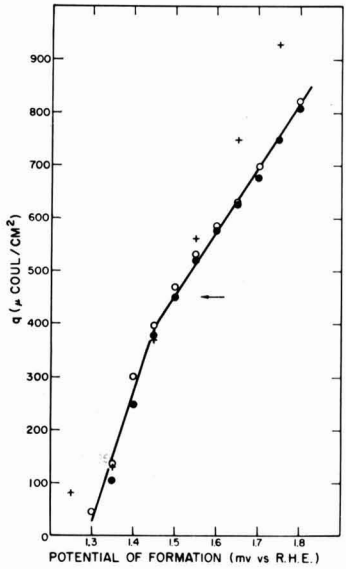

Fig. 4. Variation of cathodic charge with the potential of anodization in 1*N* $HClO_4$. Open and closed circles are from different experiments in the present study. Crosses are from the results of Laitinen and Chao (1). The arrow indicates a monolayer.

dissolution reaction, whereby the oxide disappears nonelectrochemically (no charge transfer) into solution. That this could not have been the case was shown by direct measurement of the rate of dissolution of the oxide. The electrode was left at open circuit for various times after anodization, and the oxide remaining at the end of this time was reduced galvanostatically. A dissolution rate of about 0.3 $\mu a/cm^2$, determined in this way, is in good agreement with the results of Laitinen and Chao (1) and of Vetter and Berndt (6). Thus, the q *vs.* τ relation at pH < 1 is not caused by simple chemical dissolution, but must be due to the decomposition of some active intermediate produced during electrochemical reduction. In solutions where q varied with τ the reported steady-state charges were estimated by extrapolating the q *vs.* τ line ($i \sim 30$ to 600 $\mu a/cm^2$) to $\tau = 0$.

Variation of charge with potential and pH.—The cathodic charge in 1*N* $HClO_4$ is shown as a function of potential of anodization in Fig. 4. It is seen that above ~1.45v the charge increases almost linearly with potential. The charge at 1.45v is close to that for a monolayer, 450 $\mu c/cm^2$ according to Hickling

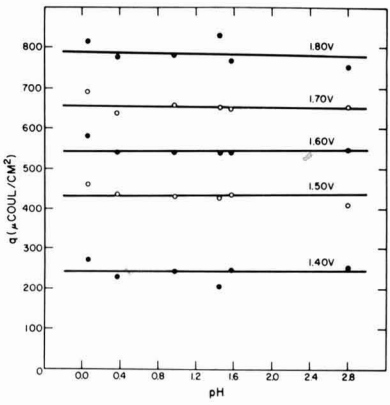

Fig. 5. Charge *vs.* pH at various potentials of formation

(4). In fact, if we regard the charge at the transition point in the q *vs.* E curve as corresponding to a monolayer, we would suggest that a monolayer of adsorbed oxygen (*i.e.*, one atom per metal atom) would be equivalent to ~400 rather than 450 $\mu c/cm^2$. The agreement with the results of Laitinen and Chao (1) is only moderate. Below about 1.35v, Laitinen and Chao found a long slow fall in the amount of surface oxidation as a function of the potential of anodization whereas we find that below ~1.45v q falls rapidly to zero, becoming too small to measure at ~1.3v.

Above ~1.45v, their results diverge systematically from ours. At 1.75v, this disagreement is about 15%. It may be that the discrepancy arises from a difference in the grain size of the gold specimens. Laitinen and Chao (1) report permanent damage to their electrodes after anodization above 1.75v, whereas we found that anodization up to ~2.1v (in 1*N* $HClO_4$) does not cause appreciable permament damage. Permanent damage would almost certainly be worst in a small-grained sample. Although the measurement is very difficult to make and is inaccurate once the charge is less than about 300 $\mu c/cm^2$, the shape of the cathodic curves is substantiated at other pH's and is also similar to that of the anodic charging curves. Therefore, we conclude that no significant amount of oxide or of adsorbed oxygen is present on Au below 1.3v.

From the charge-pH relationships shown in Fig. 5 it is evident that the main factor which determines q is the formation potential *vs.* reversible hydrogen in the same solution (or possibly against the H_2O/O_2 potential). There appears to be a slight decrease in the charge at any given potential *vs.* the H^+/H_2 couple in the same solution as the pH is raised from 0 to 2.8, but the effect is small and its magnitude is within the reproducibility of the experiments.

Kinetics of oxide reduction.—A typical series of reduction curves for gold oxide formed at different anodic potentials is shown in Fig. 6. Usually, the current potential curves were determined in the current density range 20-1000 $\mu a/cm^2$ and, in general, the deviations from the Tafel plots were ± 1 mv. Above ~1 ma/cm^2, the Tafel lines deviate slightly in the direction of greater polarization. Reasonable assumptions about iR losses lengthen the validity of the Tafel region to at least 20 ma/cm^2.

Tafel lines at the highest pH's tend to curve over rapidly at current densities substantially below those corresponding to the diffusion-limited current for hydrogen ion. At pH 2.1, the current-potential lines were so curved as to vitiate any simple analysis of their slopes. The following discussion is mainly concerned with the linear Tafel plots obtained from pH 0.06 to pH 1.6.

The slope of the Tafel lines, 39-42 mv, was independent of the potential of formation, as indicated in

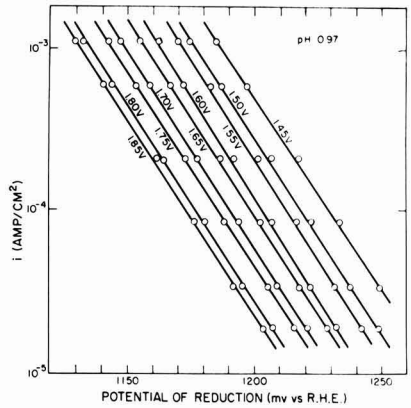

Fig. 6. Current-potential curves for reduction of films formed at various potentials.

the figure. The slope was also independent of pH in the range 0.06-1.60. In order to estimate an exchange current, i_o, for reduction, we must know the reversible potential for the reaction, and this presupposes that we have some knowledge of the composition of the oxide. The charge *vs.* potential curves are smooth, once a monolayer of oxide has been put down, and give no indication of the composition of the oxide. However, the reversible potential for the reaction

$$Au(OH)_3 + 3H^+ + 3e^- \rightleftharpoons Au + 3H_2O$$

is given by Latimer (12) as 1.45v (reduction potential), and experimentally (5, 13, 14) it has been found to be about 1.36v. Laitinen and Chao (1) observed rest potentials, after oxide formation, of about 1.30v and state that this results from a potential-determining reaction whose reversible potential is sufficiently close to 1.36v to assume that the oxide is very similar to $Au(OH)_3$. In fact, they find it reasonable to consider the surface oxide as AuOOH [$Au_2O_3 \cdot H_2O$, see Jirsa and Buryanek (15)].

The most stable normal oxide of gold is Au_2O_3 (in its various hydrated forms) and even this is thermodynamically unstable and decomposes relatively readily (7). Lower oxides are known, *viz.*, AuO (16, 17), but it has been shown (7) that experiments (3, 5, 18) suggesting the anodic formation of lower oxides are incorrect and are probably the result of base metal impurities, probably Fe. Thus, there is no *a priori* reason for assuming any well-defined stoichiometry. Certainly, it is not found for platinum [Feldberg, Enke, and Bricker (19)] and indeed it has been suggested (19) that the similarity in the anodic behavior of various noble metals may best be understood by considering the process as essentially the oxidation of water with the products being stabilized by adsorption on the metal. However, platinum and gold adsorb oxygen (or form surface oxides) at potentials which differ by nearly 0.5v, so that it is doubtful whether such a "simplification" is particularly useful.

Although there is no clear justification for assuming any stoichiometry for the oxide, it is apparent that the potential of the oxide-gold couple is close to the potential of the $Au(OH)_3/Au$ couple. For the purpose of estimating i_o's, it will be assumed that the reversible potential is that of the $Au/Au(OH)_3$ couple, *i.e.*, 1.36v, although the surface oxide may not be as completely hydrated as this. Exchange currents, obtained in this way, vary from about 5×10^{-8} to 2×10^{-9} amp/cm², and depend on the potential at which the oxide is formed (vide infra).

The ease of reduction of the oxide depends on the potential at which it is formed, although it is not clear at first whether this is a direct effect of the potential, or a result of differences in thickness. The following experiment was performed to answer this question. The metal was oxidized at a certain potential and then left on open circuit. Observations were made of the charge left on the oxide from about 1.4 monolayers to about 0.7 monolayers, and, also of the potential of reduction of the oxide at a given current density as a function of time on open circuit. If the determining factor is the thickness, we expect the potential of reduction to become more positive (in the reported experiment, by about 40 mv) as the charge on the electrode decays away. Otherwise, we do not expect much change. The reduction potential became slightly (5 mv) more negative, which clearly shows that the potential of formation and not the thickness of the oxide controls the reduction kinetics.

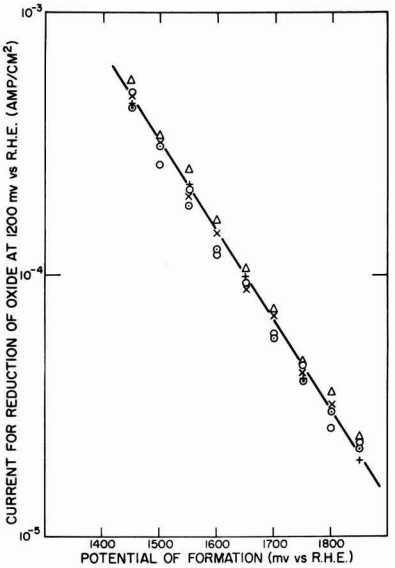

Fig. 7. Oxide reduction rate at 1200 mv as a function of potential of formation and pH. pH: ⊙, 0.07; X, 0.37; ○, 0.97; +, 1.45; △, 1.57.

The ease of reduction of the oxide, as a function of the potential of formation, is demonstrated in terms of the reduction current at fixed potential (1200 mv *vs.* R.H.E.), in Fig. 7. It is found that the reduction current decreases semilogarithmically with the increase in the potential of formation.

The pH dependence of the current at a fixed potential *vs.* the standard hydrogen electrode is shown in Fig. 8. Log i varies linearly with pH according to $(\partial \log i/\partial \mathrm{pH})_E = 1.39 \pm 0.02$. No significant variation in $(\partial \log i/\partial \mathrm{pH})_E$ is found with changes of either q or of the potential of formation.

General Discussion

To describe the mechanism of the reduction of gold oxide, we should in all, have to account for the following facts: (*A*) Most of the oxide is reduced at a fixed potential. (*B*) A Tafel slope of 41 mv is observed independent of thickness or potential of formation. (*C*) $(\partial \log i/\partial \mathrm{pH})_E$ is -1.39 independent of thickness or potential of formation. (*D*) The oxide becomes harder to reduce the higher the potential of formation. (*E*) In more acid solutions, the charge decreases linearly with increase in the transition time, at a rate in excess of that observed for simple dissolution of the oxide.

For the present we will assume, after Laitinen and Chao (1), that the oxide is essentially AuOOH ($Au_2O_3 \cdot H_2O$). A simple way of accounting for a Tafel slope of about 40 mv is to assume a three-electron reduction. However, aside from the inherent im-

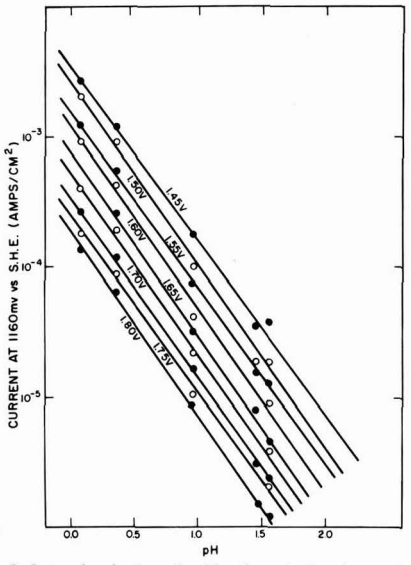

Fig. 8. Rate of reduction of oxides formed at various potentials as a function of pH.

probability of such a step, the pH dependence of the reduction rate rules out this mechanism.

A mechanism which partially satisfies (*B*) and (*C*) above is given by the following sequence of reactions

$$AuOOH + H^+ + e \overset{\text{fast}}{\rightleftharpoons} AuO + H_2O \qquad (I)$$

$$AuO + H^+ + e \overset{\text{slow}}{\rightarrow} AuOH \qquad (II)$$

$$AuOH + H^+ + e \overset{\text{fast}}{\rightarrow} Au + H_2O \qquad (III)$$

where AuO is written as the Au^{II} oxidation state and AuOH as the Au^{I} oxidation state, but either of these may be hydrated. The rate equation is

$$i = 3k_{II}(AuO)(H^+)\exp-\frac{\alpha\phi F}{RT} \qquad [1]$$

where α, the transfer coefficient, is ~0.5, and ϕ is the potential. We can solve for (AuO) by assuming that reaction (I) is fast and is in equilibrium at all potentials. Then

$$\vec{k}_I(AuOOH)(H^+)\exp-\frac{\beta\phi F}{RT} = \overleftarrow{k}_I(AuO)(H_2O)\exp\frac{(1-\beta)\phi F}{RT} \qquad [2]$$

and

$$(AuO) = K(AuOOH)(H^+)\exp-\frac{\phi F}{RT} \qquad [3]$$

where K is a constant equal to $\vec{k}_I/\overleftarrow{k}_I$ (H_2O). Then the final rate equation is

$$i = 3k_{II}K(AuOOH)(H^+)^2\exp-\frac{(1+\alpha)\phi F}{RT} \qquad [4]$$

If the surface oxide (AuOOH) is thought of as a well-defined and essentially homogeneous solid, its activity will remain constant although its concentration declines during reduction. This would account for the initial flatness of the galvanostatic reduction curve. If α, in Eq. [4], is 0.5, the Tafel slope is 39 mv, in good agreement with experiment.

The pH dependence, $(\partial \log i/\partial pH)_E$, as given by Eq. [4] is -2. This result is only in moderate agreement with the experimental observation of $(\partial \log i/\partial pH)_E = -1.39$.

A disadvantage of the above mechanism is the assumption that the reduction of Au^{II} is the slow step. Sidgwick (20) expresses the opinion that Au^{II} compounds are really complex molecules containing equal proportions of Au^{I} and Au^{III}. Although the evidence for this view is not strong, one has some doubts about postulating this form of gold as being so relatively stable. However, the large and unusual force field in a thin adsorbed layer could alter the relative stabilities of the various oxidation states.

An alternative to this scheme which yields the same Tafel slope and pH dependence can be constructed if it is assumed that the concentration of AuOOH is fixed by the equilibrium

$$AuOOH \rightleftharpoons Au + O_2 + H^+ + e \qquad (IV)$$

and that the rate-limiting step is

$$AuOOH + H^+ + e \overset{\text{slow}}{\rightarrow} AuO + H_2O \qquad (V)$$

Reaction (V) is followed by reactions (II) and (III), which are now assumed to be fast. This mechanism assumes that reaction (IV) is fast and reversible at potentials of ~1.2v in 1*N* $HClO_4$, *i.e.* it requires that the reduction of oxygen on gold proceed at a rate greater than 1000 $\mu a/cm^2$ (the observed reduction rate of the oxide) at these potentials. This is contrary to what is known about the reduction of oxygen on gold (21). In addition, this mechanism predicts a substantial effect for oxygen while, in fact, no difference was observed either in the reduction potentials or in the amount of oxide present on the surface when oxygen was bubbled over the electrode. These findings rule out this alternative mechanism.

The variation of the reduction current at fixed potential (of reduction) is expressed by Eq. [5]

$$i \alpha \exp-\frac{0.20\,F\,E_a}{RT} \qquad [5]$$

where E_a is the potential of formation of the oxide against the reversible hydrogen electrode in the same solution.

Comparison of Eq. [4] and [5] shows that the activity of (AuOOH) depends on the potential of formation according to (AuOOH) α exp $-0.20\ F\ E_a/RT$. This relation essentially expresses the qualitative observation made above, that the ease of reduction of the oxide decreases with the potential of formation, and suggests that the structure of the oxide (*e.g.*, concentration of defects) depends on the potential of its formation. There is, unfortunately, no direct evidence bearing on the comparison or structure of very thin gold oxides formed anodically, so that it is not possible to deduce from the kinetics the structural changes which might take place (22).

An alternative explanation of the pH dependence is possible in terms of cation adsorption in the inner part of the double-layer on metals covered with oxide (23). Thus, for example, the potential of zero charge of oxide-covered platinum is in excess of 2.2v (23). The unusual pH dependence of the reduction rate may result from competition between (slightly) adsorbed Na^+ and H^+ ions whose ratio changes with pH. Because of the low Tafel slope of 41 mv, small changes in the potential distribution in the vicinity of the electrode could be very important. This notion received some substantiation from experiments in concentrated $Mg(ClO_4)_2$ solutions. The object, here, was to preserve the structure of the double layer (with a high concentration of divalent cations) while changing the pH. In the main, the results were similar to those reported above. However, at pH 0.2 or less the current potential curves were much more closely spaced than we have reported above and the pH dependence, especially at high potentials of formation ($\geqslant$1.7v) was -2.0. Futher experiments, with variation of the cation are in progress and will be reported later.

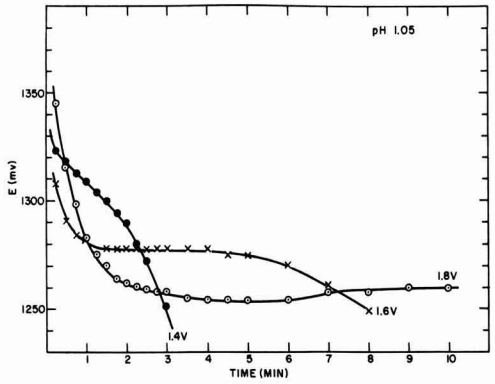

Fig. 9. Decay curves of oxides formed at various potentials

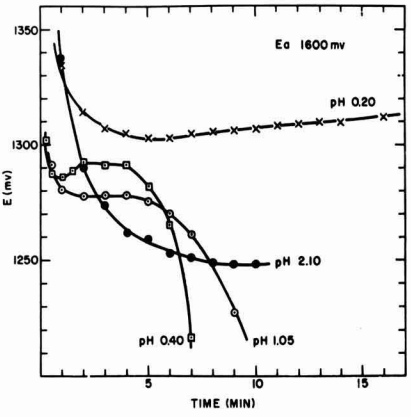

Fig. 10. Decay curves of oxides formed at 1.6v as a function of pH

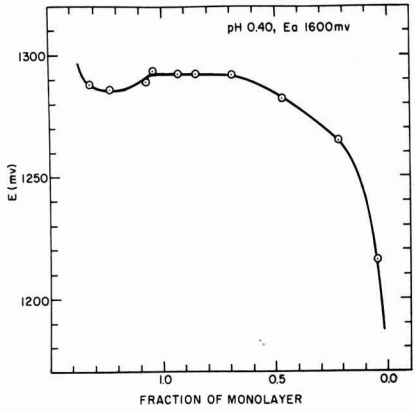

Fig 11. Open-circuit potential as a function of the amount of oxide on the surface.

The rest potential.—Decay curves (Fig. 9-11) show (*a*) that the "rest" potential is a function of the potential of formation, (*b*) that this potential varies with pH (Fig. 10), and (*c*) that frequently there is an overshoot in the decay curve (Fig. 11). Since there is little doubt that the ultimate anodic product is Au^{III} oxide (7), one expects that the higher the potential of formation, the closer to 1.36v would be the rest potential. In fact, the opposite is true. We may recall that the higher the potential of formation of the oxide, the harder it is to reduce. These observations, taken together, suggest that the rest potential is a mixed potential.

If the rest potential is a mixed potential involving an impurity couple, and if the reduction rate of the impurity is essentially controlled by its rate of diffusion to the electrode, then we expect the rest potential to vary by about 95 mv per pH unit, which is in fair agreement with the observed pH dependence (85 mv *vs.* S.H.E.). The overshoot phenomenon (Fig. 11) is similar to the overshoot observed in forced decay and probably arises from the same cause, *i.e.*, from an additional potential drop within the oxide.

The observed variation of q with the reduction current in the more acid solutions is not easily accounted for. As shown above, the dependence of q on τ cannot be explained in terms of dissolution of the oxide, but must be attributed to the decomposition of an intermediate formed during forced reduction. According to the proposed mechanism, Au^{III} and Au^{II} are in equilibrium at all potentials and, therefore, also at the potential established during free decay. Consequently, any decomposition reaction involving these species must be present during both forced and free decay, and cannot, therefore, give rise to the much higher rate of dissipation of charge during forced decay. This argument implies that Au^{I} is the unstable species. The reaction in question is obviously not the disproportionation to Au and Au^{III}, which is a well-known reaction (24), since such a process does not dissipate charge but merely alters the kinetics of reduction. A likely path for charge dissipation is, then, reaction of Au^{I} with H_2O to yield O_2, which diffuses away.

Summary and Conclusions

1. The kinetics of reduction of anodic oxide films formed on gold electrodes at potentials between 1.45 and 1.85v follow a Tafel relation with a slope of 41 mv. The exchange current (determined by extrapolation to a potential of 1.36v *vs.* H^+/H_2 in the same solution) is in the range of 10^{-7} to 10^{-9} amp/cm^2; it decreases with increasing anodic potentials of formation of the film and is almost independent of pH.

2. The electrochemical reaction order for reduction is -1.39 with respect to pH.

3. A mechanism for reduction is suggested in which it is assumed that Au^{II} and Au^{III} are in equilibrium at all potentials and that the electrochemical reduction of Au^{II} is the slow step. This reaction scheme accounts approximately for the main experimental results.

Acknowledgment

The authors are grateful to Miss Maryjane MacLaren for her skillful assistance in the experimental part. This work was supported by the Office of Naval Research under Contract Nonr 3765(00).

Manuscript received Nov. 13, 1963. This paper was presented at the New York Meeting, Sept. 29-Oct. 3, 1963.

Any discussion of this paper will appear in a Discussion Section to be published in the June 1965 JOURNAL.

REFERENCES

1. H. A. Laitinen and M. S. Chao, *This Journal*, **108**, 726 (1961).
2. G. Armstrong, F. R. Himsworth, and J. A. V. Butler, *Proc. Roy. Soc. (London)*, **A134**, 89 (1934).
3. G. Deborin and B. Ershler, *Acta Physicochim.*, **13**, 347 (1940).
4. A. Hickling, *Trans. Faraday Soc.*, **42**, 518 (1946).
5. S. E. S. El Wakkad and A. M. Shams El Din, *J. Chem. Soc.*, **1954**, 3098.
6. K. J. Vetter and D. Berndt, *Z. Elektrochem.*, **62**, 378 (1958).

7. D. Clark, T. Dickinson, and W. N. Mair, *Trans. Faraday Soc.*, **55**, 1937 (1959).
8. F. G. Will and C. A. Knorr, *Z. Elektrochem.*, **64**, 270 (1960).
9. M. Stern and A. C. Makrides, *This Journal*, **107**, 782 (1960).
10. W. J. McG. Tegart, "The Electrolytic and Chemical Polishing of Metals," p. 62, Pergamon Press, New York (1959), (first method given).
11. H. A. Laitinen and C. G. Enke, *This Journal*, **107**, 773 (1960).
12. W. H. Latimer, "Oxidation Potentials," 2nd ed., Prentice-Hall Publishing Co., New York (1952).
13. R. H. Gerke and M. D. Rourke, *J. Am. Chem. Soc.*, **49**, 1855 (1927).
14. T. F. Buehrer and W. E. Roseveare, *ibid.*, **49**, 1989 (1927).
15. F. Jirsa and O. Buryanek, *Z. Elektrochem.*, **29**, 126 (1923).
16. F. Schottlander, *Ann.*, **217**, 337 (1883).
17. G. Krüss, *ibid.*, **237**, 296 (1887).
18. J. K. Lee, R. N. Adams, and C. E. Bricker, *Anal. Chim. Acta*, **17**, 321 (1957).
19. S. W. Feldberg, C. G. Enke, and C. E. Bricker, *This Journal*, **110**, 826 (1963).
20. N. V. Sidgwick, "The Chemical Elements and Their Compounds," Oxford University Press (1962).
21. G. Bianchi, G. Caprioglio, S. Malaguzzi, F. Mazza, and T. Mussini, Air Force Office of Scientific Research, Technical Report 60-299, May, 1960.
22. For work on this topic with other systems see, for example, M. Nagyama and M. Cohen, *This Journal*, **109**, 781 (1962); *ibid.*, **110**, 670 (1963).
23. A. N. Frumkin, *Electrochim. Acta*, **5**, 265 (1961).
24. T. F. Buehrer, F. S. Wartman, and R. L. Nugent, *J. Am. Chem. Soc.*, **49**, 1272 (1927).

Anodic Oxidation of Tantalum in Formic Acid Electrolytes

D. M. Cheseldine

Sprague-TCC (Canada) Ltd., Toronto, Ontario, Canada

ABSTRACT

Duplex films formed anodically on tantalum in formic acid and other organic electrolytes have both low capacity and low optical thickness per unit formation voltage. 1/c *vs.* *V* curves show a "break point," *CV* values being lower at higher voltages. The film adjacent to the metal has the characteristics of normal Ta_2O_5 and grows simultaneously with the outer more rapidly soluble film suggesting oxygen ion mobility in this outer film. Evidence from sequential formations in organic and aqueous electrolytes indicates also tantalum ion mobility and the growth of some new oxide in the pre-existing outer layer. Conditions at the electrolyte interface may exert some control on the number of oxygen ions entering the film. Other anions influence the film structure which is thought to contain voids.

It has been observed that the film produced on tantalum in organic or concentrated electrolytes differs in certain characteristics from that formed in dilute aqueous solution. Vermilyea (1) noticed that with films formed to the same voltage, those formed in organic electrolytes were optically thinner (absolute values varying with electrolyte composition) yet showed normal capacity. The film consisted of two portions; an outer part which dissolved rapidly in HF and an inner part which dissolved at a rate similar to that of films produced in aqueous solution. Also the efficiency of the formation process in organic electrolytes was greater than 100% assuming all the charge to be used in the production of oxide.

Young (2) made measurements of overpotential and capacity of films formed in various concentrations of H_2SO_4 and found the product *CV* to be approximately constant. Masing, Orme, and Young (3) showed the outer part of the film formed in concentrated H_2SO_4 to be optically absorbing. The refractive index of the film was found to be a few per cent less than that of the normal oxide.

In the present investigation formic acid with various additions has been used as the basis of a number of organic electrolyte systems in which the anodic oxidation of tantalum has been studied.

Experimental

Capacitor grade tantalum foils 0.0003 in. thick, having a surface area of 950 cm^2 were prepared by cleaning for 2 min ultrasonically in 1% alconox solution at room temperature, rinsed, then dried at 120°C in a forced draught oven. A surface area of 50 cm^2 was used for capacity measurements.

Foils were anodized in about 250g of electrolyte which was surrounded by a water bath maintained at 20°C. Most of the anodizing was carried out at a constant current density of 0.095 ma/cm^2. Voltage was measured between the anode and cathode, and the electrolytes were adjusted to have similar resistivities. Most of the work was carried out in an electrolyte consisting of 2.8g dibasic ammonium phosphate dissolved in 100g formic acid. This electrolyte had a specific resistance of 46 ohm-cm at 25°C. The aqueous electrolyte consisted of H_2SO_4 diluted to the same resistivity. The reagents were 'ANALAR' grade and were not further purified.

The tantalum oxide film was dissolved in HF. For most of the work approximately 35% HF was used, but for some experiments concentrated HF (48% or 55%) was used, the latter giving a more defined end point at which all oxide was removed. Formed foils were cut into eight equal lengths for easier manipulation in HF solution. A large volume of HF was made up and a fresh portion (approximately 200 cc) was used for each immersion interval, used acid being collected for recirculation. Acid strength was checked at intervals by measuring the solution rate of normal tantalum oxide formed in dilute H_2SO_4.

Capacity and dissipation factor measurements were made at 120 cycles in the formation electrolyte. Optical thickness measurements were made by comparing the colors with a tantalum optical step gauge formed in dilute H_2SO_4 at 2v increments. The step gauge was used as an arbitrary scale of optical thickness, thus all thicknesses are given in terms of tantalum formation voltage.

Results

A comparison of films formed to the same voltage in formic acid electrolytes and in dilute H_2SO_4 shows that the former are optically thinner, require less coulombs for their formation, and have a slightly lower capacity. The film consists of an outer and an

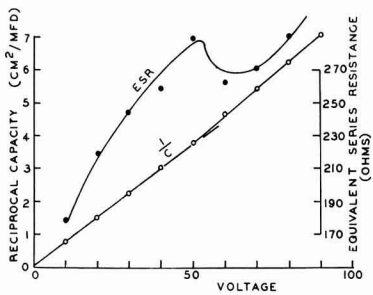

Fig. 1. Reciprocal capacity and equivalent series resistance in electrolyte 1; current density 0.3 ma/cm².

inner region with differing rates of solution in HF. Also the formation in formic acid electrolytes proceeds with greater than 100% efficiency.

Capacity and equivalent series resistance.—A typical reciprocal capacity *vs.* voltage plot is shown in Fig. 1 for formation in a formic acid electrolyte (composition 1).

The low voltage curve has a reciprocal slope (*CV*) of 13.5 μf-v/cm² compared with 12.2 μf-v/cm² for the high voltage curve. Increasing the current density from 0.3 to 1.0 ma/cm² reduced the low voltage reciprocal slope to 11.6 μf-v/cm² and the high voltage to 9.4 μf-v/cm². The break point occurred approximately 5v lower at the higher current density. The E.S.R. curve also shown in Fig. 1 exhibits a maximum.

Similar reciprocal capacity curves are found in other nonaqueous electrolytes. For instance in an electrolyte consisting of 8% concentrated H_2SO_4 and 1% water in ethylene glycol, the reciprocal slopes at low and high voltages were found to be 14.7 μf-v/cm² and 9.4 μf-v/cm², respectively. At 0.3 ma/cm² the break point in this electrolyte was found to occur at 35v.

Solution of films.—Both inner and outer films dissolve uniformly in HF but with differing solubility rates. Depending on the acid concentration the solubility rate of the metal also differs from that of the oxide. Therefore the weight of either film or of the total film can be determined.

Solution of the oxide was first applied to the whole film in an attempt to determine why the oxide forms with apparently greater than 100% current efficiency. Excess weight could be gained in either an electrochemical, chemical, or physical process which might occur in addition to the normal oxide formation.

The total film weight resulting from normal electrochemical formation of oxide and an electrochemical process involving some ion other than oxygen is given by [1]

$$W_F = W_G + C \cdot EW_{Ta5+} \qquad [1]$$

where W_F is the total weight of film in grams, W_G is the weight gain after anodizing in grams, C is the "charge to form" in faradays, and EW is the equivalent weight.

The total film weight resulting from a chemical reaction, in addition to the normal electrochemical formation of oxide, is given by [2]

$$W_F = C \cdot EW_{Ta_2O_5} + W_E \left(1 + \frac{EW_{Ta5+}}{EW_A}\right) \qquad [2]$$

where the symbols are as above. W_E is the excess weight gain in grams, and A is an anion in a tantalum compound formed by a chemical process. Values can be calculated by making assumptions regarding the nature of A.

A possible type of physical process which might occur is one in which some neutral species is occluded in the oxide film. The total weight of film is then given by [3] which gives the same value for the film weight as is given by the electrochemical process

$$W_F = C \cdot EW_{Ta_2O_5} + W_E \qquad [3]$$

Some typical results and figures showing the film weights to be expected for different processes are given in Table I. Of the three processes considered the electrochemical or physical give closest agreement with observed values.

The accurate determination of the point where all the film has been dissolved is difficult because the results appear to vary somewhat depending on the strength of HF used to dissolve the film and the parameter measured. To avoid this difficulty the total weight of film has been calculated in a number of instances from Eq. [1] or [3], *i.e.*, assuming either an electrochemical or physical process in addition to electrochemical formation of oxide. This calculation gives a result very close to the film weight determined by solubility rate in concentrated HF (Table I).

The weight and solubility rate of the outer, more rapidly dissolving film have been determined at different formation voltages. It was found that the weight of the outer part of the film is directly proportional to the formation voltage and represents a fixed fraction (about 60%) of the total weight of film present (Table II), *i.e.* both films grow simultaneously. The inner film can only grow simultaneously with the outer film if it either grows out of the latter, *i.e.*, if a conversion takes place, or if oxygen ions are supplied to the growth site. The latter appears more

Table I. Solution of tantalum anodic films

Electrolytic composition	1	2	3	Dilute H_2SO_4
Charge to form to 100v (coulombs/meter²)	1570	1530	1520	3000
Weight increase				
Calculated from charge	130	127	126	248
Measured	185	183	178	255
Excess	55	56	52	—
HF concentration	48%	48%	35%	48%
Parameter measured	weight	weight	capacity	weight
Weight of film dissolved	770	740	710	1350
Charge (faradays) × $EW_{Ta_2O_5}$ × 10^3	720	705	700	1370
Calculated weight of film:				
(*a*) Electrochemical process	775	760	750	
(*b*) Chemical process				
1. Formate	820	806	794	
2. Phøsphite	851	838	824	
3. Hydroxide	892	880	862	
4. Oxide	1024	1015	987	
(All weights in mg/meter²)				

Electrolyte Compositions:	1	2	3
Phosphorus acid	1.5	1.7	—
Diammonium hydrogen phosphate	—	—	2.8
Formic acid	90.0	100.0	100.0
Water	0.75	—	—
Triethylamine	To give specific resistance		—
Specific resistance ohm-cm at 25°C	50	60	48.0

Table II. Solubility rate in 35% HF of films formed in electrolyte 3. Current density 0.095 ma/cm²

1. Formation voltage	20	40	60	80	100
2. Weight of outer film, mg/meter²	94	170	255	345	427
Ratio 2/1	0.47	0.42	0.42	0.43	0.43
Solubility rate, mg/meter²/sec	9.4	9.4	8.9	8.2	7.1
Weight of outer film / Weight of total film[a]	0.74	0.61	0.60	0.59	0.59
Coulomb efficiency, %	148	144	135	136	142
Optical thickness, Ta voltage	—	21	31	43	60

[a] Calculated.
(All weights in mg. Solubility rate of Ta_2O_5 formed dilute H_2SO_4 = 3.6 mg/meter²/sec).

likely and implies mobility of oxygen ions in the outer film since these must originate in the electrolyte before passing through the outer film.

The formation efficiency values in Table II are typical of those obtained under controlled temperature conditions. The variations with voltage are within the reproducibility at any voltage and therefore not significant. The mean value obtained for the efficiency at 20°C from all (eight) determinations made at this temperature was 144%, all values falling within ±6% of the mean. In earlier experiments without temperature control 19 out of 30 determinations fell within this range.

For films formed above a certain voltage the solubility rate decreases with increasing voltage. An increase in the formation current density causes a marked increase in the solubility rate of the outer film. At 0.76 ma/cm² (*i.e.*, an eightfold increase of current density) a 60v film showed a solubility rate double that for a film formed at the lower current density. The relative proportion of fast dissolving oxide remained at approximately 60% of the total film. The optical thickness of the film, however, was about 7% thinner than the film formed at the lower current density. The formation efficiency at the higher current density was 152% which is slightly higher than the highest value of 148% observed at the lower current density.

Changes in capacity, weight, and optical thickness during solution of films are shown in Fig. 2 and 3. Reciprocal capacity variations with both weight and optical thickness differ widely for the inner and outer regions of the film. For solution of equal weights of film the change in reciprocal capacity is greater by a factor of 2.7 in the outer film. Variation of reciprocal capacity with optical voltage gives a value of 14.0 μf-optical volts/cm² for the inner film, which is of the order to be expected for normal Ta_2O_5. By comparison

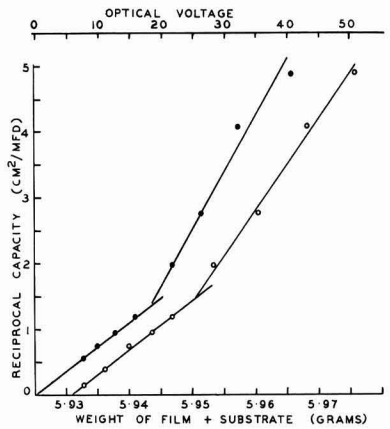

Fig. 2. Variations of reciprocal capacity with: weight of oxide + substrate, ○ - - - - ○ - - - -○; optical thickness, ● - - - - ● - - - -●; during solution in electrolyte 3.

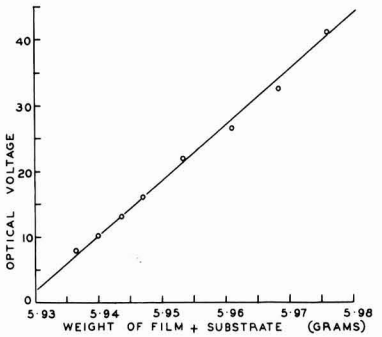

Fig. 3. Variations of optical voltage with weight of film + substrate during solution of a film formed in electrolyte 3.

the outer film gives a value of 6.2 μf-optical volts/cm². The relationship between weight and optical thickness for both films appears to be similar since no change of slope is discernible in this curve (Fig. 3).

While considering the relationship between weight and optical thickness it is interesting also to compare the formation charge required for unit increase in optical thickness. Formation in electrolyte 3 gives a value of 27 coulombs/optical volt/meter² compared with a value of 29 coulombs/optical volt/meter² for a film formed in dilute H_2SO_4. Actually the nonaqueous formation gives a composite film of which about 40% is normal Ta_2O_5. After making allowance for this it appears that the outer film grows with a coulomb expenditure/optical volt of about 12% less than normal Ta_2O_5. This difference, while significant, is quite small.

Some very interesting results are obtained when formation in a nonaqueous electrolyte is interrupted and the formation continued in an aqueous electrolyte. This type of sequential oxidation has been used by other investigators in an attempt to determine which ions carry the current through the oxide film (1, 4), the final position of the films being determined by their differing solubility rates.

If the formation is carried out first in dilute H_2SO_4 and then in a nonaqueous electrolyte the results are as might be anticipated. The outer part of the final film dissolves more rapidly in HF, this outer part amounting to about 60% of the weight of film formed in formic acid electrolyte. The remainder of the film dissolves at a uniform slower rate. This is consistent with the theory that only tantalum ions move in normal Ta_2O_5 but does not constitute proof of this theory unless it is established that all of the film formed in nonaqueous electrolyte lies above that formed in dilute H_2SO_4. This cannot be established from solubility experiments since the solubility rate of the lower film formed in nonaqueous electrolyte is the same as that of the film formed in dilute acid.

When oxidation is carried out in the reverse order it is found that the rapidly dissolving part of the film is in the middle sandwiched between two layers of less soluble oxide. This is qualitatively what might be expected still assuming only tantalum ion mobility. However, the fast dissolving part of the film is too near the air interface for this assumption to be correct, *i.e.*, when the formation is continued in dilute acid considerable growth of normal Ta_2O_5 takes place below the rapidly dissolving film formed in nonaqueous electrolyte. Also some dispersion of the fast dissolving part of the film appears to take place because the weight of this film increases. Its solubility rate also is lower than expected. Some further anomalies are noticed in the anodizing. For instance the coulombs/voltage increment in the dilute H_2SO_4 are initially exceptionally high; also the optical thickness is greater than would be expected. Figures for formations car-

Table III. Formation in electrolyte 3 followed by formation in dilute H_2SO_4

	[I]	[II]	[III]
Formation voltage			
Electrolyte 3	30	30	30
Dilute H_2SO_4	60	100	—
Optical voltage			
Electrolyte 3	16.5	16.5	16.5
Dilute H_2SO_4	54	98	—
Excess coulomb expenditure in dilute H_2SO_4, coulombs/meter^2	180	175	—
Weight of film, mg/meter^2			
Outer	188	366	132
Middle	211	388	—
Inner[a]	288	465	81
Solubility rate of film in 35% HF, mg/meter^2/sec			
Outer	4.9	4.3	9.4
Middle	6.6	5.5	—
Inner	3.4	3.4	3.4
Weight of film formed in dilute H_2SO_4 [following electrolyte 3], mg/meter^2			
Beneath existing outer film[b]	207	384	
Within existing outer film	79	256	
Above existing outer film	188	366	
Total	474	1006	

[a] By difference from the calculated weight of the total film.
[b] The inner film formed in electrolyte 3 dissolves at the same rate as the film formed in dilute acid and must be deducted to determine the weight of film added in dilute acid.

ried out first in electrolyte 3 and then in dilute H_2SO_4 are shown in Table III, [I and II] and for comparison some figures for a 30v formation in electrolyte 3 only are included [III].

These figures show that following the formation of a film in electrolyte 3, most of the oxide growth in dilute H_2SO_4 occurs above and below the outer region of the first film. Also some growth takes place within the film.

Film growth at any location indicates both anion and cation transport to that location. Therefore the sequential formation experiment is further evidence for the mobility of both ion species in the more rapidly soluble film.

Knowing the relative proportions of ions trapped in the oxide film and of ions penetrating to either interface, the proportion of charge carried by either anion or cation species can be deduced. It is assumed that the inner film is formed by anion migration and the outer film by cation migration. (When growth occurs within the film the charge must be divided equally between anion and cation transport.) For the two examples in Table III it is found that the proportion of charge carried by oxygen ions is 52% and 51% of the total for cases [I] and [II]. This agreement supports the suggested mechanism and indicates that under given formation conditions the rate at which either ion species enters the film remains constant. In this case approximately half the charge is carried by oxygen ions.

Addition of water to electrolytes.—Addition of water to a formic acid electrolyte increases the relative proportion of the inner film and also decreases the solubility rate of the outer film (Table IV).

Whereas in electrolyte 3 without any addition of water 60% of the film has a high solubility rate, with the addition of 40% water to the electrolyte this is reduced to 45%. The solubility rate is also reduced to a value very close to that of the normal oxide.

Table IV. Effect of water additions to electrolyte 3, 100v formation

Per cent water added	2	5	10	20	40
1. Weight of total film[a], mg/meter^2	830	910	990	1040	1160
2. Weight of outer film, mg/meter^2	470	503	516	483	525
Ratio 2/1	0.57	0.55	0.52	0.46	0.45
3. Solubility rate of outer film, mg/meter^2/sec	5.9	5.1	4.3	4.3	3.7
Efficiency, %	136	129	119	119	112
Optical voltage	70	77	82	84	89

[a] Calculated.

In considering the transport of ions through the film a complicating factor is that anions other than oxygen ions appear to enter the film. In particular the phosphate or phosphite ions present in the electrolytes so far considered play an important role. Without such additions the formation is characterized by increasing voltage increments per coulomb and break down at low voltages preceded by a decreasing product of capacity and voltage. The formation efficiency is still greater than 100%, and the outer part of the film has a very high solubility rate. For instance, with the addition of 5% water to an electrolyte consisting of triethylamine and formic acid (specific resistance 46 ohm-cm at 25°C) the voltage increment/coulomb increased from a value of 465 v/coulomb/cm^2 at 10v to a value of 975 v/coulomb/cm^2 at 100v. The outer film dissolved in 35% HF at a rate of 41 mg/meter^2/sec compared with a rate of 5.1 mg/meter^2/sec for a film formed in a similar electrolyte containing phosphate ions.

Further evidence of the effect phosphate ions in nonaqueous electrolytes have in decreasing the solubility rate of the formed films is obtained by forming in concentrated phosphoric acid (85% H_3PO_4). Under these conditions a film formed to 60v has an optical thickness of 40v and requires only 62% of the coulombs required to form a film to the same voltage in dilute H_2SO_4, *i.e.*, the film has the characteristics of a film formed in a nonaqueous electrolyte including a high formation efficiency. The film, however, dissolves at a uniform rate of 2.5 mg/meter^2/sec which is even lower than the rate of 3.6 mg/meter^2/sec normally observed for films formed in dilute H_2SO_4.

It therefore seems likely that some phosphate or phosphite ions are taken up by the film during formation in formic acid electrolytes containing these ions. Formate ions may also be taken up since the solubility rates of the outer films are still much greater than those of films formed in concentrated H_3PO_4.

Discussion

The experimental evidence indicates that these films consist of two regions; that both cations and anions are mobile in the outer region; and that growth can occur within this outer region. The high coulomb efficiencies indicate that some ions other than oxygen are taken up by the film, and there is evidence that such a film has a higher field strength than normal. Both coulometry and optical measurements indicate that the field strength is almost double that of a normal film. While both these methods are limited by lack of knowledge of the nature of the film there are indications that this may not differ grossly from that of oxide formed in dilute solution. Also a direct weight comparison indicates that the film formed in organic electrolyte is only about 75% of the weight of one formed to the same voltage in aqueous solution. Therefore the former must be thinner unless the density changes by an equal or greater amount. Further, in spite of the low *CV* values of the outer film (Fig. 2) the *CV* values of the duplex film are only slightly lower than those of the normal oxide indicating that the duplex film must be thinner to compensate for its lower dielectric constant.

It is thought that these phenomena can best be explained by assuming that the outer film formed in organic electrolytes has some type of voids in its structure. Film growth with pores is possible when the anion is mobile. In this case, since the cation is also mobile, growth at the neck of the pore would eventually cut it off, leaving a void embedded in the film.

Vermilyea (5) found the average field strength of films formed on contaminated surfaces to be higher than normal due to the interruptions in the ion conduction paths. In this case the voids were between the metal and the oxide film. Such voids affected growth above them due to the reduced availability of tantalum ions. Thus a tendency exists for voids to reproduce. Since they are probably being continually

created in a film growing in an organic electrolyte, they may multiply giving rise to low capacities and other effects.

Films formed in formic acid electrolytes not containing ions such as phosphate or phosphite exhibit a very rapid *CV* drop with increasing voltage after a certain voltage has been reached. Such behavior may be due to the rapid multiplication of voids. The accompanying increase in voltage increment per coulomb provides corroborating evidence. This latter behavior is not observed when phosphate or phosphite ions are added to the electrolyte. It is thought that this may be because these ions enter the film and collapse its structure (6), thus maintaining sufficiently uniform ion conductivity to prevent the excessive generation of voids. (The decreased solubility of films formed in electrolytes with phosphorous containing ions is in accord with the idea that these films are more dense.) The break in the *CV* curve would then be interpreted as a measure of their failure to completely achieve this. The maximum in the ESR curves suggests that the growth form induced by these ions is strained and that at the break point the film reverts to a slightly modified growth form.

Voids would provide a site for the further growth which occurs within the film. Such growth could restore some of the conduction paths in the film thus lowering its field strength. The excess coulombs required to form a film in aqueous solution on top of a film formed in an organic electrolyte could then be explained by the decreasing field strength of the latter.

The filling of voids also offers an explanation of the decreasing solubility rate of the outer film as it grows (Table II) or as formation is continued in an aqueous electrolyte (Table III).

The absence of voids in films grown in aqueous solution is not surprising. The conditions for their origin, *e.g.*, foreign ion inclusions, may be absent. Another possibility is that the large excess of oxygen ions present in dilute solution may fill in the voids almost as soon as they are produced. There are indications that the amount of growth within the oxide is controlled by the availability of oxygen ions at the interface. For example, in organic electrolytes an increase in current density produces less growth within the film, presumably due to slow replenishment of oxygen ions at the interface. Also, the addition of water to organic electrolytes (Table IV) is seen to give increasing growth within the outer films indicated by their decreasing solubility rates. Therefore the transition of mechanism from organic to aqueous electrolytes may be continuous. If so, one might expect to find on films grown in aqueous electrolytes, only a thin outer film containing voids which had not yet filled in. A thin surface film, showing light absorption, has in fact been observed by Young (7) during optical measurements on films formed in dilute H_2SO_4.

Summary

The following phenomena have been observed in the anodic oxidation of tantalum in formic acid electrolytes:

1. The films have many of the general features found by Vermilyea (1) for films formed in other nonaqueous media, *i.e.*, at the same voltages they are optically thinner and require less coulombs for formation than films formed in dilute aqueous electrolytes. The formation in nonaqueous media is characterized by an efficiency greater than 100%. Also the film consists of two regions, the outer part being more soluble in HF than the inner region.

2. Films formed in formic acid electrolytes have a slightly lower capacity than those formed in dilute solution, and the reciprocal capacity *vs.* voltage curve shows a break point with a lower reciprocal slope (*CV*) at voltages above the break point. A maximum in the ESR curve occurs at approximately the same voltage as the break point.

3. The inner and outer films grow at a constant rate provided the formation conditions are not varied.

4. Above a certain voltage the solubility rate of the outer film decreases with increasing formation voltage.

5. If formation in aqueous electrolyte follows formation in a formic acid electrolyte, it is found on dissolving the film that new oxide has been formed above and below the rapidly dissolving part of the film. Also this rapidly dissolving part has increased in weight with an accompanying decrease in solubility rate.

6. Increasing the formation current density increases the solubility rate of the outer film.

7. Increasing the water content of the electrolyte increases the proportion of the inner region of the film and decreases the solubility rate of the outer part of the film.

8. For equivalent weight or optical thickness the outer film has lower capacity than the inner film.

9. The addition of phosphate or phosphite ions to the electrolytes decreases the solubility rate of the outer region of films formed in such electrolytes. The additions also establish conditions under which films grow with uniform voltage increments for unit charge.

Acknowledgment

The work was carried out under contract DRB 715-00124(DGS) from the Canadian Defence Research Board to whom thanks are due for permission to publish. It was under the general direction of Dr. F. J. Burger to whom the author is indebted for consultation, encouragement, and valuable discussions throughout its course.

Manuscript received Jan 17, 1964; revised manuscript received May 5, 1964.

Any discussion of this paper will appear in a Discussion Section to be published in the June 1965 JOURNAL.

REFERENCES

1. D. A. Vermilyea, *Acta. Met.*, **2**, 482 (1954).
2. L. Young, *Proc. Roy. Soc.*, **A244**, 41 (1960).
3. L. Masing, J. E. Orme, and L. Young, *This Journal*, **108**, 428 (1961).
4. R. W. Franklin [see L. Young—Anodic Oxide Films A.P. (1961) p. 71].
5. D. A. Vermilyea, *This Journal*, **110**, 250 (1963).
6. R. A. U. Huddle and R. T. Anderson, *Advances in Catalysis*, **9**, 393.
7. L. Young, "Anodic Oxide Films," pp. 83-86, A. P. (1961).

Dielectric Loss Spectra of Corrosion Films on Zirconium

P. J. Harrop and J. N. Wanklyn

Metallurgy Division, A.E.R.E., Harwell, Berkshire, England

ABSTRACT

A technique has been developed for examining the bulk electrical properties of dry zirconium dioxide films. It has been used to determine the dielectric loss spectra of films formed by steam corrosion, and by anodization of Van Arkel zirconium. The most marked feature is a loss peak found for thermal films grown on pickled surfaces. This does not occur with anodized specimens or electropolished specimens and is postulated to be due to a fluorine-containing dipole. The dipole relaxes with an activation energy of 0.72 ± 0.04 ev. An interpretation of the data suggests a lower limit of concentration of 1 x 10^{20} fluorine ions per cubic centimeter in films of about 1500Å thickness. Anodic films show low loss curves consistent with near-stoichiometric structure.

Several workers (1-3) have attempted to make electrical measurements on dry oxide films, but they have seldom obtained reproducible results. Consequently, this work began with a study of the effective resistance of various electrode materials on flame polished platinum. A layer of unbaked colloidal graphite was found to give a variable resistance of up to 1000 ohms and was therefore rejected. Evaporated gold-palladium alloy and silver suspension in methyl isobutyl ketone were both found to be satisfactory in this respect, having less than 0.1 ohm resistance, and were tested side by side on oxidized zirconium specimens. Figure 1 shows that they gave the same loss values at all frequencies after 3 days evacuation, the time taken for the silver paint to dry out. Some specimens were measured several weeks later and these also gave the same values.

The main series of measurements reported here were made with either of the latter two electrode materials applied to the oxide face. Measurements on anodic films gave a frequency-independent dielectric constant of 22, in good agreement with wet measurements (4), indicating that significant electrode polarization did not occur.

The dielectric loss of a specimen, tan δ, is given by tan $\delta = 1/\omega R_p C_p$, with the usual notation. The variation of loss with temperature or frequency can reveal relaxation peaks and these have been studied extensively for the case of the alkali halides (5). When they exhibit the shape and behavior of Debye relaxations, they can usually be ascribed to point defect dipoles situated in the bulk material. One such peak has been found here for steam corrosion films on pickled zirconium.

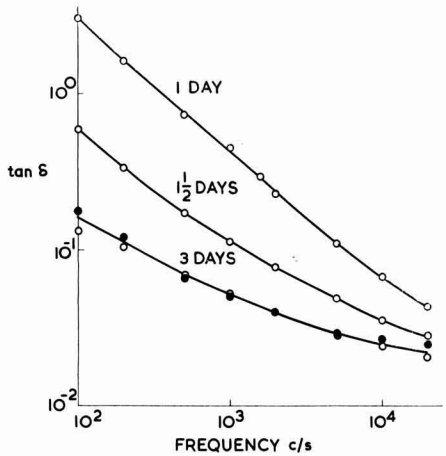

Fig. 1. Loss tangent vs. frequency for two adjacent electrodes on the same sample. ○, Silver paint, ●, evaporated AuPd.

Experimental

Apparatus.—The apparatus used was similar to that used by McMullen and Pryor, who measured the dielectric loss of anodized aluminum (6). Added precautions were the provision of a thermocouple buried in one electrode and a guard ring to prevent surface conduction across glassware. The specimen was examined under 10^{-6} Torr kinetic vacuum.

Electrical measurements were made with a Wayne Kerr Universal Bridge supplied by a Muirhead D890A Decade Oscillator and balanced by a Wayne Kerr Waveform Analyser. The equipment was checked with precision standard resistors and the complete rig was checked by loss measurements over the whole range of frequencies (100 to 20,000 cps ± 0.2%) on Cd-doped NaCl single crystals. These revealed a peak at 7800 cps, 104°C which shifted to 4600 cps at 94°C in precise agreement with the work of Haven (7).

The temperature was monitored with a chromel-alumel thermocouple, a thermostat cold junction and a Pye Universal Precision Potentiometer. This arrangement was checked at the carbon dioxide sublimation and ice points.

Materials.—Samples were prepared by the oxidation of 1 x 2 cm annealed Van Arkel zirconium specimens which then had one side scratched clean and silver painted. Electrodes were either evaporated or painted onto the oxide film on the other side, each electrode having an area of a few square millimeters, and the specimen as a whole was gripped between glass surfaces covered with platinum foil. Platinum wires welded to this foil were led out of the rig to the measuring apparatus.

Initial electropolishing was done on previously pickled specimens at 15° ± 5°C in a continuously stirred solution containing 9 parts by volume of acetic acid to one part of perchloric acid with a current density of 12 amp/dm² for a minimum of 5 min. Pickling was done in 45 parts of concentrated nitric to 5 parts of hydrofluoric acid (48% solution) plus 50 parts of redistilled water. Samples were then briefly rinsed in redistilled water and washed in warm running tap water for half an hour. They were then rinsed in redistilled water and methanol and dried. Variations from this treatment are described in the text. In both cases only visually immaculate surfaces were accepted. Anodizing was done at a few ma cm^{-2} in saturated ammonium borate.

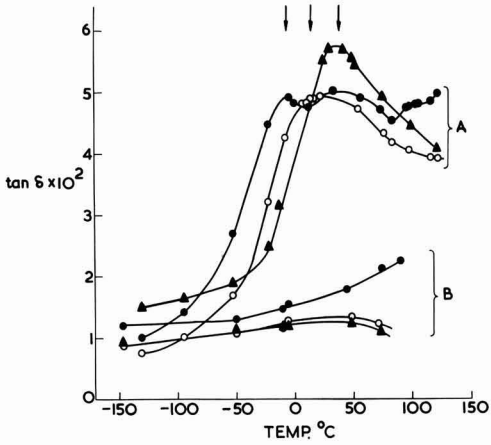

Fig. 2. Loss tangent *vs.* temperature comparing a typical steam corrosion film on a pickled surface (A), with a typical anodic film (B). ●, 159.2 cps; ○, 1592 cps; ▲, 15,920 cps. The main peak positions are indicated.

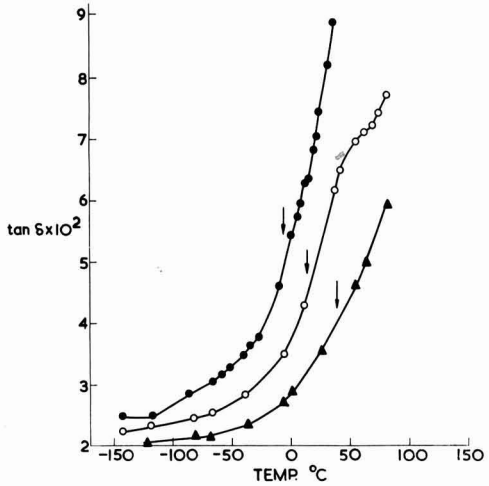

Fig. 3. Loss tangent *vs.* temperature for a typical steam corrosion film on an electropolished surface. ●, 159.2 cps; ○, 1592 cps; ▲, 15,920 cps. The mean peak positions for similar films on pickled surfaces are indicated.

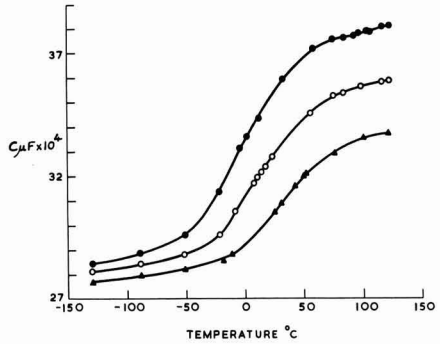

Fig. 4. Capacitance *vs.* temperature for a typical steam corrosion film on a pickled surface. ●, 159.2 cps; ○, 1592 cps; ▲, 15,920 cps.

Results

It was found that the pressure with which the specimen was gripped did not affect the reproducibility of results, provided it was below a certain maximum, at which the film tended to short out.

All measurements were made with 0.19v r.m.s. applied to the specimen. For a typical sample, doubling this voltage only caused 3% deviation from Ohm's law. Measurements made with both increasing and decreasing temperature showed that the rate of temperature change employed did not cause a significant thermocouple temperature lag.

The "background" loss curves (*i.e.*, those outside any dispersion region) measured between +150° and −150°C could be expected to be due to structure-sensitive extrinsic conductivity and therefore to be not reproducible between specimens but reproducible between different areas of the same specimen. This was found to be so.

A large loss peak, that moved to higher temperatures with increase in frequency, was found with four pickled specimens corroded separately for about 60 min in 500°C, 1 atm steam. It did not alter in height or position over several weeks at room temperature. An electropolished specimen from the same batch corroded for the same time [and, as has recently been shown (8), to a much smaller thickness] did not show the peak, nor did two other electropolished specimens corroded for 5 and 7 hr, respectively, to produce films of comparable thickness. Two anodic films grown to about 2000Å (comparable thickness), one on an electropolished and one on a pickled surface, did not give the above loss peak but merely a low loss curve. Typical examples of the three distinct types of behavior are shown in Fig. 2 and 3. The capacitance variation with temperature for a sample showing a peak is presented in Fig. 4.

The thermal films on pickled surfaces show what is strictly a set of peaks for each frequency, characterized in each case by a main peak at the low temperature end. It is this main peak that will now be analyzed. It can be seen that its shift with frequency, which gives the activation energy of dipole orientation, can be accurately determined. Mean positions for five samples are −6.6°, 13.5°, and 39.6°C for $\omega = 10^3$, 10^4, and 10^5 rad sec^{-1}, respectively. In contrast, the main peak heights are difficult to estimate due to uncertainty in interpolation of the background losses. It appears that the peaks in tan δ found for the four specimens corroded for about 60 min are all about 0.03 in height, when subtracted from interpolated background losses. The peak heights were the same, within this accuracy, for a pickled specimen corroded for 3 hr, and consequently to twice the mean thickness of a 1 hr specimen (10).

At this stage, the dipole was ascribed to either (a) an element from the pickling treatment which entered the oxide either substitutionally or interstitially, or (b) some property of the highly nonstoichiometric regions in the oxide related to the enhanced thermal oxidation rate of pickled surfaces. Experiments were undertaken to resolve this.

Two electropolished samples were copper-contaminated by dipping in copper sulfate solution. It has been found (8) that such treatment can give accelerated initial corrosion, followed by a measure of long-term inhibition, in a similar way to alloying with copper (9). Consequently, when the samples were placed in 500°C 1-atm steam for 1 hr, their corrosion rate was much greater than for the uncontaminated case, although pickling contamination was absent. Such films did not exhibit the main dielectric loss peak, but this observation was inconclusive because the loss values were found to drift markedly with time. As a further trial of a fast growing film, a clean electropolished specimen corroded at a higher tem-

perature, 600°C, in 1-atm steam for 15 min gave steady loss values and no peak.

To identify the element from the pickling treatment responsible for the loss peak, two electropolished specimens were dipped in dilute hydrofluoric acid and corroded in 500°C 1-atm steam for 1 hr. Although they corroded at a high rate, their loss values were too high for a peak of the anticipated order of magnitude to be observed. One electropolished specimen was therefore dipped for 30 sec in a pickle solution that did not contain the hydrofluoric acid component and corroded in 500°C 1-atm steam for 2 hr. It corroded at a rate similar to that for a clean electropolished surface and did not exhibit a loss peak, despite having a low background loss. It therefore seemed that either the hydrofluoric acid, or possibly the washing treatment, was responsible for the peak.

An electropolished sample was pickled in another solution consisting of equal volumes of 15 weight per cent (w/o) ammonium fluoride aqueous solution (redistilled water) and concentrated nitric acid (sp gr 1.420), washed for one half hour in cold tap water, and corroded in 500°C, 1-atm steam for 1 hr. It exhibited a peak of the same height as that in Fig. 2.

Discussion

The above examination of surfaces prepared in a variety of ways suggests that the loss peak is only present when fluoride is present, although some contribution from the washing treatment may also occur. It therefore seems that the peak is due to substitutional or interstitial fluorine ions in the oxide film, and it is, at first sight, puzzling that the peak height, giving dipole concentration, should not alter when the mean film thickness is doubled.

The explanation could be that the fluorine lies in an outer layer of oxide. However, it is instructive to note that these measurements are, in any case, relatively insensitive to mean oxide thickness, because the thin oxide grains, which grow slowly, shunt the thicker grains. With simple assumptions, the grain growth data of Wanklyn *et al.* (10) can be used to show that these thin grains increase in thickness by a factor of 1.4 when corroded to 3 hr, when the mean thickness is doubled. The corresponding decrease in peak height might not have been detected. Only about one in three grains are "seen," and these represent a thickness of about 2.2 mg/dm^2 (1500Å).

For a freely orienting dipole, the oscillation frequency ν obeys the relation $\nu = \nu_0 \exp -Q/kT$ where ν_0 is a constant and Q is the activation energy of orientation. In this case, $Q = 0.72 \pm 0.04$ ev, if all possible combinations of the mean positions of the peaks at the 3 frequencies are used. This compares with the energy of motion of an anion vacancy in monoclinic zirconia of 1.45 ev (11), a value supported by direct diffusion measurements on the cubic phase (12). Therefore, as expected, the dipolar orientation energy is less than that of free vacancy conduction.

The dipole could be composed of an interstitial fluorine ion coupled to a substitutional fluorine ion. Such a dipole would tend to occur in the nonstoichiometric oxide only, as an interstitial fluorine ion is difficult to fit into the stoichiometric zirconia lattice. This would explain why anodic films, which can be taken as near-stoichiometric, do not exhibit the peak even when grown on pickled surfaces.

The dielectric loss of a substance is defined by $\tan \delta = \epsilon''/\epsilon'$ where the complex permittivity ϵ^* is expressed by $\epsilon^* = \epsilon' - j\epsilon''$. The contribution to $\tan \delta$ of a dipolar relaxation is now considered.

The dipoles are probably present in low concentration randomly distributed throughout the solid. Their mutual interaction will undoubtedly give rise to 'internal field' effects in the dielectric properties. However, the usual form of Lorentz internal field correction used by some workers (6, 14) is only applicable for point dipoles each of which is localized at a lattice point (13). Extended dipoles, of the kind postulated here, give rise to smaller internal field effects (15), which depend on the detailed structure of the dipole. In the absence of the necessary detailed knowledge we shall omit internal field effects entirely.

The Debye equations can be applied for the case of a freely orienting dipole (16) to give, in MKS units

$$\tan \delta = \frac{(\epsilon_s - \epsilon_\infty)\,\omega\tau}{\epsilon_s + \epsilon_\infty \omega^2\tau^2} = \frac{N\mu^2}{3\epsilon_0 kT}\left(\frac{\omega\tau}{\epsilon_s + \epsilon_\infty \omega^2\tau^2}\right)$$

where ϵ_s and ϵ_∞ are the relative dielectric constants away from the relaxation to lower and higher frequencies respectively, τ is the dipolar relaxation time, N is the concentration of dipoles per cubic meter, μ is the dipole moment, and ϵ_0 the dielectric constant of free space.

In this case, $\epsilon_s \simeq \epsilon_\infty$[1] and $\tan \delta$ is a maximum when $\omega\tau = 1$. Thus

$$\tan \delta_{max} = \frac{N\mu^2}{6\epsilon_\infty \epsilon_0 kT}$$

The dipole moment can be expressed as $\mu = zea$ where z and a are the effective dipole charge and length, respectively.

Taking the values $\tan \delta_{max} = 0.03$, $T = 287$°K, $\epsilon_\infty = 22$, $z = 1$, and $a = 2.7$ Å results in a value of N of about 7 x 10^{19} dipoles per cubic centimeter. Since a few of the fluorine ions may not be paired, twice this figure must represent a lower limit of fluorine concentration. If this relates to the slower growing grains, then the relevant oxide thickness is about 1500Å.

An interesting comparison can now be made with the work of Beg and Brown (17). They used a radiotracer technique to show that pickling left a considerable amount of fluoride on Zircaloy surfaces. When the metal was corroded for 15 min in 500°C, 1 atm steam, no remaining fluoride was detected. If their lower limit of detection was about 0.1 μg/cm^2 then less than 3.2 x 10^{15} fluoride ions per square centimeter remained. This figure, related to a 1500Å film, gives an upper limit of fluoride concentration of about 2 x 10^{20} ions per cubic centimeter which is just above the dielectric loss figure.

The loss values for anodic films are much lower than for thermal films of comparable thickness. The former therefore constitute more perfect dielectrics and must be more nearly stoichiometric. This supports other spectroscopic evidence, as it has been found that similar anodic films scarcely absorb at all between the ultraviolet eigenabsorption (18), through the optical, to 12μ in the infrared region (19). In contrast, corrosion films absorb at several frequencies (19).

Conclusions

1. Oxide films grown by corrosion of Van Arkel zirconium in 500°C, 1-atm steam apparently contain fluorine ions if the metal has been previously pickled but not if it has been electropolished in acetic/perchloric acid solution. A concentration of about 1 x 10^{20} fluorine ions per cubic centimeter can be calculated for films of about 1500Å thickness grown on immaculate pickled surfaces. Since only fluorine in dipoles would be detected by this method, and a few fluorine ions may be unpaired, this can be taken as a lower limit of fluorine concentration in such films.

2. For anodic oxide films, grown to about 2000Å on Van Arkel zirconium in saturated ammonium borate at medium current densities, the much lower loss values found indicate that they are near-stoichiometric.

Acknowledgments

We are indebted to Mr. C. F. Britton for help with specimen preparation, to Dr. A. B. Lidiard for considerable help with the theory of dielectric loss and to other colleagues for criticism.

[1] It can be verified that this is true, within the accuracy of the calculation, by appropriate interpolation in Fig. 4.

Manuscript received Nov. 4, 1963; revised manuscript received April 26, 1964.

Any discussion of this paper will appear in a Discussion Section to be published in the June 1965 JOURNAL.

REFERENCES

1. R. D. Misch, "Electrical Resistance Studies of Anodic and Corrosion Oxide Films Formed on Zirconium," Report No. ANL6259, Argonne National Laboratory, May 1961.
2. P. H. G. Draper, Thesis, Metallurgy Department, University of London, 1958.
3. D. H. Bradhurst, Thesis, Metallurgy Department, University of London, 1963.
4. L. Young, "Anodic Oxide Films," p. 262, Academic Press Inc. (1960).
5. G. D. Watkins, *Phys. Rev.*, **113**, 91 (1959).
6. J. J. McMullen and M. J. Pryor, "1st International Congress on Metallic Corrosion," London, April 1961, Butterworths and Co. (1962).
7. Y. Haven, *J. Chem. Phys.*, **21**, 171 (1953).
8. N. J. M. Wilkins, Private communication.
9. J. N. Wanklyn *et al.*, "The Corrosion of Zirconium and Its Alloys by High Temperature Steam. Part I." Report No. AERE R 3655, March 1961.
10. J. N. Wanklyn *et al.*, *This Journal*, **110**, 856 (1963).
11. D. L. Douglass, "Corrosion of Reactor Materials," Conference, Saltzburg, 1962, I.A.E.C., Vienna, 1962, Vol. II.
12. W. D. Kingery, *et al.*, *J. Am. Ceram. Soc.*, **42**, 393 (1960).
13. A. B. Lidiard, Private communication.
14. R. G. Breckenridge, "Imperfections in Nearly Perfect Crystals," W. Shockley Editor, John Wiley and Sons Inc., New York (1952).
15. P. Ninomiya, *J. Phys. Soc. Japan*, **14**, 30 (1959).
16. H. Frohlich, "Theory of Dielectrics," p. 70, Oxford University Press Ltd. (1948).
17. F. Brown, Private communication.
18. R. E. Salomon, W. M. Graven, and G. J. Adams, *J. Chem. Phys.*, **32**, 310 (1960).
19. N. J. M. Wilkins, *Corrosion Science*, **4**, 17 (1964).

Kinetics of Anodic Dissolution of Germanium

P. J. Boddy

Bell Telephone Laboratories, Murray Hill, New Jersey

ABSTRACT

A study has been made of the potential distribution at germanium (100), (110), and (111) surfaces undergoing anodic dissolution. The data for (100) and (110) were shown to be consistent with the dissolution mechanism proposed by Beck and Gerischer. For (111) complications arise because the potential distribution over the surface may be nonuniform. The morphology of extensively etched surfaces has been examined and shown to be generally consistent with the kinetics.

The behavior of a semiconductor (sc) differs markedly from that of a metal in that a considerable portion of any potential difference (p.d.) applied across the sc-aqueous electrolyte interface generally occurs within the space charge region of the electrode. This is in distinct contrast with a metal electrode in contact with a concentrated aqueous electrolyte where practically all of the applied p.d. occurs within the Helmholtz double layer in the absence of a diffusion controlled process in the solution and is frequently of primary kinetic significance for any process involving transfer of charged species across that region. In the case of dilute aqueous solutions, it is necessary to take into account the p.d. across the diffuse part of the double layer in the solution and its influence on the concentration of charged species close to the electrode surface (1).

The sc problem is similar in principle to that of a dilute aqueous solution. For the simplest case of no change in adsorbed species (e.g., ions or oriented dipoles) or in the charge trapped in surface states it has been calculated (2, 3) for moderate space charge p.d. (ψ_s) that the p.d. across the Helmholtz double layer due to free charge on a germanium electrode is a negligibly small fraction of the p.d. across the sc space charge region. In view of this the kinetic significance of the overvoltage at a sc electrode (in the concentrated electrolyte case) must be quite different from that at metal electrodes since most of the potential change occurs across the sc space charge region, not the Helmholtz double layer. Germanium, the most investigated sc electrode, does not behave exactly according to this simple model. It has been concluded on the basis of measurements of interfacial capacity (4, 5) and surface photovoltage (6) that the steady overvoltage at a germanium anode in neutral sulfate solutions is distributed between the sc space charge and the Helmholtz double layer. No evidence of changes in the occupancy of fast surface states sufficient to explain the observed potential change (ΔV_H) across the Helmholtz double layer is found in the experiments. Slow surface states in the surface physics sense are considered unlikely due to the absence of thick oxide films (7), hence ΔV_H has been tentatively ascribed to changes in the density of oriented dipoles adsorbed at the interface (5).

Since the detailed separation of the overvoltage can now be made it was considered of interest to reexamine the anodic dissolution of germanium to determine the relative significance of the sc space charge and Helmholtz double layer p.d.'s to the kinetics. The data suggest that the mechanism for anodic dissolution of germanium (100) proposed by Beck and Gerischer (8) (B and G) is correct and that (110) dissolution proceeds by a similar mechanism at low c.d. The (111) exhibits behavior that cannot be simply interpreted, but is believed to be due to the complexity of the nucleation process or to complications arising because of the detailed morphology of the dissolving surface.

Experimental

Electrodes were single crystal n- or p-type germanium polyhedra with all faces of each particular electrode oriented to the same plane, either (100), (110), or (111). Electrical connection was made by means of a soldered copper wire protected by a wax-filled glass tube. The solution was M/10 K_2SO_4, phosphate buffered to pH 7.4, gettered with germanium crushed *in situ*. The electrodes were polished in CP4 and then partially immersed in the solution and anodized at *ca.* 400 μa cm^{-2} for 15 min before measurements were commenced. The solution contacted only germanium.

The experiments were conducted in the dark at 25°C in an atmosphere of purified helium, which was also used to deoxygenate the solution prior to use. A separate cathode compartment with a diffusion barrier was used since the electrode potential of germanium

at low anodic current densities is sensitive to dissolved hydrogen (9). The electrode potential was determined at high impedance about 10 min after the imposition of a constant current. The interfacial capacity was calculated from the voltage response to a short duration (1-5 μsec) current pulse (10). The true surface area was deduced from the minimum value of the interfacial capacity (4).

Results

Typical plots of overvoltage *vs.* current density for the three low index planes of p-type electrodes are shown in Fig. 1. The curves for n-type were very similar. The tendency to saturation at the highest current densities on n-type was slight ($\sim$400 μa cm^{-2}) since the electrodes were close to intrinsic. A capacity *vs.* electrode potential curve taken simultaneously with some of the data in Fig. 1 is shown in Fig. 2. By analysis of the capacity, ψ_s may be deduced (11). The relationship previously used by us (5) and similar to that given by Green (12)

$$\Delta V_E = \Delta V_H - \Delta\psi_s \qquad [1]$$

where ΔV_E is the change in electrode potential, is assumed to apply since changes in potential across the diffuse layer in the solution should be negligible (the capacity of the sc space charge is two to three orders of magnitude smaller than that of the solution space charge). We have previously discussed this equation in more detail (19). In this way each curve in Fig. 1 can be separated into two parts, overvoltage across the sc space charge (η_s) and overvoltage across the Helmholtz double layer (η_H) *vs.* current density. This is shown in Fig. 3, 4, and 5 for the three faces of n- and p-type electrodes.

The overvoltages are defined as follows.

$$\eta_s = \psi_s - {}_o\psi_s \qquad [2]$$

where ${}_o\psi_s$ is the value at the reversible potential (which is not observed in practice) and

$$(\eta_H + \text{constant}) - (\eta_s + \text{constant}) = V_E \qquad [3]$$

where V_E is the electrode potential *vs.* SCE. Since ${}_o\psi_s$ is not known, (η_s + constant) is taken arbitrarily as the measured value of $\psi_s - (RT/F)\ln\lambda$, where $\lambda = p/n_i$, p being the hole concentration in the sample and n_i the intrinsic electron concentration. The term (η_H + constant) is chosen to numerically balance Eq. [3], *i.e.*, (η_H + constant) = $V_E + \psi_s - (RT/F)\ln\lambda$ in Fig. 3-5. It should be noted that only changes in p.d. are involved in the final analysis.

Discussion

(100) Surface.—A proposed mechanism (8) for the anodic dissolution of (100) is shown in Fig. 6. The rate-determining process is assumed to be the breaking of a surface bond (step 3) after a hole has been trapped in it (step 2) by coulombic interaction with the negative end of the dipole created by ionization of a surface hydroxyl group (step 1). Thus is may be seen from steps 2 and 3 that the rate-determining process is first order in the surface concentration of holes.

Considering the general case of a positively charged surface species which is subsequently transferred across the Helmholtz double layer into solution [as-

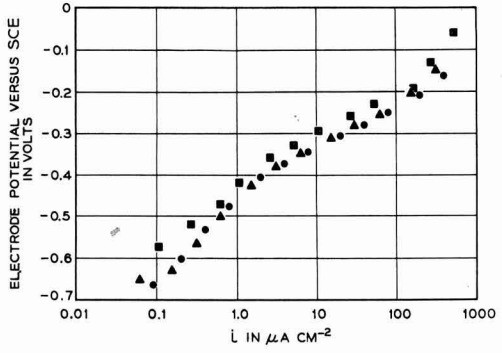

Fig. 1. Tafel curves for (100) (●) 35.6 ohm-cm, (110) (▲) 41.3 ohm-cm, and (111) (■) 38.65 ohm-cm, all p-type.

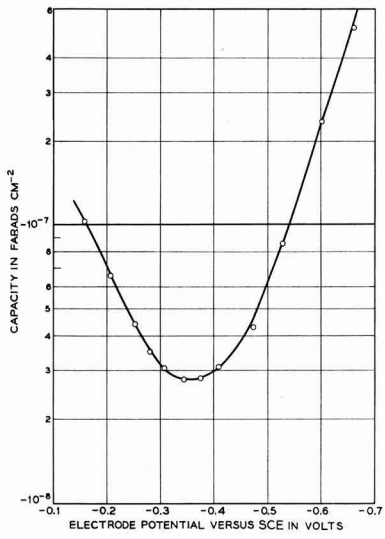

Fig. 2. Capacity taken simultaneously with Tafel curve in Fig. 1 for (100) electrode.

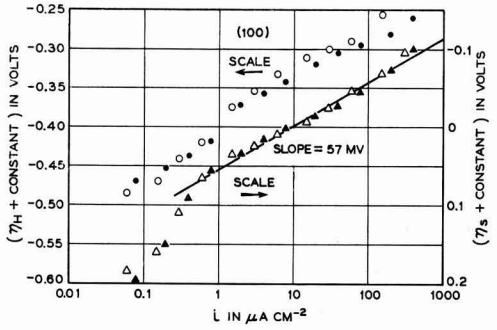

Fig. 3. Separation of overvoltage for (100) into components across Helmholtz region (○,●) and semiconductor space charge (△,▲). Open points p-type, filled points n-type 34.05 ohm-cm.

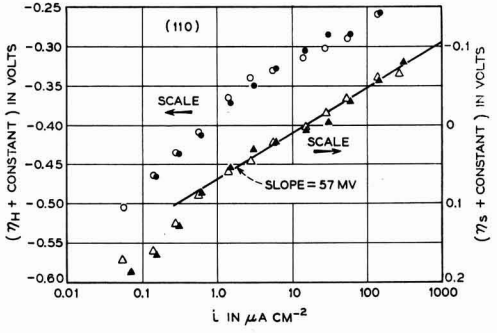

Fig. 4. Same as Fig. 3 but for (110) and n-type 28.7 ohm-cm

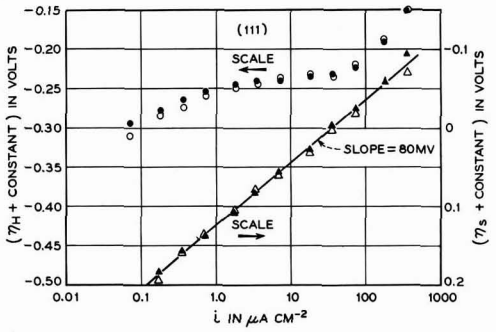

Fig. 5. Same as Fig. 3 but for (111) and n-type 38.8 ohm-cm

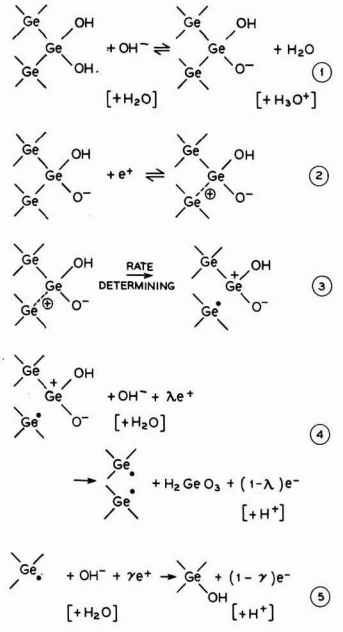

Fig. 6. Beck and Gerischer's mechanism for the anodic dissolution of germanium in alkaline solutions. Alternatives for acid solution in parentheses.

suming, as indicated by a large body of experimental evidence (13, 14), that holes are the carriers involved in the formation of the surface species], we may write

$$Ge^{x+} + mp_s \rightarrow Ge^{<m+x>+} \quad [4]$$

where Ge^{x+} is a surface atom in the $(+x)$ oxidation state, p_s is a hole close to the surface, and $Ge^{<m+x>+}$ is the species on the RHS of step 2 in Fig. 6, followed by

$$Ge^{<m+x>+} \rightarrow Ge^{(m+x)+} \quad [5]$$

and

$$Ge^{(m+x)+} \rightarrow Ge^{4+} \text{ (complexed in solution)} \quad [6]$$

where $Ge^{(m+x)+}$ is the species on the RHS of step 3 in Fig. 6. From Eq. [4]

$$[Ge^{<m+x>+}] \propto [p_s]^m \quad [7]$$

It is assumed that in step 5 of Fig. 6 the steady state lies very far to the right and also that $\theta_{Ge^{<m+x>+}}$ and $\theta_{Ge^{(m+x)+}}$ are small, hence $\theta_{Ge^{x+}} \approx$ constant.

From Eq. [4]

$$v_4 - v_{-4} = k_4\,\theta_{Ge^{x+}}[p_s]^m - k_{-4}\,\theta_{Ge^{<m+x>+}} \quad [8]$$

and since

$$[p_s] = [p_o] \exp\{-F\psi_s/RT\} \quad [9]$$

where $[p_o]$ is the hole concentration in the bulk, then combining k_4 and $\theta_{Ge^{x+}}$ into k'_4 we have

$$v_4 - v_{-4} = k'_4\,[_op_s]^m \exp\{-m\eta_sF/RT\} - k_{-4}\,\theta_{Ge^{<m+x>+}} \quad [10]$$

From Eq. [5]

$$v_5 - v_{-5} = k_5\,\theta_{Ge^{<m+x>+}} - k_{-5}\,\theta_{Ge^{(m+x)+}} \quad [11]$$

From Eq. [6] neglecting the reverse reaction when $\eta_H > 2RT/F$

$$v_6 = k_6\,\theta_{Ge^{(m+x)+}} \exp\{\alpha(4-m-x)\eta_HF/RT\} \quad [12]$$

In the steady state

$$v_4 - v_{-4} = v_5 - v_{-5} = v_6 = i/4F \quad [13]$$

Eliminating $\theta_{Ge^{<m+x>+}}$ and $\theta_{Ge^{(m+x)+}}$ we obtain

$$i = (4Fk'_4[_op_s]^m \exp\{-m\eta_sF/RT\})(k_5k_6 \exp\{\alpha(4-m-x)\eta_HF/RT\}) \ldots . \ldots (k_5k_6 \exp\{\alpha(4-m-x)\eta_HF/RT\} + k_{-4}\,[k_{-5}+k_6 \exp\{\alpha(4-m-x)\eta_HF/RT\}])^{-1} \quad [14]$$

Since [5] is assumed to be slow we may put

$$k_6 \exp\{\alpha(4-m-x)\eta_HF/RT\} >> k_{-5} \quad [15]$$

and also

$$k_{-4} >> k_5 \quad [16]$$

whence Eq. [14] simplifies to

$$i = 4Fk'_4k_{-4}^{-1}k_5[_op_s]^m \exp\{-m\eta_sF/RT\} \quad [17]$$

and

$$d\eta_s/d\log i = -2.303\,RT/mF \quad [18]$$

Equation [17] indicates that the rate is dependent on the space charge overpotential and independent of the Helmholtz overpotential. This arises because we have assumed that the rate-determining step (Eq. [5]) takes place outside the region where the Helmholtz overpotential occurs.

On a germanium (100) surface the atoms are already in the (+2) oxidation state, *i.e.*, $x = +2$. The possible choices of values for m then become zero, one, or two. The observation that $(d\eta_s/d\log i)_{(100)}$ in Fig. 3 is close to —59 mv implies that $m = 1$ in Eq. [18] and is consistent with B and G's mechanism, but does not prove it. It is clear that there is also a variation in η_H of approximately equal magnitude to the variation in η_s. More complex models could possibly be constructed in which changes in η_H assumed kinetic significance. No analysis of this kind will be made here.

(110) Surface.—From Fig. 3 and 4 it is clear that the data for the (110) dissolution are very similar to those for (100). The atoms on the (110) surface are triply bonded to the lattice (*i.e.*, $x = +1$) and hence should not undergo dissolution as readily as the doubly bonded atoms on the (100) surface. This difference is illustrated two-dimensionally in Fig. 7. However, the (110) surface may readily be nucleated to undergo dissolution through the removal of doubly bonded atoms simply by breaking one bond between surface atoms. The atoms at each end of this broken bond are only doubly bonded to the lattice (*i.e.*, $x = +2$) and may be removed by B and G's mechanism. The process can propagate along a given row of atoms entirely across the crystal. Provided the rate of supply of such nuclei is sufficient that their concentration is not noticeably decreased by the current flow, and that dissolution takes place only through these doubly

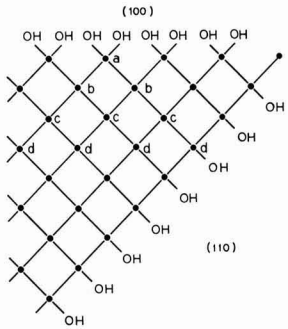

Fig. 7. Two-dimensional representation of (100) and (110) surfaces

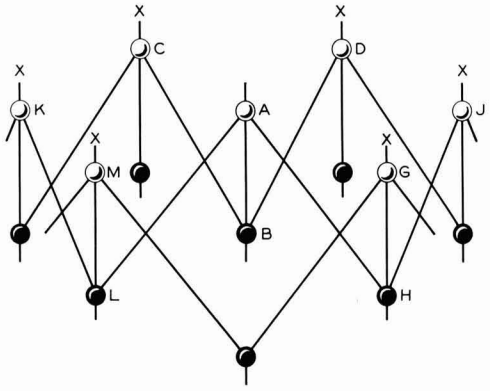

Fig. 8. Perspective view of part of a (111) surface. Atoms of one color are in one plane.

bonded atoms, then the (110) should exhibit similar kinetics to the (100). The nucleation process may occur by thermal generation of broken bonds in the surface plane, or by intersection of vacancies or appropriate impurity atoms in the surface plane. Differences between Tafel slopes for (100) and (110) have been observed at higher current densities (16, 17) and in other aqueous solutions (18).

(111) Surface.—The bonding on the (111) surface is shown in Fig. 8, and as before we will base our argument on the assumption of atomically perfect surfaces.

The mechanism of dissolution for (111) is not established. A possible scheme involves nucleation by breaking one bond between a surface and subsurface atom, or alternatively a dislocation may intersect the surface. The surface atom is now doubly bonded to the lattice and may be removed by B and G's mechanism. This constitutes the initial step in the formation of an etch pit, and the atoms along the sides of this pit are essentially in (110) orientation. Removal of one side wall can be nucleated by the breaking of any bond made by any of the three atoms in that wall to another germanium atom.

It might be expected if the rate-determining step were nucleation of the (110) oriented atoms that kinetics similar to (100) and (110) faces would be observed. The data in Fig. 5 show $(d\eta_s/d \log i)_{(111)}$ to be about 80 mv and hence seen to imply (from Eq. [13]) that the reaction is of fractional order in the surface hole concentration.

Dewald has suggested reasons for apparent fractional order hole kinetics. The dissolution reaction may take place through the participation of surface states (*i.e.*, localized holes) distributed exponentially in the energy (3), or alternatively discrete bound states for

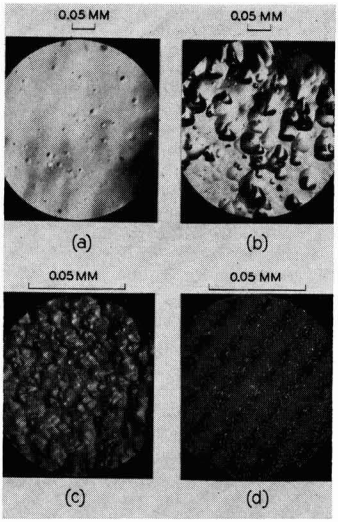

Fig. 9. (a) (100) surface after CP4 etch; (b) (111) surface after 1 ma cm^{-2} for 24 hr; (c) p-(100) surface, same treatment; (d) n-(100) surface, same treatment (with illumination).

carriers near the surface may occur if the field in the germanium space charge region is sufficiently high (20). The first suggestion requires that we postulate surface states at a (111) surface but not at (100) and (110) surfaces in approximately the same energy range. Although this is not impossible, our measurements of capacity give no indication of fast surface states on any face in this energy region. The second explanation is ruled out by the fact that our data are obtained in the region of small bending of the bands (*i.e.*, $+200 \text{ mv} > \psi_s > -100 \text{ mv}$).

A much more likely explanation, since the dissolution takes place with the formation of etch pits with sides of orientation different from (111) (as we will discuss later), is that the nonuniformity of the potential distribution over the surface precludes any exact analysis of these data.

Morphology of Anodized Germanium Surfaces

In a further series of experiments we have examined the nature of the surfaces produced after extensive anodic dissolution at constant current in neutral K_2SO_4 solution. The behavior of the three surfaces is quite distinctly different, but for any one face both n- and p-type behave similarly indicating that the observed effects are actually due to orientation. Figure 9(a) shows the typical appearance of a CP4 etched surface before anodizing. Currents of about 1 ma cm^{-2} were passed for about 24 hr, after which the surfaces were examined by optical microscopy. Results are shown in Fig. 9(b), (c), and (d) for p-(111), p-(100), and n-(100) surfaces. The (110) is not illustrated since no features were developed. On p- and n-type (111) surfaces distorted triangular etch pits were observed. On p-type (100) hillocks formed, and on n-type (100) we saw a finer structure that could not be resolved.

The probable role of dislocations is illustrated in Fig. 10. Figures 10(a) and 10(b) show areas of a p-type (111) surface after CP4 etching and the same area after anodizing. It is clear that dissolution has occurred primarily from around pits, presumably marking emerging dislocations, on the original CP4 etched surface.

The p-type (100) surface had fewer and smaller pits when CP4 etched, but in one case we located an area where the lines of pits shown in Fig. 10(c) were observed. This pattern was sufficiently distinctive that

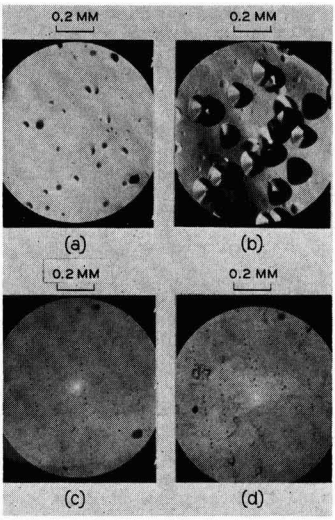

Fig. 10. (a) Area of CP4 etched (111) surface; (b) same area after anodic etching; (c) area of CP4 etched (100) surface; (d) same area after same anodic etching as in (b).

it could be located after anodizing. This (100) crystal was anodized at the same current density for the same length of time as the (111) surface in Fig. 10(b). The result is shown in Fig. 10(d). There appears to have been no preferential dissolution from the etch pits in this case. The absence of structure similar to Fig. 9(c) is due to the lower magnification and the different illumination, which was optimized to reveal the pits.

(110) Surface.—Anodic etching of this surface produced no obvious features on either n- or p-type electrodes. The surfaces retained the same polished but somewhat undulating appearance produced by the original CP4 etch. This fact is consistent with both the mechanism of anodic dissolution previously discussed and with the surface geometry. Since the number of atoms dissolved per nucleation is large [rather than a few localized at the site of the nucleation as on (111)] etch pits would not be expected. Also any blocking effect (discussed in the next section) due to slow dissolving impurities would not propagate through the lattice as on (100), since each surface atom is bonded to only one atom in the plane below (see Fig. 7) and neither of the atoms in the surface plane bonded to a blocked atom is itself blocked.

(100) Surface.—Prolonged anodizing of a (100) surface (1 ma cm^{-2} for 24 hr) resulted in a surface with a matte appearance which under high magnification has the structure shown in Fig. 9(c). The features are square pyramidal etch hillocks, the largest being $\sim 5\mu$ on a side and oriented with respect to the crystal as shown in Fig. 11. If only low index planes are involved, the sides of the hillock may be of (110) orientation. The sides cannot be (111) since then the hillocks would be rotated 45° about an axis perpendicular to the plane of the paper.

The formation of hillocks can be understood if it is postulated that there are impurity atoms in the lattice which undergo dissolution considerably less rapidly than germanium. Consider that atom marked (a) in the surface (100) plane of Fig. 7. If it remains behind after the rest of that plane has dissolved, it will inhibit the dissolution of atoms (b) in the second plane since they are now triply bonded to the lattice (*i.e.*, +1 oxidation state). The process is repeated in the next plane where the dissolution of four atoms is blocked. [Since Fig. 7 is a two-dimensional representation only three are shown. The center (c) atom

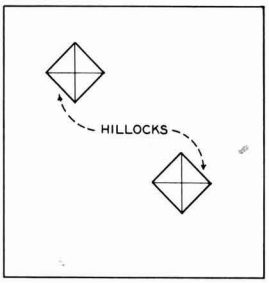

Fig. 11. Orientation of hillocks on the (100) surface. The large square represents one face of a cube having all (100) faces.

is actually two atoms superimposed. Similarly the two center (d) atoms are actually two atoms superimposed, etc.] In this way a square pyramid with (111) sides is generated as the blocking effect propagates through the lattice. Eventually the sides of all such pyramids intersect, and no (100) surface remains. On the line between the apex and the corners of these pyramids the atoms are in (110) orientation. Further dissolution of the crystal (which must occur due to the constant current imposed) is much more likely to do so from these (110) regions than from the (111) faces for the kinetic reasons described previously. Consequently the (110) faces appear at the expense of the (111) and the pyramid eventually attains the observed orientation. Figure 9(c) represents a case where the dissolution was sufficiently prolonged that the surface was entirely covered with hillocks and no (100) surface was left exposed.

The formation of such hillocks on a p-type sample was found to be reproducible. With an n-type sample at the same current density the behavior was also reproducible but different from p-type. In this case the surface was hazy rather than matte and the microscope revealed a fine granularity which was not resolved at the highest available magnification [Fig. 9(d)]. A possible explanation is that a greater density of hillocks formed before their sides intersected and converted the surface to a convoluted (110). Since the hillocks would intersect sooner they would be smaller.

We may make a rough estimate of the reasonableness of our postulate that the hillocks are caused by impurity atoms. Referring to Fig. 9(c), since the largest hillocks are about 5μ on a side at the base and assuming (110) orientation (*i.e.*, angle between opposite faces at the apex equals 90°) the maximum height is $\sim 2.5\mu$. Assuming that the peaks of all the observed pyramids occur within this depth and making an estimate of the average dimensions at the base as 1μ we then calculate a density of impurity atoms (at the peaks) of 4×10^{11} cm^{-3}. If this mechanism is correct it implies that we have detected by electrochemical means some impurity present at approximately one part in 10^{11}.

(111) Surface.—The (111) surfaces [Fig. 9(b)] exhibited distorted triangular pits, all oriented in the same direction as shown in Fig. 12.

The orientation of the walls of the pits has not been determined, but they are definitely not (100) as had been previously suggested (21) since in this case the pits would be rotated by 60° from their observed orientation. If the vertical nucleation were rate determining, then the pits would tend to be flat bottomed or very shallow. Some features of this type do occur in Fig. 9(b) and may be due to this cause or possibly to dislocations which intersected the original surface but which have terminated at a relatively small depth into the crystal. The rounded shape of the pits could be due to inhibition of dissolution in the corners by concentration polarization. This causes the solution to become more acid in these regions, and

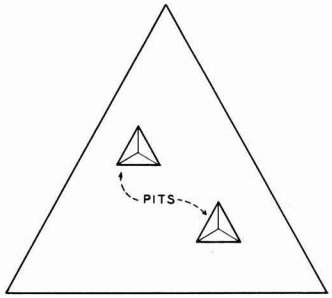

Fig. 12. Orientation of pits on the (111) surface. The large triangle represents one face of a regular tetrahedron having all (111) faces.

as a consequence the p.d. across the Helmholtz region will change in such a direction as to include an increased fraction of the total anodic overvoltage (22, 5), thus reducing the space charge overvoltage and hence the rate of dissolution.

Many of the pits appear to have sides of different slope. This may be due to the dislocation line being at some angle other than normal to the surface of the crystal (*e.g.*, 60° dislocations) assuming that the three walls grow equally rapidly from the nucleation point.

Conclusions from Anodic Etching Experiments

The effect of the morphology of the surfaces on these and other measurements we have made is as follows. For the (111) surface in the early stages of dissolution the pits are quite small so that we are very largely dealing with a macroscopic (111). Consequently measurements of interfacial capacity refer principally to the (111) so that our previous conclusions based on capacity of this surface still hold. The measurement of overvoltage, as pointed out above, is likely to be incorrect since the potential measurements refer to (111) while dissolution takes place from the sides of the pits [possibly (110)], but may in any case be subject to concentration polarization within the pits.

Since the (110) surface does not develop any obvious features it is assumed that our measurements on (110) oriented crystals are correct.

On the (100) it is clear that after extensive anodizing we are dealing with a convoluted surface, possibly (110). In fact as we have observed both in capacity measurements and in dissolution kinetics the (100) and (110) oriented crystals behave similarly. This could be due to the fact that even on a sample which has been CP4 etched and then only mildly anodized the surface consists of microscopic (110) facets. The results on (100) may be open to the question as whether they are truly representative of a (100) surface or are affected by (110) faceting. However, some of our earlier measurements on mildly anodized surfaces (4, 6) indicate quite low values (~1.3) for the roughness factor. This suggests that under these circumstances faceting is not a problem.

Summary

The kinetics of anodic dissolution of germanium (100) have been shown to be consistent with Beck and Gerischer's mechanism. The (110) surface behaved similarly to the (100) at low c.d. The (111) surface showed more complex behavior which was ascribed to the requirements of a nucleation process or to nonuniform distribution of potential. The morphology of anodized surfaces has been discussed with respect to the dissolution kinetics.

Acknowledgment

It is a pleasure to acknowledge continuing cooperation and advice from Dr. W. H. Brattain. The author is also indebted to Dr. W. W. Harvey of the Kennecott Copper Corporation for discussion of his results on anodic etching of germanium prior to publication, to Dr. P. C. Milner for discussion of electrode kinetics, and to Mr. W. J. Sundburg for technical assistance.

Manuscript received Nov. 20, 1963; revised manuscript received April 16, 1964. This paper was presented at the Pittsburgh Meeting, April 15-18, 1963.

Any discussion of this paper will appear in a Discussion Section to be published in the June 1965 JOURNAL.

REFERENCES

1. A. N. Frumkin, *Z. physik. Chem.*, **164**, 121 (1933).
2. M. Green in "Modern Aspects of Electrochemistry," J. O'M. Bockris, Editor, Butterworths Scientific Publications, London (1959).
3. J. F. Dewald in "Semiconductors," N. B. Hannay, Editor, Reinhold Publishing Co., New York (1959).
4. W. H. Brattain and P. J. Boddy, *This Journal*, **109**, 574 (1962).
5. P. J. Boddy and W. H. Brattain, *ibid.*, **110**, 570 (1963).
6. P. J. Boddy and W. H. Brattain, *Ann. N. Y. Acad. Sci.*, **101**, 683 (1963).
7. M. Lasser, C. Wysocki, and B. Bernstein in "Semiconductor Surface Physics," R. H. Kingston, Editor, University of Pennsylvania Press (1957).
8. F. Beck and H. Gerischer, *Z. Elektrochem.*, **63**, 500 (1959).
9. (a) W. W. Harvey, "Quarterly Progress Report Solid-State Research," Lincoln Laboratory, Lexington, Mass. (November 1958); (b) P. J. Boddy and W. H. Brattain, Unpublished results.
10. P. J. Hillson and E. K. Rideal, *Proc. Roy. Soc.*, **199A**, 225 (1949).
11. C. G. B. Garrett and W. H. Brattain, *Phys. Rev.*, **99**, 376 (1955).
12. M. Green, *J. Chem. Phys.*, **31**, 200 (1959).
13. W. H. Brattain and C. G. B. Garrett, *Bell System Tech. J.*, **34**, 129 (1955).
14. Yu. V. Pleskov, *Doklady Akad. Nauk S.S.S.R.*, **126**, 111 (1959).
15. B. Lovrecek and J. O'M. Bockris, *J. Phys. Chem.*, **63**, 1368 (1959).
16. W. Mehl, reported in "Advances in Electrochemistry and Electrochemical Engineering," P. Delahay, Editor, p. 184, Interscience Publishers, New York (1961).
17. J. A. Harrison and H. Gerischer, *Z. Elektrochem.*, **66**, 762 (1962).
18. P. J. Boddy and W. H. Brattain, Extended Abstracts of the Theoretical Division of the Electrochemical Society, **1**, 16 (1963).
19. W. H. Brattain and P. J. Boddy, *Proc. Nat. Acad. Sci.*, **48**, 2005 (1962).
20. J. F. Dewald, *Ann. N. Y. Acad. Sci.*, **101**, 872 (1963).
21. H. Gerischer in "Advances in Electrochemistry and Electrochemical Engineering," P. Delahay, Editor, Interscience Publishers, New York (1961).
22. M. Hoffman-Perez and H. Gerischer, *Z Elektrochem.*, **65**, 771 (1961).

Preparation of InAs-InSb Alloys

J. C. Woolley[1] and J. Warner[2]

Department of Physics, University of Nottingham, Nottingham, England

ABSTRACT

The preparation of solid samples of InAs-InSb alloys suitable for optical transmission and electrical measurements is considered. Cross sectional slices of ingots produced by slow directional freezing and slow zone recrystallization have been investigated by x-ray powder photograph techniques, and results are given for the variation of composition with position along ingot and for homogeneity of the slice. Annealed powder samples have been used to check the previous data for the variation of lattice parameter with composition. Specimens have also been observed by photomicrograph methods and by use of an electron probe microanalyzer. The x-ray, photomicrograph, and microanalyzer data are compared for various samples with different degrees of homogeneity.

Very little information is so far available on InAs-InSb alloys. It has been shown that single phase solid solution can be obtained at all compositions (1), but compressed powder specimens need to be annealed at temperatures very close to the solidus curve for periods of six months or more before such conditions are approached. Similar annealing of solid samples needs very much longer times. The data obtained by annealing compressed powders gave the variation of lattice parameter with composition and the solidus curve shown in Fig. 1 and 2. The liquidus curve in Fig. 2 was obtained by Shih and Peretti (2) using normal cooling curve methods. Here the preparation of samples of InAs-InSb alloys in solid form suitable for optical and electrical work is discussed. The investigation of the semiconductor parameters of the alloys is discussed elsewhere (3).

Methods of Preparation of Solid Specimens

Two methods of preparation have been considered, viz., (a) slow directional freezing, and (b) slow zone recrystallization of suitable ingots. All of the ingots were produced by melting together appropriate amounts of high purity InAs and InSb. Both of the compounds were from zone refined ingots to give good purity and both were n type with approximate carrier concentrations of 2 x 10^{16}/cm^3 for InAs and 1.5 x 10^{16}/cm^3 for InSb.

Preparation by powder annealing.—In the case of both the directionally frozen and the zone recrystallized ingots, the composition of any cross sectional slice was to be determined by finding the lattice parameter and using the data in Fig. 1 to give the corresponding composition. Therefore, as some powdered samples were to be used in the optical work (to be published elsewhere), these were used to check the data of Fig. 1. Small samples were made by melting together under vacuum appropriate amounts of the two compounds, quenching in water, and coarsely powdering the resultant ingots. (Coarse powdering was required, since a further powdering had to be carried out in the equilibrium condition to give new surfaces necessary for the optical diffuse reflection measurements.) The powders were then compressed and sealed under vacuum as described previously (1) and annealed for some six months at closely controlled temperatures chosen to be 10°-15°C below the relevant solidus temperature as given in Fig. 2. Even after this time of annealing, the powders were not in good equilibrium condition, the higher order x-ray reflections being blurred. Nevertheless values of lattice parameter accurate to ±0.007Å could be obtained, and these are shown in Fig. 1 together with the previous results for which the lattice parameter determination was less accurate. The agreement between the two sets of data is good, confirming the results of Fig. 1 and also therefore the solidus data in Fig. 2 obtained by the use of lattice parameter values.

Preparation by slow directional freezing.—In the case of GaSb-InSb and GaAs-InAs alloys, it has been found (4) that homogeneous polycrystalline samples of the alloys can be obtained by a slow directional

[1] Present address: Physics Department, University of Ottawa, Ottawa 2, Canada.

[2] Present address: R.R.E., Great Malvern, England.

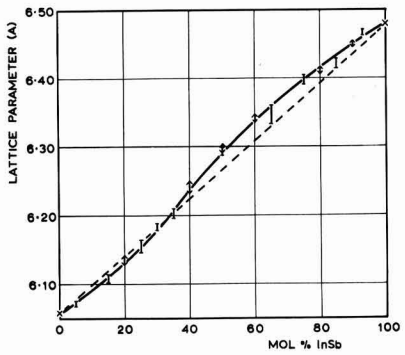

Fig. 1. Variation of lattice parameter with composition for InAs-InSb alloys. I Woolley and Smith (1), ↕ present work.

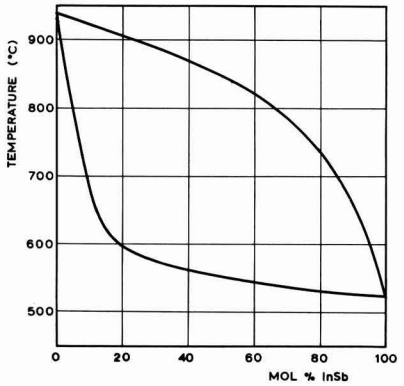

Fig. 2. Phase diagram of InAs-InSb system. Liquidus curve, Shih and Peretti (2); solidus curve, Woolley and Smith (1).

freezing of an ingot some 15-20 cm in length. In these cases, ingots cooled in a temperature gradient of the order 10°C/cm and at a rate of 5°-10°C/day were found to be reasonably homogeneous over their whole length. This method of preparation is very convenient for the initial investigation of the semiconductor properties of an alloy system in that the variation of the composition of cross sectional slices with length gives a wide range of sample composition and hence the properties across the whole composition range can be investigated using, at the most, two or three ingots of different mean composition. It was decided therefore to try a similar method of preparation for the InAs-InSb alloys.

The ingots used were of an equimolar mean composition, had a mass of approximately 40g, and were 15-20 cm long. Initially a furnace with a temperature gradient of 10°C/cm over about 20 cm was used and the temperature controlled by a switched control unit, so that the time required to completely freeze the ingot was approximately 2-3 months. In an attempt to improve the homogeneity of the material, a second ingot was cooled in the same furnace at 5°C/day, while a third similar ingot was cooled in a furnace having a temperature gradient of 7°C/cm and controlled by a continuous control unit so that the short term temperature fluctuations at 600°C were less than ±0.2°C. The rate of cooling in this last case was 4°C/day and the freezing process required approximately 6 months to complete. The variation of composition of a cross sectional slice with distance along the ingot for the case of the third ingot is shown in Fig. 3. It was found that each end of the ingot was in good single phase condition, the Cu-Kα doublet being well resolved in the x-ray photographs, and that the composition varied from 3 to 12 mole % InSb at one end and 88 to 98 mole % InSb at the other. In between these regions, however, there was some 3 cm of the ingot where there was a very rapid change in composition with position and where the material was not in an equilibrium condition, being two phase with each phase showing considerable broadening of the high angle x-ray reflections. The corresponding spread in composition is indicated by the vertical lines in Fig. 3.

Comparison of the three ingots showed that the third was the best of the three in that the single phase regions of this ingot were more homogeneous than for the previous ones, and at each end the composition range of the single phase region was a few mole per cent greater. In addition, electrical measurements showed that single phase samples from the third ingot had lower carrier concentrations and higher mobility values. These improvements can be attributed to the use of a slower movement of the freezing surface and to the better control of the furnace temperature. From a knowledge of the variation of temperature profile of the furnace in the temperature range concerned, the composition variation along the ingot in Fig. 3 and

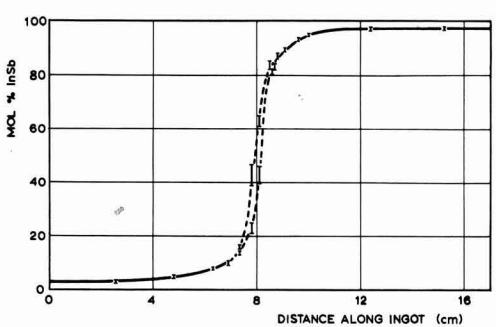

Fig. 3. Variation of composition of cross sectional slice as a function of position in a directionally frozen ingot (DF3).

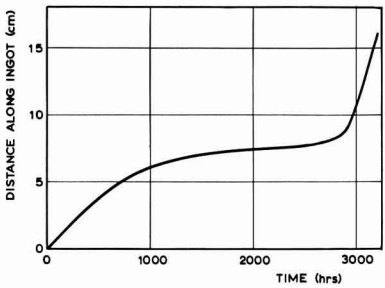

Fig. 4. Position of freezing surface as a function of time in a directionally frozen ingot (DF3).

the solidus curve of Fig. 2, the movement of the freezing surface with time can be calculated. This curve is shown in Fig. 4. This is only approximate in the two phase region where an average composition must be assumed. In the ranges where single phase material was obtained, it is seen that the rates of movement of the freezing surface are 0.2 cm/day at the beginning of the ingot and 0.65 cm/day at the end. The temperature control of ±0.2°C will give fluctuations in freezing surface position larger than this, and so a slower rate of cooling is of no use unless more accurate temperature control is used.

The rate of movement of the freezing surface was much slower in the central region (~0.02 cm/day). Here, however, the inhomogeneity was similar for all ingots, and the different cooling conditions produced little difference in homogeneity. It is apparent that other effects, *e.g.*, constitutional supercooling (5), become important. This is supported by the fact that the composition of the solid at which inhomogeneity begins to occur corresponds to a point on the liquidus where the slope of the liquidus changes rapidly and becomes much steeper, as is seen in Fig. 2. Thus with the small temperature gradients used in these directional freeze techniques, constitutional supercooling is always likely to occur. Hence this particular method is not suitable for alloys in the center of the composition range.

Preparation by slow zone recrystallization.—An alternative method for preparing ingots of these alloys is the zone recrystallization technique. Here larger temperature gradients are used so that constitutional supercooling should be less of a problem, and the rate of movement of the freezing surface is directly controlled by the movement of the heater relative to the ingot. The ingots used here were of equimolar mean composition and the same dimensions as in the previous case. Two background furnaces were used to maintain an over-all temperature of the ingot at about 550°C, and the hot zone was produced by two "Crusilite' heater rods placed between the background furnaces, one above and one below the ingot. To reduce the width of the hot zone, two water cooled copper plates were placed between the heater rods and the backing furnaces. The resulting molten zone of the ingot was of the order 5 cm in length. This is considerably wider than that used for normal zone recrystallization work with compounds, *etc.*, but it was hoped with this method to obtain some advantage of the directional freeze method, *i.e.*, the variation in composition along the ingot which would provide samples over a range of alloy compositions. The molten zone was moved along the ingot by holding the ingot stationary and moving the whole furnace system along the ingot length. The velocity of the zone along the ingot was approximately 0.5 cm/day.

The ingots produced showed little difference one to another and the variation of composition with length for one case is shown in Fig. 5. Again the ingot is homogeneous at the two ends but is inhomogeneous in the center. The beginning section of the ingot ex-

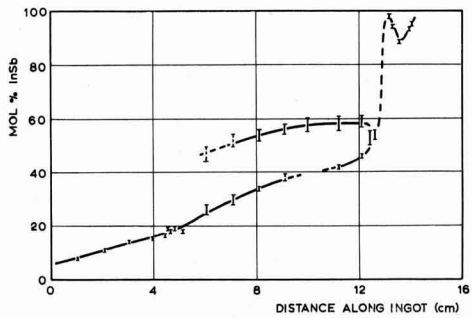

Fig. 5. Variation of composition of cross sectional slice as a function of position in a zone recrystallized ingot (ZL2).

tended the available range of homogeneous alloys out to 20 mole % InSb, but beyond this again the cross sectional slices were two phase, each phase showing some blurring of the high angle x-ray lines. However the intensity of the x-ray lines showed that the amount of second phase was small in some places (shown by dotted vertical lines in Fig. 5) and occasionally, as at a point 10 cm from the beginning of the ingot, only one phase is observed. Thus by careful selection, single phase alloy samples over a considerable range of composition could be obtained.

Again it is seen that this preparation is not satisfactory for alloys in the center of the composition range. One problem is the initial width of the molten zone and, second, the fact that the zone width and hence the temperature gradient at the freezing surface varies considerably with the composition of the zone. It would appear that to improve this, a different means (*e.g.*, R.F. heating) is needed to produce the zone, and careful programming of the heating as a function of position along the ingot is required.

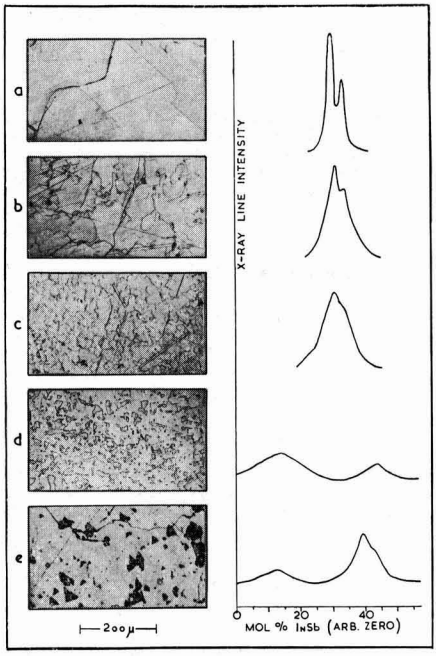

Fig. 6. Photomicrographs and x-ray line profiles of representative specimens of InAs-InSb alloys. (a) Composition 4 mole % InSb, 4 sec etch, x-ray reflection 553 and 731. (b) Peak composition 89 mole % InSb, 4 sec etch, x-ray reflection 553 and 731. (c) Peak composition 68 mole % InSb, 6 sec etch, x-ray reflection 553 and 731. (d) Peak compositions 34 mole % and 64 mole % InSb, 5 sec etch, x-ray reflection 620. (e) Peak compositions 26 mole % and 49 mole % InSb, 6 sec etch, x-ray reflection 620.

Comparison of X-Ray any Metallurgical Data

Samples of varying degrees of homogeneity taken from the ingots described above have been studied by x-ray powder photography and by optical photomicrography, and in certain cases Metals Research Ltd., Cambridge, have studied the samples with an electron probe microanalyzer. The aim here was to observe how the inhomogeneity as seen by metallurgical techniques could be correlated with the x-ray data and to see whether the broadening of the x-ray reflections was associated with any inhomogeneity easily observed under the microscope.

To present the x-ray data, a suitable x-ray reflection was chosen (the choice had to be varied to some extent because of accidental coincidence of lines from different phases) and the intensity profile of the line on the x-ray film determined using a Hilger and Watts comparator microphotometer. The position on the film can be correlated with Bragg angle, hence with lattice parameter, and so with composition of the alloy. Hence the line profiles given here have been plotted as intensity *vs.* mole per cent InSb.

The specimens for the photomicrographs were produced by embedding suitable samples in an epoxy resin and polishing with various powders down to 0.1μ γ alumina. The samples were then etched in an etchant consisting of equal volumes of nitric acid, hydrofluoric acid, and distilled water.

The results with typical samples are shown in Fig. 6, where specimens a, b, and c were single phase but with increasingly broadened x-ray lines, and d and e were two phase specimens. It is seen that for d and e the presence of two phases is easily observed on the photomicrograph, while for a the photomicrograph shows a single phase condition with grain boundaries, *etc.* In samples b and c the trend toward inhomogeneity can be observed, but the interpretation of the photomicrograph would be difficult without the help of the x-ray line profile.

Specimens b, c, and d were investigated by Metals Research Ltd. using a Cambridge Instruments Co.

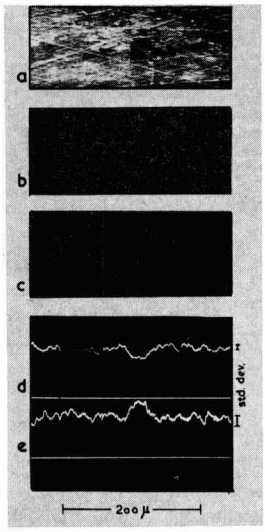

Fig. 7. Electron probe microanalysis results for specimen d (see legend of Fig. 6). (a) Electron image. (b) Antimony Kα image. (c) Arsenic Kα image. (d) Antimony Kα line scan trace. (e) Arsenic Kα line scan trace.

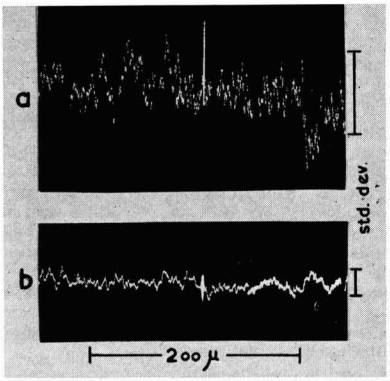

Fig. 8. Electron probe microanalysis results for specimen c (see legend of Fig. 6). (a) Arsenic Kα line scan trace. (b) Antimony Kα line scan trace.

electron probe microanalyzer, a Microscan. The results for specimen d are shown in Fig. 7. Figure 7a is the electron image of a region of the specimen, showing polishing scratches at this higher magnification and a dark area near the center of the photograph. Figures 7b and c are x-ray images of the same region of the specimen with the x-ray spectrometer tuned to the characteristic radiations of antimony and arsenic, respectively. A careful observation of these photographs shows that the density of spots in the area corresponding to the dark area of Fig. 7a is greater than average in Fig. 7c and smaller than average in Fig. 7b, indicating that this region of the sample is arsenic rich. This is confirmed by the curves in Fig. 7d and e which give a scan of the intensity along the line XX′ with antimony and arsenic radiation, respectively. The standard deviation, taken as the square root of the number of quanta observed, is shown at the right of the curve. It is seen that the deviation at the area concerned is considerably larger than the standard deviation, confirming that this area is arsenic rich and antimony deficient.

Similar results were taken with specimen c. Here the electron image and x-ray images appeared quite uniform and no inhomogeneity could be observed. Figures 8a and b show the results for a line scan taken with arsenic and antimony radiation, respectively. Here the standard deviation for arsenic radiation is larger because of the small mean percentage of arsenic for the specimen. However the deviations in the line scan are not significantly larger than the standard deviation and give no indication of inhomogeneity on any appreciable scale. With specimen b similar results were obtained.

It is seen that the use of x-ray powder diffraction is the most sensitive method for observing inhomogeneities in composition in the case of alloys of this system. Thus by either electron probe method or standard photomicrograph techniques the presence of inhomogeneities is clear only for samples where the x-ray photograph shows two distinct phases. Alloys such as specimen c above appear reasonably homogeneous to the electron probe and photomicrograph even though the x-ray data indicates an effective spread in composition of the order of 10 mole %. This confirms that the inhomogeneity is on a considerably smaller scale than that observed by normal microscope work and is probably due to clustering effects in the atomic lattice.

Acknowledgments

The authors are indebted to Professor L. F. Bates for the facilities of his laboratory and to Metals Research Ltd., Cambridge, for the electron probe data. The work described forms part of an investigation carried out for the Admiralty.

Manuscript received March 23, 1964; revised manuscript received May 1, 1964.

Any discussion of this paper will appear in a Discussion Section to be published in the June 1965 JOURNAL.

REFERENCES

1. J. C. Woolley and B. A. Smith, *Proc. Phys. Soc.*, **72**, 214 (1958).
2. C. Shih and E. A. Peretti, *J. Am. Chem. Soc.*, **74**, 608 (1953).
3. J. C. Woolley and J. Warner, In press *Can. J. Physics.*
4. J. C. Woolley, "Preparation of III-V Compounds," R. K. Willardson and H. L. Goering, Editors, Reinhold Publishing Co., New York (1963).
5. W. G. Pfann, K. M. Olsen, and B. Sawyer, "Transistor Technology, Volume I," H. E. Bridgers, J. H. Scaff, and J. N. Shive, Editors, Van Nostrand & Co., New York.

Germanium-Silicon Alloy Heterojunctions

J. Shewchun[1] and L. Y. Wei

University of Waterloo, Waterloo, Ontario, Canada

ABSTRACT

Germanium-silicon heterojunctions have been prepared by an alloy process. By controlling the impurity concentrations, abrupt junctions having widths from 6000Å to as low as 80Å have been realized. Forward and reverse bias characteristics of several typical heterojunctions are presented. No Esaki effect was observed for thin heterojunctions (<100Å). This is attributed to masking by an abnormally high excess current. This excess current is a tunneling current *via* defect states caused by the large dislocation densities present in the junction.

Interest in heterojunction devices was stimulated in the late 1950's by the work of Kroemer. The concept of quasi-electric and magnetic fields for variable energy-gap semiconductors was first posed by him (1, 2), and shortly thereafter he presented the theory for the wide band-gap emitter transistor (3). In the following years, a number of articles by other investigators were published (4-6), which dealt with similar considerations. An unsuccessful attempt to fabricate a wide band-gap emitter transistor by the diffusion of phosphorus into gallium arsenide was reported by Jenny (7). The interest in heterojunctions has also spread to the field of solar energy converters (8, 33). Theoretical considerations by Emtage (9) have shown that

[1] Present address: Interdisciplinary Fellow in Materials Sciences, Brown University, Providence, Rhode Island.

it might be possible to incorporate a heterojunction type structure into a photovoltaic converter which could give an efficiency as high as 40%.

With the advent of epitaxial vapor growth techniques (10), considerable interest was stimulated in heterojunctions where one crystal was vapor deposited upon another. The first such heterojunctions were reported by Marinace (electrical properties) (11) and Anderson (analysis) (12). In a series of papers (12-14), Anderson proposed an energy-band model for these heterojunctions which included energy discontinuities in the conduction and valence band edges at the junction interface. More recently, a group consisting of Messrs. Perlman, Oldham, Williams, Feucht, and Milnes have carried out a more intensive investigation into the Ge-GaAs system originally studied by Anderson and extended the work to other systems as Ge-Si and InP-GaAs. In a series of papers (15-19, 34), the general conclusion reached seems to be that there are a large number of unexplained discrepancies which make uncertain the complete validity of the discontinuous energy-gap model. Continuing work by Howard and Fang (20, 21) on n-n Ge-GaAs diodes has shown that these heterojunctions have subnanosecond switching times but suffer the disadvantage of having a low reverse breakdown voltage.

In this paper, we wish to report our experimental investigations on the germanium-silicon system by means of alloy heterojunctions. The evidence that such a system should yield reasonably good junctions is based on the work on germanium-silicon "alloy" crystals. That germanium and silicon show good alloying affinity was demonstrated as far back as 1939 by Stohr and Klemm (22). It was noted that the lattice constant varied monotonically from that of silicon (5.43Å) to that of germanium (5.66Å) depending on the percentage of germanium in the silicon (0→100%). Both silicon and germanium are diamond-type crystals. A germanium-silicon substitutional alloy can be formed where the germanium and silicon atoms are arranged at random at lattice sites of a diamond-type lattice. More recent work on "single crystals" of such alloys has been carried out by a number of people at Radio Corporation of America (23, 24). Herman has considered such alloy crystals on a theoretical basis (25). Since an alloy is not a perfect crystal but disordered, it does not have an energy-band structure in the strict sense, but rather regions of high density allowed states (allowed bands) and regions of low density allowed states (forbidden bands). The transition from an allowed to a forbidden band is not as sharp as in a perfect crystal, at least theoretically. However, experimental evidence has shown that such tailing of the band edges is negligible for the Ge-Si system. Present work on the Ge-Si system seems to be concentrated on an accurate determination of the energy-band structure (26, 27). Since the lattice constants of germanium and silicon do differ by a few per cent, it is expected that the alloy crystal would have irregularities. It has been shown (28) that such lattice mismatches can be accommodated through a dislocation formation mechanism. Experimental observations by Goss, Benson, and Pfann (29) tend to confirm this. There is, on the basis of the work just described, every reason to believe that an alloy type p-n heterojunction between germanium and silicon is possible.

Fabrication

Germanium-silicon heterojunction diodes were made, as mentioned, by the alloying technique. The starting materials consist of single crystal silicon and germanium wafers. The silicon is prepared by first mechanically lapping it with suitable silicon-carbide abrasives, and then etching it to a mirror finish in CP4 (4 parts HNO_3, 3 parts CH_3COOH, 3 parts HF). After rinsing and drying, the wafer is broken or cut into small pieces suitable for the alloy process. The germanium is similarly treated and crushed into very small chips from which are extracted small particles being more or less spheroids of diameter between 5 and 20 mils. The alloying apparatus consists of a high current strip heater with an electrical timer for the control of the temperature cycle.

The alloying is carried out by placing a silicon wafer of thickness between 10 and 20 mils on the heater with a selected spheroid of germanium on top. The area of the junction is approximately determined by the size of the germanium used. The alloy cycle consists of an abrupt heating to a temperature between 950° and 1200°C for periods of 3-15 sec, followed by a similar abrupt cooling. Short alloy times have been deliberately employed in an effort to form thin abrupt junctions and to minimize the diffusion of the doping elements in the germanium and the silicon. In order to obtain good wetting between the germanium and silicon, the alloying is carried out in an atmosphere of dry hydrogen.

After the junction has been formed, a second alloy is carried out in which a gold wire is attached to the body of the silicon to form one of the ohmic contacts. In some cases this is replaced by a gold plate on the silicon undersurface which can then be soldered. The unit is lightly etched, washed, dried, and then mounted on a standard header and a second ohmic contact of the pressure type is made to the germanium side.

In order to determine some of the physical properties of the junction, several units were cross-sectioned by mounting them in a holding jig and lapping with silicon carbide paper abrasives followed by an etch to remove surface damage. Since the luster of polished germanium is noticeably different from that of silicon, and the rate of attack of the etch on the two semiconductors also differs considerably, it was hoped that this would contribute to a relatively easy visual location of the junction. Figure 1 shows a cross-section. The polyphase region of germanium and single crystal wafer of silicon can be easily identified. The junction region appears as a dark line. Some surface irregularities present are due to the non-uniform attack of the etch. The junction region is approximately 10μ wide, but this does not represent the regrowth layer. The diameters of the junctions range from 300 to 500μ. Figure 2 also shows a cross-section. Care has been taken to control the attack of the etch so that a

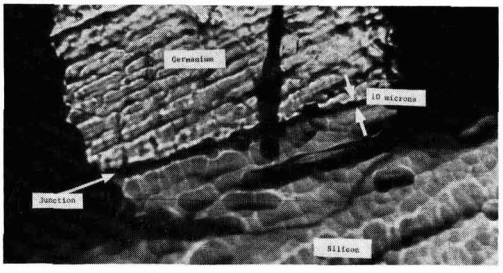

Fig. 1. Cross-section of a germanium-silicon heterojunction magnified approximately 65X.

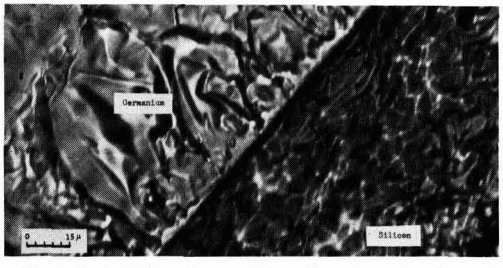

Fig. 2. Cross-section of a germanium-silicon heterojunction magnified approximately 170X.

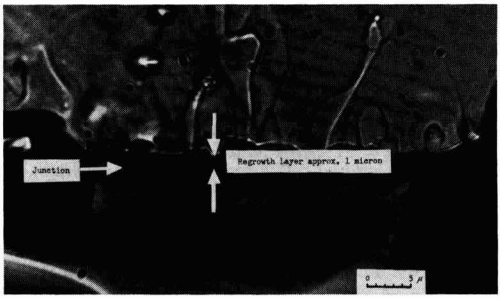

Fig. 3. Cross-section of a germanium-silicon heterojunction magnified approximately 465X.

more uniform surface is obtained on which the junction features are more clearly visible.

The junction itself is believed to consist of an abrupt transition from silicon to germanium through a germanium-silicon regrowth layer. Higher magnifications of the junction region, as in Fig. 3, show a demarkation line between the two regions. The actual regrowth layer is less than 1μ wide.

Junctions were formed using both p and n silicon wafers of 0.001, 0.01, and 1 ohm-cm resistivity. The silicon doping agent was phosphorus for the n-type and boron for the p-type. The small single-crystal spheroids of germanium were of 0.001, 0.01, 0.1, and 1 ohm-cm. For the germanium the p-type doping agent was gallium and the n-type agent was either antimony or phosphorus. The various germanium-silicon structures that were fabricated are listed in Table I. The grouping according to types will be explained in the next section.

The quantity in the brackets indicates the resistivity of the starting material. There is no *a priori* reason for assuming that the germanium side of the junction will have the same impurity concentration (resistivity) as that of the starting material, especially since the germanium must be melted in the process of junction formation. Direct resistivity measurement is not possible since the junction areas are so small. The indirect technique of junction capacitance measurement was used to determine the impurity concentration on the germanium side of the junction.

Over 250 diodes have been made with the reproduction (essentially similar electrical characteristics) of any one type in the above list being quite good.

Electrical Characteristics

In order to examine the various germanium-silicon structures that were produced, a grouping as shown in Table I was used. The symbol + is used to indicate that

Table I. Fabricated germanium-silicon structures

Type 1	n(1)Si-p(1)Ge
nSi-pGe	n(1)Si-p(0.01)Ge
pSi-nGe	p(1)Si-n(1)Ge
	p(1)Si-n(0.01)Ge
	n(0.01)Si-p(1)Ge
	n(0.01)Si-p(0.01)Ge
	p(0.01)Si-n(1)Ge
	p(0.01)Si-n(0.1)Ge
	p(0.01)Si-n(0.01)Ge
Type 2	n(0.001)Si-p(0.001)Ge
n+Si-pGe	n(0.001)Si-p(0.01)Ge
p+Si-nGe	n(0.001)Si-p(1)Ge
	p(0.001)Si-n(0.001)Ge
	p(0.001)Si-n(0.01)Ge
	p(0.001)Si-n(0.1)Ge
	p(0.001)Si-n(1)Ge
Type 3	
nSi-p+Ge	p(0.01)Si-n(0.001)Ge
pSi-n+Ge	n(0.01)Si-p(0.001)Ge
	p(1)Si-n(0.001)Ge
	n(1)Si-p(0.001)Ge
Type 4	n+(0.001)Si-p+(0.001)Ge
n+Si-p+Ge	p+(0.001)Si-n+(0.001)Ge
p+Si-n+Ge	

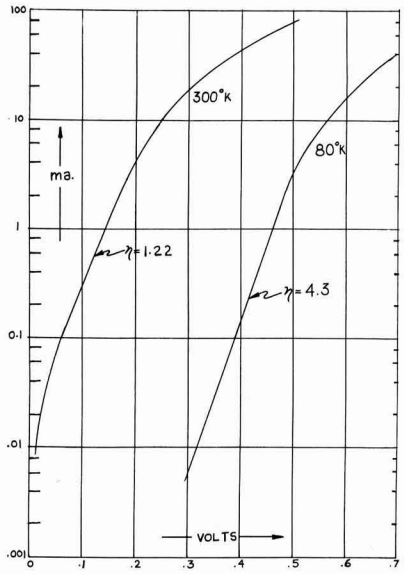

Fig. 4. Forward bias characteristics for a typical n(0.01)Si-p(0.01)Ge diode, unit AUG 8-10-63.

the Fermi level is either above (or extremely close to) the conduction band edge, or below (or extremely close to) the valence band edge.

Figure 4 shows the forward bias current-voltage characteristics of a typical type 1 heterojunction, n(0.01)Si-p(0.01)Ge, at room and liquid air temperatures. At room temperature, the characteristic exhibits an exponential region between approximately 10^{-4} and 10^{-2} amp., with a slope $e/\eta\ kT$, where e is the electronic change, k is Boltzmann's constant, T is temperature, and $\eta = 1.22$. Since the normal theory for rectification in a homogeneous diode leads to an expression

$$J_D = J_S\left[\exp\left(\frac{eV_A}{\eta kT}\right) - 1\right]$$

where J_S is the saturation current, $\eta = 1$, and V_A is the applied bias, an increase in the slope of a plot of log J *vs.* V_A with decreasing temperature is expected.[2] From Fig. 4, it is clear that the expected behavior is not followed with η taking a value of 4.3 at liquid air temperatures. This type of behavior has been observed by Chynoweth and McKay (30) in narrow silicon p-n junctions where field emission is prevalent. For the other Type 1 structures η was generally lower, the lowest value being 1.09 for n(1)Si-p(0.01)Ge heterojunctions.

The characteristics for type 2 and type 3 heterojunctions were much the same as those just described, except for those heterojunctions where the junction width was less than about 800Å. (Junction widths were determined using the formula for an abrupt impurity distribution (3). Impurity concentrations were obtained from junction capacitance measurements and were checked against the observed heterojunction diffusion potentials.) In these cases, the log plot of current *vs.* voltage showed several distinct inflections, as in Fig. 5 for a typical p(0.001)Si-n(0.001)Ge diode. This wobble about a straight line was very reproducible from diode to diode and can be qualitatively ac-

[2] While the above equation cannot be applied directly to a heterojunction, our analysis (publication to appear in the *Physical Review*) indicates that the rectification equation for a heterojunction can be reduced to a similar form, where J_S and η are functions of the physical properties of the two materials employed in the heterojunction. The temperature variation is still properly described by this simple equation.

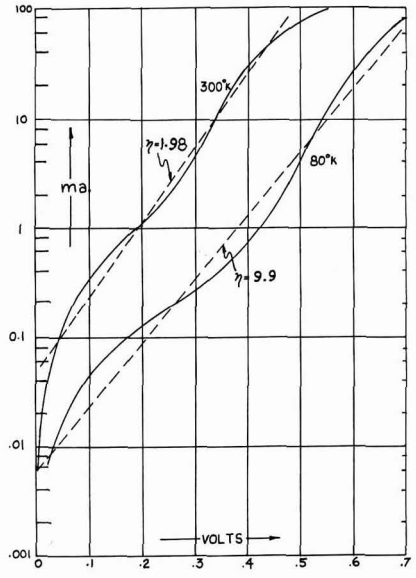

Fig. 5. Forward bias characteristics for a typical p(0.001)Si-n (0.001)Ge diode, unit OCT 22-3.

counted for by the inclusion of an additive saturation current term of the form

$$J = A(V_D - V_A)^n \exp\left(-\frac{B}{V_D - V_A}\right)$$

to the rectification equation (30). In this expression V_D is the diffusion potential, V_A the applied voltage, and A, B, n are dimensional constants. This additive saturation current represents the internal field emission process occurring in the junction due to its "thinness." At liquid air temperatures this characteristic wobble becomes more pronounced indicating an enhancement of tunneling.

Capacitance measurements on a large number of n(0.001)Si-p(0.001)Ge and p(0.001)Si-n(0.001)Ge diodes showed that impurity concentrations on the germanium side were sufficiently high to cause the Fermi level to lie above the conduction band edge for n material and below the valence band edge for p material. These type 4 diodes were expected to exhibit the Esaki effect in the forward bias direction, provided no complicating effects interfered. The experimental units did not show any negative resistance regions but rather an abnormally high current at low bias levels. In addition, these diodes had "apparent" diffusion potentials which were much lower than expected. It is believed that all Ge-Si heterojunctions contain large numbers of defect states in the forbidden band gap and tunneling can occur via these states in thin tunneling junctions, giving rise to a very large excess current J_X. The total current for junction is

$$J = J_t + J_X + J_D$$

where J_D is the diffusion current, as before. If J_X is very large, it will mask J_t (normal tunneling current) completely. This appears to be the case for the type 4 heterojunctions. The defect states by which tunneling takes place are undoubtedly the regions of fairly large dislocation densities mentioned earlier.

Since the junction width depends on the donor and acceptor impurity concentrations on both sides of the heterojunction and the reverse bias characteristic depends strongly on the junction width, a large variation in the form of the reverse bias characteristic was observed in the process of examining the different structures listed in Table I. Figures 6-11 show typical characteristics that were observed for several diode types. The junction widths for the n(1)Si-p(1)Ge and n(1)Si-p(0.01)Ge heterojunctions in Fig. 6 and 7 were estimated to be 5900Å and 3100Å, respectively. Both units have "hard" characteristics with a soft knee prior to a sharp breakdown. This sharp breakdown is a characteristic feature of avalanche breakdown (31), along with the observation that the breakdown voltage decreases considerably on lowering of the heterojunction temperature to 80°K. The softness prior to breakdown is not normally found in homogeneous junctions, but our analysis indicates that is an inherent feature of a heterojunction. For thinner junctions such as the p(0.01)Si-n(0.01)Ge unit shown in Fig. 8 at 1200Å, there is a possibility of field emission or tunneling across the junction. When the temperature is lowered, the reverse current drops somewhat at moderate values of bias, but then increases more rapidly and crosses over the room temperature characteristic, thus leading to a lower breakdown voltage. The slight lowering of reverse current at moderate values of bias indicates field emission, while the drop in breakdown voltage indicates avalanche breakdown. This heterojunction represents transition region behavior where ionization and field emission occur simultaneously. At sufficiently high current densities, a "second" breakdown occurs (32) which will be discussed in a subsequent publication. This breakdown consists of the formation of a negative resistance region along with a hysteresis loop.

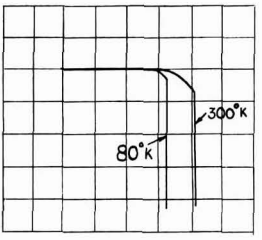

Fig. 6. Reverse characteristics for a typical n(1)Si-p(1)Ge diode, unit JUL 23-2-63. Scale: 20 v/div. horiz., 1 ma/div. vert.

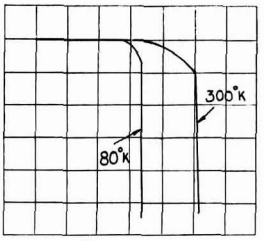

Fig. 7. Reverse characteristic for a typical n(1)Si-p(0.01)Ge diode, unit AUG 8-10-63. Scale: 10 v/div. horiz., 1 ma/div. vert.

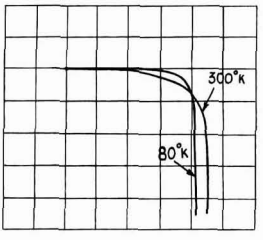

Fig. 8. Reverse characteristic for a typical p(0.01)Si-n(0.01)Ge diode, unit JUL 24-4-63. Scale: 2 v/div. horiz., 20 ma/div. vert.

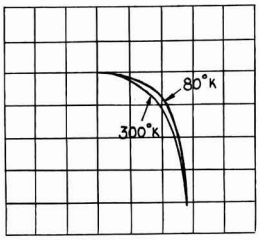

Fig. 9. Reverse characteristic for a typical n(0.01)Si-p(0.01)Ge diode, unit FEB 21-5. Scale: 2 v/div. horiz., 20 ma/div. vert.

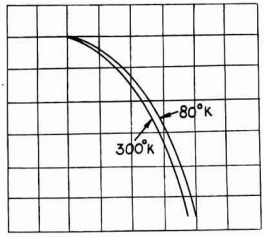

Fig. 10. Reverse characteristic for a typical n(0.001)Si-p(0.001)Ge diode, unit JUL 6-2. Scale: 1 v/div. horiz., 10 ma/div. vert.

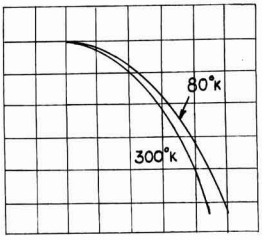

Fig. 11. Reverse characteristic for a typical p(0.001)Si-n(0.001)Ge diode, unit FEB 12-3. Scale: 0.5 v/div. horiz., 20 ma/div. vert.

Figures 9, 10, and 11 show how the reverse characteristic gets progressively softer as the junction width decreases (to about 300Å for the n(0.001)Si-p(0.001)Ge and p(0.001)Si-n(0.001)Ge heterojunctions), and the complete reversal in breakdown voltage shift with decreasing temperature.

Additional evidence was obtained to show that the electrical junction occurred at the material interface and not in either the silicon or the germanium. First, the measured diffusion potentials were in agreement with the calculated ones based on the appropriate heterojunction model. Second, reverse bias breakdown radiation in the form of microplasma spots was observed at the material interface, and the spectral distribution of the radiation indicated that both germanium and silicon were playing an active role in forming a true heterojunction.

Conclusions

Germanium-silicon heterojunctions have been successfully fabricated by an alloy process. A wide variety of structures were formed in which the impurity concentrations on either side of the junction were determined by the resistivity of the single crystal germanium or silicon that was employed.

The forward bias characteristics tend to resemble those of normal homogeneous junctions except when "thin" junctions are encountered. Theoretically, type 4 diodes were expected to show the Esaki effect, but, experimentally, no such effect was observed. Instead, an abnormally high current was found which was attributed to tunneling *via* defect states caused by the large dislocation densities present in the junction. This excess current was sufficiently large to mask out the negative-resistance region that was expected.

The reverse bias characteristics of germanium-silicon heterojunctions were also examined. For sufficiently large junction widths (low impurity concentrations), a heterojunction was expected to show normal avalanche breakdown with a soft knee rather than a sharp knee. The degree of softness was found to depend on the tunneling and image effects. For thin junctions (high impurity concentrations), Zener or field emission "breakdown" was predominant. A continuous transition of characteristics from hard to extremely soft was observed as the junction width of the heterojunctions varied from a few thousand angstroms to less than 100Å.

Manuscript received Feb. 24, 1964; revised manuscript received April 15, 1964.

Any discussion of this paper will appear in a Discussion Section to be published in the June 1965 JOURNAL.

REFERENCES

1. H. Kroemer, *Bull. Am. Phys. Soc.*, **2**, 143 (1956).
2. H. Kroemer, *R.C.A. Rev.*, **18**, 1332 (1957).
3. H. Kroemer, *Proc. I.R.E.*, **45**, 535 (1957).
4. J. Tauc, *Rev. Mod. Phys.*, **21**, 307 (1957).
5. A. Armstrong, *Proc. I.R.E.*, **46**, 1307 (1958).
6. T. K. Lakshmanan, *ibid.*, **48**, 1646 (1960).
7. D. A. Jenny, *ibid.*, **46**, 959 (1958).
8. M. Wolf, *ibid.*, **48**, 1246 (1960).
9. P. R. Emtage, *J. Appl. Phys.*, **33**, 1950 (1962).
10. R. Ruth, J. C. Marinace, and W. Dunlap, *ibid.*, **31**, 995 (1960).
11. J. C. Marinace, *I.M.B. J. Res. & Dev.*, **4**, 280 (1960).
12. R. L. Anderson, *ibid.*, **4**, 283 (1960)
13. R. L. Anderson, *Solid-State Electronics*, **5**, 341 (1962).
14. R. L. Anderson, *Trans. I.R.E.*, ED.-9, 509 (1962).
15. S. S. Perlman, D. L. Feucht, and R. M. Williams, *ibid.*, ED.-9, 509 (1962).
16. W. S. Oldham and A. G. Milnes, *ibid.*, ED.-9, 509 (1962).
17. W. S. Oldham and A. G. Milnes, *Solid-State Electronics*, **6**, 121 (1963).
18. S. S. Perlman, *Trans. I.R.E.*, ED.-10, 335 (1963).
19. W. S. Oldham and A. G. Milnes, *ibid.*, ED.-10, 335 (1963).
20. F. Fang and W. E. Howard, Conference Paper, 1962 Electron Devices Meeting in Washington, D. C.
21. W. E. Howard and F. Fang, *Trans. I.R.E.*, ED.-10, 336 (1963).
22. H. Stohr and W. Klemm, *Z. anorg. allgem. Chem.*, **241**, 305 (1939).
23. E. R. Johnson and S. M. Christian, *Phys. Rev.*, **95**, 846 (1954).
24. A. Levitas, C. C. Wang, and B. H. Alexander, *ibid.*, **95**, 846 (1954).
25. F. Herman, *Proc. I.R.E.*, **43**, 1703 (1955).
26. R. Braunstein, *Phys. Rev.*, **130**, 869 (1963).
27. R. Braunstein, *ibid.*, **130**, 879 (1963).
28. F. C. Frank and J. H. Van der Merwe, *Proc. Roy. Soc. London*, **A198**, 205 (1949).
29. A. J. Goss, K. E. Benson, and W. G. Pfann, *Acta Met.*, **4**, 332 (1956).
30. A. G. Chynoweth and K. G. McKay, *Phys. Rev.*, **106**, 418 (1957).
31. K. G. McKay, *ibid.*, **94**, 877 (1954).
32. L. Y. Wei and J. Shewchun, *I.E.E.E.*, **5**, 946 (1963).
33. K. Lehovec, *Proc. I.R.E.*, **40**, 1408 (1952).
34. W. G. Oldham *et al.*, *This Journal*, **110**, 536 (1963).

Diffused Junction Diodes of PbSe and PbTe

J. F. Butler

Lincoln Laboratory,[1] Massachusetts Institute of Technology, Lexington, Massachusetts

ABSTRACT

A technique is described for producing diffused p-n junctions in Pb salt single crystals which utilizes an interdiffusion mechanism to introduce controlled deviations from stoichiometry, excess Pb giving rise to n-type and excess Se and Te to p-type PbSe and PbTe, respectively. An analysis of the p-n junction depths on the basis of Fick's law of diffusion results in the following effective interdiffusion constants: $D_\Delta = 4 \times 10^{-8}$ cm^2 sec^{-1} for producing a p-layer on n-type PbSe at 600°C; $D_\Delta = 9 \times 10^{-9}$ cm^2 sec^{-1} for an n-layer on p-type PbSe at 650°C; $D_\Delta = 6 \times 10^{-7}$ cm^2 sec^{-1} for an n-layer on p-type PbTe at 650°C. In the first case the diffusion has been studied as a function of time, and the results show that the assumption of Fick's law of diffusion was valid. As expected the interdiffusion constants are two to three orders of magnitude larger than the self-diffusion constants. Electrical characteristics of the diffused diodes are presented and can be explained as resulting from a combination of diffusion and tunneling current components.

Diodes of the Pb salt semiconductors have been the subject of a number of papers (1-9). It is of historical interest that PbS was one of the first materials with which the phenomenon of rectification was observed (1) and that the galena crystal detector was one of the earliest semiconductor devices (2). The evaluation of interdiffusion constants in these materials from the penetration distances of p-n junctions has been carried out to a limited degree (10-12).

This paper describes the electrical properties of diffused junction diodes of PbSe and PbTe, gives the fabrication procedures followed in making these diodes, and presents values for the effective interdiffusion constants near 600°C. The diffusion technique which is described below for diffusing an n-layer into single crystal p-type PbSe and PbTe and for diffusing a p-layer into n-type single crystal PbSe has the advantage of using an isothermal closed system and of consequent simplicity.

The diffusion method was suggested by the work of Brebrick and Gubner (13, 14) and of Brebrick and Allgaier (15) who measured stability limits as functions of temperature for PbSe and PbTe by introducing deviations from stoichiometry into crystals of these semiconductors. Their method was to bring a small single crystal of the material into equilibrium through the vapor phase with a two-phase ingot of the same material rich in one or the other of the constituents. The equilibrium conditions were "frozen in" by quenching the crystals to room temperature, and the concentration of the excess constituent at the equilibrium temperature was assumed equal to the measured concentration of extrinsic charge carriers. The field of stability of PbSe was found to be roughly symmetric about the stoichiometric composition and that of PbTe to be predominantly on the p-type, Te rich side [other work (16) shows the field of stability of PbS to be predominantly on the n-type, Pb rich side]. According to Brebrick (17) the approach to equilibrium in these experiments proceeds by a mechanism of interdiffusion and may be described in terms of concentration gradient by an effective interdiffusion constant. Thus, the diffusive flow of deviation from stoichiometry

$$J_\Delta = J_C - J_A = -(D_C^* + D_A^*)\,(S/kT)\,\text{grad}\,\mu_C \quad [1]$$

can be written as

$$J_\Delta = -D_\Delta\,\text{grad}\,\Delta \quad [2]$$

[1] Operated with support from the U.S. Air Force.

where D_C^* and D_A^* are the cation and anion self-diffusion constants, S is the concentration of cation or anion lattice sites, μ_C is the chemical potential of the cation, $\Delta = N_C - N_A$ is the deviation from stoichiometric composition and

$$D_\Delta = (D_C^* + D_A^*)\,(S/kT)\,(d\mu_C/d\Delta) \quad [3]$$

is the effective interdiffusion constant. As shown by Brebrick (17) the factor $(1/kT)\ (d\mu_C/d\Delta)$ is of the order of the reciprocal of the total concentration of lattice point defects and the interdiffusion constant is therefore 10^2-10^6 times as large as the larger of the self-diffusion constants. For the case of conversion from one conductivity type to another, the process may be visualized as a plane between p and n material moving inward from the surface. For this case, quenching the crystal before equilibrium is attained will result in a p-n junction. The diffusion method described in detail below, then, consists of heating a single crystal of material of one conductivity type in a sealed container with a two phase ingot of the same material of opposite conductivity type and quenching the system before equilibrium is attained.

Fabrication Procedures

The two phase ingots used as the source of excess Se or Te were prepared by chemically combining the elements in sealed quartz tubes. Quartz tubes were etched in a 1-1 solution of nitric and hydrofluoric acids, rinsed in distilled water, drained dry, and vacuum baked at 1100°C until the final pressure was less than 10^{-6} mm Hg. The elements (99.999% pure Se and Te, 99.9999% pure Pb) were weighed out individually to the nearest milligram so that the combined weight was about 10g and the composition was either 49 or 51 atomic per cent Pb. The Pb was cut from the interior of a bar. The materials were loaded into a tube which was then outgassed at 150°C for 3 hr and sealed off at a pressure less than 10^{-6} mm Hg. The sealed tube was exposed to a carefully controlled torch flame long enough to bring about partial reaction of the contents and was then heated for 3 hr at 950°C for PbTe and 1050°C for PbSe and quenched in water. The resulting two phase ingot was removed from the tube and ground to a coarse powder. Such a ground ingot could be used with predictable results for four or five diffusions.

Most of the single crystal PbSe used in these experiments was obtained from a larger crystal grown from a near stoichiometric melt by the Bridgman tech-

nique by Dr. A. J. Strauss of Lincoln Laboratory. This crystal contained substantial portions of both p and n material with 77°K carrier concentration and Hall mobility of approximately 3 x 10^{18} cm^{-3} and 15,000 cm^2 v^{-1} sec^{-1}, respectively. The PbTe, taken from an undoped p-type single crystal obtained from Battelle Memorial Institute, had a room temperature hole concentration and Hall mobility of approximately 3 x 10^{18} cm^{-3} and 750 cm^2 v^{-1} sec^{-1}, respectively. Rectangular parallelepipeds approximately 1 mm thick and several millimeters in the other two dimensions were cleaved from the crystals. The wafers were cleaned by scrubbing with boiling high purity methanol. The diffusions were performed with the crystal and source ingot in separate, open compartments of a quartz ampoule which was etched and vacuum baked immediately before use in the manner described above for quartz tubes. The ampoule and contents were outgassed at 120°C for 1 hr, sealed off at about 10^{-6} mm Hg, and placed in the uniform temperature zone of a furnace which had been preheated to the desired temperature. The temperature was usually 600°C for the diffusion of excess Se into n-type PbSe and 650°C for the diffusion of excess Pb into p-type PbSe or PbTe. At the end of a run, the sealed ampoules were quenched in water. On freshly cleaved surfaces junctions were often directly observable under magnification as faint white lines or discontinuities in the general appearance, and junction depths were measured by visual observations in conjunction with thermoelectric microprobing.

Figure 1 shows junction depth plotted against the square root of time for four diffusions at 600°C of excess Se into n-type PbSe. The electron concentration of the wafer used in the 3 hr run was determined by Hall measurements to be 3.0 x 10^{18} cm^{-3}; the remainder of the wafers were taken from the same portion of the parent crystal and probably had nearly the same concentration. The same complete source ingot was used in all four runs. For the diffusion of excess Pb into p-type PbSe, a representative set of values is a junction depth of 8.9 x 10^{-3} cm for a 1 hr run at 650°C and an initial hole concentration of 1.9 x 10^{18} cm^{-3}. The diffusion of excess Pb at 650°C for 1 hr into p-type PbTe with an initial hole concentration of 3.0 x 10^{18} cm^{-3} produced a junction depth of 8.9 x 10^{-3} cm.

The diffused junction material was usually cleaved into dice with linear dimensions of 0.1-1.0 mm and alloyed to standard metal base tabs. An artist's sketch of a diode is shown in Fig. 2. Ohmic contacts to p-type regions were generally made with pure Au or a Au-Tl alloy and to n-type regions with pure Pb or a Pb-In alloy. In general, Se, Te, Ag, Au, and Tl have been found to behave as acceptors and Pb, In, Sn, and Bi as donors. Alloying was performed on a carbon resistance heating strip enclosed in a gas tight volume of about 1 liter into which could be introduced a reducing atmosphere. The system was purged with a 5 min gas flow before each heating step and the semiconductor surface was cleaned with boiling methanol after each step. Relative temperatures were recorded for reproducibility of operations, but precise alloying temperatures were not determined. Alloying times were generally less than a minute. In some cases, a mesa structure was formed on material with a shallow junction depth by etching with a solution of potassium hydrochloride, ethylene glycol, and hydrogen peroxide as described by Coates, Lawson, and Prior (18). This etch has been found to be most effective on cleaved surfaces. The finished diodes were mounted on transistor headers with In plated Ag wires soldered to the top contacts.

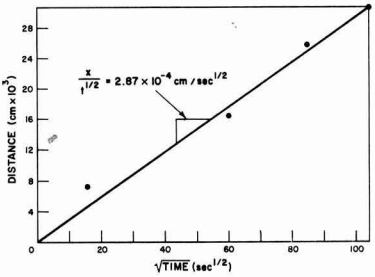

Fig. 1. Junction depths for diffusions in n-type PbSe

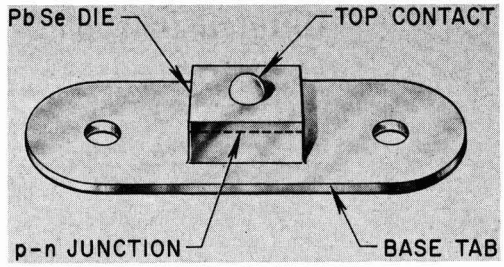

Fig. 2. Artist's sketch illustrating fabrication of diffused junction diodes.

Electrical Characteristics

Figures 3 and 4 show the current-voltage characteristics at three temperatures for a typical PbSe diode. The p-n junction resulted from a diffusion of excess Pb into p material at 600°C and was 3 x 10^{-3} cm deep. The surface was etched to a mesa structure with a junction area of about 10^{-3} cm^2. The reverse current for the room temperature characteristic shows saturation near 50 ma. The reverse characteristics of PbSe diodes were found to be extremely dependent on previous surface treatment. The diode of Fig. 3 and 4 was vacuum baked and had been stored in a dessicator for a week before its characteristics were measured. No attempt was made to develop a surface treatment for optimum performance. Measurements of capacitance as a function of voltage at 77°K were made on a 5 x 10^{-4} cm^2 area PbSe diode from the same diffusion run as that of Fig. 3 and 4, using a radio frequency bridge at 50 megacycles. Accuracy of these measurements was limited by breakdown effects which became evident at reverse biases greater than about 0.5v and by large reverse currents. The results show voltage proportional to the square of reciprocal capacitance and the data are plotted in this manner in Fig. 5.

The current-voltage curves of a PbTe diode are presented in Fig. 6 and 7. The junction, formed by a

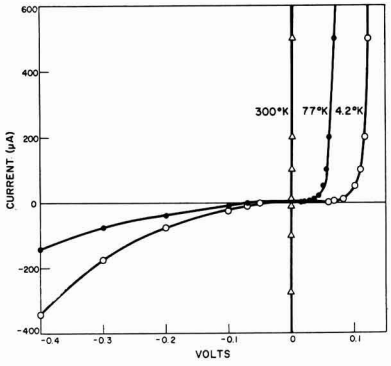

Fig. 3. Current-voltage characteristics of a diffused junction PbSe diode at various temperatures.

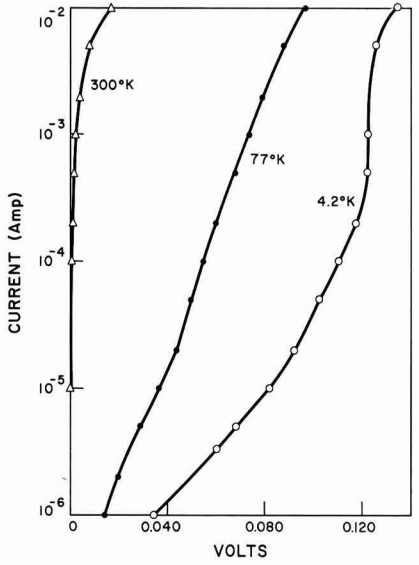

Fig. 4. Forward current-voltage characteristics on a semi-logarithmic scale of diffused junction PbSe diode of Fig. 3 at various temperatures.

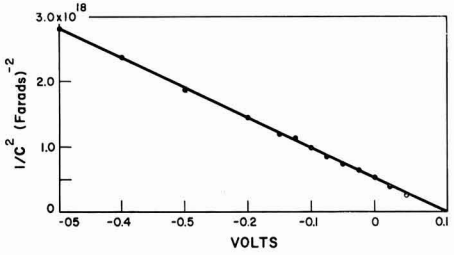

Fig. 5. Diode capacitance as a function of voltage for a PbSe diffused junction diode at 77°K.

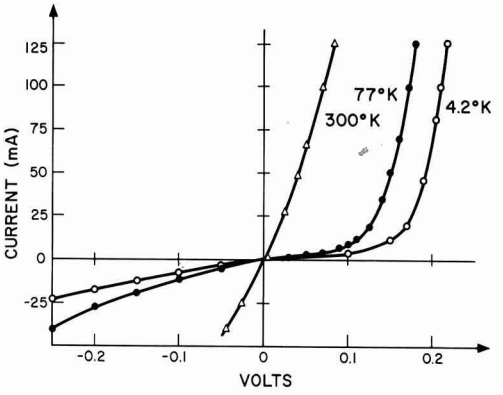

Fig. 6. Current-voltage characteristics of a diffused junction PbTe diode at various temperatures.

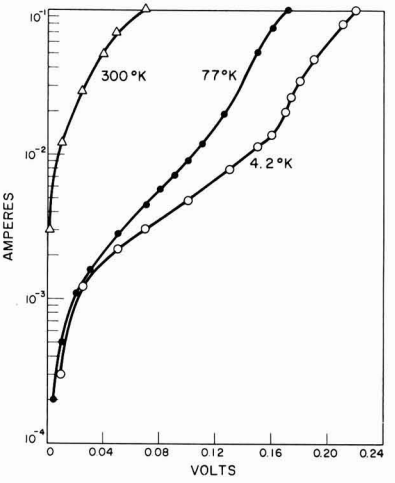

Fig. 7. Forward current-voltage characteristics on a semi-logarithmic scale of δ diffused junction PbTe diode of Fig. 6 at various temperatures.

diffusion of excess Pb into p material at 650°C, was 8.9 x 10^{-3} cm deep and about 10^{-2} cm^2 in area. The reverse current at room temperature shows saturation near 50 ma. The reverse characteristics of this diode were less sensitive to surface conditions than those of the PbSe diode.

Discussion

The linear relation between junction depth and the square-root of time evident in Fig. 1 implies that the interdiffusion process can be described by a simple constant. In order to obtain a value for D_Δ, it is assumed that the quantity $\Delta(x,t) = N_C(x,t) - N_A(x,t)$ diffuses into an initially homogeneous semi-infinite slab with a constant surface concentration. The initial deviation from stoichiometry within the slab, Δ_o, can be determined from the initial carrier concentration if the semiconductor is in the exhaustion range. It is assumed that the surface deviation Δ_s due to the source is given by the stability limit at the diffusion temperature of the component in question. Under these conditions, the solution of [2] is

$$\Delta(x,t) = (\Delta_s - \Delta_o)\ \mathrm{erfc}\ (x/2\sqrt{D_\Delta t}) + \Delta_o \qquad [4]$$

It will be assumed that the p-n junction occurs where $\Delta(x,t) = 0$.

Substituting $x/t^{1/2}$ from the slope of the curve in Fig. 1 and $\Delta_s = 6.0 \times 10^{18}$ cm^{-3} from the data of Brebrick and Gubner (13) into [4] and assuming an exhaustion range semiconductor, gives $D_\Delta = 4 \times 10^{-8}$ cm^2 sec^{-1} for excess Se in n-type PbSe at 600°C. It is instructive to compare this value with a diffusion constant of 10^{-12} cm^2 sec^{-1} for the self-diffusion of Se in 10^{18} cm^{-3} n-type PbSe at 600°C, as extrapolated from the data obtained by radioactive tracer diffusion by Boltaks and Mokhov (19). For the diffusion of an excess Pb layer in p-type PbSe at 650°C, the measured values of junction depth, time and initial concentration, and $\Delta_s = 5.5 \times 10^{18}$ from the data of Brebrick and Gubner (13) give $D_\Delta = 9 \times 10^{-9}$ cm^2 sec^{-1}. Seltzer and Wagner (20), using Pb-210 diffusion, obtained a diffusion constant of approximately 1.5×10^{-10} cm^2 sec^{-1} for the self-diffusion of Pb in 10^{18} cm^{-3} p-type PbSe at this temperature. Taking $\Delta_s = 6 \times 10^{17}$ cm^{-3} from the data of Brebrick and Gubner (14) and using measured values in [4] results in $D_\Delta = 6 \times 10^{-7}$ cm^2 sec^{-1} for the diffusion of an excess Pb layer in p-type PbTe. Boltaks (11) has obtained diffusion constants for excess Pb in 10^{17} cm^{-3} p-type PbTe over a range of temperatures by using a delta function source and measuring junction depths. The conditions of his experiments were such that his "self-diffusion" constant corresponds approximately to the interdiffusion constant discussed here. Extrapolated to 650°C, his values give $D_\Delta = 2 \times 10^{-8}$ cm^2/sec, in rather poor agreement with the value given above.

Two points are of interest in connection with the effective interdiffusion constants obtained in the present work. They were 2-3 orders of magnitude larger than the self-diffusion constants, in agreement with prediction (17). Second, the average interdiffusion constant for the movement of an n-p junction into p-type PbSe is smaller than that for the movement of a p-n junction into an n-type crystal for comparable values of Δ_s-Δ_o. Intuitively, this is what is to be expected if, as Seltzer and Wagner propose (20), the predominant point defects in PbSe are Frenkel defects in the Pb sub-lattice with the interstitial Pb possessing a much larger mobility than the Pb vacancy.[2] An alternative explanation is that p-type PbSe contains electrically inactive Se as a dislocation precipitate which acts as a sink for diffusing Pb. This is consistent with results of experiments on p-type PbTe (14) and with the fact that it is difficult to quench in the high temperature state of p-type PbSe (13).

Figure 4 shows that the low temperature forward current-voltage curves of the PbSe diode are characterized by a low bias region in which current rises slowly with voltage, followed by a middle region of rapid rise and a high bias region dominated by series resistance. In the 77°K curve the middle region shows an exp (qv/nkT) dependence of current on voltage with $n = 1$ between about 20 and 100 μa and $n = 1.25$ between 150 and 5000 μa. The 4.2°K curve has a middle region between 500 and 1500 μa with $n = 1.5$ over most of the range. The forward current at room temperature shows a rapid non-exponential rise from zero and is dominated by series resistance at a low bias. The low temperature reverse currents increase with voltage, that at 4.2°K rising the most rapidly. The reverse current at 300°K rapidly reaches a definite saturation value. These features can be explained in a qualitative manner as resulting from a combination of diffusion controlled and tunneling current components. In view of the nonparabolicity of the band edges (21), and the uncertainty in values of energy gap and lifetime, no attempt will be made here to verify the explanation quantitatively. At the carrier concentrations of this material, one would expect degeneracy near room temperature. Strong evidence that the low temperature reverse current is due primarily to tunneling is supplied by the fact that its magnitude increases with decreasing temperature (the energy gap of PbSe is known to increase linearly with temperature over most of the range under consideration). The occurrence of tunneling probably also explains the large low-bias forward currents at low temperatures.

The current-voltage characteristics of the PbTe diode show the same general behavior as those of the PbSe diode, but the large low bias currents override most of the rapidly rising middle region. The reverse current has been observed with an oscilloscope to increase in magnitude with decreasing temperature between about 250° and 77°K in the same manner as the PbSe diode and probably results from tunneling. The fact that the reverse current at 4.2°K is less in magnitude than that at 77°K is of interest and not readily explained.

Extending the linear regions of the 77° and 4.2°K semilogarithmic curves of Fig. 4, one finds the resulting straight lines to intersect at a voltage about 20% lower than the energy gap deduced by extrapolating the optical data of Gibson (22) to 0°K. Although less clear, a similar result can be obtained from the PbTe curves of Fig. 7. Furthermore, the capacitance data indicate an energy barrier in the PbSe diode at 77°K approximately 30% lower than the measured optical energy gap (22). For a degenerate semiconductor, one would expect the barrier height and optical energy gap to more nearly coincide. Any explanation for these discrepancies based on a "Burstein shift" (23) tends to be ruled out by the facts that the PbSe used in the experiments described above had about the same carrier concentration as that used by Gibson and, second, that Gibson observed no dependence of the position of the absorption edge on concentration. These differences could arise from the occurrence of an indirect minimum energy gap. According to experimental results of Ellett and Cuff (21), however, the valence and conduction band extremes of PbSe occur at identical points in the Brillouin zone. Another mechanism resulting in a difference between thermal and optical energy gaps is the redistribution of ionic charge associated with the intrinsic ionization process (24). This mechanism would give rise to a difference energy approximately proportional to $(\kappa_s - \kappa_o)/\kappa_s\kappa_o$, where κ_s and κ_o are the static and optical dielectric constants, respectively, of the material. As pointed out by Scanlon (25) this effect may be important in polar semiconductors such as the Pb salts.

[2] The author is indebted to Dr. R. F. Brebrick for bringing this point to his attention.

Summary

A method has been developed for producing diffused p-n junctions in PbSe and PbTe which utilizes an interdiffusion mechanism to introduce controlled deviations from stoichiometry. The method should be applicable to any compound semiconductor whose conductivity type can be determined by deviations from stoichiometry and for which the vapor pressure of at least one component is large enough to provide the necessary mass transfer. It could certainly be applied to PbS. The measured electrical properties of the PbSe and PbTe diffused diodes are consistent with those resulting from a current flow comprised of both diffusion and tunneling components.

Acknowledgments

The author wishes to thank Dr. R. F. Brebrick and Mr. A. R. Calawa for valuable suggestions and discussions, and Mr. R. H. Hancock for technical assistance in all phases of fabrication.

Manuscript received February 11, 1964.

Any discussion of this paper will appear in a Discussion Section to be published in the June 1965 JOURNAL.

REFERENCES

1. F. Braun, *Ann. Phys. Chem.*, **153**, 556 (1874).
2. J. C. Bose, U.S. Pat 755, 840 (1904).
3. H. K. Henisch and J. W. Granville, "Semiconducting Materials" (Report of Reading Semiconductor Conference, (1950) 87, Butterworth (1953).
4. A. F. Gibson, *Proc. Phys. Soc., London*, **B65**, 196, 214 (1952).
5. P. C. Banbury, H. A. Gebbie, and C. A. Hogarth, "Semiconducting Materials" (Report of Reading Semiconductor Conference, 1950) 87, Butterworth (1951).
6. C. A. Hogarth, *Proc. Phys. Soc., London*, **B65**, 958; *ibid.*, **B66**, 216 (1953).
7. R. H. Rediker and A. R. Calawa, *J. Appl. Phys.*, **32** (suppl.), 2189 (1961).
8. Y. Kanai and K. Shono, *Jap. J. Appl. Phys.*, **2**, 6 (1963).
9. M. F. Kimmitt and A. C. Prior, *This Journal*, **108**, 1034 (1961).
10. R. F. Brebrick and W. W. Scanlon, *Phys. Rev.*, **96**, 598 (1954).
11. B. I. Boltaks, "Diffusion in Semiconductors," p. 293, Academic Press, New York (1963).
12. E. J. Brady, *This Journal*, **101**, 466 (1954).
13. R. F. Brebrick and E. Gubner, *J. Chem. Phys.*, **36**, 170 (1962).
14. R. F. Brebrick and E. Gubner, *ibid.*, **36**, 1283 (1962).
15. R. F. Brebrick and R. S. Allgaier, *ibid.*, **32**, 1826 (1960).
16. J. Bloem and F. O. Kroeger, *Z. Phys. Chem.* (Frankfurt), **7**, 1 (1956).
17. R. F. Brebrick, *J. Appl. Phys.*, **30**, 811 (1959).
18. D. G. Coates, W. D. Lawson, and A. C. Prior, *This Journal*, **108**, 1038 (1961).
19. B. I. Boltaks and Y. N. Mokhov, *Soviet Phys. Tech. Phys.*, **28**, 1045 (1958).
20. M. S. Seltzer and J. B. Wagner, Jr., *J. Chem. Phys.*, **36**. 130 (1962).
21. M. R. Ellett and K. F. Cuff, American Physical

Society Meeting, Pasadena (Dec. 19-21, 1963): Abstract in *Bull. Am. Phys. Soc.*, **8**, 601 (1963).
22. A. F. Gibson, *Proc. Phys. Soc., London*, **B65**, 378 (1952).
23. E. Burstein, *Phys. Rev.*, **93**, 632 (1954).
24. F. Seitz, "Modern Theory of Solids," ch. 13, McGraw-Hill Book Co., New York (1940).
25. W. W. Scanlon in "Solid State Physics," **9**, p. 112, F. Seitz and D. Turnbull, Editors, Academic Press, New York (1959).

Thermodynamic Analyses of Open Tube Germanium Disproportionation Reactions

A. Reisman and S. A. Alyanakyan

Thomas J. Watson Research Center, International Business Machines Corporation, Yorktown Heights, New York

ABSTRACT

In order to define conditions most suitable for iodine transport of pure or gallium doped germanium, the equilibria that obtain when these elements, singly or together, are mixed with iodine or hydrogen iodide in the presence of hydrogen and/or inert gases were analyzed using computer techniques. It was found that Ge in the presence of an inert carrier gas should transport via a hot to cold process at all iodine pressures studied. These results are markedly perturbed when H_2 is substituted for the inert gas due to the establishment of a competing equilibrium whose enthalpic change is opposite in sign to that of the equilibrium responsible for semiconductor transport. The effects of the competing equilibrium in turn may be modified by using a mixture of H_2 and He. Under certain sets of conditions, in fact, temperature insensitive regions develop which appear to be suitable as semiconductor source and seed sites. The results for the gallium-iodine equilibrium are to a good first approximation independent of the nature of the carrier gas and indicate that hot to cold transport is to be expected over a wide range of iodine concentrations. Analyses of the three phase equilibrium in Ge-Ga-halogen systems show them to also be independent of the nature of the carrier gas.

The lack of fundamental information has hindered the controlled optimized use of open tube systems for Ge transport via a disproportionation mechanism. Where such information is available, as is the case for Ge-I_2 (1) interactions, it is not readily employed because of the difficulty in putting it into usable form. When competing reactions due to the presence of reactive carrier gases and/or impurities are involved in the transport process, the problem becomes even more formidable.

To provide a firmer basis for studying the parameters affecting Ge transport via disproportionation mechanisms, it appeared worthwhile to attempt thermodynamic analyses of several potentially interesting systems. While in practice the kinetics of the vapor transport and solid-vapor reactions, not the equilibrium boundaries, represent the limiting factors in a transport process, it is evident that these boundaries at least define upper limits for a set of specified conditions.

This report is concerned with an evaluation of the equilibria that obtain when Ge and/or Ga are mixed with iodine, hydrogen iodide, hydrogen and/or inert gases in systems subject to a constant total pressure constraint.

General Considerations

Effects of simultaneous equilibria.—Given a simple equilibrium of the type represented by Eq. [1], the direction of reaction with increasing or decreasing temperature is readily deduced. Thus, if for Eq. [1]

$$a A_{\text{solid}} + b B_{\text{vapor}} \overset{\Delta H_p}{\rightleftarrows} x\, AB \qquad [1]$$

the enthalpic change for the process as written, ΔH_p, is positive, the van't Hoff expression, Eq. [2],

$$K_2/K_1 = e^{-\Delta H_p/R(1/T_2 - 1/T_1)} \qquad [2]$$

where the K's refer to the ratios $(p_{AB})^x/(p_A)^a\,(p_B)^b$ at the temperatures T_2 and T_1, leads to the following conclusion: With ΔH_p positive and $T_2 \geqq T_1$, $K_2 \geqq K_1$. Consequently, with increasing temperature, the reaction as written is driven to the right. In order to effect a vapor phase transport of the solid A via the model specified by Eq. [1], it is necessary that the source temperature of solid A be greater than the sink temperature for this material. With introduction of secondary reactions which tend to compete for one or more of the main transport reaction components, the prediction of transport direction in a temperature gradient is not as readily discernible. For example, in addition to the reaction described by Eq. [1], where for simplicity we will assume the coefficients a, b, and x are unity, in which event ΔH_p is the molar enthalpy of formation of AB, consider the simultaneously occurring equilibrium depicted by Eq. [3] where $\Delta H'_p$ is similar in magnitude to ΔH_p but has a negative sign, and again represents a molar enthalpy of formation.

$$d D_{(v)} + b B_{(v)} \overset{\Delta H_p'}{\rightleftarrows} y\, DB_{(v)} \qquad [3]$$

Suppose that to a container in which one mole of A, and one mole of B have been placed we add a small fraction of a mole of D and an equal quantity of B. The ΔH^*_p for the complete process represented by Eq. [4] at a given temperature

$$a A_{(s)} + (b + d') B_{(v)} + d' D_{(v)} \overset{\Delta H_p^*}{\rightleftarrows} x AB_{(v)} + y' DB_{(v)} \qquad [4]$$

$$0 < \Delta H_p^* < \Delta H_p$$

will be positive in sign but slightly less in magnitude than ΔH_p. If subsequent experiments are performed in which the quantity of D is increased, a point will be reached ultimately at which reaction [1] now represents a perturbation on reaction [3], and ΔH^*_p will be negative in sign and transport will occur from the cold to hot regions of the system. Since the coefficients a and b may have any value, *viz.*, Eq. [1] may be multiplied by any number, it is evident that depending on the quantities of A and B initially present and

the relative magnitudes of ΔH_p and $\Delta H_p'$, the effect of addition of a defined quantity of D on both the magnitude, and more important the sign of ΔH_p^* for a given set of conditions will be different. Thus for increasing quantities of A and B the direction of transport will be less likely to change when a specified quantity of D is added. If in addition to all of the above, a vaporous species AD tends to form, the problem is further amplified. Because, as shown above, ΔH_p^* can have an infinite number of values depending on the set of experimental conditions imposed, a knowledge of its sign rather than its absolute value is of greater interest in designing a transport experiment. The sign of ΔH_p^* can be readily obtained by visual inspection of plots of semiconductor/halogen component vapor phase ratios as a function of temperature, as proposed by Lever (1).

Assumptions.—In order to enable analytical treatment of the multispecies systems of interest, it was necessary to involve such commonly employed assumptions as those pertaining to vapor phase ideality and the constancy of enthalpic changes accompanying each reaction with varying temperature. For the temperature and pressure ranges considered neither of these assumptions appears unreasonable. In addition, it was assumed that all pertinent vapor phase species were known and that halogens and halogen compounds were confined solely to the vapor phase in the temperature interval of practical interest. No attempt was made to discontinue analyses below dew point temperatures for the semiconductor halides, all analyses arbitrarily being performed in the temperature interval 0°-800°C. In practice, the data for all, except the highest halogen source pressures, are not affected by dew point considerations above 300°C.

As will become evident, it was necessary to assume that the species pressures of halogens and halogen acids bear a simple relationship to the hypothetical component pressures of halogens and halogen acids at sources of the latter. In other portions of the system this assumption was not required. Based on the available thermodynamic data for iodine and hydrogen iodide dissociation at the temperatures considered this assumption is not unreasonable.

All equilibrium data are based on a standard state choice of 1 mm Hg with species pressures specified with the same dimensions.

Finally, all systems were considered for a total pressure constraint of 760 mm Hg.

Symbols and system representations.—Each of the systems to be discussed is represented by component designations considered most appropriate for the reactions involved. Thus, in some systems, counting of iodine is based on the designation I. In other systems the molecular conservation of this halogen is based on the designation I_2. Description of a system for example by the notation Ge-I_2-He indicates that component counting is based on moles of diatomic iodine, etc.

Table I presents a list of symbols employed throughout the following discussions.

Table I. Explanation of symbols employed

P	=	total pressure in mm	
p_x	=	the partial pressure of the vapor phase species x where x has values from 1-12 inclusive, each number referring to a different species	
P_x	=	the hypothetical pressure of the component x whose designations coincide with those for p_x	
M_x	=	the component mole quantity	
m_x	=	the species mole quantity	
x	=	1—I	7—He
		2—I_2	8—Ga
		3—HI	9—GaI
		4—H_2	10—GaI_3
		5—GeI_2	11—Ge
		6—GeI_4	12—H

* An asterisk superscript to one of the above, such as P_x^*, refers to the pressure at the first point considered in the system.

' A prime superscript to one of the above, such as P_x', refers to the pressure at the second point considered in the system.

Analyses of Systems

The System Ge-I_2-He

Experimentally, the treatment relates to a transport apparatus in which an inert gas, He, is transpired through an iodine source bed at some temperature, T, necessary to provide an equilibrium component pressure of iodine, P_2^*. The saturated gas, in which $P_2^* + P_7^* = 760$ mm, is then carried through a germanium source with which the iodine reacts and with which the resulting vapor phase species equilibrate. Since the component I_2 is assumed to be confined to the vapor phase, the component ratio He/I_2, X, established at the iodine source remains constant thereafter.

From the phase rule it is seen that two parameters are necessary to completely define the isobaric system comprised of three components coexisting in two phases. For convenience, the temperature and the component ratio X, defined above, were chosen. Values of this ratio may be experimentally established at the iodine source bed. At this point in the system, the constant total pressure constraint together with the assumption of the relation between component and species pressures at halogen sources requires that

$$P_7^* = 760 - P_2^* = 760 - p_2^* \qquad \text{(I-1)}$$

Since

$$p_7^* = m_7^* RT/V \qquad \text{(I-2)}$$

and

$$p_2^* = m_2^* RT/V \qquad \text{(I-3)}$$

we obtain after dividing (I-2) by (I-3) for the value of X

$$X = \frac{760 - p_2^*}{p_2^*} \qquad \text{(I-4)}$$

For specified values of X and T, therefore, the complete system Ge-I_2-He will possess unique values of the partial pressures of the species assumed present. These species are I, I_2, GeI_2, GeI_4, and He, and the five independent relationships employed to calculate their partial pressures at given values of X and T are:

$$I_{2(v)} \rightleftarrows 2I_{(v)};\ K_1 = p_1^2/p_2;\ \log_{10} K_1 = 8.362 - 7991/T \quad \text{(2)} \qquad \text{(I-5)}$$

$$Ge_{(s)} + I_{2(v)} \rightleftarrows GeI_{2(v)};\ K_3 = p_5/p_2;\ \log_{10} K_3 = 2.45 + 434/T \quad \text{(1)} \qquad \text{(I-6)}$$

$$Ge_{(s)} + GeI_{4(v)} \rightleftarrows 2GeI_{2(v)};\ K_4 = p_5^2/p_6;\ \log_{10} K_4 = 12.56 - 7936/T \quad \text{(1)} \qquad \text{(I-7)}$$

$$P = p_1 + p_2 + p_5 + p_6 + p_7 \qquad \text{(I-8)}$$

$$X = P_7/P_2 = p_7/(1/2\,p_1 + p_2 + p_5 + 2p_6) \qquad \text{(I-9)}$$

The values of the species partial pressures, p_x, were then used to compute the ratio $(Y)_X = f(T)$ where

$$(Y)_X = \frac{P_{11}}{P_2} = \frac{p_5 + p_6}{1/2\,p_1 + p_2 + p_5 + 2p_6} \qquad \text{(I-10)}$$

The ratio $(Y)_X$ is an efficiency factor which shows the number of moles of Ge carried in the vapor phase for each mole of the component I_2 present. Since the component I_2 is confined to the vapor phase, it is evident that if $(Y)_X$ increases with increasing T, the concentration of the component Ge in the vapor must be increasing with increasing T. Consequently, the transport process is a hot to cold one. This implies, therefore, that the sign of ΔH_p^* for the combined processes (I-5)-(I-7) is positive.

In the temperature interval treated, 0°-800°C, Ge deposition occurs primarily as a result of the disproportionation reaction (I-7). The species responsible for this deposition is GeI_2, the GeI_4 being a disproportionation product. The efficiency factor $(Y)_X$, however, does not discriminate between the disproportionation product GeI_4 and the effective species GeI_2. A Ge availability factor which may be used in place of Y in the temperature region in question is defined by

$$(Y')_X = p_5/(1/2\,p_1 + p_2 + p_5 + 2p_6) \qquad \text{(I-11)}$$

which to a reasonable first approximation is given in simplified form by

$$(Y')_X \sim p_5/(p_5 + 2p_6) \sim \frac{(Y)_X - 0.5}{0.5} \quad \text{(I-12)}$$

It is to be noted that the values of Y′ vary between 0 and 1 in distinction to the values of Y which vary between 0.5 and 1. In the temperature interval in which the quantities p_1 and p_2 are not trivial and in which as a matter of fact Ge may be deposited via (I-6) and (I-7), the ratio $(Y')_X$ is no longer valid. If one considers both temperature ranges, then the initial ratio $(Y)_X$ must be employed. This ratio will then encompass the range 0-1. The $(Y)_X$ data provide a family of constant total pressure curves each curve being at constant X, and the family being projected on the Y-T plane.

The System Ge-I_2-H_2

In this system the iodine component value is again based on the I_2 molecule. Experimentally the physical system is that defined in I above. Chemically the systems differ in that a reactive gas also functions as a carrier. For the three component-two phase equilibrium under a constant pressure constraint, two degrees of freedom are again required to fix the state of the system. Those chosen are the temperature and the H_2/I_2 component ratio, X. The species assumed present are I, I_2, HI, H_2, GeI_2, and GeI_4 requiring specification of six independent relations in order to solve for the several species pressures, p_x, at specified values of T and X. The independent set utilized includes (I-5)-(I-7) as well as

$$H_{2(v)} + I_{2(v)} \rightleftarrows 2HI_{(v)};\ K_2 = p_3^2/p_2p_4;$$

$$\log_{10} K_2 = 0.834 + \frac{622.4}{T} \quad (3) \quad \text{(II-1)}$$

$$P = \sum_1^6 p_x \quad \text{(II-2)}$$

$$X = \frac{P_4}{P_2} = \frac{760 - p^*_2}{p^*_2} = \frac{p_4 + 1/2\,p_3}{1/2\,p_1 + p_2 + 1/2\,p_3 + p_5 + 2p_6} \quad \text{(II-3)}$$

The partial pressures as a function of T for specified values of X were used to compute values of $(Y)_X = f(T)$ where

$$(Y)_X = P_{11}/P_2 = (p_5 + p_6)/(1/2\,p_1 + p_2 + 1/2\,p_3 + p_5 + 2p_6) \quad \text{(II-4)}$$

The System Ge-I_2-H_2-He

Experimentally, the physical system conforms to one in which He and hydrogen sources are used to provide a carrier mixture having a H_2 mole fraction F. This mixed gas is then transpired through an iodine source supply where setting of the pressure of iodine fixes the ratio H_2/I_2, X. The four component system coexisting in two phases possesses three degrees of freedom. These have been chosen as F, X, and T. The seven species, I, I_2, HI, H_2, He, GeI_2, and GeI_4 are assumed present in the complete system. For specified values of F, X, and T the partial pressures of these species were obtained by simultaneous solution of (I-5)-(I-7), (II-1) and

$$P = \sum_1^7 p_{x's} \quad \text{(III-1)}$$

$$F = \frac{P_4}{P_4 + P_7} = \frac{1/2\,p_3 + p_4}{1/2\,p_3 + p_4 + p_7} \quad \text{(III-2)}$$

$$X = \frac{P_4}{P_2} = \frac{1/2\,p_3 + p_4}{1/2\,p_1 + p_2 + 1/2\,p_3 + p_5 + 2p_6} \quad \text{(III-3)}$$

Experimentally, values for F and X are established at the points of mixing of hydrogen and helium and at the iodine source, respectively. Since the components H_2, He, and I_2 are always confined to the vapor phase, these ratios once established remain constant thereafter. At the point of mixing of H_2 and He it is the case that

$$F = \frac{P_4^*}{P_4^* + P_7^*} = \frac{P_4^*}{760} \quad \text{(III-4)}$$

Since the system is constrained by the total pressure being equal to 1 atm, and since the gas behavior is assumed to be ideal, it is seen that at the point of mixing of He and H_2

$$\frac{\text{Flow rate of } H_2}{\text{Total flow rate}} = F \quad \text{(III-5)}$$

In transpiring this mixture F through the iodine source the sum of the pressures of hydrogen and helium $p'_4 + p'_7$ no longer = 760 mm since p'_2 will account for part of the total. The ratio X may be defined experimentally as follows. As the combined pressure of He + H_2 at the iodine source is given by

$$(P'_4 + P'_7) = (760 - P'_2) \quad \text{(III-6)}$$

and the mole fraction of H_2 relative to He and H_2 must remain constant everywhere in the system, we see that dividing (III-6) by P'_4 and rearranging leads to

$$P'_4 = F\,(760 - P'_2) \quad \text{(III-7)}$$

Thus, X can be specified by

$$X = \frac{F(760 - P'_2)}{P'_2} \quad \text{(III-8)}$$

in the region of the iodine source.

Solutions to the several $p_{x's}$ as a function of T were obtained for specified values of X and F. These p_x data were then used to compute families of Y curves, each curve in a family representing the variation of Y with T at constant F and X, and each family being specified at constant P'_2. The expansion of $(Y)_{F,X}$ has the same form as (II-4). It is evident that in order to obtain finite and physically significant solutions it is necessary that $0 < F < 1$ and $0 < P'_2 < 760$ mm Hg.

The System Ge-HI-H

This case is thermodynamically equivalent to that defined in (II) above insofar as the same species are assumed present, and the equilibrium relationships employed are the same. The treatment is, however, based on a different choice of component stoichiometries, more consistent with the experiment in mind. It is to be noted that the hydrogen species content in the present instance cannot independently be brought to zero. As implied by the system designation, component counting is accomplished in terms of Ge, HI, and H, a differentiation being made between hydrogen derived from a source tank and from the halogen acid. In addition, hydrogens are counted singly. As before, two degrees of freedom exist at constant total pressure. These were chosen as the temperature and the component ratio H/HI, X^+. In an experiment, X^+ is established as follows: At the point of mixing of HI and H_2 the mole fraction of the component HI, k, is fixed for the entire system. At this mixing point, therefore, we may write

$$k = \frac{P_3^*}{760} = \frac{\text{Flow rate of HI}}{\text{Total flow rate}} \quad \text{(IV-1)}$$

Since at this same point

$$X^+ = \frac{P_{12}^*}{P_3^*} = \frac{2P_4^*}{P_3^*} = \frac{2(760 - P_3^*)}{P_3^*} \quad \text{(IV-2)}$$

it is seen from (IV-1) and (IV-2) that

$$X^+ = \frac{2(1-k)}{k} \quad \text{(IV-3)}$$

Solutions for the six species partial pressures were obtained from (I-5)-(I-7), (II-1), (II-2), and

$$X^+ = \frac{P_{12}}{P_3} = \frac{2p_4 - 2p_2 - p_1 - 2p_5 - 4p_6}{p_1 + 2p_2 + p_3 + 2p_5 + 4p_6} \quad \text{(IV-4)}$$

The partial pressures were then used to compute values of the efficiency factor $(Y^+)_{X+} = f(T)$ with $(Y^+)_{X+}$ defined by

$$(Y^+)_{X+} = \frac{P_{11}}{P_3} = \frac{p_5 + p_6}{p_1 + 2p_2 + p_3 + 2p_5 + 4p_6} \quad \text{(IV-5)}$$

The System Ge-HI-H-He

This system is thermodynamically equivalent to that described in case (III), and makes use of the same equilibrium relationships. The three degrees of freedom for the system at constant pressure were chosen as the temperature, the component ratio 1/2 H/(1/2H + He), F^+, and the component ratio H/HI, X^+.

At the point of mixing of hydrogen and helium, the ratio F^+ is given by

$$F^+ = \frac{1/2\ P_{12}^*}{760} = \frac{\text{Flow rate of } H_2}{\text{Total flow rate}} \quad \text{(V-1)}$$

At the point of mixing of the hydrogen-helium mixture with HI, the mole fraction of HI in the total gas mixture is given by

$$k = \frac{P'_3}{760} = \frac{\text{Flow rate of HI}}{\text{Total flow rate}} \quad \text{(V-2)}$$

Since the pressure of the component H at this point is given by

$$P_{12} = 2F^+(760 - P'_3) \quad \text{(V-3)}$$

it is seen that

$$X^+ = \frac{P_{12}}{P_3} = \frac{2F^+(1-k)}{k} \quad \text{(V-4)}$$

In the system containing all of the components, the equations for F^+ and X^+ used in addition to (I-5)-(I-7), (II-1), and (III-1), for obtaining simultaneous solutions for the seven species partial pressures are

$$F^+ = \frac{p_4 - 1/2\,p_1 - p_2 - p_5 - 2p_6}{p_4 - 1/2\,p_1 - p_2 - p_5 - 2p_6 + p_7} \quad \text{(V-5)}$$

and

$$X^+ = \frac{P_{12}}{P_3} = \frac{2F^+(1-k)}{k} = \frac{2p_4 - p_1 - 2p_2 - 2p_5 - 4p_6}{p_1 + 2p_2 + p_3 + 2p_5 + 4p_6} \quad \text{(V-6)}$$

Families of curves $(Y^+)_{F+,X+} = f(T)$ were computed, each family derived at constant total P and P'_3, with the expanded form of $(Y^+)_{F+,X+}$ equal to that shown in Eq. (IV-5).

The System Ga-I-He

The treatment follows that for case (I), excepting that iodine counting is based on a monatomic stoichiometry. In addition to Eq. (I-5), the following were employed to obtain partial pressures for the six species I, I_2, Ga, GaI, GaI_3, and He.

$$P = p_1 + p_2 + \sum_{7}^{10} p_x \quad \text{(VI-1)}$$

$Ga_{(l)} = Ga_{(v)}$; $K_5 = p_8$;

$$\log_{10} K_5 = -\frac{14{,}900}{T} - 0.515 \log_{10} T + 10.22 \ (4) \quad \text{(VI-2)}$$

$2Ga_{(l)} + GaI_{3(v)} = 3GaI_{(v)}$; $K_6 = \frac{p^3_9}{p_{10}}$;

$$\log_{10} K_6 = -\frac{11{,}000}{T} + 18.6 \ (5) \quad \text{(VI-3)}$$

$Ga_{(v)} + \frac{3}{2} I_2(v) = GaI_{3(v)}$; $K_7 = \frac{p_{10}}{p_2^{3/2} p_8}$;

$$\log_{10} K_7 = -9.565 \log_{10} T + \frac{24{,}780}{T} + 15.78 \ (6) \quad \text{(VI-4)}$$

The variable X^o is defined by

$$X^o = \frac{P_7}{P_1} = \frac{760 - P_2^*}{2P_2^*} = \frac{p_7}{p_1 + 2p_2 + p_9 + 3p_{10}} \quad \text{(VI-5)}$$

Derived data were used to compute a family of curves of $(R^o)_{Xo} = f(T)$ where

$$(R^o)_{Xo} = \frac{P_8}{P_1} = \frac{\sum_{8}^{10} p_x}{p_1 + 2p_2 + p_9 + 3p_{10}} \quad \text{(VI-6)}$$

The System Ga-HI-H

This Ga analog of system (IV) is defined on the basis of the seven species model, I, I_2, HI, H_2, Ga, GaI, and GaI_3 and makes use of the variables X^+ and T in addition to the equilibrium statements (I-5), (II-1) and (VI-2)-(VI-4). The total pressure constraint is given by

$$P = \sum_{1}^{4} p_x + \sum_{8}^{10} p_x \quad \text{(VII-1)}$$

and X^+ in expanded form by

$$X^+ = \frac{P_{12}}{P_3} = \frac{2(1-k)}{k} = \frac{2p_4 - p_1 - 2p_2 - p_9 - 3p_{10}}{p_1 + 2p_2 + p_3 + p_9 + 3p_{10}} \quad \text{(VII-2)}$$

The ratio $(R^+)_{X+} = f(T)$ was derived, providing a family of curves all at constant total P. $(R^+)_{X+} = f(T)$ is defined by

$$(R^+)_{X+} = \frac{P_8}{P_3} = \frac{\sum_{8}^{10} p_x}{p_1 + 2p_2 + p_3 + p_9 + 3p_{10}} \quad \text{(VII-3)}$$

The System Ga-HI-H-He

The species assumed present were I, I_2, HI, H_2, He, Ga, GaI, and GaI_3. The same degrees of freedom were utilized as in case (V). As in the previous Ga treatments (I-5), (II-1), and (VI-2)-(VI-4) were employed. P is defined by

$$P = \sum_{1}^{4} p_x + \sum_{7}^{10} p_x \quad \text{(VIII-1)}$$

F^+ by

$$F^+ = \frac{\frac{1}{2} P_{12}^*}{760} = \frac{p_4 - \frac{1}{2}p_1 - p_2 - \frac{1}{2}p_9 - \frac{3}{2}p_{10}}{p_4 - \frac{1}{2}p_1 - p_2 - \frac{1}{2}p_9 - \frac{3}{2}p_{10} + p_7} \quad \text{(VIII-2)}$$

and X^+ by

$$X^+ = \frac{P_{12}}{P_3} = \frac{2F^+(1-k)}{k} = \frac{2p_4 - p_1 - 2p_2 - p_9 - 3p_{10}}{p_1 + 2p_2 + p_3 + p_9 + 3p_{10}} \quad \text{(VIII-3)}$$

values of $(R^+)_{F+,X+} = f(T)$ were derived providing families of curves each at constant total P and P'_3.

$(R^+)_{F+,X+}$ is defined by (VII-3).

The System Ge-Ga-I-He

This analysis was attempted in order to define conditions for maximum incorporation of Ga in an epitaxial Ge film. Consequently, it is based on a treatment for the three-phase equilibrium Ge (solid solu-

tion)-liquid-vapor. Two approaches were utilized. The first assumed that the solubility of Ga in Ge is small enough so that $p_{Ge}/p^{o}_{Ge} = 1$, and the liquid in equilibrium with solid Ge is for all practical purposes pure liquid Ga. The second approach makes use of the first assumption but not the second. In its place the assumption is made that if the solid-liquid curve for Ge solid is ideal, the liquid-vapor equilibrium obeys Raoult's law. In either case the systems are such that experimentally they are approximated by having a mixed bed of liquid Ga saturated with Ge, and Ge solid saturated with Ga, all in transpiration with a vapor stream. Species assumed present were I, I_2, GeI_2, GeI_4, He, Ga, GaI, and GaI_3. The two degrees of freedom chosen were T and the ratio He/I, X^o.

Approach 1.—The equilibria used were (I-5)-(I-7) and (VI-2)-(VI-4) along with

$$P = \sum_{1}^{2} p_x + \sum_{5}^{10} p_x \qquad \text{(IX-1)}$$

$$X^o = \frac{P_7}{P_1} = \frac{760 - p_2^*}{2p_2^*} = \frac{p_7}{p_1 + 2p_2 + 2p_5 + 4p_6 + p_9 + 3p_{10}} \qquad \text{(IX-2)}$$

Values of $(Y^o)_{Xo} = f(T)$ and $(R^o)_{Xo} = f(T)$ were derived providing two families of curves. The expanded forms of these efficiency factors are given by

$$(Y^o)_{Xo} = \frac{P_{11}}{P_1} = \frac{p_5 + p_6}{p_1 + 2p_2 + 2p_5 + 4p_6 + p_9 + 3p_{10}} \qquad \text{(IX-3)}$$

and

$$(R^o)_{Xo} = \frac{P_8}{P_1} = \frac{\sum_{8}^{10} p_x}{(p_1 + 2p_2 + 2p_5 + 4p_6 + p_9 + 3p_{10})} \qquad \text{(IX-4)}$$

An indication of the final state, that is, whether the deposit is richer or poorer than the source in Ge or Ga, can be discerned from a consideration of $(R^o/Y^o)_{Xo} = f(T)$. Where this ratio increases with decreasing temperature, it is the case that the bulk deposit is poorer in Ga than the source. Similarly, when the ratio decreases, the bulk deposit is richer in Ga.

Approach 2.—Everything specified in 1 above with the exception of (VI-2) is utilized. In place of (VI-2) a modified relation based on the following argument is used. Thurmond and Kowalchick (7) have indicated that to a good first approximation the solubility of Ge in liquid Ga is predicted by the simple van't Hoff relationship, and that at temperatures not too far removed from the melting point of Ge, $\Delta H_{\text{fusion Ge}}$ can be considered constant. With this information and the assumption that the liquid-vapor equilibrium obeys Raoult's law when the solid-liquid equilibrium is ideal, the vapor pressure curve along the Ge liquidus may be deduced.

Let the vapor pressure of pure liquid Ga at any temperature T be designated p^o_{Ga}. For the equilibrium (VI-2) we write

$$K_5 = p^o_{Ga} \qquad \text{(VI-2)}$$

Along the ideal liquidus we may then write

$$p_{Ga} = N_{Ga} \cdot p^o_{Ga} \qquad \text{(IX-5)}$$

for the equilibrium

$$Ga_{\text{liquid solution}} \gtrless Ga_{\text{Vapor}} \qquad \text{(IX-6)}$$

where p_{Ga} = the partial pressure of Ga over the solution and N_{Ga} = the mole fraction of Ga.

Since

$$N_{Ga} = 1 - N_{Ge} \qquad \text{(IX-7)}$$

in the liquid, and

$$N_{Ge} = -\frac{\Delta H_{Ge}}{R}\left(\frac{1}{T} - \frac{1}{T_{Ge}}\right) \qquad \text{(IX-8)}$$

ΔH_{Ge} being the heat of fusion of Ge and T_{Ge} being the melting point of Ge, we may substitute for p^o_{Ga} and N_{Ga} in (IX-5), the equivalencies given by (VI-2) and (IX-7). Thus

$$p_{Ga} = N_{Ga} K_5 = K_9 \qquad \text{(IX-9)}$$

$$\log K_9 = \log K_5 + \log N_{Ga} \qquad \text{(IX-10)}$$

As

$$N_{Ge} = 10^{\left(-\frac{1770}{T} + 1.46\right)} \qquad (7) \quad \text{(IX-11)}$$

it is seen that

$$\log_{10} N_{Ga} = \log_{10}\left[1\text{-}10^{\left(-\frac{1770}{T} + 1.46\right)}\right] \qquad \text{(IX-12)}$$

and finally that

$$\log_{10} K_9 = -\frac{14{,}900}{T} - 0.515 \log_{10} T + 10.22 + \log_{10}\left[1\text{-}10^{\left(-\frac{1770}{T} + 1.46\right)}\right] \qquad \text{(IX-13)}$$

The same data were extracted as in Approach 1.

The System Ge-Ga-HI-H

As in the preceding analysis two approaches were employed using the identical assumptions.

Approach 1.—In addition to (I-5)-(I-7), (II-1) and (VI-2)-(VI-4), the two chosen degrees of freedom were the temperature and the ratio X^+. The expansions for P and X^+ were as follows:

$$P = \sum_{1}^{6} p_x + \sum_{8}^{10} p_x \qquad \text{(X-1)}$$

$$X^+ = \frac{P_{12}}{P_3} = \frac{2(1-k)}{k} = \frac{2p_4 - p_1 - 2p_2 - 2p_5 - 4p_6 - p_9 - 3p_{10}}{p_1 + 2p_2 + p_3 + 2p_5 + 4p_6 + p_9 + 3p_{10}} \qquad \text{(X-2)}$$

Solutions were as usual obtained for the p_x's and the efficiency factors. These are

$$(Y^+)_{X+} = \frac{P_{11}}{P_3} = \frac{p_5 + p_6}{p_1 + 2p_2 + p_3 + 2p_5 + 4p_6 + p_9 + 3p_{10}} \qquad \text{(X-3)}$$

$$(R^+)_{X+} = \frac{P_8}{P_3} = \frac{p_8 + p_9 + p_{10}}{p_1 + 2p_2 + p_3 + 2p_5 + 4p_6 + p_9 + 3p_{10}} \qquad \text{(X-4)}$$

The ratios $(R^+/Y^+)_{X+} = f(T)$ were also obtained.

Approach 2.—Equation (VI-2) is replaced by (IX-13), everything else remaining unchanged.

The System Ge-Ga-HI-H-He

This final system containing 10 species and three degrees of freedom was treated using two approaches, one making use of (VI-2)-(VI-4) plus the appropriate Ge equations and (II-1), and the other using (IX-13) instead of (VI-2). Both make use of (XI-1)-(XI-3). Solutions were obtained for $(Y^+)_{X+,F+}$ and $(R^+)_{X+,F+}$ both as a function of T, defined by (X-3) and (X-4) and the ratio $(R^+/Y^+)_{X+,F+} = f(T)$.

$$P = \sum_{1}^{10} p_x \qquad \text{(XI-1)}$$

$$F^+ = \frac{1/2\, P_{12}^*}{760} = \frac{p_4 - 1/2p_1 - p_2 - p_5 - 2p_6 - 1/2p_9 - 3/2p_{10}}{p_4 - 1/2p_1 - p_2 - p_5 - 2p_6 - 1/2p_9 - 3/2p_{10} + p_7} \qquad \text{(XI-2)}$$

$$X^+ = \frac{P_{12}}{P_3} = \frac{2F^+(1-k)}{k}$$

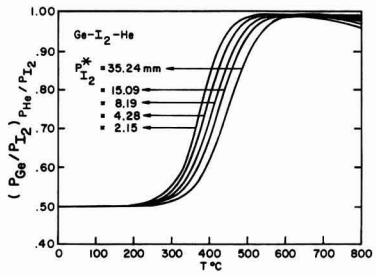

Fig. 1. Efficiency curves for the system Ge-I_2-He at varying iodine source bed pressures.

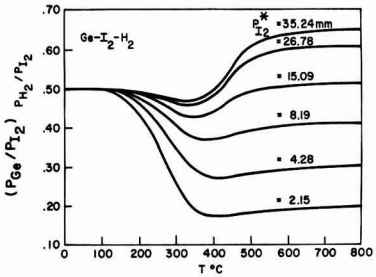

Fig. 2. Efficiency curves for the system Ge-I_2-H_2 at varying iodine source bed pressures.

$$= \frac{2p_4 - p_1 - 2p_2 - 2p_5 - 4p_6 - p_9 - 3p_{10}}{p_1 + 2p_2 + p_3 + 2p_5 + 4p_6 + p_9 + 3p_{10}} \quad \text{(XI-3)}$$

Results and Discussion

The System Ge-I_2-He

Figure 1 graphically depicts the variation of the component ratio $Ge/I_2 = Y$ as a function of temperature. Each projected curve represents a different He/I_2 ratio, X, consequently each coincides with a different iodine source bed temperature. The curves all exhibit the same general shape and are indicative of hot to cold transport over most of the temperature range surveyed. At the low temperature end of the scale plateaus develop at approximately 220° and a Y value of 0.5, the proper value for a vapor phase species stoichiometry of GeI_4. The 220° plateaus are experimentally unimportant since this temperature lies below the dew points of both GeI_4 and GeI_2 for the iodine pressures considered. At the high temperature end of the scale plateaus also develop, the highest X curve flattening at 550°C and the lowest at 600°C. These plateaus, as will be discussed below, are experimentally significant.

It is significant that the efficiency of forming GeI_2 (higher Y values) decreases with increasing I_2 source bed pressure (decreasing X values) over most of the temperature range. This conclusion is most clearly focused upon by a consideration of Table II which lists calculated values of the pressures of GeI_2 and GeI_4 at different germanium and iodine source bed temperatures. It is seen that, while the absolute value of GeI_2 increases with increasing I_2 source bed pressure, excepting at high Ge source bed temperatures, a disproportionate percentage of the vapor phase Ge content is present as the product of the disproportionation process and therefore unavailable as a deposition species.

The large slopes in the temperature interval in which seeds might be placed indicate that extremely close tolerance seed temperature control would be required in order to effect reproducible deposition rates. On the other hand if Ge source temperatures are made coincident with the high-temperature plateau intervals, close temperature control tolerance at the Ge source sites is not very critical. Furthermore, use of these plateaus would obviate the efficiency question discussed above. In all the systems discussed it is evident that even when transpiration conditions are attained at source beds, control of flow rates will represent a critical factor in achieving reproducible deposition rates, all other factors remaining constant.

The System Ge-I_2-H_2

Figure 2 shows an equivalent plot to that given in Fig. 1 for the case where the carrier gas is also a reactive component. It is noted on comparison of Fig. 1 and 2 that whereas the Ge/I_2 ratio never drops below 0.5 in the nonreactive carrier gas system it does so when H_2 is present. This is believed due to the competition for iodine between Ge and H_2. Since the heat of formation of HI is negative [Eq. (II-1)] the effects of this competition decrease with increasing temperatures and are greatest at low iodine pressures and low temperatures. In the present analysis, two other marked perturbations are evident. First, the efficiency in terms of formation of GeI_2 increases with increasing iodine source bed temperature and, second, the competition for iodine results in the occurrence of low temperature cold to hot transport regions which generate minima in the curves. These minima fall in convenient temperature regions for seed locations providing less temperature sensitive sites. Aside from the higher pressure curves, however, the utility of the system in its described form is questionable since the system is inefficient, the Y ratio not approaching one at any temperature due to the large quantity of HI present. This is seen by examination of Table III which presents several P_{I_2}* source values and the resulting pressures of GeI_2, GeI_4, and HI in the thermodynamic system.

A comparison of Fig. 1 and 2 raised the interesting possibility of developing low-temperature minima in usable seed site temperature intervals by employing mixtures of H_2 and He as carrier gases. Thus, it is

Table II. Selected data for the Ge-I_2-He System

T_{Ge} source, °C	$P^*_{I_2}$ mm	$pGeI_2$ mm	$pGeI_4$ mm
350	35.24	3.308	16.34
400	35.24	8.920	13.47
450	35.24	18.29	8.665
500	35.24	27.65	3.865
550	35.24	32.67	1.284
350	15.09	2.096	6.562
400	15.09	5.382	4.901
450	15.09	9.975	2.578
500	15.09	13.30	0.895
550	15.09	14.56	0.255
350	2.154	0.698	0.729
400	2.154	1.446	0.354
450	2.154	1.954	0.099
500	2.154	2.105	0.022
550	2.154	2.136	0.005

Table III. Source values and pressures

T_{Ge} source, °C	$P^*_{I_2}$ mm	$pGeI_2$ mm	$pGeI_4$ mm	pHI mm
350	35.24	3.042	13.82	10.38
400	35.24	7.686	9.998	16.02
450	35.24	14.28	5.281	21.25
500	35.24	19.39	1.901	24.21
550	35.24	21.57	0.560	25.07
350	15.09	1.775	4.704	8.001
400	15.09	3.974	2.673	11.64
450	15.09	6.117	0.970	14.10
500	15.09	7.120	0.256	14.91
550	15.09	7.448	0.067	14.99
350	2.154	0.287	0.123	3.242
400	2.154	0.355	0.021	3.512
450	2.154	0.377	0.004	3.539
500	2.154	0.389	0.001	3.525
550	2.154	0.398	0.000	3.507

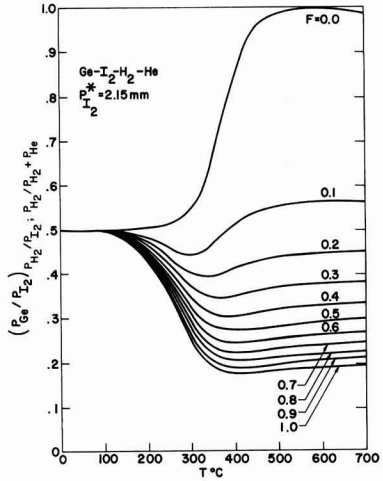

Fig. 3. Efficiency curves for the system Ge-I_2-H_2-He at an iodine source bed pressure of 2.15 mm and varying $H_2/(H_2 + He)$ fractions.

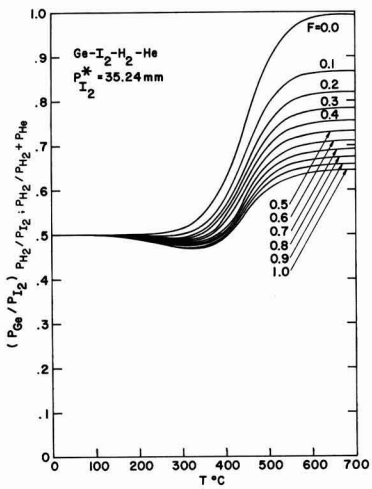

Fig. 4. Efficiency curves for the system Ge-I_2-H_2-He at an iodine source bed pressure of 35.24 mm and varying H_2/H_2 + He fractions.

observed that the minima in Fig. 2 for a particular iodine source temperature lie at higher temperatures than the low-temperature plateaus of Fig. 1. It was reasoned that if the H_2 carrier is diluted with He, the competitive action of H_2 would decrease causing the minima to shift to lower temperatures and to become more shallow in the process. This possibility occasioned the analysis of the following system.

The System Ge-I_2-H_2-He

Figures 3 and 4 show the variations of Ge/I_2 ratio with temperature for two families of curves, each family being at constant P_{I2}* and each curve in a family representative of a different H_2-He mixture. Thus, the data for a given curve depicts $(Y)_{F,X} = f(T)$. Present in each family are reiterations of the curves derived from the analysis of systems I and II to provide a complete picture. Figures 5 and 6 present some of the data in a different fashion, namely, with constant $H_2/(He + H_2)$ mole fractions, where the values of Y are plotted as a function of T, each curve depicting a different iodine source temperature. Figure 1 repre-

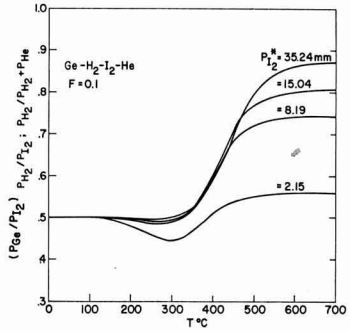

Fig. 5. Efficiency curves for the system Ge-I_2-H_2-He at a $H_2/(H_2 + He)$ fraction of 0.1 and varying iodine source bed pressures.

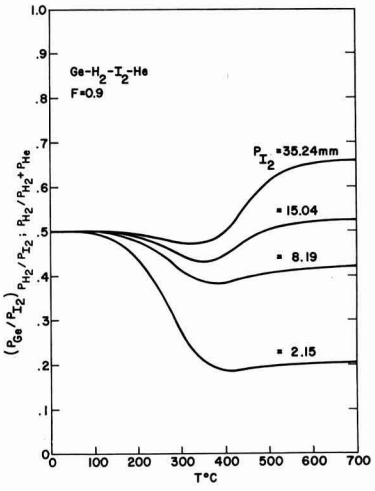

Fig. 6. Efficiency curves for the system Ge-I_2-H_2-He at a $H_2/(H_2$ + He) fraction of 0.9 and varying iodine source bed pressures.

sents the case of $F = 0$ and Fig. 2 the case for $F = 1$.

As seen from Fig. 3 and 4 the perturbation of the pure He curves increases with increasing $H_2/(He + H_2)$ mole fraction (increasing F), the higher I_2 source pressure curves being most efficient over-all and providing what appear to be the least temperature sensitive seed site regions, coupled with high relative GeI_2 formation efficiency.

The System Ge-HI-H

The data for this system (Fig. 7) are presented in the form of Ge/HI ratios, a value of 0.25 now coincident with pure GeI_4 and 0.5 coincident with pure GeI_2. The range of iodine pressures covered, 1.9 mm I_2-361 mm I_2, is larger than those treated in the I_2 systems previously discussed. It is seen that as found in system II, the efficiency of GeI_2 formation increases with increasing iodine pressure. Furthermore, at the highest P_{HI}* pressures the minima give way to low temperature plateaus with relative temperature insensitivity up to 400°.

The System Ge-HI-H-He

The data for this system are depicted in a manner similar to those of system III. Thus, Fig. 8-14 present families of curves each family at constant component HI mole fraction k and Fig. 15 and 16 depict two families of curves at constant H_2 mole fraction relative to H_2-He mixtures. From the first set of graphs it is seen that as the P_{HI}* values increase, the effect of varying $H_2/(H_2 + He)$ mole fraction diminishes, finally result-

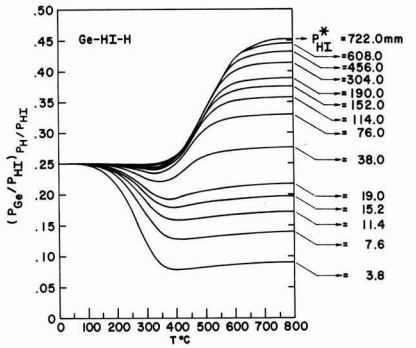

Fig. 7. Efficiency curves for the system Ge-HI-H at varying hydrogen iodide source pressures.

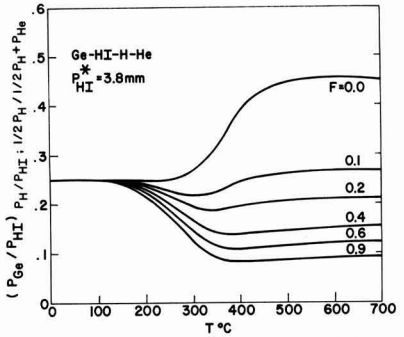

Fig. 8. Efficiency curves for the system Ge-HI-H-He at an HI source pressure of 3.8 mm and varying $H_2/(H_2 + He)$ fractions.

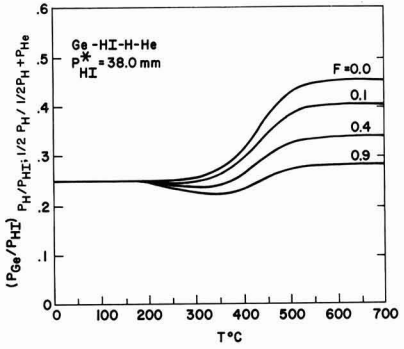

Fig. 9. Efficiency curves for the system Ge-HI-H-He at an HI source pressure of 38.0 mm and varying $H_2/(H_2 + He)$ fractions.

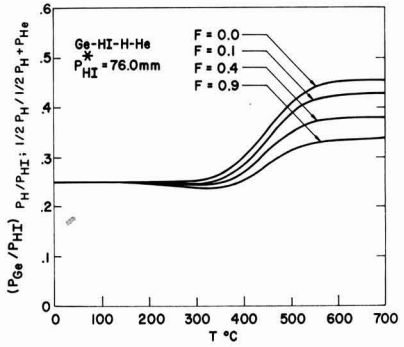

Fig. 10. Efficiency curves for the system Ge-HI-H-He at an HI source pressure of 76.0 mm and varying $H_2/(H_2 + He)$ fractions.

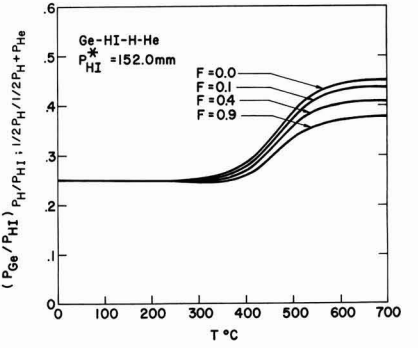

Fig. 11. Efficiency curves for the system Ge-HI-H-He at an HI source pressure of 152.0 mm and varying $H_2/(H_2 + He)$ fractions.

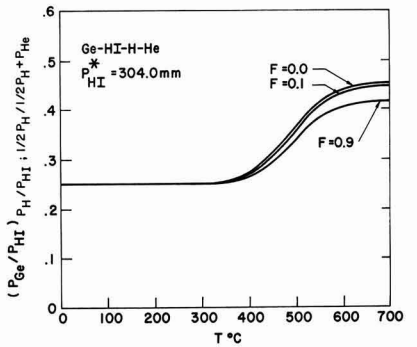

Fig. 12. Efficiency curves for the system Ge-HI-H-He at an HI source pressure of 304.0 mm and varying $H_2/(H_2 + He)$ fractions.

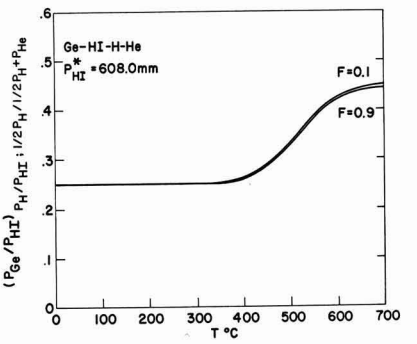

Fig. 13. Efficiency curves for the system Ge-HI-H-He at an HI source pressure of 608.0 mm and varying $H_2/(H_2 + He)$ fractions.

ing in data at 722 mm P_{HI}* in which the curves for $F = 0.1$ and 0.9 are indistinguishable. Since the minimum component pressure value of hydrogen possible in these systems coincides with the partial pressure of component iodine, the Y^+ values are always less efficient than the Y values of system I. At low $H_2/(H_2 + He)$ mole fractions it is the case that over appreciable temperature regions the high P_{HI}* curves are more efficient than the lower pressure ones. However, the slopes and temperatures of plateau or minima occurrence appear more usable in the lower pressure cases.

It is to be pointed out that the figures include data for $F = 0$. These were obtained from a separate partial analysis of the system Ge-HI-He, arguments for which are not presented, but whose format is similar

to the related systems. A constraint was employed setting the H/I ratio = 1.

The System Ga-I-He

Figure 17 shows the results for this system. In essence the data are quite similar to those for the Ge analog, system I, and need not be discussed further.

The System Ga-HI-H

The data for this system, Fig. 18, are completely unlike those for the Ge analog, systems II and IV. First, the efficiency in formation of the transporting species GaI is greater at lowest P_{HI}^* pressures. Second, no minima develop. These results are not unexpected in view of the large values for the Ga-I equilibrium constants which preclude any competition for iodine by

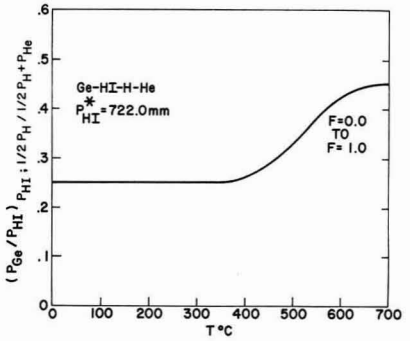

Fig. 14. Efficiency curves for the system Ge-HI-H-He at an HI source pressure of 722.0 mm and varying $H_2/(H_2 + He)$ fractions.

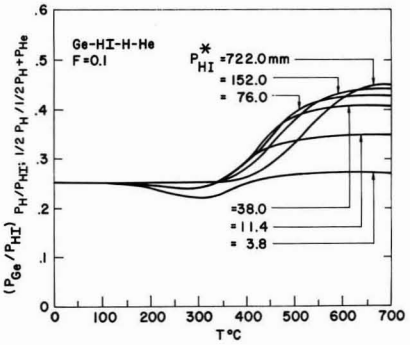

Fig. 15. Efficiency curves for the system Ge-HI-H-He at a $H_2/(H_2 + He)$ fraction of 0.1 and varying hydrogen iodide source pressures.

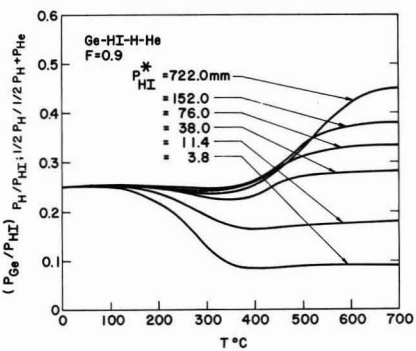

Fig. 16. Efficiency curves for the system Ge-HI-H-He at a $H_2/(H_2 + He)$ fraction of 0.9 and varying hydrogen iodide source pressures.

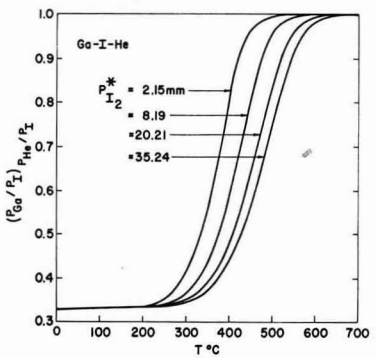

Fig. 17. Efficiency curves for the system Ga-I-He at varying iodine source bed pressures.

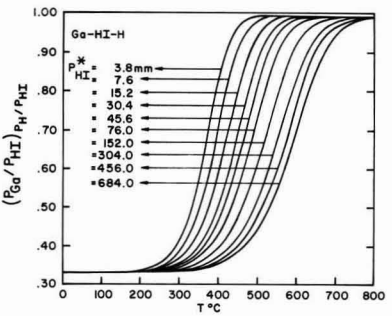

Fig. 18. Efficiency curves for the system Ga-HI-H at varying hydrogen iodide source pressures.

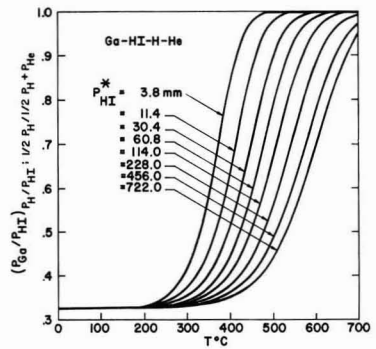

Fig. 19. Efficiency curves for the system Ga-HI-H-He at varying hydrogen iodide source pressures, and representing all $H_2/H_2 + He$ fractions between 0.1 and 0.9.

hydrogen. This system represents a clear case where one reaction dominates all others, independent of the signs of the ΔH_p's, and remains essentially unperturbed in the presence of a reactive carrier gas.

The System Ga-HI-H-He

The data are presented in the form of a single family of curves at constant F^+ value, Fig. 19. Again, because of the domination of competing equilibria by the primary one, the effect of inert-reactive carrier gas mixtures is undetectable. Thus, depending on P_{HI}^* alone, the $(R^+)_{X+,F+}$ values appear to be determined, the system behaving as one of only three components.

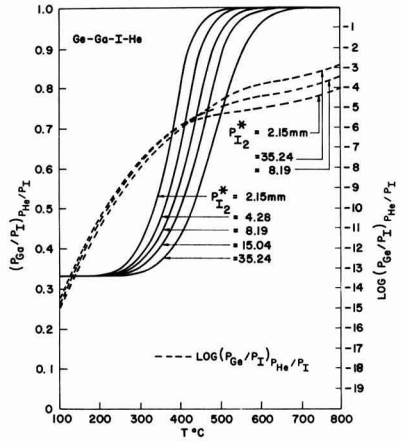

Fig. 20. Efficiency curves for the system Ge-Ga-I-He at varying iodine source bed pressures.

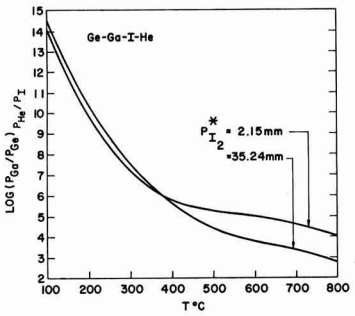

Fig. 21. Variation of Ga/Ge vapor phase content in the system Ge-Ga-I-He at two different iodine source bed pressures.

The System Ge-Ga-I-He

As discussed previously, two approaches were employed. These led to sets of data essentially indistinguishable from one another and as a consequence only one set of results, Fig. 20, is presented, that from the second approach. In Fig. 20 $(R^o)_{X_o}$ and $\log_{10}(Y^o)_{X_o}$ values are plotted as a function of T. It is to be noted that while the R^o data vary in the range 0-1, the Y^o data vary in the range 10^{-22}-10^{-4}. This implies that in the mixed transport, the quantity of Ge moved from the source is many orders of magnitude smaller than the quantity of Ga transported. Also, while the R^o curves follow the same general contours as where no Ge is present, the Y^o curves exhibit no plateaus. It is also to be observed that an efficiency cross-over occurs in the Y^o data. Figure 21 shows a $\log_{10}(R^o/Y^o)_{X_o}$ plot *vs.* temperature. It is seen that starting at a source temperature of 800°, the vapor is some 2-4 orders of magnitude richer in Ga, but that this value increases to between 5 and 6 orders of magnitude at 400°. Thus, the removal of Ge from the vapor at a potential seed site appears fairly efficient in a hot to cold transport process.

The System Ge-Ga-HI-H

The data for this system, Fig. 22 and 23, are similar to those in the previous system not being perturbed to any great extent by either of the approaches employed or the use of H_2 as a carrier. The noticeable effects are that the high-temperature plateau for the R^+ curves develop at slightly lower temperatures and the amount of Ge in the vapor phase is somewhat greater in the present system.

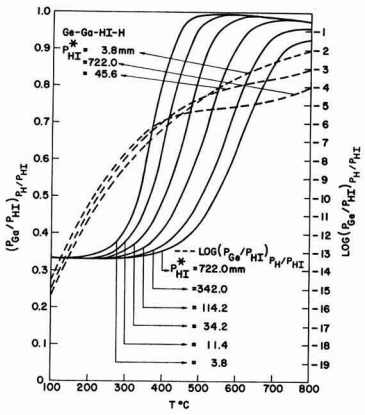

Fig. 22. Efficiency curves for the system Ge-Ga-HI-H at varying hydrogen iodide source pressures.

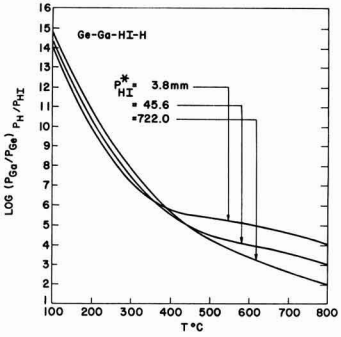

Fig. 23. Variation of Ga/Ge vapor phase content in the system Ge-Ga-HI-H at three different hydrogen iodide source pressures.

The System Ge-Ga-HI-H-He

The data for this system are equivalent to those of system X and need not be repeated.

Acknowledgment

The authors are indebted to the following IBM Research personnel: Dr. R. P. Kelisky of the Mathematical Sciences Department for his continued efforts, during the entire course of this work, toward developing mathematical treatments amenable for computer analyses (8). They also wish to thank Miss A. G. Kuhlke, J. Reinke, Mrs. E. Smith, Mrs. J. K. Somorjai, and R. A. Stevens of the Computing Center for their tireless efforts in carrying the analyses to successful conclusions. In addition, the authors are grateful to G. Cheroff, R. F. Lever, and M. Berkenblit of the Solid State Science Department for their many stimulating discussions and invaluable suggestions concerning the chemical implications of the several systems considered.

Manuscript received Nov. 12, 1963; revised manuscript received March 2, 1964. This paper was presented in part at the New York Meeting, Sept. 29-Oct. 3, 1963 and the work was supported in part by A.F.C.R.L. Contract No. AF19(628)-2468.

Any discussion of this paper will appear in a Discussion Section to be published in the June 1965 JOURNAL.

REFERENCES

1. R. F. Lever, Private communication. Certain of his data were presented at the Los Angeles Meeting of the Society, May 6-10, 1962, Electronics Division Abstracts Vol. 11, p. 240.
2. Selected Values of Chemical Thermodynamic Prop-

erties, Natl. Bur. Standards Circ. 500, Series III, Washington, D. C. (1952).
3. G. M. Murphy, *J. Chem. Phys*, **4**, 344 (1936).
4. C. N. Cochran and L. M. Foster, *This Journal*, **109**, 144 (1962).
5. V. J. Silvestri and V. J. Lyons, *ibid.*, **109**, 963 (1962).
6. Calculated from data from L. L. Quill, "The Chemistry and Metallurgy of Miscellaneous Materials, Thermodynamics," University Microfilms, Ann Arbor, Mich. (1961); W. Fischer and O. Jübermann, *Z. anorg. u. allgem. Chem.*, 227 (1936).
7. C. D. Thurmond and M. Kowalchick, *Bell System Tech. J.*, **39**, 169 (1960).
8. The mathematical techniques used for computer analyses are described in "Numerical Methods and Fortran Programming" by D. D. McCracken and W. S. Dorn, John Wiley & Sons, Inc., New York (1964).

Incorporation of Zinc in Vapor Grown Gallium Arsenide

V. J. Silvestri and F. Fang

Thomas J. Watson Research Center, International Business Machines Corporation, Yorktown Heights, New York

ABSTRACT

A vertical sealed tube configuration has been used to deposit epitaxially Zn doped GaAs on Te doped substrates. The vapor grown junctions were characterized through capacitance measurements. Linearly graded, nonuniform, and abrupt impurity profiles were observed. The nature of these junctions is shown to correlate with the zinc dopant concentrations present in the vapor. The distribution of zinc between the vapor phase and solid GaAs were determined for the junction growth conditions, and this distribution was found to follow Henry's law for the range investigated. The results of these investigations indicate that autodoping phenomena are involved in producing the variety of junctions observed.

The epitaxial growth of GaAs using various transporting agents has become well established among many investigators (1-6). Little has been reported, however, on the nature of incorporation of impurities during the growth process. The recent interest in the electroluminescence of GaAs p-n junctions has created a renewed interest in these doping aspects during the growth process, particularly in connection with junction fabrication.

In this investigation the incorporation of zinc in vapor grown GaAs has been examined through variation of vapor dopant concentrations, and the effects which these variations produced in junctions are discussed. In addition, the zinc in solid (Zn_s)-zinc in vapor (Zn_v) distribution was determined from Hall measurements of grown layers doped to various concentrations.

1 Provided by S. E. Blum of this laboratory.

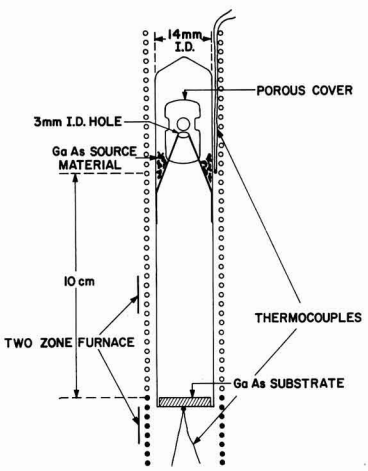

Fig. 1. Vertical tube configuration employed for depositing gallium arsenide.

Experimental

Figure 1 shows the vertical closed tube configuration which was employed for the depositions. Temperatures in the source and seed regions were independently controlled at 800° and 630°C, respectively. Iodine was introduced at a concentration of 2 mg/cm^3 to effect transport via the GaAs-I reaction (7). In a first series of experiments carried out to obtain p-n junctions the substrates used were from pulled crystals which were doped with Te to carrier concentrations of 5 x 10^{17}/cc.[1] These substrates were oriented in the <111> direction, and the depositions were on the gallium side.

Zinc was incorporated in the deposits primarily through the introduction of $ZnAs_2$, but the effects of using Zn doped source material were also evaluated. When using $ZnAs_2$ as a dopant, the source consisted of vapor grown GaAs which had been synthesized at 750°C from high purity Ga and As using the iodine reaction. In depositing the junctions, the amounts of dopant added were varied such as to supply different ZnI_2 overpressures. From thermodynamic considerations (8) ZnI_2 is more stable than the gallium iodides, and in separate experiments it was shown that the reaction between $ZnAs_2$ and iodine goes virtually to completion to form ZnI_2. The amounts of dopant were chosen such that at the transport temperatures no condensed phase of ZnI_2 was present. Even at the highest zinc concentration used, the formation of ZnI_2 did not significantly deplete the iodine hence there was always sufficient iodine available for the transport of GaAs.

In this first series the epitaxial layers were used for junction evaluation and were grown to thicknesses of from 1-4 mils. Most depositions were completed within 5 hr and from these structures diodes were fabricated. Initially through electrical probing it was determined that the junctions were located within the grown region in some instances being closer to the physical interface than others. Through subsequent etching it was found that the junction locations varied depending on the experimental conditions employed. The etching solution used to indicate junction positions relative to the physical interface consisted of 10 H_2O : 1 HF, 1, 30% H_2O_2. Figure 2 is a photograph of a stained cross section taken through a physical interface and junction

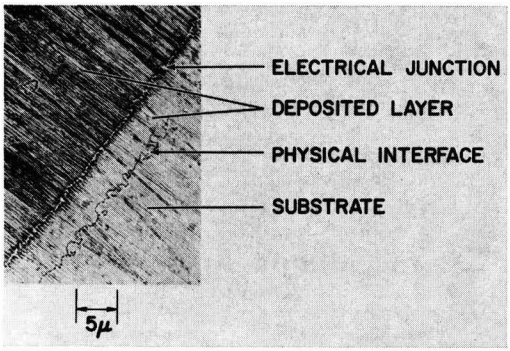

Fig. 2. Microphotograph of a stained cross section through the physical interface and vapor grown electrical junction.

which was lapped on a 3° angle block prior to etching. In addition to staining, the junctions also were electrically probed to determine conductivity type and gave results consistent with the etching delineations.

A second series of depositions was also conducted in which ZnI_2 vapor content was varied over a range similar to that of series one under which the junctions were grown. The purpose of this second study was to determine the distribution of Zn between the vapor phase and solid GaAs. These layers were deposited on <111> high purity substrates to thicknesses of from 12-22 mils. From these more thickly grown regions Hall samples were sectioned and electrically characterized.

The diodes fabricated from series one were characterized through capacitance measurements. It is well known that the differential capacitance of a junction is a result of the electrical dipole double layer of the space charge region. In particular, it is a measure of the fixed charge density near the edge of the space charge region. These fixed charges are ionized impurity centers of the semiconductor. It can be readily shown (9) that for an abrupt junction with a uniform impurity concentration N_a and N_d in both p and n type materials, the differential capacitance per unit area is given by

$$C = \left[\frac{KqN}{8\pi(V_D + V_A)}\right]^{1/2} \quad [1]$$

where K is the absolute dielectric constant, q the electronic charge, V_D the diffusion potential of the junction, V_A the applied voltage and $1/N = 1/N_a + 1/N_d$.

For an unsymmetrical junction, *i.e.*, N_a and N_d differ appreciably, N approaches the smaller of the two. Most of the experimental junctions reported here are highly unsymmetrical. The substrates are heavily doped. Thus, the N's determined from the voltage dependence of the junction capacitance are in general indicative of the lightly doped vapor grown side. It can be shown quite generally that for this type of unsymmetrical junction if N is a function of the distance x_I from the junction, then

$$N(x_I) = \frac{8\pi}{Kq}\frac{dV_A}{d(1/C^2)} \quad [2]$$

where x_I is given by

$$x_I = \frac{K}{4\pi C} \quad [3]$$

analogous to the parallel plate capacitors.

Finally, if the composite impurity profile is a linear function of the distance from the junction, *i.e.*, $|N_a - N_d| = ax$ where a is the impurity gradient, the junction capacitance becomes

$$C = \left[\frac{K^2 qa}{192\pi^2(V_D + V_A)}\right]^{1/3} \quad [4]$$

Table I. Representative data for junctions grown under various ZnI_2 concentrations

ZnI_2 concentration in vapor (moles/cc)	P_{ZnI_2} (Torr)	Impurity gradient classification	Width of space charge region over which gradient is found (mm)	Gradation (atoms/cm⁴)
7.8×10^{-10}	0.043	Nonuniform	5.8×10^{-4}	
5.2×10^{-9}	0.29	Linearly graded	3.2×10^{-4}	2.7×10^{21}
4.2×10^{-8}	2.34	Linearly graded	1.3×10^{-4}	3.3×10^{22}
4.2×10^{-7}	23.7	Abrupt	2.9×10^{-5}	
4.2×10^{-6}	236.0	Abrupt	1.8×10^{-5}	
Using a Zn doped GaAs source (2×10^{17} atoms/cc)				
4.2×10^{-10}*	0.023	Nonuniform	5.5×10^{-4}	

* This value represents an upper limit for Zn vapor content.

In what follows, the grown junctions are conveniently classified into three categories, namely, abrupt, linearly graded, and nonuniform. The abrupt junctions are those whose capacitances have bias dependence as shown in Eq. [1]. The impurity concentration in these junctions is uniform beyond the zero bias space charge width. The linearly graded junctions have voltage dependent capacitance shown in Eq. [4]. The "nonuniform" junctions are those whose impurity profiles found by [2] are nonlinear functions of x. In the vapor grown nonuniform junctions reported here, they were usually found to be either superlinear, *i.e.*, $|N_a - N_d| \propto x^n$ where $n > 1$ or exponential, where $|N_a - N_d| \propto \exp. x$.

Results

In Table I representative results for these measurements of series one are shown. All three types of junctions have been produced depending on the growth conditions. The data indicate that the space charge region over which the impurity distribution occurs narrows, and that there is a corresponding steepening of the impurity gradient with increasing Zn vapor content.

At the low ZnI_2 concentration (7.8×10^{-10} moles/cc), experimentally produced by either the addition of small quantities of $ZnAs_2$ or the use of Zn doped source, "nonuniform" impurity gradients occurred. In addition, at these low concentrations the formation of a second junction was sometimes found to occur if the layer was allowed to grow sufficiently thick.

Experimentally, with increase of vapor phase dopant concentrations, the electrical junctions were found to occur closer to the physical interface. At the very highest ZnI_2 concentration (4.2×10^{-6} mole/cc) the grown junctions were found to be abrupt. In such cases staining confirmed that the physical interface and junction were not observably separated.

The data obtained from series two are given in Fig. 3. Since information concerning carrier concentration

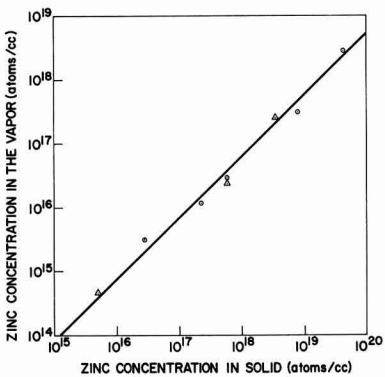

Fig. 3. Distribution of zinc between the vapor phase and solid gallium arsenide as determined from Hall and capacitance measurements; temperature, 630°C; ○, Hall samples; △, capacitance data.

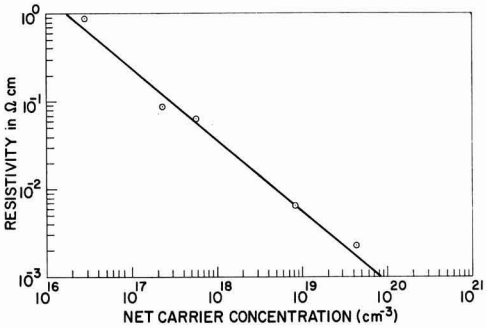

Fig. 4. Plot of resistivity as a function of carrier concentration for zinc in vapor grown gallium arsenide.

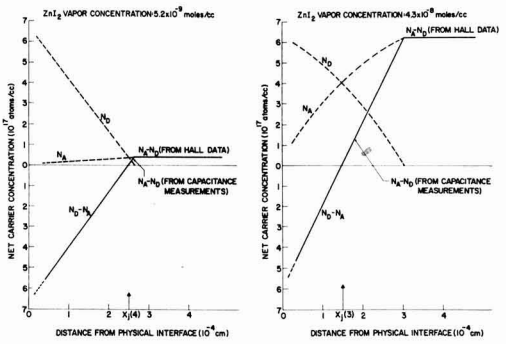

Fig. 5(a, left; b, right). Impurity profiles for two linearly graded junctions grown under dissimilar ZnI_2 overpressures. Solid lines indicate experimentally determined impurity concentrations. Broken lines indicate hypothetical profiles for substrate impurity (N_D) and vapor dopant (N_A) in the grown layers.

was also derivable from some of the capacitance measurements these values have been included and show good agreement. The distribution of Zn experimentally observed between vapor and solid may be represented by the equation

$$\log C_V = \log C_S - 1.16$$

where C_V, the concentration in the vapor, is proportional to C_S, the concentration in the solid (Henry's law). In Fig. 4 the variation of resistivity with net carrier concentration for the deposited Hall samples is also shown.

Discussion

From the material control aspects these variety of junction characteristics are of some interest. The junctions were found to change consistently from nonuniform through linearly graded to abrupt profiles in the order of increasing ZnI_2 overpressures. Staining experiments in both the linearly graded and nonuniform junctions confirmed that they were always found in the grown region at some distance from the physical interface. In addition it was noted that the degree of displacement of these electrical junctions diminished with increasing zinc overpressures. These experimental observations indicated that process effects were involved.

Autodoping phenomena in vapor grown Ge have been reported previously (10). These process effects in junction growth have also been examined in Si. The effect of vapor contamination as introduced by the substrate and system were described in producing a "junction lag" effect (11-13). The basic observation made in both investigations was that the impurities present in the substrate contaminate the vapor and are then redistributed in the growing layer at a constantly decreasing concentration as growth continues. It appears that a similar model can be used to describe the junction displacements reported here. It might in fact be expected that autodoping effects would be even more pronounced in a sealed system.

It is believed that the vapor etching which occurs initially from the reaction of GaAs with iodine facilitates the introduction of seed impurities to the vapor.

If one now considers a model such as described by Kahng, Thomas, and Manz for the autodoping process in silicon (11-13) which involves, namely, repetitive etching, mixing, and growth steps, one can see that the Te introduced from the initial substrate etching undergoes dilution such that the Te content (N_D) approaches zero as the layer grows. The Zn concentration (N_A), however, simultaneously is approaching a value determined by the particular zinc overpressure used. Under such conditions a compensating process would ensue and the electrical junction would occur within the grown region at some distance from the physical interface. Such a descriptive model fits the experimental data. In Fig. 5a and b the impurity profiles for two linearly graded junctions grown under dissimilar ZnI_2 overpressures are shown. Through the junction positions $x_j(3)$ and $x_j(4)$ (determined through staining and electrical probing) the impurity profiles have been plotted. Extrapolations of this capacitance data have been made both to the physical interface and to the expected final Zn doping level for the conditions of growth as obtained from the distribution data (Fig. 3).

Diffusion effects were considered; however, calculations based on reported diffusion constants (14) indicated that for the experimental conditions used such effects could not contribute significantly to junction positioning. Under different growth conditions diffusion effects could become important. However, the junction displacements reported here appear to result primarily from an autodoping effect.

At very low Zn concentrations, one has the special case in which the depletion of Zn from the vapor phase is significant and in combination with the autodoping effects is important in shaping the impurity profiles. In Fig. 6 a descriptive representation of this depletion effect is shown. The first junction, $x_j(1)$, orginates from the autodoping effects described above. In cases in which a significant background donor level was present in the source material a second junction could also be formed. This second junction, $x_j(2)$ resulted from the Zn vapor depletion which produced an impurity profile for N_A of the type shown. An example of this n-p-n structure is shown in Fig. 7.

In using Zn doped source material similar depletion effects were observed since the Zn vapor content was

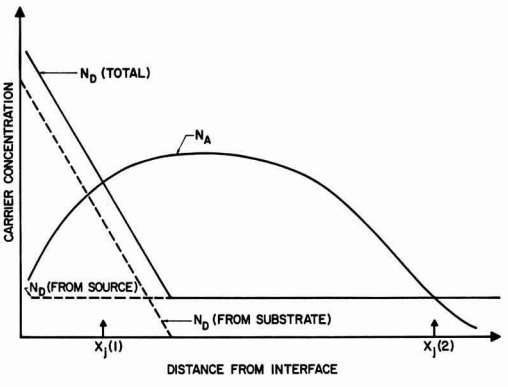

Fig. 6. General type of impurity distribution found when using low ZnI_2 overpressures combined with a source GaAs containing a background donor level.

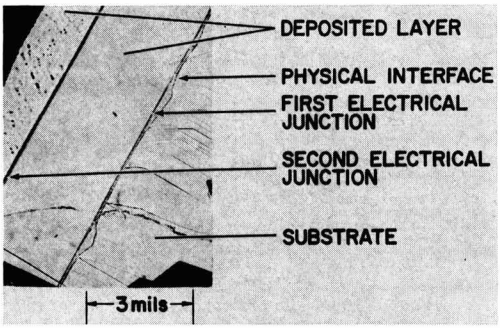

Fig. 7. Microphotograph of a cleaved cross section showing a double junction formation.

always in the low concentration range. The specific impurity profiles in such cases however, depend on factors such as the Zn diffusion rate from the source, the rate of source etching, and the depositing layer depletion rate. Generally, it was found that the impurity profiles for junctions grown using Zn doped source material were not readily reproduced.

With increasing vapor dopant, the per cent perturbation of Zn vapor content due to incorporation is insignificant, and no depletion effects are observed. The impurity profile is then primarily the result of redistribution of substrate impurity.

Similar autodoping effects have been observed in depositing Cd doped layers on Te doped substrates and Zn doped layers on Si doped substrates.

Summary

In the formation of junctions in sealed tubes through deposition of GaAs by vapor transport autodoping phenomena were found to influence both junction location and impurity distributions. The junction variations in the system employed appear to result from (i) the time required for the arrival of ZnI_2 to the vapor, (ii) the distribution which is established between (Zn_S)-(Zn_V), and (iii) the reincorporation of the vapor contaminant initially introduced through seed etching.

Acknowledgments

The authors wish to acknowledge the helpful discussions with Drs. H. Leonhardt and A. Reisman. We also wish to thank Dr. J. F. Woods and Mr. S. R. Baliozian for the Hall measurements and Mr. M. E. Cowher for his experimental assistance.

Manuscript received Feb. 25, 1964. This paper was presented at the New York Meeting, Sept. 30-Oct. 3, 1963.

Any discussion of this paper will appear in a Discussion Section to be published in the June 1965 JOURNAL.

REFERENCES

1. V. J. Lyons and V. J. Silvestri, *This Journal*, **108**, 177C (1961), Abstract 140.
2. R. R. Moest and B. R. Shupp, *ibid.*, **108**, 178C (1961), Abstract 143.
3. F. V. Williams and R. A. Ruehrwein, *ibid.*, **108**, 177C (1961).
4. N. Holonyak, Jr., D. C. Jillson and S. F. Bevacqua, *Proc.* AIME (1961); Conf. on the Met. of Semiconductor Materials, Los Angeles, Aug. 1961, vol. 15, p. 49, John Wiley and Sons, Inc., New York (1962).
5. R. L. Newman and N. Goldsmith, *This Journal*, **108**, 1127 (1961).
6. C. J. Frosch and C. D. Thurmond, Abstracts of "Recent News" Papers, Electrochemical Society Meeting, Sept. 16-20, 1962.
7. V. J. Silvestri and V. J. Lyons, *This Journal*, **109**, 963 (1962).
8. L. L. Quill, "The Chemistry and Metallurgy of Miscellaneous Materials, Thermodynamics," McGraw Hill Book Co., Inc., New York (1950).
9. See for example: W. Ehrenberg, "Electric Conduction in Semiconductors and Metals," Oxford Press (1958).
10. E. Matovich and R. J. Andres, *This Journal*, **108**, 177C (1961), Abstract 137.
11. D. Kahng, R. C. Manz, M. M. Atalla, and C. O. Thomas, *ibid.*, **108**, 177C (1961), Abstract 135.
12. C. O. Thomas, D. Kahng, and R. C. Manz, *ibid.*, **109**, 1055 (1962).
13. D. Kahng, C. O. Thomas, and R. C. Manz, *ibid.*, **110**, 394 (1963).
14. B. Goldstein, *ibid.*, **118**, 1024 (1960).

The Determination of the Density of Ta, Nb, and Anodically Formed Ta_2O_5 and Nb_2O_5

A. J. Schrijner and A. Middelhoek

N. V. Philips Gloeilampenfabrieken, Zwolle, The Netherlands

ABSTRACT

By refining a method used by Young we have determined the density of Ta, Nb, Ta_2O_5, and Nb_2O_5. It has been found that the forming electrolyte has some influence on the density of the Ta_2O_5 formed by anodizing. This can be interpreted by assuming that some electrolyte has been built in.

In investigations of the anodic oxidation of metals the density of the oxide film plays an important role, *e.g.*, it can be used to determine the thickness of the oxide layer.

In an article by Young (1) a method is given to determine the density of anodically formed Ta_2O_5 without separating the oxide layer from the base metal. The method consists of weighing a piece of Ta foil in air and under water before and after forming of the oxide layer.

A disadvantage of Young's method is that a small surface area (~100 cm^2 foil) is used which results in a low accuracy. This article describes a variation on this method which gives a greater accuracy as a sintered slug with a larger surface area is employed.

Experimental Procedure

The Ta and Nb anodes listed in Table I were used. The surface area of such a Ta anode is about 400 cm^2 and of the Nb anode about 450 cm^2. To enlarge the surface area five anodes were welded to a common Ta wire. This assembly is called a group. The following groups were used: 4 groups of Ta anodes (I, II, III, IV), 4 groups of Nb anodes (V, VI, VII, VIII), and combinations of groups I+II, III+IV, V+VI, and VII+VIII.

Table I. Ta and Nb anodes used

	Ta	Nb
Powder weight, g	3.00	2.00
Diameter (pressed), mm	6.6	6.6
Length (pressed), mm	10.2	13.0
Green density, g/ml	8.7	4.6
Wire diameter, mm	0.8	0.8
Sintering conditions	1 hr 2000°C	30 min 1700°C

The determinations mentioned below were made by means of a Mettler B6 balance with a reproducibility of 0.03 mg. The groups were degreased and then dried to a constant weight. After the determination of the "dry" weight the groups were impregnated in water to a constant weight.The "wet" weight determinations were made by suspending the groups to the balance by means of a thin nylon wire, so that the groups did not at all emerge from the water. After impregnation all the groups remained under water.

To determine the density of the water during the wet weighings it is necessary to measure the temperature of the water.

Forming Procedure

In the case of Ta, two different electrolytes were used, *viz.*, a very dilute type (0.01% HNO_3) and a concentrated type (50% H_2SO_4).[1] The purpose was to detect whether the density of the Ta_2O_5 films depends on the type of electrolyte.

In the literature no value has been published for the density of anodically formed Nb_2O_5; it is the purpose of this paper to determine this value.

The groups were formed with a constant current to 100v resp. 150v, thereupon they were formed at a constant voltage to a final current of 8 ma/group resp. 15 ma/group.

After forming the anodes were rinsed for 15 hr in deionized water and dried to a constant weight. Hereafter the dry and wet weighing process was repeated.

List of Symbols

A	"Dry" weight of a Ta or Nb group.
B	"Wet" weight of a Ta or Nb group.
a	"Dry" weight of a $(Ta + Ta_2O_5)$ c.q. $(Nb + Nb_2O_5)$ group.
b	"Wet" weight of a $(Ta + Ta_2O_5)$ c.q. $(Nb + Nb_2O_5)$ group.
ρ_{Ta}	density of Ta.
ρ_{Nb}	density of Nb.
ρ_w	density of water.
$M_{Ta_2O_5}$	molecular weight of Ta_2O_5.
$M_{Nb_2O_5}$	molecular weight of Nb_2O_5.
M_O	atomic weight of oxygen.
M_{Ta}	atomic weight of Ta.
M_{Nb}	atomic weight of Nb.

The density of Ta or Nb can be calculated by means of the formula

$$\rho_{Ta\ Nb} = \frac{A\rho_w}{A - B}$$

The formula for the calculation of $\rho_{Ta_2O_5}$ c.q. $\rho_{Nb_2O_5}$ is somewhat more complicated. It can be derived in the following way

$$\rho_{Ta_2O_5} = \frac{\text{weight } Ta_2O_5}{\text{volume } Ta_2O_5}$$

The weight of Ta_2O_5 can be found from the difference in dry weight of a group before and after forming:

[1] Weight per cent.

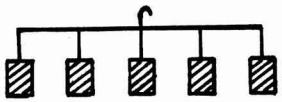

Fig. 1. Assembly of anodes

Table II. Forming conditions

	Ta anodes		Nb anodes
Numbers of the groups	I + II	III + IV	V + VI + VII + VIII
Forming electrolyte and concentration	HNO_3 0.01%	H_2SO_4 50%	H_3PO_4 0.1%
Forming current per group temperature of the forming bath	35 ma 17°-20°C	35 ma 17°-20°C	100 ma 17°-20°C
Formed with constant current to	100v	100v	150v
Formed to final current	8 ma/group	8 ma/group	15 ma/group

$a - A$. This difference equals the weight of the oxygen in the oxide film. Assuming that the oxide is Ta_2O_5 we find for the weight of the Ta_2O_5

$$\frac{M_{Ta_2O_5}}{5M_o}(a - A)$$

The volume of the Ta_2O_5 is equal to the volume of $(Ta + Ta_2O_5)$ minus the initial volume of Ta, and plus the volume of Ta which has been transformed in Ta_2O_5. So we find

$$\text{Volume } Ta_2O_5 = \frac{a - b}{\rho_w} - \frac{A - B}{\rho_w} + \frac{(a - A)2M_{Ta}/5M_o}{A/A - B\,\rho_w}$$

Hence, the density of Ta_2O_5 is

$$\rho_{Ta_2O_5} = \frac{\frac{M_{Ta_2O_5}}{5M_o}(a - A)}{\frac{a - b}{\rho_w} - \frac{A - B}{\rho_w} + \frac{(a - A)(A - B)}{A\,\rho_w}\frac{2M_{Ta}}{5M_o}}$$

To calculate $\rho_{Nb_2O_5}$ the same formula is used, except that $M_{Ta_2O_5}$ is replaced by $M_{Nb_2O_5}$ and M_{Ta} by M_{Nb}.

Corrections

The wet weight B and b have to be corrected for the weight of the nylon wire. The dry weight of the nylon wire was subtracted from all wet weights, which in turn necessitates a correction x for that portion of the wire which was immersed in the water.

The correction x consists of two parts p and q. The correction for the buoyancy of the part of the nylon wire which is immersed in the water is called p. In the experiment this part is kept as small as possible. The physical interpretation of q is more complicated; it is connected with the creeping up of the electrolyte on the nylon wire. Therefore

$$B = B_1 + (p + q)$$

where B_1 is the wet weight of a group and the dry weight of the nylon wire.

$$B^{I} = B_1{}^{I} + (p + q)$$

$$B^{II} = B_1{}^{II} + (p + q)$$

and

$$B^{I+II} = B_1{}^{I+II} + (p + q)$$

in which I and II denote the group number. Thus

$$B^{I} + B^{II} - B^{I+II} = B_1{}^{I} + B_1{}^{II} - B_1{}^{I+II} + (p + q)$$

Now it is clear that

$$B^{I} + B^{II} - B^{I+II} = 0$$

Further, we define x as follows

$$x = B_1{}^{I} + B_1{}^{II} - B_1{}^{I+II}$$

Therefore:

$$O = x + (p + q)$$

$$x = -(p + q)$$

so:

$$B = B_1 - x$$

Table III. Density of Ta, Nb, Ta_2O_5, and Nb_2O_5

Group	Density Ta	Density Ta_2O_5	Group	Density Nb	Density Nb_2O_5
I	16.596	8.034	V	8.576	4.750
II	16.594	8.049	VI	8.577	4.743
I+II	16.596	8.034	V+VI	8.576	4.752
III	16.599	7.853	VII	8.578	4.734
IV	16.600	7.892	VIII	8.578	4.735
III+IV	16.600	7.861	VII+VIII	8.577	4.734
Mean	16.598	8.039* 7.869†	Mean	8.577	4.741

* Density of Ta_2O_5 formed in 0.01% HNO_3.
† Density of Ta_2O_5 formed in 50% H_2SO_4.

Table IV. Standard deviations and standard deviations of the mean calculated from the results

	Density Ta	Density Ta_2O_5 0.01% HNO_3	Density Ta_2O_5 50% H_2SO_4	Density Nb	Density Nb_2O_5
S	0.003	0.009	0.021	0.001	0.008
S_m	0.001	0.005	0.012	0.0005	0.003

As it appeared from the experiment that x is positive, q has to be negative and $-q > p$.

Results

The results of the experiment are collected in Table III. It appears that the density of Ta_2O_5 formed in 0.01% HNO_3, differs appreciably from the density of Ta_2O_5 formed in 50% H_2SO_4. The densities of Ta and Nb metal, determined in this manner, are in good agreement with those found in literature.

The calculated standard deviations (S) of these series and the standard deviation of the mean (S_m) are reported in Table IV. The standard deviations of the density of the metals are lower than those of the oxides. This is so because the weight of the oxide is found as a small difference of two large weights. To increase the accuracy it is necessary to take a large surface area with respect to the metal volume. The standard deviations are in good agreement with the standard deviations which can be calculated from the weighing results.

Conclusions

1. For the density of Ta we find 16.598 ± 0.001 g/ml which is in good agreement with literature data mentioned below. So we may say that the porous anodes are totally impregnated in the case of the wet weighings.

2. It appears that the density of anodically formed Ta_2O_5 depends on the forming electrolyte. For dilute electrolytes we find:

Ta formed in 0.01% HNO_3 : $\rho_{Ta_2O_5} = 8.039 \pm 0.005$ g/ml
Ta formed in 0.1% H_3PO_4 : $\rho_{Ta_2O_5} = 8.03 \pm 0.04$ g/ml
Ta formed in 1% H_3SO_4 : $\rho_{Ta_2O_5} = 8.01 \pm 3\%$ g/ml[2]

For Ta formed in a concentrated electrolyte (50% H_2SO_4) we find

$$\rho_{Ta_2O_5} = 7.87 \pm 0.01 \text{ g/ml}$$

This shows that in concentrated H_2SO_4 the density is much lower than in dilute solutions which can be interpreted by assuming that some electrolyte has been "built in" when forming takes place in concentrated sulfuric acid. Additional evidence can be found in an article by Vermilyea (9) which states that in concentrated H_2SO_4 the apparent Faraday efficiency is much higher than 100%.

[2] Measured by Young.

3. For the density of Nb_2O_5 we find 4.741 ± 0.003 g/ml. This is much higher than the literature value mentioned below for amorphous Nb_2O_5 which has been prepared by hydrolysis of $NbCl_5$ in water and drying at 100°C.

Literature Data

A wide range of values for the density of Ta_2O_5 and Nb_2O_5 is found in literature.

1. In Gmelin-Kraut's Handbook (2) a broad spectrum of values is reported for the density of chemically prepared Ta_2O_5. The values given vary from 7.028 to 8.257 and concern amorphous, glassy, and crystalline oxides.

2. The "Handbook of Chemistry and Physics" (3) gives: $\rho_{Ta} = 16.6$ g/ml; $\rho_{Ta_2O_5} = 8.735$ g/ml (rhombic). Waber *et al.* (4) and Vermilyea (5) both used this value for the density of Ta_2O_5 in their studies on thermal and anodic oxide films. The source of this number is unknown but we found it in the International Critical Tables (6) from 1926 without further reference.

3. Güntherschulze (7): $\rho_{Ta_2O_5} = 8.27$ g/ml.

4. Reisman *et al.* (8): $\rho_{Ta_2O_5}(\beta) = 8.18$ g/ml; $\rho_{Ta_2O_5}(\alpha) = 8.37$ g/ml.

5. Young (1): $\rho_{Ta_2O_5} = 7.95$; 7.82; 8.25; 8.01 g/ml; or averaged $\rho_{Ta_2O_5} = 8.01$ g/ml. Young himself neglected the value 8.25 g/ml, hence his average is 7.93 ± 3% g/ml. He formed the Ta_2O_5 layer in approximately 1% H_2SO_4. This was the first time the density of anodically formed Ta_2O_5 was measured directly.

6. In an earlier experiment we found for Ta_2O_5 formed in 0.1% H_3PO_4: $\rho_{Ta_2O_5} = 8.03 \pm 0.04$ g/ml (estimated error).

7. Holtzberg *et al.* (10) give for Nb_2O_5: amorphous oxide, $\rho_{Nb_2O_5} = 4.36$ g/ml; crystalline oxide (γ), $\rho_{Nb_2O_5} = 5.17$ g/ml; crystalline oxide (α), $\rho_{Nb_2O_5} = 4.55$ g/ml.

8. The "Handbook of Chemistry and Physics" (3): $\rho_{Nb} = 8.55$ g/ml, $\rho_{Nb_2O_5} = 4.47$ g/ml (rhombic).

9. Kirk Othmer (11): $\rho_{Nb} = 8.57$ g/ml.

10. Gulbransen and Andrew (12): $\rho_{Nb_2O_5} = 4.95$ g/ml (crystalline).

The above data for $\rho_{Nb_2O_5}$ are commonly used for the density of the anodic oxide films.

Acknowledgment

The authors are greatly indebted to Mr. M. Vogels and Mr. A. Meyer for carrying out the experiments and part of the calculations and also for helpful discussions.

Manuscript received Dec. 20, 1963.

Any discussion of this paper will appear in a Discussion Section to be published in the June 1965 JOURNAL.

REFERENCES

1. L. Young, *Proc. Roy. Soc.*, **A244**, 41 (1958).
2. Gmelin-Kraut's "Handbuch der anorganischen Chemie," Band VI, Abteilung 1, pp. 291, 292 (1928).
3. "Handbook of Chemistry and Physics," C. D. Hodgman, Editor, 41st ed., pp. 617, 667, Chemical Rubber Publishing Co., Cleveland (1959).
4. J. T. Waber, G. E. Sturdy, E. M. Wise, and C. R. Tipton, Jr., *This Journal*, **99**, 121 (1952).
5. D. A. Vermilyea, *Acta Met.*, **1**, 282 (1953).
6. International Critical Tables, Vol. I, p. 135, McGraw-Hill Book Co., Inc., New York (1926).
7. A. Güntherschulze and H. Betz, "Elektrolytkondensatoren," 2nd ed., p. 89, Technischer Verlag Herbert Cram, Berlin (1952).
8. A. Reisman, F. Holtzberg, M. Berkenblit, and M. Berry, *J. Am. Chem. Soc.*, **78**, 4514 (1956).
9. D. A. Vermilyea, *Acta Met.*, **2**, 482 (1954).
10. F. Holtzberg, A. Reisman, M. Berry, and M. Berkenblit, *J. Am. Chem. Soc.*, **79**, 2039 (1957).
11. "Encyclopedia of Chemical Technology," vol. IV, R. E. Kirk and D. F. Othmer, Editors, p. 318, The Interscience Encyclopedia, Inc., New York (1954).
12. E. A. Gulbransen and K. F. Andrew, *This Journal*, **105**, 4 (1958).

Torsion Effusion Study of the Vapor Pressure and Heat of Sublimation of Gallium

Zuhair A. Munir and Alan W. Searcy

Department of Mineral Technology and Lawrence Radiation Laboratory, Inorganic Materials Research Division, University of California, Berkeley, California

ABSTRACT

The vapor pressure of gallium was measured by the torsion effusion method between 1174° and 1603°K. The pressure, in atmospheres, is given by the expression: $\log P = 5.5458 - (13\ 743/T)$ in that temperature range. The heat of sublimation of gallium is calculated by the third-law method to be 65.4 kcal. A second-law determination is in reasonable agreement.

Harteck (1) in 1928 and Speiser and Johnston (2) in 1952 measured the vapor pressure of gallium by the Knudsen effusion method with quartz effusion cells. However, more recently a mass spectrometric study (3) showed that gallium reacted with quartz, giving a considerable concentration of $Ga_2O(g)$ above 865°C. This evidence suggested that the reported gallium vapor pressures might be too high. To clarify the situation, Cochran and Foster (4) investigated the apparent vapor pressures of gallium in alumina Knudsen cells with and without added silica or magnesia. Apparent pressures obtained with silica added agreed well with the pressures of Speiser and Johnston, but pressures measured when only gallium was present were four- to fivefold lower. Cochran and Foster concluded that the previous studies in quartz cells were in error because the reaction $2Ga(l) + SiO_2(c) = SiO(g) + Ga_2O(g)$ yielded higher weight losses than did the direct vaporization of gallium.

At the time that the paper of Cochran and Foster appeared, we were engaged in a redetermination of the vapor pressure of gallium by the torsion effusion method (5-8) with use of a graphite cell. A mass spectrometer study by Drowart and Honig (9) had demonstrated that atomic gallium is the only major vapor species when gallium is heated in graphite. Nonetheless, the pressures measured in our research are in good agreement with the average of the data of Harteck and of Speiser and Johnston and thus are four to five times the pressures reported by Cochran and Foster.

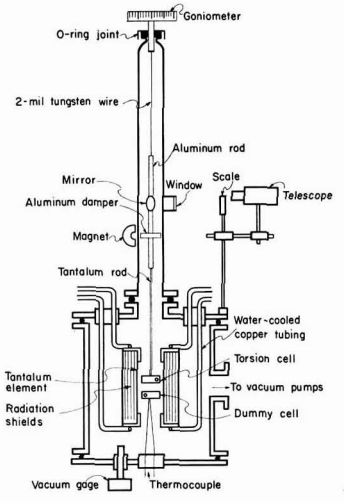

Fig. 1. Schematic diagram of torsion apparatus

Experimental

Figure 1 shows a schematic diagram of the torsion effusion apparatus. The vacuum chamber is a cylinder about 35 cm in diameter and about 46 cm long. In the center a 7.8 cm diameter cylinder of 0.5 mm tantalum sheet forms the heating element. Several layers of tantalum radiation shields are wrapped around this element. A glass tube of approximately 10 cm diameter and 92 cm length forms the upper part of the apparatus. Above this tube a goniometer acts as the anchor point for the suspension system by means of an aluminum rod which enters the top of the glass tube through an O-ring seal. A 0.05 mm diameter annealed tungsten wire 28 cm long hangs from the aluminum rod. To the lower end of the tungsten wire, a second aluminum rod is attached. A 1.3 cm diameter circular mirror is glued to this rod directly in front of a window which has an optically flat surface. An aluminum disk attached to the rod serves as a damper when a permanent magnet is placed near it. A 0.25 cm diameter tantalum rod is joined to the aluminum one, and the graphite torsion cell is rigidly attached to the bottom of this rod. During a run the cell hangs free in the center of the heating element.

The exterior cell dimensions were 2.5 x 1.3 x 1.3 cm. Two sets of orifices, one set of 6.3 mm^2 cross-sectional area and the other of 1 mm^2 area, were used.

Angular deflections resulting from the force of the effusing vapors were determined by returning the suspension system to its original (null) position. Measurements were made by sighting through a telescope on the mirror that reflects a scale placed outside the vacuum system just below the telescope. After returning the suspension assembly to its original position, deflection angles were read from the goniometer. With this arrangement, it was possible to measure angles to the nearest 0.01°. A vacuum of better than 10^{-5} mm Hg was maintained by means of an oil diffusion pump and a liquid nitrogen trap.

A 30-kva transformer supplied the power at a maximum of 10v. Temperature measurements were made by means of a calibrated 0.5 mm Pt-Pt + 10% Rh thermocouple. The thermocouple bead was inserted in a small hole in the bottom of a "dummy" graphite cell located 1.3 cm below the effusion cell. The freezing points of gold, silver, copper, and aluminum measured in the dummy cell in the furnace were used as standard points in the calibration of the thermocouple.

In order to verify the assumption that the temperature of the dummy cell was the same as that of the effusion cell for a given power setting, the dummy cell was moved up and down over a distance of 8 cm in the middle portion of the heating element. The temperature remained constant to within 3°. This experiment was repeated at different power inputs, and

Table I. Torsion cell constants

Cell	Orifice diameters, cm d_1	d_2	Mount arms, cm q_1	q_2	Orifice correction factors f_1	f_2	Orifice length-to-radius ratio l/r_1	l/r_2
1	0.2563	0.2436	1.2626	1.1216	0.840	0.827	0.539	0.589
2	0.1016	0.1001	1.1242	1.1221	0.7726	0.7359	1.05	0.985

the results were all identical. The thermocouple leads were led through a Kovar seal to the outside and were protected with alumina tubes. A mixture of ice and distilled water formed the cold junction, and the emf was measured by a potentiometer. The output of the thermocouple was fed to a strip chart recorder. Measurements were made only after the temperature had reached a constant value.

The gallium used was 99.97% pure material obtained from the Aluminum Company of America.

As a test of the apparatus, the vapor pressure of tin was redetermined. Results are described in the discussion section.

Results

Pressures were calculated from the equation

$$P = 2D\phi/(q_1 a_1 f_1 + q_2 a_2 f_2) \qquad [1]$$

where P is the vapor pressure, atm; D the torsion constant of the wire, dyn-cm; ϕ the angle of deflection, radians; q_1, q_2 perpendicular distances from the center of the effusion hole to the axis of rotation, cm; a_1, a_2 areas of effusion holes, cm^2; f_1, f_2 correction factors for finite orifice lengths (10, 11).

Constants for the two sets of cells used and for the torsion wire are summarized in Table I. A 2-mil tungsten wire with $D = 3.416$ was used for all runs. Figure 2 shows the agreement between pressures calculated with the two orifices. Data collected below 1200°K are clearly seen from Fig. 2 to be unreliable because the force of effusing vapor is too low for accurate measurement, and these data were not used in subsequent calculations.

The heat of sublimation ΔH_s was determined by using both the second- and third-law methods (12). Apparent pressures less than 10^{-6} atm were not used in making these calculations because background torsional effects obscured the lower pressure readings. An experimental investigation by Schulz (15) has shown that Eq. [1] can be used up to pressures for which the ratio of mean-free-path to orifice diameter becomes unity. From the diameters of the orifices and the van der Waals radius for gallium (13), this pressure is calculated to be about 10^{-2} atm. The highest pressure measured in this work was 8×10^{-4} atm.

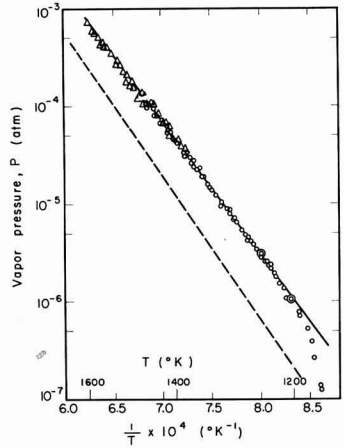

Fig. 2. Vapor pressure of gallium (*l*): ○, this work, orifice $d \approx 2.5$ mm; △, this work, orifice $d \approx 1.0$ mm; ——, Hultgren *et al.*, selected values (13); - -, Cochran and Foster (10).

Table II. Third law heats of sublimation of gallium (*l*)

T, °K	$-R\ln P$, cal/deg	$\Delta H°_{298}$ cal	T, °K	$-R\ln P$, cal/deg	$\Delta H°_{298}$ cal
		A. Cell 1			
1204	27.308	65 452	1326	22.414	65 392
1204	27.286	65 425	1326	22.429	65 412
1211	27.244	65 749	1333	22.281	65 552
1213	26.784	65 296	1336	22.089	65 429
1213	26.869	65 399	1340	21.909	65 388
1221	26.559	65 438	1350	21.594	65 430
1227	26.217	65 330	1352	21.569	65 488
1229	26.088	65 275	1355	21.152	65 070
1234	25.859	65 243	1360	21.269	65 451
1234	25.652	64 987	1366	21.139	65 563
1238	25.652	65 192	1367	20.812	65 154
1241	25.544	65 217	1370	20.964	65 507
1243	25.544	65 318	1374	20.707	65 335
1249	25.280	65 232	1382	20.381	65 248
1250	25.205	65 245	1384	20.572	65 602
1250	25.205	65 245	1386	20.406	65 462
1257	24.948	65 281	1390	20.203	65 374
1261	24.721	65 195	1398	19.848	65 236
1262	24.721	65 252	1403	19.831	65 442
1266	24.548	65 233	1405	19.836	65 536
1270	24.491	65 359	1410	19.453	65 224
1270	24.385	65 225	1416	19.408	65 422
1275	24.239	65 280	1416	19.473	65 514
1281	24.056	65 330	1419	19.195	65 258
1289	23.741	65 330	1426	19.134	65 482
1290	23.703	65 337	1429	18.934	65 334
1294	23.501	65 271	1435	19.037	65 740
1295	23.565	65 396	1440	18.710	65 493
1303	23.256	65 395	1446	18.724	65 770
1304	23.101	65 234	1448	18.404	65 393
1305	23.065	65 242	1455	18.225	65 437
1314	22.836	65 379	1459	18.416	65 900
1316	22.755	65 368	1465	18.223	65 887
1318	22.957	65 729	1466	17.879	65 417
		B. Cell 2			
1380	20.260	64 991	1491	17.361	65 716
1391	20.192	65 396	1495	17.041	65 403
1394	19.858	65 073	1498	17.253	65 852
1411	19.546	65 391	1506	16.787	65 493
1416	19.213	65 146	1508	17.044	65 961
1421	19.073	65 143	1513	16.579	65 471
1427	19.093	65 459	1519	16.299	65 287
1432	19.010	65 564	1529	16.246	65 620
1437	18.624	65 233	1530	16.047	65 363
1448	18.219	65 125	1544	15.730	65 446
1453	18.192	65 305	1556	15.433	65 486
1466	17.823	65 335	1561	15.411	65 654
1469	18.210	66 023	1566	15.263	65 626
1471	17.861	65 593	1567	15.350	65 794
1473	17.611	65 325	1575	15.034	65 622
1477	17.711	65 638	1585	14.824	65 690
1482	17.908	66 146	1588	14.770	65 729
1485	17.321	65 393	1603	14.310	65 588

Second-law calculation by the least-square method gave $\Delta H_T = 61.96$ kcal with a standard deviation of 0.24 kcal and $\Delta S_T = 24.34$ eu with a standard deviation of 0.17 eu. From this $\Delta H_{s,298} = 64.2$ kcal/mole. Third-law calculations based on free-energy functions selected by Hultgren (14) are given in Table II. The average value calculated for the heat of sublimation of gallium at 298°K from data collected with 2.5 mm diameter orifices is 65.39 kcal/mole and with 1.0 mm orifices is 65.50 kcal. The over-all average $\Delta H_{s,298}$ is 65.44 kcal/mole with an average deviation of 0.23 kcal. The third-law evaluation gave the following expression for the vapor pressure of gallium, in atmospheres, between 1174° and 1603°K:

$$\log P = 5.458 - 13\,743/T \qquad [2]$$

Discussion

Recent studies by Cochran and Foster (4) appeared to demonstrate conclusively that any studies of the vapor pressure of gallium that were carried out in the presence of silica are in error because of extensive reaction to yield volatile oxides. But the vapor pressures measured for gallium in the present investigation are higher by about a factor of four, than the vapor pressures reported by Cochran and Foster, and the heats of sublimation calculated from the data of the present research are in excellent agreement with the heat reported by Hultgren *et al.* (14) from analysis of the results of the two studies made with silica effusion cells.

The possibility of errors that could make the apparent pressures of the present investigation higher than the true pressures by a factor of four will be discussed, and then evidence for the possibility of error in the work of Cochran and Foster will be examined.

The factors that might cause systematically high apparent pressures in the present investigation are contribution to the vapor of products of reaction of gallium with the graphite effusion cell, faulty temperature calibration, faulty pressure calibration, and leakage of vapor through the cell wall. Strong evidence can be adduced that none of these factors caused the observed discrepancy.

The possibility that gaseous products of some reaction of gallium with the graphite of the effusion cell were formed in significant concentration is disproved by the mass spectrometer study by Drowart and Honig of the effusion of gallium from a graphite cell (9). No ions other than Ga^+, Ga_2O^+, and Ga_2^+ were observed. The GaO^+ and Ga_2^+ intensities rapidly decayed to negligible levels, indicating that these ions were produced from oxides that were introduced with the initial sample, but that were soon removed by heating.

The possibility of a temperature error in this work of more than 5° at most appears excluded by the calibration of the readings of the dummy cell against the melting points of four metals measured in the actual furnace in which the vapor pressure measurements were made. Furthermore, the furnace was demonstrated to have a uniform hot zone over the region in which the dummy cell and torsion effusion cell were placed. A temperature error of 90° would be required to introduce an error of a factor of four in the pressure measurements at the midpoint of the experimental range.

Evidence that the apparatus was calibrated correctly is provided by agreement to within 10% of the vapor pressure plot obtained for tin with this apparatus and the "best" vapor pressure curve for tin as selected by Hultgren *et al.* (14). From nineteen separate measurements of the vapor pressure of tin with two different wires that had torsion constants which differed by a factor of 18, the heat of sublimation of tin at 298°K is calculated to be 72.4 kcal compared to 72.2 kcal calculated by Hultgren *et al.* from previous work and compared to 71.8 kcal which was obtained by Schulz in an extensive study of the reliability and limitations of the torsion-effusion method for vapor pressure determinations (15).

To test the reliability of their apparatus and techniques, Cochran and Foster also studied the vapor pressure of tin. Their three pressure measurements lie considerably lower than the pressures calculated by Stull and Sink (16) or Hultgren *et al.* from evaluation of the data in the literature. We calculate from the Cochran and Foster data a heat of sublimation of tin at 298°K of 74.0 ± 0.6 kcal/mole.

Cochran and Foster commented that the vapor pressure data accepted by Stull and Sinke as the most reliable are probably in error because of unrecognized leakage through walls of the graphite crucibles that were used for the pressure studies.

There certainly is evidence that the quantity of metal that escapes from a graphite cell may sometimes be comparable to the quantity that escapes through an orifice of the dimensions normally employed in effusion studies (17). However, in the torsion-effusion method, if the cell side walls are uniform in thickness, the escape of molecules by leakage through the walls will contribute no net torque to the assembly. As part of his investigation Schulz heated tin in cells in which no orifices were drilled and found that no measurable torque was produced by any leakage that may have taken place (15).

While the present investigation of gallium did not include measurement of the torque produced when a sample was heated in a cell that had no orifices, the study did include measurement of the pressure with sets of orifices that had areas that differed by more than a factor of six. The calculated pressures agree within the small random scatter in data. If leakage contributed significantly to the torque, this excellent agreement between the pressures calculated with these two sets of orifices would not have been obtained.

The heat of sublimation for tin calculated from the data of Cochran and Foster is thus 1.8-2.2 kcal higher than the heats calculated from the best available studies. Similarly the heat of sublimation of silver calculated from three pressure measurements by Cochran and Foster is 0.9 kcal higher than the selected value of Hultgren *et al.* (14).

Gallium is more volatile than tin and less volatile than silver. The heat of sublimation for gallium calculated from the Cochran and Foster data can be expected to be subject to a systematic error in pressure determination that would contribute an error in the derived heat of sublimation of +1 to +2 kcal. Their heat of sublimation is 3.6 kcal higher than that found in the present work, so about half the discrepancy in results for gallium remains unaccounted for.

Furthermore, a systematic error in the measurements of Cochran and Foster would not invalidate their conclusion that in the presence of silica the weight loss is increased by a factor of four or five because of volatile oxide formation. Remaining to be explained, therefore, is the question of how the studies of Harteck (1) and of Speiser and Johnston (2) which were both conducted in silica cells, could agree with the results of the present investigation in graphite.

A possible explanation is that the surface area at which the heterogeneous reaction between the gallium and silica could occur in silica Knudsen cells is much smaller than the surface provided for reaction by the coarse silica powder added to the cells in the experiments of Cochran and Foster. As a result, although some reaction must have occurred in the silica cells, the extent of reaction may well have been considerably less than was measured in the experiments of Cochran and Foster.

This hypothesis is substantiated by the results of the mass spectrometer study of gallium vaporization from a silica cell. The observed intensity ratio Ga^+/Ga_2O^+ was about 10/1 at 1140° to 1300°K (3). From the assumptions normally applied to calculate pressures from ion intensities and usually claimed to be correct to within a factor of two (18), these intensities would yield a Ga/Ga_2O pressure ratio of 22/1. The heat of sublimation calculated for gallium by a third-law method from weight losses measured at 1300°K and with the assumption that the total weight loss was of elemental gallium would be low only by about 0.3 kcal because of neglect of Ga_2O and SiO effusion.

The heat of formation calculated by Cochran and Foster from effusion studies with gallium-silica mixtures is in good agreement with the heats calculated from another study (19). This fact implies that their effusion studies were not subject to significant systematic errors. The possibility remains, therefore, that their results for gallium are more nearly correct than ours, but we conclude that the heat of sublimation of gallium obtained by the third-law method in the present investigation, 65.4 kcal/mole is probably correct to within ±1 kcal.

Acknowledgment

Dr. Lies N. Finnie provided valuable help and counsel during the preparation of this manuscript. The research was supported by the U.S. Atomic Energy Commission.

Manuscript received Nov. 4, 1963.

Any discussion of this paper will appear in a Discussion Section to be published in the June 1965 JOURNAL.

REFERENCES

1. P. Harteck, *Z. physik. Chem.*, **134**, 1 (1928).
2. R. Speiser and H. L. Johnston, *J. Am. Chem. Soc.*, **75**, 1469 (1952).
3. S. Antkiw and V. H. Dibeler, *J. Chem. Phys.*, **21**, 1890 (1953).
4. C. N. Cochran and L. M. Foster, *This Journal*, **109**, 144 (1962).
5. M. Volmer, *Z. physik. Chem.* (Bodenstein Festband), **1931**, 863.

6. K. Neumann and E. Völker, *Z. physik. Chem.*, **161A**, 33 (1932).
7. A. W. Searcy and R. D. Freeman, *J. Am. Chem. Soc.*, **76**, 5529 (1954).
8. J. L. Margrave, "Vapour Pressure," Chap. 10 in "Physico-Chemical Measurements at High Temperatures," J. O'M. Bockris, J. L. White, and J. D. Mackenzie, Editions, Butterworths Scientific Publications, London (1959).
9. J. Drowart and R. E. Honig, *Bull. Soc. Chim. Belges*, **66**, 411 (1957).
10. R. D. Freeman and A. W. Searcy, *J. Chem. Phys.*, **22**, 762 (1954).
11. D. A. Schulz and A. W. Searcy, *ibid.*, **36**, 3099 (1962).
12. R. Ackerman and R. Thorn, *Progr. Cer. Sci.*, **1**, 39 (1961).
13. L. Pauling, "Nature of the Chemical Bond," 3rd ed., Cornell University Press (1960).
14. R. Hultgren, R. L. Orr, P. D. Anderson, and K. K. Kelley, "Selected Values of Thermodynamic Properties of Metals and Alloys," John Wiley & Sons, Inc., New York (1963).
15. D. A. Schulz, Ph.D. Thesis, University of California, Berkeley, 1961 (unpublished).
16. R. D. Stull and G. Sinke, "Thermodynamic Properties of the Elements," American Chemical Society, Washington, D. C. (1956).
17. R. K. Edwards and J. H. Downing, *J. Phys. Chem.*, **59**, 1079 (1955).
18. J. W. Otvos and D. P. Stevenson, *J. Am. Chem. Soc.*, **78**, 546 (1956).
19. C. J. Frosch and C. D. Thurmond, *J. Phys. Chem.*, **66**, 877 (1962).

Methods for the Calculation of Polarization in Porous Electrodes

F. A. Posey

Chemistry Division, Oak Ridge National Laboratory, Oak Ridge, Tennessee

ABSTRACT

Solutions in closed form are presented for the polarization behavior and the distribution of current and potential in idealized, one-dimensional porous electrodes in the case of a simple oxidation-reduction reaction under pure activation control. Exact solutions are derived for transfer coefficients of 1/3, 1/2, and 2/3 for electrodes of finite length, while solutions for semi-infinite electrodes are given for transfer coefficients of 1/4, 1/3, 1/2, 2/3, and 3/4. An approximate method for calculating current and potential distributions in porous electrodes is proposed which is valid for any value of the transfer coefficient, and exact and approximate solutions are compared.

Studies on the distribution of current and potential in porous electrodes have received considerable stimulus from the intensive development of fuel cells in recent years (1, 2). Porous electrodes are also widely used in battery technology and in the chemical process industries. The theory of electrochemical reactions at simple, planar electrodes having a well-defined interface has been developed extensively, and a comprehensive monograph is available (3). In contrast, the theory of the polarization behavior of porous electrodes is relatively less advanced because a number of factors which are unimportant or easily treated in the case of planar electrodes greatly complicate the calculation of reaction rates in porous electrodes. These factors include parameters pertaining to the physical structure of the electrode, such as the porosity, specific surface area, and conductivity of both solid and electrolyte phases.

A number of authors have reported solutions to the problem of the distribution of current and potential in porous or tubular electrodes (4-33). The generality of these solutions depends on the model adopted and on the assumptions or approximations made for each special case in order to obtain solutions in closed form. A one-dimensional model of porous electrodes is most frequently used; this choice avoids considerable mathematical difficulty and at the same time provides solutions which are in reasonable agreement with experiment. The one-dimensional model assumes a system of idealized, liquid-filled pores in an electronically conducting matrix together with uniform, average values of parameters such as porosity, specific surface area, resistivity, etc. The current or reaction rate, the interfacial potential difference, and the concentrations of reactants then vary throughout the length of the electrode in a manner determined by the physical parameters, the rate law for reaction at the interface, mass transfer conditions, and initial and boundary conditions.

The fundamental differential equation governing the distribution of potential in porous electrodes was derived by Daniel'-Bek (4). This equation, a Poisson-type relation, has since been integrated for a number of important cases occurring in the operation of porous electrodes. In the case of constant reactant concentrations throughout the length of the porous electrode, solutions for the polarization characteristics and for the distribution of current and potential may be classified according to the type of electrochemical reaction rate law assumed and the type of electrode, *i.e.*, whether the electrode is finite or semi-infinite. In general, the boundary conditions for semi-infinite electrodes are simpler than those for electrodes of finite length, and the solutions are correspondingly simpler in form. The reaction rate law, or the relation between the current density of the interfacial electrochemical reactions and the interfacial potential difference at any point in the electrode, has been used in three different forms: (*a*) current density depends linearly on potential difference (or overpotential), the linear law; (*b*) current density depends exponentially on potential difference, the exponential (or Tafel) law; and (*c*) current density is a more general function of overpotential, the general or exact law. Cases (*a*) and (*b*) are special cases of the general law (*c*) which considers both forward and reverse rates of the partial processes in the usual manner (3). For the linear law, solutions for the semi-infinite electrode are given by Frumkin (5), Buvet, Guillou, and Warszawski (21), and Guillou and Buvet (30), while solutions for the finite electrode are due to Daniel'-Bek (4), Euler and Nonnenmacher (16), and Newman and Tobias (20). In the case of the exponential law, the semi-infinite electrode is treated by Ksenzhek (17) for the case of diffusion supply of reagents, and solutions for the finite electrode are given by Daniel'-Bek (4) and Newman and Tobias (20). General solutions, those valid for both large and small values of polarization for reactions under pure activation control, are reported only for the case of a symmetrical polarization law, *i.e.*, the transfer coefficient equals 1/2. General solutions of this type for the semi-infinite electrode are given by Frumkin (5) and

Ksenzhek and Stender (8, 9), while general solutions for the finite electrode are due to Ksenzhek (18) and Winsel (19).

In addition to the previous work, other solutions for special cases in the operation of porous electrodes are available. The polarization resistance of finite electrodes with a linear polarization law and forced solution flow is given by Perskaya and Zaidenman (11, 13, 14). Tubular electrodes are specifically considered by Frumkin (5), Ksenzhek and Stender (9), Mueller (27), and Blaedel, Olson, and Sharma (33). Operation of porous electrodes in a steady state with diffusion supply of reagents and with forced supply is treated by Ksenzhek (17) and Gurevich and Bagotskii (24, 25, 26). Potentiostatic and galvanostatic transient discharge characteristics of porous electrodes are treated according to special models by Euler (22) and Winsel (19). Response of porous electrodes to alternating current is considered by Ksenzhek and Stender (9), Winsel (19), and de Levie (31). The determination of the specific surface area of porous electrodes by measurement of interfacial capacity using a-c and d-c methods is treated by Ksenzhek and Stender (7), Ksenzhek (28), and de Levie (31). Ksenzhek (10) gives an interpretation of the meaning of activation energy measurements on porous electrodes. Euler (29) and de Levie (31) discuss the influence of diffusion. Euler and Müller (32) consider the accuracy to which distributions of current and potential can be calculated. Winsel (19) reports a general method for the calculation of potential and current distribution in idealized, cylindrical pores which considers the effect of cylindrical symmetry. Mueller (27) employs the equations for current and potential distribution in tubes to calculate the throwing power in anodic and cathodic protection of pipes.

This paper presents solutions to the problem of the distribution of current and potential in porous electrodes for the case of unsymmetrical rate laws having certain values of the transfer coefficient.[1] Solutions in closed form are given for transfer coefficients of 1/3, 1/2, and 2/3 for an electrode of finite length, while solutions for the semi-infinite electrode are given for transfer coefficients of 1/4, 1/3, 1/2, 2/3, and 3/4.[2] Dimensionless parameters are used for economy of notation and ease in the comparison of solutions. In addition, an approximate method for calculating current and potential distributions in porous electrodes is proposed which is valid for any value of the transfer coefficient.

Fundamental Equations and Transformation to Dimensionless Form

A schematic diagram of an idealized, one-dimensional porous electrode is shown in Fig. 1. The total current, i, flows from the polarizing electrode into the pores of the porous electrode of length, l. Because of the finite conductivity of the solution phase, the passage of current introduces a gradient of the potential in the solution phase, $\phi_s(x)$, throughout the length of the pores. As a consequence, the interfacial potential difference, $\Delta\phi(x) = \phi_M - \phi_s(x)$, varies and with it the current density of the electrochemical reactions occurring at the interface between solid and liquid phases, $j(x)$. Since the resistivity of the metallic phase is assumed negligible, ϕ_M is constant and $j(x)$ is largest near $x = 0$.

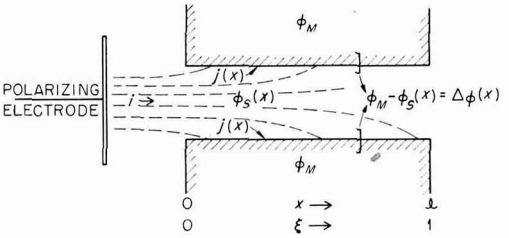

Fig. 1. Schematic diagram of idealized, one-dimensional porous electrode.

The rate law for reaction at the interface is assumed to be given by Eq. [1], which is of the conventional form for a simple oxidation-reduction reaction under pure activation control (3). In Eq. [1], j_o is the exchange current density of the reaction at the reversible potential ($\Delta\phi_o$), β is the transfer coefficient ($0 < \beta < 1$), RT/F is the thermal volt equivalent, and $\eta(x) = \Delta\phi(x) - \Delta\phi_o$ is the overpotential. The total current is obtained by integrating the current density over the length of the electrode, according to Eq. [2]. In Eq. [2], S is the surface area of the porous electrode per unit length. The gradient of potential in the solution phase and the gradient of the overpotential are given by Eq. [3] obtained from Ohm's law, in which A is the average cross-sectional area of the electrolyte in the electrode and σ is the specific conductance of the solution. Differentiation of Eq. [3] leads to Eq. [4], which is Daniel'-Bek's fundamental relation (4) for the distribution of potential in porous and tubular electrodes.

$$j(x) = j_o \left\{ \exp\left[+ \frac{\beta F \eta(x)}{RT} \right] - \exp\left[- \frac{(1-\beta) F \eta(x)}{RT} \right] \right\} \quad [1]$$

$$i = S \int_o^l j(x)\, dx \quad [2]$$

$$\frac{1}{A}\left[i - S \int_o^x j(x)\, dx \right] = \sigma \frac{d\phi_s(x)}{dx} = -\sigma \frac{d\eta(x)}{dx} \quad [3]$$

$$\frac{d^2\eta(x)}{dx^2} = \frac{S}{\sigma A} j(x) \quad [4]$$

A simplified notation is obtained if some of the parameters in the preceding equations are converted to dimensionless form. A reduced length is defined by $\xi = x/l$ (cf. Fig. 1); a relative or reduced current density or reaction rate is defined by $\rho(\xi) = j(\xi)/j_o$; a reduced total current is given by $I = i/i_o$, where $i_o = Slj_o$ is the exchange current of the electrode; $\kappa = (i_o l F)/(\sigma A R T)$ is a resistance parameter which is essentially a ratio of solution impedance to interfacial impedance; and $\phi(\xi) = [F\eta(\xi)]/RT$ is a reduced overpotential. In this notation, the fundamental relations of Eq. [1]-[4] are replaced by Eq. [5]-[8].

$$\rho(\xi) = e^{+\beta\phi(\xi)} - e^{-(1-\beta)\phi(\xi)} \quad [5]$$

$$I = \int_o^1 \rho(\xi)\, d\xi \quad [6]$$

$$\frac{d\phi(\xi)}{d\xi} = -\kappa \left[I - \int_o^\xi \rho(\xi)\, d(\xi) \right] \quad [7]$$

$$\frac{d^2\phi(\xi)}{d\xi^2} = \kappa\rho(\xi) \quad [8]$$

[1] It is assumed throughout this paper that the resistivity of the metallic phase is negligible compared to that of the liquid phase. Situations where the resistivities of the phases are comparable are discussed by Daniel'-Bek (4), Ksenzhek and Stender (8), Euler and Nonnenmacher (16), Newman and Tobias (20), and Euler (22). The effects of concentration polarization and of changes of reactant concentrations with time are not considered. These solutions therefore apply most directly to two situations: (a) the distribution of current and potential in a porous electrode during the first moments following the application of a current, before significant changes in reactant concentrations occur; (b) the distribution obtained with a flow of solution through the electrode so large that concentration changes due to the electrochemical reaction are negligible.

[2] The solutions for a transfer coefficient of 1/2 are the same or alternative forms of those of Frumkin (5), Ksenzhek and Stender (8, 9), Ksenzhek (18), and Winsel (19). They are included here for the sake of completeness and for comparative purposes.

The distribution of potential is obtained by integration of Eq. [8] subject to the boundary conditions

$$\left(\frac{d\phi(\xi)}{d\xi}\right)_{\xi=0} = -\kappa I; \left(\frac{d\phi(\xi)}{d\xi}\right)_{\xi=1} = 0$$

The distribution of (relative) current density is then calculable from Eq. [5] and the total current follows from Eq. [6] or by use of the boundary condition at $\xi = 0$.

A first integration of Eq. [8] leads to Eq. [9], where the

$$\frac{d\phi(\xi)}{d\xi} = -(2\kappa)^{1/2}\left\{\frac{1}{\beta}[e^{+\beta\phi(\xi)} - e^{+\beta\phi(1)}] + \frac{1}{(1-\beta)}[e^{-(1-\beta)\phi(\xi)} - e^{-(1-\beta)\phi(1)}]\right\}^{1/2} \quad [9]$$

boundary condition for $\xi = 1$ is used to evaluate the integration constant. Equation [9] and the boundary condition at $\xi = 0$ lead to Eq. [10], an expression

$$I = \left(\frac{2}{\kappa}\right)^{1/2}\left\{\frac{1}{\beta}[e^{+\beta\phi(0)} - e^{+\beta\phi(1)}] + \frac{1}{(1-\beta)}[e^{-(1-\beta)\phi(0)} - e^{-(1-\beta)\phi(1)}]\right\}^{1/2} \quad [10]$$

for the (reduced) total current. For large anodic polarization, if $\phi(0) >> \phi(1)$, Eq. [10] reduces to Eq. [11], which is the equation for the anodic Tafel

$$I = \left(\frac{2}{\beta\kappa}\right)^{1/2} e^{+\beta\phi(0)/2} \quad [11]$$

line of porous electrodes having a highly nonuniform current distribution. The slope of the Tafel line, $d\phi(0)/d\ln I$, equals $2/\beta$, or twice the slope of the Tafel line for the same reaction on a planar electrode. The intercept at $\phi(0) = 0$ is a function of both the transfer coefficient (β) and the resistance parameter (κ).

Evaluation of the potential distribution is accomplished by integration of Eq. [9], which may be rearranged into the form of Eq. [12].

$$\frac{d\phi(\xi)}{\left\{\frac{1}{\beta}[e^{+\beta\phi(\xi)} - e^{+\beta\phi(1)}] + \frac{1}{(1-\beta)}[e^{-(1-\beta)\phi(\xi)} - e^{-(1-\beta)\phi(1)}]\right\}^{1/2}} = -(2\kappa)^{1/2}\,d\xi \quad [12]$$

Expressions equivalent to Eq. [12] were solved by Ksenzhek (18) and Winsel (19) for $\beta = 1/2$, the case of the symmetrical rate law. Solutions in closed form may also be obtained for certain other values of β, and these are presented below.

The Finite Electrode

The substitutions, $y = \exp\{1/2[\phi(\xi) - \phi(1)]\}$ for $\beta = 1/2$, or $y = \exp\{1/3[\phi(\xi) - \phi(1)]\}$ for $\beta = 1/3$ or $2/3$, transform Eq. [12] into integrable expressions. Integration of the resulting equations is accomplished by use of Jacobian elliptic functions and integrals (34). Table I presents equations derived in this manner for the potential distribution in finite electrodes for the cases, $\beta = 1/3$, $1/2$, and $2/3$. Elliptic functions used in Table I and elsewhere are defined below in the list of Symbols. Alternative forms of Eq. [13] are given by Ksenzhek (18) and Winsel (19). In order to compute potential distributions, values of u, the *incomplete elliptic integral* of the first kind, and of k, the modulus, are obtained from the expressions in the third and fourth columns of Table I as a function of $\phi(1)$. Values of $\phi(\xi)$ may then be calculated from the formulas in the second column, with the aid of tables of the Jacobian elliptic functions (35).

The total current may be calculated from Eq. [10] and values of $\phi(0)$ and $\phi(1)$ obtained from Eq. [13], [14], or [15] of Table I, or from the formulas of Table II. Three types of polarization curves may be computed from the equations of Table II; I may be evaluated as a function of $\phi(0)$, of $\phi(1)$, or of $\phi(0) - \phi(1)$. A family of curves corresponding to Eq. [16] is presented below.

The Semi-Infinite Electrode

Relations for the potential distribution in semi-infinite porous electrodes may be derived from the equations presented above with a modified notation. On replacing the length variable for finite electrodes, ξ, by the distance, x, Eq. [5]-[8] are transformed into Eq. [19]-[22]. The resistance parameter κ' in Eq. [21] and [22] replaces κ of

$$\rho(x) = e^{+\beta\phi(x)} - e^{-(1-\beta)\phi(x)} \quad [19]$$

$$I' = \int_o^\infty \rho(x)\,dx \quad [20]$$

$$\frac{d\phi(x)}{dx} = -\kappa'\left[I' - \int_o^x \rho(x)\,dx\right] \quad [21]$$

$$\frac{d^2\phi(x)}{dx^2} = \kappa'\rho(x) \quad [22]$$

Eq. [7] and [8]; $\kappa' = (j_o SF)/(\sigma ART)$ is a resistance parameter for semi-infinite electrodes. The (reduced) total current [$I' = i/(Sj_o)$] has the dimensions of a

Table I. Equations for the calculation of potential distributions in porous electrodes of finite length for transfer coefficients of 1/3, 1/2, and 2/3

β	y (Potential Distribution)	u	k^2	Equation No.
1/2	$\exp\{1/2[\phi(\xi) - \phi(1)]\} = \dfrac{dn^2(u,k)}{cn^2(u,k)}$	$\dfrac{(1-\xi)\kappa^{1/2}}{2} e^{+\phi(1)/4}$	$e^{-\phi(1)}$	[13]
1/3	$\exp\{1/3[\phi(\xi) - \phi(1)]\} = \dfrac{1-\gamma sn^2(u,k)}{cn^2(u,k)}$ *	$\dfrac{(1-\xi)\kappa^{1/2}}{2k\sqrt{3}} e^{-\phi(1)/3}(1+8e^{+\phi(1)})^{1/4}$	$\dfrac{2e^{-\phi(1)}[1+8e^{+\phi(1)}]^{1/2}}{4-e^{-\phi(1)}\{1-[1+8e^{+\phi(1)}]^{1/2}\}}$	[14]
2/3	$\exp\{1/3[\phi(\xi) - \phi(1)]\} = \dfrac{dn^2(u,k)}{1-\delta sn^2(u,k)}$ *	$\dfrac{(1-\xi)\kappa^{1/2}}{2\sqrt{3}} e^{+\phi(1)/3}(1+8e^{-\phi(1)})^{1/4}$	$\dfrac{4e^{-\phi(1)} - 1 + [1+8e^{-\phi(1)}]^{1/2}}{2[1+8e^{-\phi(1)}]^{1/2}}$	[15]

* $\gamma = (1/4)\,e^{-\phi(1)}\{1+[1+8e^{+\phi(1)}]^{1/2}\}$; $\delta = \dfrac{3+[1+8e^{-\phi(1)}]^{1/2}}{2[1+8e^{-\phi(1)}]^{1/2}}$.

Table II. Equations for the calculation of polarization curves of porous electrodes of finite length for transfer coefficients of 1/3, 1/2, and 2/3

β	Polarization Equation*	Equation No.
1/2	$I = \frac{2}{(\kappa)^{1/2}} e^{+\phi(1)/4} \frac{(k')^2 sn\,(u_o,k)}{dn\,(u_o,k)}$	[16]
1/3	$I = \frac{\sqrt{3}\, e^{+\phi(1)/6}}{\sqrt{2}\,(\kappa)^{1/2}} \{4 - e^{-\phi(1)}(1-[1+8e^{+\phi(1)}]^{1/2})\}^{1/2}(1-\gamma)\, tn\,(u_o,k)\, dn\,(u_o,k)$	[17]
2/3	$I = \frac{\sqrt{3}\, e^{+\phi(1)/3}}{(\kappa)^{1/2}} [1+8e^{-\phi(1)}]^{1/4} \frac{(\delta - k^2)\, sd\,(u_o,k)\, cn\,(u_o,k)}{1-\delta\, sn^2\,(u_o,k)}$	[18]

* Values of u_o and k are given by the formulas in Table I for $\xi = 0$; γ and δ are defined in the footnote to Table I.

length and is equal to the current divided by the exchange current per unit length of electrode. The potential distribution is obtained on integration of Eq. [22] with the revised boundary conditions

$$\left(\frac{d\phi(x)}{dx}\right)_{x=0} = -\kappa' I';\ \phi(\infty) = 0$$

A first integration of Eq. [22], with use of the boundary condition, $\phi(\infty) = 0$, leads to Eq. [23], which is similar in form to Eq. [9].

$$\frac{d\phi(x)}{dx} = -(2\kappa')^{1/2} \left\{\frac{1}{\beta}[e^{+\beta\phi(x)} - 1] + \frac{1}{(1-\beta)}[e^{-(1-\beta)\phi(x)} - 1]\right\}^{1/2} \quad [23]$$

Use of the boundary condition at $x = 0$ with Eq. [23] leads to Eq. [24]

$$I' = \left(\frac{2}{\kappa'}\right)^{1/2} \left\{\frac{1}{\beta}[e^{+\beta\phi(0)} - 1] + \frac{1}{(1-\beta)}[e^{-(1-\beta)\phi(0)} - 1]\right\}^{1/2} \quad [24]$$

for the total current. This equation is quite general for the polarization behavior of the semi-infinite electrode having the rate law of Eq. [19]; it is valid for any value of the transfer coefficient $\beta\,(0 < \beta < 1)$. An equation for the anodic Tafel line of the semi-infinite electrode is obtained from Eq. [24] for large $\phi(0)$. This relation is given in Eq. [25]

$$I' = \left(\frac{2}{\beta\kappa'}\right)^{1/2} e^{+\beta\phi(0)/2} \quad [25]$$

which is of the same form as Eq. [11]. Separation of the variables in Eq. [23] leads to Eq. [26], the counterpart of Eq. [12]. Relations

$$\frac{d\phi(x)}{\left\{\frac{1}{\beta}[e^{+\beta\phi(x)} - 1] + \frac{1}{(1-\beta)}[e^{-(1-\beta)\phi(x)} - 1]\right\}^{1/2}} = -(2\kappa')^{1/2} dx \quad [26]$$

corresponding to Eq. [26] were integrated by Frumkin (5) and Ksenzhek and Stender (8, 9) for the case of the symmetrical rate law ($\beta = 1/2$). Other solutions in closed form for different values of β are given below.

The substitutions, $y = \exp[(1/2)\phi(\xi)]$ for $\beta = 1/2$, $y = \exp[(1/3)\phi(\xi)]$ for $\beta = 1/3$ or 2/3, or $y = \exp[(1/4)\phi(\xi)]$ for $\beta = 1/4$ or 3/4, transform Eq. [26] into integrable expressions. The resulting potential distributions may be calculated from the equations of Table III. Equation [27] is equivalent to the solutions reported by Frumkin (5) and Ksenzhek and Stender (8, 9). Polarization curves for these and other cases of the semi-infinite electrode may be calculated directly from Eq. [24]. The function $\pi\{u, \alpha^2/(\alpha^2 - 1)\}$ in Eq. [30] and [31] is Legendre's incomplete elliptic integral of the third kind (34, 36). The symbols $u_{1,0}$, $u_{2,0}$, and f_o denote values of the functions given in the footnote to Table III for $x = 0$.

An Approximate Method

The formulas presented in the previous sections provide exact solutions in closed form to the problem

Table III. Equations for the calculation of potential distributions in semi-infinite porous electrodes for transfer coefficients of 1/4, 1/3, 1/2, 2/3, and 3/4

β	Potential distribution function	Equation No.
1/2	$\tanh[\phi(x)/8] = \tanh[\phi(0)/8]\exp[-(\kappa')^{1/2} x]$	[27]
1/3	$\frac{(2\exp[\phi(x)/3]+1)^{1/2}-\sqrt{3}}{(2\exp[\phi(x)/3]+1)^{1/2}+\sqrt{3}} = \frac{(2\exp[\phi(0)/3]+1)^{1/2}-\sqrt{3}}{(2\exp[\phi(0)/3]+1)^{1/2}+\sqrt{3}} \exp[-(\kappa')^{1/2} x]$	[28]
2/3	$\frac{\exp[\phi(0)/3]-1}{\exp[\phi(x)/3]-1} = \frac{2\exp[\phi(0)/3]+1-\sqrt{3}\exp[\phi(0)/6](2+\exp[\phi(0)/3])^{1/2}}{2\exp[\phi(x)/3]+1-\sqrt{3}\exp[\phi(x)/6](2+\exp[\phi(x)/3])^{1/2}} \exp[-(\kappa')^{1/2} x]$	[29]
1/4	$(u_1 - u_{1,o}) + [1/(\alpha-1)][\pi\{u_1, \alpha^2/(\alpha^2-1)\} - \pi\{u_{1,o}, \alpha^2/(\alpha^2-1)\} + \alpha(f - f_o)] = \mu x^*$	[30]
3/4	$(u_2 - u_{2,o}) + [1/(\alpha-1)][\pi\{u_2, \alpha^2/(\alpha^2-1)\} - \pi\{u_{2,o}, \alpha^2/(\alpha^2-1)\} - \alpha(f - f_o)] = -\mu x^*$	[31]

* $cn\ u_1 = \frac{\sqrt{3}\exp[\phi(x)/4]-1}{\sqrt{3}\exp[\phi(x)/4]+1}$; $cn\ u_2 = \frac{\exp[\phi(x)/4]-\sqrt{3}}{\exp[\phi(x)/4]+\sqrt{3}}$; $\alpha = \frac{\sqrt{3}+1}{\sqrt{3}-1}$; $k^2 = \frac{\sqrt{3}-1}{2\sqrt{3}}$;

$\mu = \frac{\sqrt{3}+1}{3^{1/4}\sqrt{2}}(k')^{1/2}$; $f = \frac{1}{2}\left[\frac{\alpha^2-1}{k^2+(k')^2\alpha^2}\right]^{1/2} \ln\left[\frac{(\alpha^2-1)^{1/2}\, dn\, u + \{k^2+(k')^2\alpha^2\}^{1/2}\, sn\, u}{(\alpha^2-1)^{1/2}\, dn\, u - \{k^2+(k')^2\alpha^2\}^{1/2}\, sn\, u}\right]$

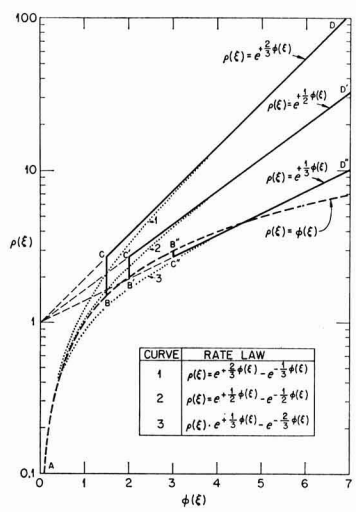

Fig. 2. Comparison of exact and approximate reaction rate laws for $\beta = 1/3, 1/2,$ and $2/3$.

of the distribution of current and potential in porous electrodes for several values of the transfer coefficient (β) in the rate laws of Eq [5] and [19]. Although these exact solutions should be useful for calculations on the operation of porous electrodes in the special cases for which they are valid, the computations are tedious. An approximate method of calculation is presented below which circumvents a great part of the arithmetical difficulty, but which provides approximate solutions which are in good agreement with the exact solutions.

The nature of the approximation is shown in Fig. 2 for $\beta = 1/3$, 1/2, and 2/3. Curves 1, 2, and 3 show the exact rate laws for $\beta = 2/3$, 1/2, and 1/3, respectively. The corresponding approximate rate laws are given by curves ABCD, AB'C'D', and AB''C''D''. The approximate rate law follows the linear polarization relation, $\rho(\xi) = \phi(\xi)$, up to the potential, $\phi(\xi_o)$, where a discontinuity transition (BC, B'C', and B''C'') occurs to the exponential rate law, $\rho(\xi) = \exp[\beta\phi(\xi)]$. At $\phi(\xi_o)$, the slopes of both linear and exponential rate laws in the plot of Fig. 2 are equal, and $\phi(\xi_o) = 1/\beta$. Equations for the polarization behavior and the distribution of current and potential in both finite and semi-infinite porous electrodes according to this approximation are presented below.

The Finite Electrode.[3]—Three special cases arise in the application of the approximate method to the finite electrode: (*a*) $\phi(\xi_o) = 1/\beta \geq \phi(0) > \phi(1) \geq 0$ (for anodic polarization), so that in this case the entire electrode operates with the linear rate law, $\rho(\xi) = \phi(\xi)$; (*b*) $\infty > \phi(0) > \phi(1) \geq \phi(\xi_o) = 1/\beta$, where the rate processes everywhere in the electrode follow the exponential law, $\rho(\xi) = \exp[\beta\phi(\xi)]$; and (*c*) $\phi(0) > \phi(\xi_o) > \phi(1)$, a transition region where $0 < \xi_o < 1$ and ξ_o is a function of $\phi(0)$.

For case (*a*), when $\phi(\xi_o) = 1/\beta \geq \phi(0) \geq 0$, integration of Eq. [8] with the linear rate law, $\rho(\xi) = \phi(\xi)$, leads to Eq. [32] and [33] of Table IV for the potential distribution and the polarization curve. The value of $\phi(0)$ when $\phi(1) = \phi(\xi_o) = 1/\beta$ may be determined from:

$$\phi(0) = \frac{2}{\beta} \ln \frac{\exp(1/2)}{\cos(\beta\kappa e/2)^{1/2}} \qquad (\xi_o = 1)$$

Therefore when $\phi(0)$ is greater than this value, Eq. [8] may be integrated with $\rho(\xi) = \exp[\beta\phi(\xi)]$ to give the potential distribution and polarization curve for case (*b*), Eq. [34] and [35] of Table IV.

The potential distribution functions and the polarization curve of case (*c*), when $0 < \xi_o < 1$ and $\phi(0) > \phi(\xi_o) = 1/\beta > \phi(1)$, are given by Eq. [36], [37], and [38] of Table IV. The distribution of Eq. [36] holds in the region $0 < \xi < \xi_o$, while Eq. [37] gives the distribution in the region $\xi_o < \xi < 1$. The parameter ξ_o may be computed from the relation given in Table IV as a function of $\phi(0)$. Once ξ_o is known, Eq. [36] and [37] are used to calculate $\phi(\xi)$ and the total current is calculated from Eq. [38].

The effect of the discontinuity in the rate law is averaged out to a considerable extent, so that potential distributions calculated in this manner are quite close to those found with the exact methods discussed previously. This averaging effect may be utilized further to calculate more precise values of the (reduced) reaction rate, $\rho(\xi)$, than would result from the use of the discontinuous rate law. For this calculation, the exact rate law of Eq. [5] is used with values of the potential, $\phi(\xi)$, calculated from Eq. [36] and [37]. By use of this technique, the major effect of the use of a discontinuous rate law appears in the calculated polarization curves rather than in the calculated potential and current distributions.

The Semi-infinite Electrode.[3]—The boundary conditions are somewhat simpler in the case of the semi-infinite electrode than for the finite electrode, and only

[3] Nearly all parameters used in this section and the next are defined above in the sections dealing with the exact treatment of the finite and semi-infinite electrodes; others are defined as they occur. The equations are derived for the case of anodic polarization; cathodic polarization may be treated similarly.

Table IV. Equations for the approximate calculation of potential distributions and polarization curves of porous electrodes of finite length

Case	Potential distribution	Equation No.	Polarization equation	Equation No.
(*a*) Linear law $1/\beta \geq \phi(0) > \phi(1) \geq 0$	$\phi(\xi) = \phi(0)\dfrac{\cosh[(\kappa)^{1/2}(1-\xi)]}{\cosh[(\kappa)^{1/2}]}$	[32]	$I = \dfrac{\phi(0)}{(\kappa)^{1/2}} \tanh(\kappa)^{1/2}$	[33]
(*b*) Exponential law $\infty > \phi(0) > \phi(1) \geq 1/\beta$	$\cos^{-1}\{\exp(-\beta/2[\phi(\xi) - \phi(1)])\} = \cos^{-1}\{\exp(-\beta/2[\phi(0) - \phi(1)])\} - [(\beta\kappa/2)e^{+\beta\phi(1)}]^{1/2}\xi$ where: $\exp[(\beta/2)\phi(0)] = \dfrac{\exp[(\beta/2)\phi(1)]}{\cos[\beta\kappa/2\, e^{+\beta\phi(1)}]^{1/2}}$	[34]	$I = \{(2/\beta\kappa)[e^{+\beta\phi(0)} - e^{+\beta\phi(1)}]\}^{1/2} = [(2/\beta\kappa)e^{+\beta\phi(1)}]^{1/2} \tan[(\beta\kappa/2)e^{+\beta\phi(1)}]^{1/2}$	[35]
(*c*) Transition region $(0 < \xi_o < 1)$	$\cos^{-1}[Qe^{-\beta\phi(\xi)}]^{1/2} = \cos^{-1}[Qe^{-\beta\phi(0)}]^{1/2} - \left[\dfrac{\beta\kappa Q}{2}\right]^{1/2}\xi \quad [0 < \xi < \xi_o]$ where: $Q = e^{+1} - \dfrac{\tanh^2[(\kappa)^{1/2}(1-\xi_o)]}{2\beta}$ $\phi(\xi) = \dfrac{\cosh[(\kappa)^{1/2}(1-\xi)]}{\beta\cosh[(\kappa)^{1/2}(1-\xi_o)]} \quad [\xi_o < \xi < 1]$	[36] [37]	$I^2 = \dfrac{\tanh^2[(\kappa)^{1/2}(1-\xi_o)]}{\beta^2\kappa} + (2/\beta\kappa)(e^{+\beta\phi(0)} - e^{+1})$ ξ_o is computed from: $e^{+\beta\phi(0)} = \dfrac{Q}{\cos^2\{\cos^{-1}[Q/e]^{1/2} + (\beta\kappa Q/2)^{1/2}\xi_o\}}$	[38]

Table V. Equations for the approximate calculation of potential distributions and polarization curves of semi-infinite porous electrodes

Case	Potential distribution	Equation No.	Polarization equation	Equation No.
(a) Linear law $1/\beta \cong \phi(0) > 0$	$\phi(x) = \phi(0) \exp[-(\kappa')^{1/2}x]$	[39]	$I' = \phi(0)/(\kappa')^{1/2}$	[40]
(b) General case $\infty > \phi(0) > 1/\beta$	$\cos^{-1}[Q' e^{-\beta\phi(x)}]^{1/2} = \cos^{-1}[Q' e^{-\beta\phi(0)}]^{1/2} - \left(\frac{\beta\kappa' Q'}{2}\right)^{1/2} x \; [0<x<x_o]$ where: $Q' = e^{+1} - 1/2\beta$	[41]	$(I')^2 = \frac{1}{\beta^2\kappa'} + \frac{2}{\beta\kappa'}(e^{+\beta\phi(0)} - e^{+1})$ x_o is computed from: $x_o = \left(\frac{2}{\beta\kappa' Q'}\right)^{1/2} \cos^{-1}[Q' \exp\{-1/2[1+\beta\phi(0)]\} + \{(1-Q'e^{-\beta\phi(0)})(1-Q'e^{-1})\}^{1/2}]$	[43]
	$\phi(x) = 1/\beta \exp[-(\kappa')^{1/2}(x-x_o)] \; [x_o<x<\infty]$	[42]		

two special cases arise in the application of the approximate method. For case (a), when $\phi(x_o) = 1/\beta \cong \phi(0) > 0$, the linear rate law is a good approximation everywhere in the electrode, and integration of Eq. [22] for $\rho(x) = \phi(x)$ leads to Eq. [39] and [40] of Table V for the potential distribution and the polarization curve in this region.

For case (b), when $\infty > \phi(0) > \phi(x_o) = 1/\beta$, the potential distribution functions and the polarization curve are given by Eq. [41], [42], and [43] of Table V. The distribution of Eq. [41] holds in the region $0 < x < x_o$, while Eq. [42] gives the distribution in the region $x_o < x < \infty$. The parameter x_o may be computed from the relation given in Table V as a function of $\phi(0)$. Once x_o is known, Eq. [41] and [42] are used to calculate $\phi(x)$ at any point in the electrode. An approximate polarization curve may be calculated by use of Eq. [40] and [43], or the exact polarization curve may be computed by use of Eq. [24].

Discussion

A family of polarization curves for the finite porous electrode is shown in Fig. 3. These curves were computed for the case of the symmetrical rate law ($\beta = 1/2$) by use of Eq. [13] and [16] in Tables I and II and tables of the Jacobian elliptic functions (35). The solid line in Fig. 3 is the polarization curve of finite porous electrodes when the reaction is distributed uniformly throughout the electrode; it is identical to the polarization curve of a planar electrode of the same surface area. As the resistance parameter (κ) increases, the potential and current distributions become increasingly nonuniform at constant total current (I). For sufficiently large κ, the polarization curve consists of a single Tafel line of slope, $d\phi(0)/d\ln I = 2/\beta$, and $\phi(1)$ is quite small compared to $\phi(0)$. For sufficiently small κ, two Tafel lines may be observed in the polarization curve of the finite porous electrode. At small currents, $\phi(0)$ is not much different from $\phi(1)$, the reaction distribution is essentially uniform, and the polarization behavior of a planar electrode is obtained. At large currents, $\phi(0)$ eventually becomes large compared to $\phi(1)$, the reaction distribution becomes highly nonuniform, and a typical porous electrode polarization curve is obtained. The dashed lines in Fig. 3 correspond to Eq. [11]. At large I, $\phi(1)$ approaches a limiting value which depends only on κ. The value of this limiting potential is determined by the equation, $u_o = K$, where $K(k)$ is the complete elliptic integral of the first kind (34) and u_o is defined in Eq. [13] of Table I for $\xi = 0$. Curves similar to those in Fig. 3 are discussed by Winsel (19).

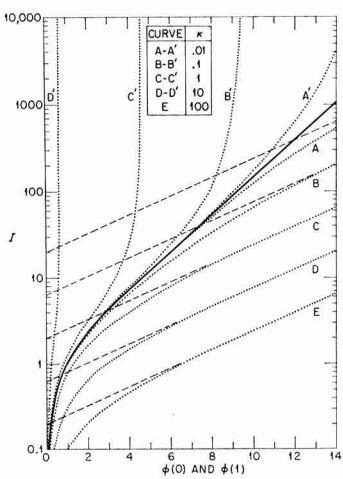

Fig. 3. Polarization curves for the finite porous electrode as a function of the resistance parameter, κ, for the case of the symmetrical rate law ($\beta = 1/2$). Curves A-E plot $\phi(0)$ vs. I; curves A'-D' plot $\phi(1)$ vs. I; dashed lines are extrapolations of the Tafel lines.

The distribution of potential and current in the finite electrode as a function of the polarization is shown in Fig. 4 and 5 for the case of symmetrical rate law ($\beta = 1/2$) and $\kappa = 1$. The parameter Φ of Fig. 4 is a relative potential function which is useful for plotting potential distributions on a convenient scale. For small currents, the relative potential distribution is essentially independent of I (cf. curve A). This limiting potential distribution occurs when the linear rate law is a good approximation, and an expression for the limiting distribution is given by Eq. [44], which is obtained from Eq. [32] of

$$\Phi = \frac{\phi(\xi) - \phi(1)}{\phi(0) - \phi(1)} = \frac{\cosh[(\kappa)^{1/2}(1-\xi)] - 1}{\cosh[(\kappa)^{1/2}] - 1} \qquad [44]$$

Table IV. With increasing current, the potential distribution becomes more nonuniform. The relative reaction rate function, $\rho(\xi)/\rho(0) = j(\xi)/j(0)$, of Fig. 5

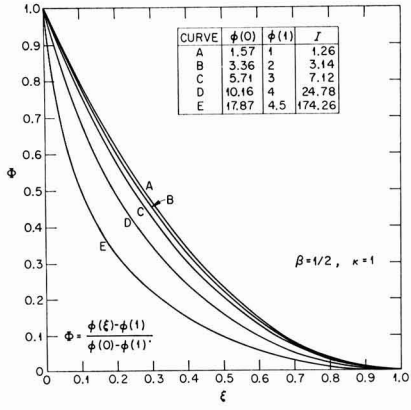

Fig. 4. Plot of the relative potential function, Φ, against ξ

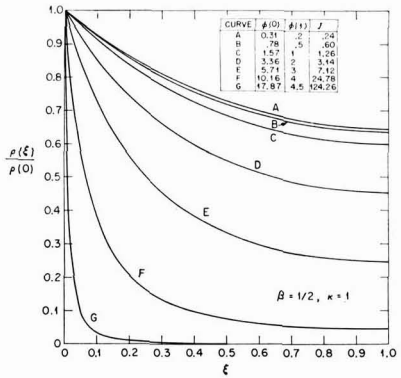

Fig. 5. Plot of the relative reaction rate function, $\rho(\xi)/\rho(0)$, against ξ.

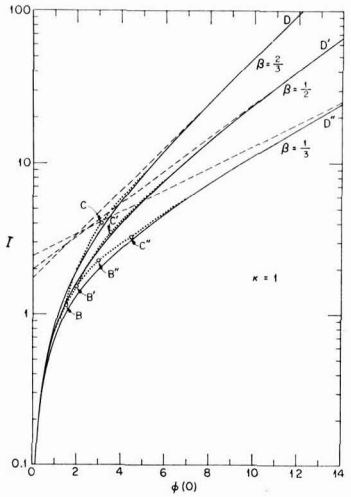

Fig. 6. Comparison of exact and approximate methods for the calculation of polarization curves of the finite porous electrode. Solid lines are the exact solutions; dotted lines are the approximate solutions; dashed lines are extrapolations of the Tafel lines.

also shows a limiting behavior for small polarization. Equation [45] is an expression for this limiting behavior. The

$$\frac{\rho(\xi)}{\rho(0)} = \frac{\cosh[(\kappa)^{1/2}(1-\xi)]}{\cosh[(\kappa)^{1/2}]} \qquad [45]$$

distributions of Fig. 4 and 5 correspond to points on curves C and C′ of Fig. 3. Polarization curves and potential and current distributions in the case of $\beta = 1/3$ and 2/3 are quite similar to those shown in Fig. 3-5.

A comparison of polarization curves for the finite electrode calculated by use of both exact and approximate methods is shown in Fig. 6. The solid lines are exact solutions computed from Eq. [16], [17], and [18] of Table II for $\kappa = 1$. Sections AB, AB′, and AB″ of the approximate solutions were calculated from Eq. [33] of Table IV; points B, B′, and B″ correspond to the condition $\phi(0) = 1/\beta$. Sections BC, B′C′, and B″C″ were calculated with Eq. [38] of Table IV and represent the transition region between operation of the entire electrode with a linear reaction rate law and operation with an exponential law. Sections CD, C′D′, and C″D″ were calculated from Eq. [35] of Table IV; points C, C′, and C″ correspond to the condition, $\phi(1) = 1/\beta$. The correspondence between exact and

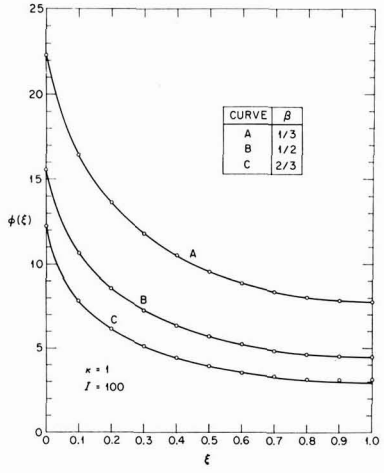

Fig. 7. Potential distribution in the finite porous electrode as a function of the transfer coefficient (β) at constant current (I). Solid lines are calculated with exact equations, open circles with approximate method.

approximate solutions decreases in the sequence: AB′C′D′, ABCD, AB″C″D″. Reference to Fig. 2 shows that this sequence might have been anticipated from the relative behavior of the exact and approximate rate laws. The major effect of the assumption of a discontinuous rate law as an approximation to the more exact law is exhibited in the calculation of the polarization curve of the finite electrode. As shown below, the effect of the discontinuity in the rate law is averaged out over the length of the electrode, and exact and approximate methods for the calculation of potential and current distributions agree well.

Potential and reaction rate distributions in the finite electrode, computed by use of both exact and approximate methods, are shown in Fig. 7 and 8 as a function of the transfer coefficient. Curves A, B, and C in Fig. 7 and 8 were calculated from Eq. [14], [13], and [15] of Table I, with $\kappa = 1$ and $I = 100$; the open circles were calculated from Eq. [34] of the approximate method. The agreement between exact and approximate methods is very good. Since the total current (I) is constant, the reaction rate curves of Fig. 8 intersect.

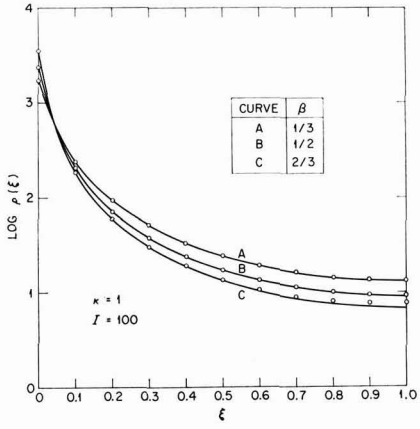

Fig. 8. Reaction distribution in the finite porous electrode as a function of the transfer coefficient (β) at constant current (I). Solid lines are calculated with exact equations, open circles with approximate method.

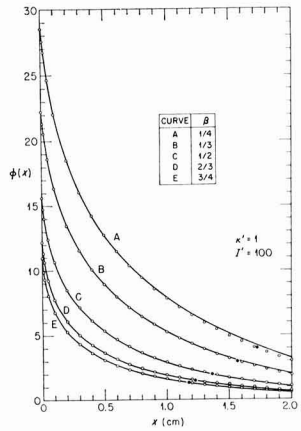

Fig. 9. Potential distribution in the semi-infinite porous electrode as a function of the transfer coefficient (β) at constant current (I'). Solid lines are calculated with exact equations, open circles with approximate method; filled circles denote x_o, where $\phi(x_o) = 1/\beta$ and the rate law changes from $\rho(x) = \exp[\phi(x)]$ to $\rho(x) = \phi(x)$.

Potential distributions for the semi-infinite electrode are shown in Fig. 9 as a function of the transfer coefficient for the parameters $\kappa' = 1$ and $I' = 100$. The exact distributions were calculated from Eq. [27] to [31] of Table III. Values of incomplete elliptic integrals of the third kind occurring in Eq. [30] and [31] were computed by use of tables (36). The approximate distributions were calculated by use of Eq. [41] and [42] of Table V. The locus of the point x_o was calculated in each case from the formula in Table V. Since x_o represents the transition point between linear and exponential rate laws, it is a useful measure of the degree of penetration of the reaction into the porous electrode. As for the case of the finite electrode, the agreement between exact and approximate methods is good. The best agreement is found for the case of the symmetrical rate law ($\beta = 1/2$). The distributions of reaction rates corresponding to the potential distributions of Fig. 9 are similar in form to those of Fig. 8.

In contrast to the calculation of polarization curves for the finite electrode (cf. Fig. 6), calculation of the potential profile using the approximate method proposed here shows little effect of the assumption of a discontinuous rate law. Furthermore, as shown in Fig. 7-9, both exact and approximate methods provide essentially the same distributions. Figures 7 and 9 show that the potential distribution in porous electrodes is a rather sensitive function of the value of the transfer coefficient in the reaction rate law. Although the exact solutions reported above should be useful for computational purposes in special cases, their utility is somewhat limited for arbitrary values of the transfer coefficient which are likely to occur with practical porous electrodes. The approximate method outlined above then affords a much easier and still relatively exact technique for the calculation of polarization behavior and potential and current distributions in porous electrodes under pure activation control.

Acknowledgment

The author wishes to express grateful appreciation to K. A. Kraus and F. Nelson of this Laboratory for illuminating discussions of their observations on phenomena occurring in porous electrodes and for continued interest and encouragement of this work.

Manuscript received Nov. 8, 1963; revised manuscript received March 31, 1964. This paper was presented at the Toronto Meeting, May 3-7, 1964. This paper is based on work performed for the Office of Saline Water, U. S. Department of the Interior, at the Oak Ridge National Laboratory, Oak Ridge, Tennessee, operated by the Nuclear Division, Union Carbide Corporation, for the U. S. Atomic Energy Division.

Any discussion of this paper will appear in a Discussion Section to be published in the June 1965 JOURNAL.

SYMBOLS

A	Average cross-sectional area of electrolyte in porous electrode, cm^2
$cn(u, k)$	Jacobian elliptic function, cosine amplitude u
$dn(u, k)$	Jacobian elliptic function, delta amplitude u
f, f_o	Functions occurring in exact treatment of semi-infinite electrode for $\beta = 1/4$ or $3/4$; defined in Table III
i	Total current of porous electrode, amp
i_o	Total exchange current of finite porous electrode, amp
I	Dimensionless reduced total current of finite electrode; $I = i/i_o = i/Slj_o$
I'	Reduced total current of semi-infinite electrode; $I' = i/Sj_o$, cm
$j(\xi), j(x)$	Current density of electrochemical reactions occurring at the interface between solid and liquid phases in finite and semi-infinite porous electrodes, respectively, amp/cm^2
j_o	Exchange current density of porous electrode, amp/cm^2
k	Modulus of Jacobian elliptic functions and integrals
k'	Complementary modulus; $k' = (1 - k^2)^{1/2}$
K	Complete elliptic integral of the first kind
l	Length of finite porous electrode, cm
Q, Q'	Dimensionless integration constants occurring in the approximate treatments of finite and semi-infinite electrodes, respectively; defined in Tables IV and V
RT/F	Thermal volt equivalent, volts
$sd(u, k)$	$sd(u, k) = sn(u, k)/dn(u, k)$
$sn(u, k)$	Jacobian elliptic function, sine amplitude u
S	Surface area of porous electrode per unit length, cm
$tn(u, k)$	$tn(u, k) = sn(u, k)/cn(u, k)$
u	Incomplete elliptic integral of the first kind
u_o	Value of u when $\xi = 0$ or $x = 0$
x	Distance parameter of semi-infinite porous electrode, cm
x_o	Point of transition between linear and exponential rate laws in approximate treatment of semi-infinite electrode, cm
y	Convenient functions used in exact treatments of finite and semi-infinite porous electrodes
α	Parameter occurring in exact treatment of semi-infinite electrodes for $\beta = 1/4$ or $3/4$; defined in Table III
β	Transfer coefficient of the anodic reaction $(0 < \beta < 1)$
γ	Parameter occurring in exact treatment of finite electrode for $\beta = 1/3$; defined in Table I
δ	Parameter occurring in exact treatment of finite electrode for $\beta = 2/3$; defined in Table I
$\eta(\xi), \eta(x)$	$\eta(\xi) = \Delta\phi(\xi) - \Delta\phi_o$; $\eta(x) = \Delta\phi(x) - \Delta\phi_o$; overpotential in finite and semi-infinite electrodes, respectively, volts
κ, κ'	$\kappa = (i_o lF)/(\sigma ART)$; $\kappa' = (j_o SF)/(\sigma ART)$; resistance parameters occurring in treatment of finite and semi-infinite electrodes, respectively ($\kappa' = \text{cm}^{-2}$)
μ	Parameter occurring in exact treatment of semi-infinite electrodes for $\beta = 1/4$ or $3/4$; defined in Table III
ξ	Dimensionless distance parameter of finite porous electrodes

ξ_0	Point of transition between linear and exponential rate laws in approximate treatment of finite electrode
$\pi\{u,\alpha^2/(\alpha^2-1)\}$	Legendre's incomplete elliptic integral of the third kind; occurs in Eq. [30] and [31] of Table III
$\rho(\xi),\rho(x)$	$\rho(\xi) = j(\xi)/j_0$; $\rho(x) = j(x)/j_0$; dimensionless reduced reaction rates in finite and semi-infinite electrodes, respectively.
σ	Specific conductance of solution, $ohm^{-1}\,cm^{-1}$
ϕ_M	Potential of the metallic phase of porous electrodes, here assumed constant, volts
$\phi_S(\xi),\phi_S(x)$	Potential of the solution phase of finite and semi-infinite porous electrodes, respectively, volts
$\phi(\xi),\phi(x)$	$\phi(\xi) = F\eta(\xi)/RT$; $\phi(x) = F\eta(x)/RT$; dimensionless reduced overpotentials in finite and semi-infinite electrodes, respectively
$\phi(0)$	Dimensionless reduced overpotential at $\xi = 0$ or $x = 0$
$\phi(1)$	Dimensionless reduced overpotential at $\xi = 1$
$\phi(\xi_0),\phi(x_0)$	$\phi(\xi_0) = \phi(x_0) = 1/\beta$; dimensionless reduced potential of transition between linear and exponential rate laws in approximate treatments of finite and semi-infinite electrodes, respectively
$\Delta\phi(\xi),\Delta\phi(x)$	$\Delta\phi(\xi) = \phi_M - \phi_S(\xi)$; $\Delta\phi(x) = \phi_M - \phi_S(x)$; interfacial potential difference in finite and semi-infinite porous electrodes, respectively, volts
$\Delta\phi_0$	Reversible interfacial potential difference, volts
Φ	$\Phi = [\phi(\xi) - \phi(1)]/[\phi(0) - \phi(1)]$; relative potential function

REFERENCES

1. G. J. Young, Editor, "Fuel Cells," Reinhold Publishing Co., New York (1960).
2. G. J. Young, Editor, "Fuel Cells," Vol. II, Reinhold Publishing Co., New York (1963).
3. K. J. Vetter, "Elektrochemische Kinetik," Springer-Verlag, Berlin (1961).
4. V. S. Daniel'-Bek, *Zhur. Fiz. Khim.*, **22**, 697 (1948).
5. A. N. Frumkin, *ibid.*, **23**, 1477 (1949).
6. J. J. Coleman, *This Journal*, **98**, 26 (1951).
7. O. S. Ksenzhek and V. V. Stender, *Doklady Akad. Nauk S.S.S.R.*, **106**, 487 (1956).
8. O. S. Ksenzhek and V. V Stender, *ibid.*, **107**, 280 (1956).
9. O. S. Ksenzhek and V. V. Stender, *Zhur. Fiz. Khim.*, **31**, 117 (1957).
10. O. S. Ksenzhek, *Ukrain. Khim. Zhur.*, **23**, 443 (1957).
11. R. M. Perskaya and I. A. Zaidenman, *Doklady Akad. Nauk S.S.S.R.*, **115**, 548 (1957).
12. E. Justi, M. Pilkuhn, W. Scheibe, and A. Winsel, "Hochbelastbare Wasserstoff-Diffusions-Elektroden für Betrieb bei Umgebungstemperatur und Niederdruck," Akad. Wiss. u. Lit., Nr. 8, Komm. Verlag Steiner, Wiesbaden, 1959.
13. I. A. Zaidenman and R. M. Perskaya, *Zhur. Fiz. Khim.*, **33**, 50 (1959).
14. I. A. Zaidenman, *ibid.*, **33**, 437 (1959).
15. J. Euler and L. Horn, *Elektrotech. Zeit.*, **81**, 566 (1960).
16. J. Euler and W. Nonnenmacher, *Electrochim. Acta*, **2**, 268 (1960).
17. O. S. Ksenzhek, *Zhur. Fiz. Khim.*, **36**, 243 (1962).
18. O. S. Ksenzhek, *ibid.*, **36**, 633 (1962).
19. A. Winsel, *Z. Elektrochem.*, **66**, 287 (1962).
20. J. S. Newman and C. W. Tobias, *This Journal*, **109**, 1183 (1962).
21. R. Buvet, M. Guillou, and B.Warszawski, *Electrochim. Acta*, **6**, 113 (1962).
22. J. Euler, *Electrochim. Acta*, **7**, 205 (1962).
23. J. C. Sohm, *ibid.*, **7**, 629 (1962).
24. I. G. Gurevich and V. S. Bagotskii, *Inzhenerno-Fiz. Zhur.*, **6** (**2**), 60 (1963).
25. I. G. Gurevich and V. S. Bagotskii, *ibid.*, **6** (**3**), 69 (1963).
26. I. G. Gurevich and V. S. Bagotskii, *ibid.*, **6** (**5**), 75 (1963).
27. W. A. Mueller, *This Journal*, **110**, 698 (1963).
28. O. S. Ksenzhek, *Zhur. Fiz. Khim.*, **37**, 2007 (1963).
29. J. Euler, *Electrochim. Acta*, **8**, 409 (1963).
30. M. Guillou and R. Buvet, *ibid.*, **8**, 489 (1963).
31. R. de Levie, *ibid.*, **8**, 751 (1963).
32. J. Euler and K. N. Müller, *ibid.*, **8**, 949 (1963).
33. W. J. Blaedel, C. L. Olson, and L. R. Sharma, *Anal. Chem.*, **35**, 2100 (1963).
34. P. F. Byrd and M. D. Friedman, "Handbook of Elliptic Integrals for Engineers and Physicists," Springer-Verlag, Berlin (1954).
35. G. W. Spenceley and R. M. Spenceley, "Smithsonian Elliptic Functions Tables," Smithsonian Institute, Washington, 1947.
36. R. G. Selfridge and J. E. Maxfield, "A Table of the Incomplete Elliptic Integral of the Third Kind," Dover, New York (1958).

Transport Numbers in Pure Molten $AgNO_3$ and AgCl by a Simplified Weighing Method

Paul Duby[1] and Herbert H. Kellogg

Department of Mineral Engineering, Columbia University, New York, New York

ABSTRACT

A very simple technique is described for measuring transport numbers in pure fused salts. The transport of matter due to ionic electromigration is determined by recording continuously during electrolysis, the weight change of a movable half-cell, which consists merely of a vertical tube closed at its lower end by a coarse-fritted Pyrex plug. A small but significant decrease of the silver transport number with increasing temperature is found in both molten $AgNO_3$ and AgCl.

A number of techniques have been used for measuring transport numbers in pure molten salts. Most of these techniques have been criticized because of experimental limitations. More recently, the principle of the measurement itself has been questioned, and doubts have been expressed about the concept of the transport number (1). Devising new independent methods of measurements has therefore a twofold purpose. First, it will make possible the selection of the most appropriate technique in each case, and it will improve the reliability of presently available data. Second, each new measurement brings more facts to support theories about the experimental significance of the transport number concept.

1 Present address: School of Metallurgical Engineering, University of Pennsylvania, Philadelphia, Pa.

The present paper describes a very simple technique for measuring transport numbers, which is directly derived from the weighing method previously reported by the authors (2, 3). Both techniques are based on the measurement of the equivalent mass transport due to electromigration. The first one records the displacement of the center of gravity of a horizontal cell when the electrical current passes through it. The second one measures directly the weight change of one electrode compartment while the electrolysis proceeds. This is done by suspending a half-cell from a recording balance so that it dips into the vessel containing the melt and the other electrode.

This simplified weighing technique does not yield results with as high precision as the more elaborate one, but in this respect it is still as good or better as recently reported radiotracer experiments (4). The apparatus is quite simple and the procedure is very fast. It is recommended for rapid measurement of transport numbers within a few per cent.

Let us consider a molten salt MX, being electrolyzed between two electrodes of the metal M, separated by a porous membrane which defines the two electrode compartments. An equivalent mass M_t is transferred per faraday from the anode toward the cathode

$$M_t = T_M M_M - T_X M_X \qquad [1]$$

where M_M, M_X are the equivalent masses of components M and X, and T_M, T_X are the transport numbers measured with respect to the porous plug.

A volume change of the melt in the electrode compartments also takes place. It produces a level difference between the electrode compartments, from which a mechanical flow results. It has been shown (3) that the total rate of weight change due to both the electromigration and the return flow is a function of time,

$$\frac{d}{dt} W(t) = M_t \frac{I}{F} g - (V_t + V_e) \frac{I}{F} \rho g \, (1 - e^{-at}) \qquad [2]$$

where $W(t)$ is the weight of the moving half-cell; I, the electrical current; F, the faraday constant; g, the gravitation constant; V_t and V_e, the volume changes due to electromigration and to the electrode reaction; ρ, the density of the melt; a, a time constant which defines the rate of hydraulic flow through the porous membrane; t, the time.

For the system described above

$$V_t + V_e = T_X V_{MX} - V_M{}^o \qquad [3]$$

where V_{MX} is the equivalent volume of the salt and $V_M{}^o$ is the equivalent volume of the metal in the electrode.

The rate of weight change per unit of electric current depends only on the transport number and the hydraulic characteristics of the plug. If the duration of the run is small compared with $1/a$, the second term vanishes in Eq. [2] and the initial weight change is a direct measurement of the equivalent mass transport and hence the transport number

$$T_M = \frac{M_t + M_X}{M_M + M_X} \qquad [4]$$

With coarse fritted disks, $1/a$ is rather small and the last term of Eq. [2] cannot be neglected. The magnitude of this term can be evaluated from a measurement of the time constant, a. In the experiments reported below, the measured weight change was always corrected in this manner in order to compute the equivalent mass transport. This correction amounted to about 0.01 on the transport number.

Experimental

The apparatus is represented on Fig. 1 The electrolysis cell consists of a 30 mm-diameter Pyrex vessel containing the molten salt. Inside hangs the movable half cell. The latter consists merely of a 8 mm-diameter Pyrex tube closed at its bottom by a coarse porosity fritted plug. The two electrodes are made of silver wire (⅛ in. diameter). One hangs inside the half-cell, the other is exterior to it and is formed into a loop at the bottom of the outer vessel. A thermocouple, protected by a Pyrex tubing also dips into the melt.

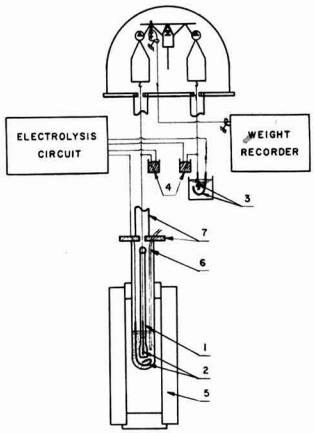

Fig. 1. Diagrammatic sketch of apparatus. 1, movable half-cell with porous membrane; 2, silver electrodes in molten salt; 3, silver electrodes in aqueous silver nitrate solution; 4, mercury contacts; 5, furnace; 6, chromel-alumel thermocouple; 7, heat and draft shields (not completely shown).

The cell is contained in a small resistance furnace with a viewport, so that the free motion of the half-cell can be observed. The temperature is controlled by a proportional controller, receiving its signal from a thermocouple located under the cell. The temperature is constant to about 2°C over a length of 4 cm around the porous membrane.

The movable electrode compartment hangs from the left pan of an Ainsworth semimicro recording balance. The fine michrome suspension wire (B + S No. 36) also serves to carry the electrical current to the electrode.

With such an experimental set-up, the force acting on the balance, F, equals the weight of the half-cell, W, minus the buoyancy, B, plus the resultant of surface tension forces, S. If one assumes that the surface tension forces remain constant, then a change of weight of the half-cell, ΔW, produces a displacement of the left pan ΔX, and accordingly a change of buoyancy, ΔB. The resulting change of the force acting on the balance is, ΔF, given by

$$\Delta F = \Delta W - \Delta B = \Delta W - \rho g A \Delta X \qquad [5]$$

where A is the cross-section of the movable electrode compartment. If k is the proportionality constant of the automatic balance mechanism which relates ΔX to ΔF, then

$$\Delta F = \frac{\Delta W}{1 + kA\rho g} \qquad [6]$$

In the conditions of our experiments the expression $1 + kA\rho g$ is approximately equal to 20, which means that the sensitivity of our apparatus is reduced to about 1/20 the nominal sensitivity of the balance. One division of the chart (1/10 in.) represents accordingly 2 mg instead of the nominal 0.1 mg.

A first series of measurements were made with the apparatus as described so far. The system was calibrated by changing weights on the right pan. Allowing for some oscillation of the balance, which was probably due to thermal convection currents above the cell, the readability was found equal to half a division or 1 mg. The reproducibility of the calibration, however, was uneven and seemed to depend on the

speed with which the weights were applied. This was attributed to a change of the surface tension forces on the movable half cell as a function of the speed or acceleration of its motion. To take care of that, another calibration procedure was adapted, as follows:

From the right pan of the balance hangs a piece of silver wire (⅛ in. diameter) dipping into an aqueous solution of 10% silver nitrate. A second silver electrode is fixed into the vessel containing the solution so that the whole cell constitutes a silver coulometer. The calibration of the balance is done by passing a known electrical current through the coulometer in order to cause a rate of weight change roughly equal to the expected rate of weight change due to electrolysis of the molten salt. In this maner, the very same displacement occurs during the calibration and the actual run.

By this method the rate of weight change is, indeed, calibrated. The measurement is then merely the comparison of two slopes on the weight *vs.* time plot recorded by the balance: one for current through the cell, the other for curernt through the coulometer.

The same apparatus can be used also as a zero-method, by passing simultaneously two different current intensities through the cell and through the coulometer and varying one of them until the balance beam is maintained in equilibrium. The result is then computed from the ratio of electrical currents. This method has also been applied successfully.

Results and Discussion

The experimental procedure is very similar to the one used by Harrington and Sundheim (5) to measure leakage rates through porous diaphragms in order to evaluate their possible use for transport experiments. We have, however, improved this technique in two ways. First, the use of a recording balance makes the experiment easier and more reliable. Second, the use of the silver coulometer improves the calibration since it makes possible the actual calibration of the rates of weight change.

Measurements have been made first with molten silver nitrate in order to evaluate the technique by comparison with the results obtained with the horizontal cell. Figure 2 shows all the data. They are somewhat more scattered than the other ones but the general agreement is quite good. The two values obtained by Laity and Duke with their bubble cell (6) are also indicated. The following temperature dependence has been obtained by the least square technique

$$T_{Ag} = 0.798 - 5.6\ 10^{-4}\ (\theta - 200)$$

with a standard deviation 0.006.

A series of measurements have been made with molten AgCl. Figure 3 shows the results. A small but significant temperature dependence is found. It is very similar to the one observed for silver nitrate. The best line obtained by a least square calculation is

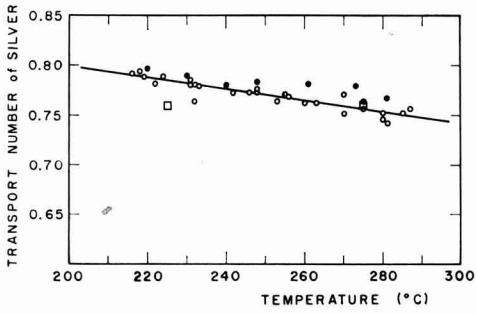

Fig. 2. Temperature dependence of transport number in molten silver nitrate. $AgNO_3$: ○, vertical half-cell; ●, horizontal cell (3); □, Laity and Duke (6).

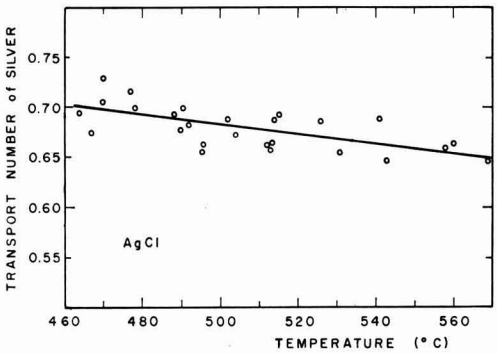

Fig. 3. Temperature dependence of transport number in molten silver chloride.

$$T_{Ag} = 0.682 - 4.8\ 10^{-4}\ (\theta - 500)$$

with a standard deviation 0.016. The two other measurements of transport number in molten silver chloride, which we know of, disagree among themselves and with our results. We have so far no explanation for those differences. First, Duke and co-workers (7) found $T_{Cl} = 0$, and accordingly $T_{Ag} = 1$, in the 500°-600°C temperature range, by means of a radiotracer technique in a Pyrex cell. It must be recalled, however, that Lunden (8) concludes from his own experience with the radiotracer technique that "it seems wise always to check the results by using both anion and cation tracers." Accordingly, Duke and co-workers' value should eventually be checked by a more thorough investigation. Second, Murguliscu and Marta (9) found an average value of $T_{Ag} = 0.54$ by weighing the anodic compartment after passing the current. Their results. however, are scattered between a lower value 0.45 and an upper one 0.68. Taking this scattering into account, those data seem no longer very different from ours.

Summarizing, this simplified weighing method gives quick and reproducible transport number measurements. The slight temperature dependences of transport numbers in both silver nitrate and silver chloride appear significant. It is to be compared with the dependence on temperature found by Fisher and Klemms (10) for zinc chloride and thallium chloride and the one already reported (3) for lead bromide.

Acknowledgment

The authors wish to acknowledge the generous support of the National Science Foundation under contract NSF-G-20879.

Manuscript received Feb. 3, 1964.

Any discussion of this paper will appear in a Discussion Section to be published in the June 1965 JOURNAL.

REFERENCES

1. R. W. Laity, *J. Chem. Ed.*, **39**, 67 (1962).
2. H. H. Kellogg and P. Duby, *J. Phys. Chem.*, **66**, 191 (1962).
3. P. Duby and H. H. Kellogg, *J. Phys. Chem.*, **68**, 1755 (1964).
4. E. D. Wolf and F. R. Duke, *This Journal*, **110**, 311 (1963).
5. G. Harrington and B. S. Sundheim, *J. Phys. Chem.*, **62**, 1454 (1957).
6. R. W. Laity and F. R. Duke, *This Journal*, **105**, 97 (1958).
7. F. R. Duke, M. L. Bowman, E. Wolf, and H. Garfinkel, *Ann. N. Y. Acad. Sc.*, **79**, 1023 (1960).
8. I. G. Murgulescu and L. Marta, *Acad. rep. populare Romine, Studii cercetari chim.*, **8**, 375 (1960).
9. A. Lunden, *This Journal*, **109**, 260 (1962).
10. W. Fisher and A. Klemm, *Z. Naturforsch.*, **16a**, 563 (1961).

Some Observations on the High-Temperature Oxidation of Lanthanum

W. L. Phillips

Engineering Materials Laboratory, Engineering Research Division, Engineering Department, E. I. du Pont de Nemours & Company, Inc., Wilmington, Delaware

Loriers (1) showed that lanthanum is attacked by dry air until a constant weight increase of 0.45 mg/cm² was reached after 25 min at 300°C. More recently Vorres and Eyring (2) reported that this element oxidizes in a parabolic manner. Above 300°C lanthanum transforms from hcp (hexagonal-close-packed) to fcc (face-centered-cubic). The volume ratio of the oxide to the fcc phase is 1.11 (3).

Testing was carried out in an Ainsworth aperiodic milligram analytical balance. The balance was modified to accommodate a 12-in. long sapphire rod supporting a zirconia crucible in a vertical furnace (4). Samples of 99.5% pure lanthanum were purchased from the American Chemical and Potash Company. Since lanthanum oxidizes readily at room temperature, the paraffin-protected ingots were cut under oil into samples approximately 0.1 x 0.2 x 1 cm. Each sample was then dried under vacuum at 100°C for 5 hr prior to oxidation. Density measurements showed that the samples were 100% dense. The lack of oxidation before testing was indicated by the absence of white La_2O_3. The time of transfer from the vacuum chamber to the oxidation apparatus was ~ 25 sec.

Representative weight-gain *vs.* time plots for lanthanum at 700°C are shown in Fig. 1. The initial linear weight gain is constant at the same rate in repetitive tests. At times varying from 750 to 1200 sec, the weight gain discontinuously jumps to a constant value of 32 ± 1.0 mg/cm². Figure 2 is a plot of the weight gain *vs.* time for samples tested at temperatures of 600° to 850°C. In the temperature range of 600°-700°C, the samples obeyed a single linear law until a time varying from 810 to 2150 sec when the weight gain jumped to 32 ± 1 mg/cm². Above 700°C two distinct linear regions were observed. In the times investigated, 2400 sec, no discontinuities were observed until the samples reached a weight gain of 32 ± 1.0 mg/cm². At this weight no further gain was observed. The initial linear-weight-gain constant reached a maximum at 810°C. Figure 3 is a plot of the initial linear-weight-

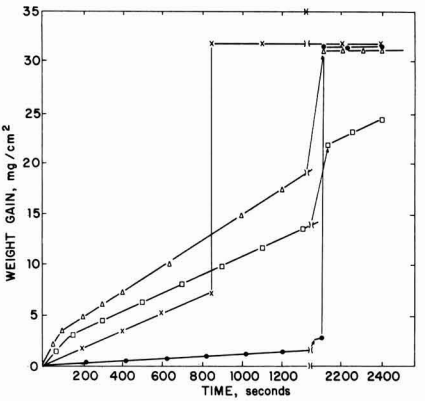

Fig. 2. Weight gain *vs.* time for lanthanum oxidized at the temperatures indicated: ○, 600°C; X, 700°C; △, 800°C; □, 850°C.

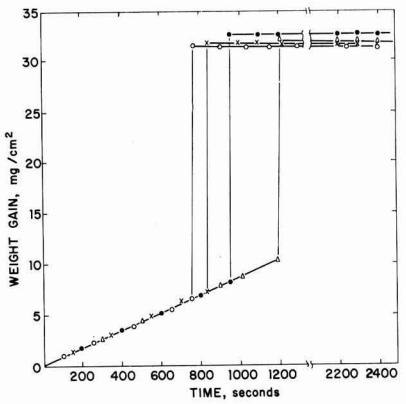

Fig. 1. Weight gain *vs.* time for lanthanum oxidized at 700°C: ●, No. 1; X, No. 2; ○, No. 3; △, No. 4.

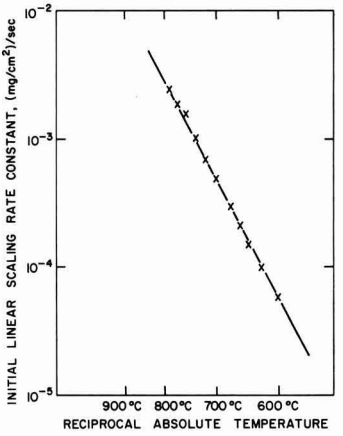

Fig. 3. Initial linear scaling rate constant *vs.* reciprocal absolute temperature.

gain constant in the temperature range of 600°-810°C as a function of reciprocal absolute temperature. The activation energy was ~32.8 kcal/mole. X-ray examination indicated that La_2O_3 was the only oxidation product at all temperatures.

These results demonstrate that lanthanum oxidizes linearly in the temperature range of 600°-850°C. This is in disagreement with the results of Vorres and Eyring (2). No reason is advanced for this discrepancy.

The weight gain of the samples used in the present investigation, if all the lanthanum were oxidized to lanthanum oxide, would be ~35 mg/cm². This agrees within experimental limits with the observed value of 32 mg/cm². Loriers used samples which, if completely oxidized, would gain 0.42 mg/cm². This is also in agreement with the observed value of 0.45 mg/cm². These observations and x-ray data indicate that lanthanum oxidizes completely to lanthanum oxide by either a continuous or discontinuous mechanism.

The observation of a discontinuity in the weight-gain-*vs.*-time plots and the decrease in the initial rate as the temperature increases has been observed in columbium by Kolski (5). The discontinuity is much sharper in lanthanum. Although the phenomena observed in the two metals may be related, normal metallographic practices are unsuitable for studying lanthanum because of its instability even at room temperature.

Manuscript received April 15, 1964.

Any discussion of this paper will appear in a Discussion Section to be published in the June 1965 JOURNAL.

REFERENCES

1. J. C. Loriers, *Acad. Sci. Paris*, **229**, 547 (1949); **231**, 522 (1950).
2. K. S. Vorres and L. R. Eyring, "High Temperature Oxidation of Rare Earth Metals," p. 119-23. Rare Earth Research Seminar, Lake Arrowhead, Calif. (1960).
3. O. Kubaschewski and B. E. Hopkins, "Oxidation of Metals and Alloys," p. 7, Academic Press, New York (1953).
4. W. L. Phillips, Jr., *J. Less Common Metals*, **5**, 97 (1963).
5. T. L. Kolski, *Trans. ASM*, **55**, 119 (1962).

Diffusion of Oxygen in Hafnium

J. P. Pemsler

Ledgemont Laboratory, Kennecott Copper Corporation, Lexington, Massachusetts

Some years ago I first reported on the determination of the diffusion coefficient of oxygen in hafnium (1). The technique was one used previously to measure the diffusion of oxygen in zirconium (2) and consisted of observations of the dissolution rate of anodically deposited interference colored oxide films. At the time of the hafnium study no data were available regarding the hafnium-oxygen phase diagram, and since calculations based on this technique required a knowledge of the solubility limit of oxygen in hafnium, the diffusion coefficient was reported for each of three assumed solubility limits. Since this publication there have been three papers by other authors concerned with this subject. Gadd and Evans (3) report measurements of the diffusion coefficient of oxygen in hafnium in the temperature range 700°-1200°C based on microhardness measurements made on oxidized samples. Wallwork and Smeltzer (4) report values for the diffusion coefficient at temperatures of 800° and 950°C based on microhardness indentations on oxidized samples and calculated on the basis of a theory involving a steady-state solution for the oxygen gradient in the metal phase during linear oxidation. Rudy and Stecher (5) in a determination of the hafnium-oxygen phase diagram report a value of the solubility limit of oxygen in hafnium as 20.5 at. % at 1350°C and almost independent of temperature.

In recent studies I have shown that the concentration gradient of oxygen beneath the oxide/metal interface in oxidized samples of zirconium (6) and hafnium (7) can be accurately predicted by a theoretical expression involving diffusivity, time, and oxide thickness. This enables the diffusivity of oxygen in the metal to be calculated when the other parameters are accurately known. In addition, the depth of penetration of oxygen was found to increase with time during protective oxidation and, on the onset of linear oxidation, begins to decrease. Zones of constant hardness at high oxygen concentration probably due to ordered hafnium-oxygen alloys were reported.

It is the purpose of this communication to review the data concerning the diffusion of oxygen in hafnium in the light of the subsequent publications and some additional studies carried out in this Laboratory.

Experimental and Results

In conjunction with the aforementioned study (7) the diffusion coefficient of oxygen in hafnium was redetermined by the anodization technique, this time performing measurements within a single grain of hafnium to avoid the necessity of estimating average colors, and hence average thicknesses, of interference films on a large number of grains in a polycrystalline sample. The new measurements were performed at 575°, 614°, and 655°C. The diffusion coefficient D may be expressed as

$$D = \frac{(x')^2}{4b^2t}$$

where b satisfies the equation

$$b(1 + \operatorname{erf} b) = \frac{C_o}{m_o\sqrt{\pi}}e^{-b^2}$$

Here in time, t, there is a displacement of the oxide/metal boundary, x', which is related to the observed decrease ΔL in thickness of oxide film by the following expression involving the respective molecular volumes

$$x' = \frac{V_{\text{Hf saturated}}}{V_{\text{HfO2}}}\Delta L$$

The quantity C_o is the difference between the saturated concentration, C_s, and initial concentration of oxygen in the metal, and m_o represents the weight of oxygen removed from the HfO_2 consumed in the generation of unit volume of saturated hafnium ($HfO_{0.258}$). Values for the constants used are $\rho HfO_2 = 10.13$ g/cm³ (8), ρHf saturated estimated as 13.29 g/cm³, $C_s = 0.300$ g/cm³ (5), $m_o = 2.03$ g/cm³, $x' = 0.661\ \Delta L$, and $b = 0.0764$.

In order to determine whether extrapolation of the low-temperature diffusion data to high temperatures is justified, ¾ in. diameter hafnium spheres were oxidized at 950°C for 111 hr and 1050°C for 64 hr. The sample was sectioned through the center, polished metallographically, and photographed at 400X and 800X magnifications at each of sixteen equidistant positions around the perimeter. The thickness of the oxide was determined with a planimeter and used to calculate the total quantity of oxygen contained in the oxide scale. This value when subtracted from the total weight gain gives the quantity of oxygen in solution in the metal substrate. In the case under consideration about 50% of the oxygen absorbed was contained in the metal substrate. These data were then used to calculate the diffusion coeffi-

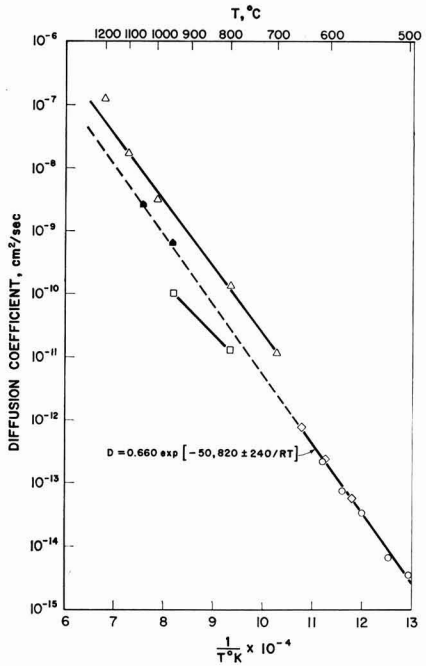

Fig. 1. Temperature dependence of the diffusion coefficient of oxygen in hafnium. Open triangle, Gadd and Evans (3); Open square, Wallwork and Smeltzer (4); Open circle, Pemsler (1); Open diamond, this work, anodic dissolution; Solid pentagon, this work, weight gain.

cient of oxygen in hafnium at 950° and 1050°C according to equations derived previously (6, 7).

Results of the investigations to date are summarized in Fig. 1.

The excellent agreement of the point at 950° and 1050°C with an extrapolation of the low-temperature data indicates that hafnium, like zirconium, conforms to an Arrhenius plot over many decades in values of the diffusion coefficient. A least square solution of the data from anodic dissolution measurements gives a value for the diffusion coefficient as

$$D = 0.660 \exp [-50,820 \pm 240/RT]$$

A variation in the diffusion coefficient of a factor of about two among the differently oriented grains was reported in my initial study (1). A more precise redetermination indicates that the variation with orientation is a factor of about 1.4 and that in a polycrystalline sample relatively few grains show this extreme; the large majority vary by a factor of no more that 1.1. Studies on single crystal material are planned to further clarify the orientation dependence.

Discussion

The work of Gadd and Evans may be criticized from several viewpoints. First, their oxidations were carried out in air so that in addition to the development of a hafnium-oxygen gradient in the metal they must have had a superimposed hafnium-nitrogen gradient. Although the diffusion of nitrogen in hafnium is undoubtedly much slower than that of oxygen, it would be expected to penetrate to a significant depth at the temperatures of their investigation. In addition, the anomalous microhardness of concentrated hafnium-oxygen alloys were not taken into account.

Since Wallwork and Smeltzer worked in pure oxygen and obtained microhardness readings as an average of five hardness scans, their data may represent adequate approximations to the diffusion gradient. However, I am in disagreement with their interpretation of a steady-state gradient during the course of linear oxidation, and the disagreement between our diffusion coefficients may be ascribed to these differences in interpretation.

Manuscript received May 18, 1964.

Any discussion of this paper will appear in a Discussion Section to be published in the June 1965 JOURNAL.

REFERENCES

1. J. P. Pemsler, *This Journal*, **106**, 1067 (1959).
2. J. P. Pemsler, *ibid.*, **105**, 315 (1958).
3. J. D. Gadd and E. B. Evans, *Corrosion*, **17**, 441t (1961).
4. G. R. Wallwork and W. W. Smeltzer, *This Journal*, **110**, 943 (1963).
5. E. Rudy and P. Stecher, *J. Less-Common Metals*, **5**, 78 (1963).
6. J. P. Pemsler, *This Journal*, **111**, 381 (1964).
7. J. P. Pemsler, *ibid.*, to be published.
8. J. Adam and M. D. Rogers, *Acta Cryst.*, **12**, 951 (1959).

Growth of As_2O_3 on GaAs

M. E. Straumanis and C. D. Kim

Department of Metallurgical Engineering, School of Mines and Metallurgy, University of Missouri at Rolla, Rolla, Missouri

It was frequently observed that on polished sections of GaAs, if etched with diluted HNO_3 (1:10 by volume), crystallites (not etch pits) were produced. These crystallites were a product of growth because of their slight elevation above the surface of GaAs. The same observation was made by Yeh and Blakeslee (1).

If GaAs is etched with concentrated HNO_3, the process of growth of the salt-like compound is very fast, as the surface becomes whitish dull in a short time. The microscope revealed clearly that on the surface of the GaAs a deposit is formed, with the black matrix of the arsenide still shining through (Fig. 1). By careful scratching of the surface with a blade tiny amounts of a white substance could be removed, of which very good x-ray powder patterns were obtained. They turned out to be clear patterns of As_2O_3. Evidently the latter was formed by oxidation of As with HNO_3, while the $Ga(NO_3)_3$ went into solution

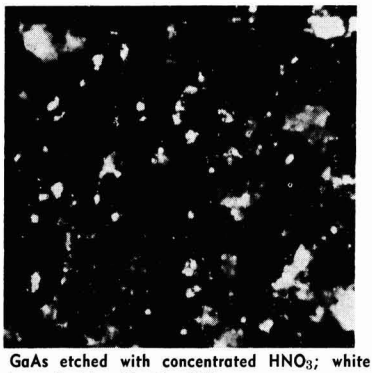

Fig. 1. GaAs etched with concentrated HNO_3; white deposit on the black matrix. Magnification 60X.

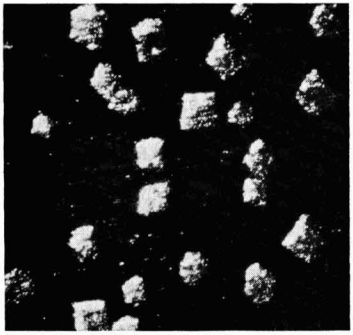

Fig. 2. As_2O_3 platelets, formed on GaAs in 3 hr, 10% HNO_3, lateral illumination. Magnification 60X.

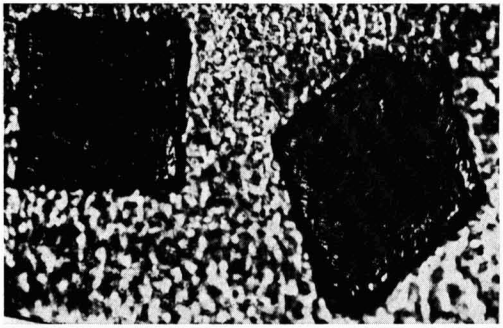

Fig. 3. As_2O_3 platelets, 10μ thick, [110] and [001] perpendicular to the GaAs surface, vertical illumination, 10% HNO_3. Magnification 320X.

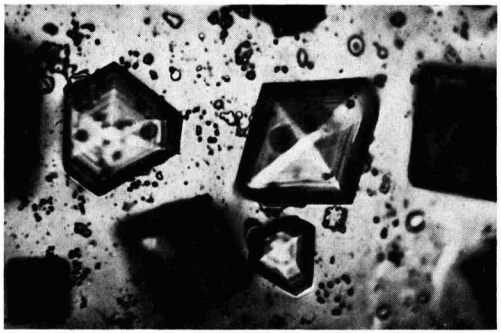

Fig. 4. As_2O_3 crystals on GaAs. Steps are discernible on the planes; etchant: aqua regia. Magnification 580X.

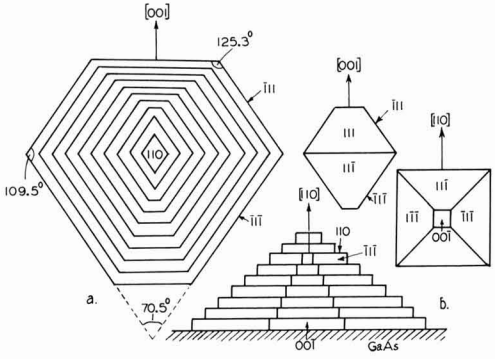

Fig. 5. Schematized growth of As_2O_3 crystals on GaAs: a, top view; b, front view.

$$2As + 2HNO_3 = As_2O_3 + H_2O + 2NO$$

Since the solubility of As_2O_3 in water is not very good (2.1g in 100 ml of H_2O at 25°C), the oxide crystallized out on the surface of GaAs.

The process of As_2O_3 crystallization was much slower in dilute HNO_3 (1:10). But in such a case thin, crystal platelets on the GaAs surface (Fig. 2) were formed. The orientation of these crystals, as can be seen, is at random (1), on the large monocrystalline grains of GaAs. However, many of them, if observed under a larger magnification, appeared as beautiful platelets having two preferred orientations: with the direction [110] or [001] nearly perpendicular to the GaAs surface (Fig. 3), while their orientation in the surface itself was random. The rhomb-shaped crystals appeared most frequently.

If instead of HNO_3, aqua regia (HNO_3 : HCl = 1:3) is used, in about 20 min very beautiful thick As_2O_3 crystals, sticking well to the GaAs surface are obtained (Fig. 4).

All these crystals were combinations of cubic, rhombic, and octahedral planes [the latter are typical for As_2O_3 (2)], with two preferred orientations relatively to the substrate, as already mentioned (see Fig. 3). The growth of such crystals is explained on Fig. 5a and b. First, thin crystal platelets are formed (Fig. 3) with the direction [110] approximately perpendicular to the dissolving GaAs surface, and the [001] in the surface. Then the same kind of layers with the same orientation grow on each other stepwise, as can be seen from Fig. 4 and is shown schematically in Fig. 5. The angles of the rhomb-shaped crystals (Fig. 3 and 4), as drawn in Fig. 5a, are close to the theoretical angles between two (111) planes and between the (100) and (111) planes. Of course, it cannot be said whether or not the square on Fig. 3 is a cube plane or a top view of an octahedron. An ideal cubo-octahedron in two projections is shown on Fig. 5.

Acknowledgment

The authors thank the Office of Naval Research for support.

Manuscript received June 4, 1964.

Any discussion of this paper will appear in a Discussion Section to be published in the June 1965 JOURNAL.

REFERENCES

1. T. H. Yeh and A. E. Blakeslee, *This Journal*, **110**, 1018 (1963).
2. G. A. Wolff, *Amer. Mineral.*, **41**, 60 (1956).

Silicon Phosphide Precipitates in Diffused Silicon

P. F. Schmidt and R. Stickler

Westinghouse Research and Development Center,
Pittsburgh, Pennsylvania

The presence of a silicon phosphide phase in the surface layers of heavily phosphorus-diffused silicon was suggested by the results of tracer experiments. Investigation of suitably thinned silicon specimens then led to the direct observation of the precipitate by transmission electron microscopy, and to its crystallographic identification by means of electron diffraction.

Tracer Work

The occurrence of a steep spike in the phosphorus concentration at the Si/SiO_2 interface, extending into the silicon for a distance of only 1-2,000Å, as detected by tracer techniques has been reported before (1). Figure 1 shows the profile of such a spike, obtained by step-wise dissolution of the phosphorus-doped anodic oxide film which had been used as the diffusion source (1), subsequent multiple anodization of the silicon, and dissolution of the anodically formed oxide in HF between each step. The sloping of the phosphorus concentration in the oxide from left to right is due to the fact that the doped oxide was not protected by a nondoped SiO_2 layer, and that the diffusion was carried out in a sealed quartz tube. Under these conditions initially a large quantity of phosphorus was lost from the doped anodic oxide to the surroundings, but did not diffuse deeply into the quartz walls because of the density of the latter. During the later stages of these long-time diffusion runs the oxide became depleted of phosphorus, and eventually some of the phosphorus from the walls diffused back into the anodic oxide. The activity of the P^{32} contained in the silicon layer which was converted to oxide by anodization, was determined after evaporating the HF solution to dryness in a Teflon tray. The reproducibility of the magnitude of the spike as determined in this fashion was poor, whereas the adjoining portion of the diffusion profile could be reproduced quite accurately from run to run. This fact suggested that the phosphorus in the region of the spike might be present either as elemental phosphorus, precipitated at dislocations, or as silicon phosphide. The existence of a silicon phosphide phase (and its gettering properties for gold), has been suggested by Kooi (2).

In the tracer experiments reported here the P-32 tagged silicon wafers were counted: (*a*) after anodization in the radioactive solution; (*b*) after diffusion; (*c*) after stripping of the original oxide; (*d*) after anodization in nontracer solution (pyrophosphoric acid in tetrahydrofurfuryl alcohol); (*e*) after stripping of the oxide formed by anodization. In addition, the activity of the HF used for stripping the oxide was also determined. It was found that the activity lost from the system when stripping the oxide in HF could be accounted for by the activity of the HF solution, within the somewhat high limit of error of determining the activity in the tray; apparently the distribution of the residue in the tray is not uniform, leading to uncertainties in the analysis.

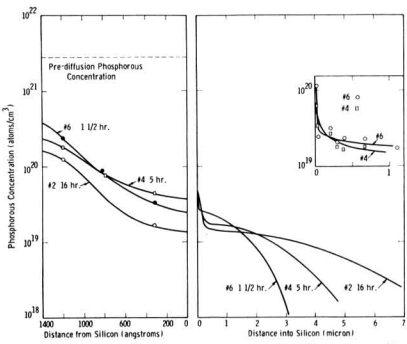

Fig. 1. (left) Phosphorous concentration profile in anodic oxide source after diffusion; (right) phosphorous concentration profile in silicon after diffusion from anodic SiO_2(P) source; parameter: diffusion time at 1175°C.

A large loss of activity from the silicon samples occurred during the first anodizing step, *i.e.*, the phosphorus contained in the surface layer of the silicon was not all incorporated into the oxide, but was largely lost to the anodizing solution. Table I presents the normalized count from two wafers during the various steps described above. The anodization was to 200v at constant current only. On less highly doped silicon, this voltage would correspond to a surface layer of silicon of 332Å ± 5% converted to oxide. In the present case, due to the heavy loss of phosphorus originally contained in the silicon, the increment could be somewhat larger than 332Å.

It is noteworthy that the phosphorus surface concentration, determined after the first anodization from junction depth and sheet resistance, assuming an erfc distribution and using Irvin's data (3), was only 5.2 x 10^{19}/cc on one sample (see Table I).

The assumption of very heavy doping of the outermost layers of the silicon is in agreement with infrared transmission measurements performed on another set of phosphorus diffused wafers. After stripping the original anodic oxide source, these wafers showed a strong structureless absorption, increasing approximately with the square of the wavelength in the region between 2 and 9μ. The strong absorption disappeared completely after the first three anodizations.

The outstanding feature in Table I is the large drop in activity after the anodization step. It is, however, not entirely clear whether any phosphorus is also leached out of the silicon itself when the oxide source is dissolved in HF. The shape of the phosphorus diffusion profile in the oxide (Fig. 1) suggests that this should only be a second order effect, if present at all. The observed behavior, loss of phosphorus from the silicon during anodization, but no or little loss during removal of the oxide in cold HF, is in agreement with the reported chemical properties of

Table I. Normalized count above background from 2 phosphorus-32 diffused silicon wafers

(*a*) Diffused for 54 min at 1050°C in sealed quartz tube with argon backfilling;
(*b*) Diffused for 14 min at 1250°C in sealed quartz tube with argon backfilling.

	1	2	3	4	5
	After anodization in tracer solution	After diffusion	After stripping original oxide	After anodization in nontracer solution	After stripping anodic oxide
(*a*)	226	163	100	36.4	33.5
(*b*)	201	126	100	52.1	44.6

	Sheet resistance after step 5, ohms/square	Junction depth, μ	Phosphorus surface conc. assuming erfc
(*a*)	29	1.07	1.2 x 10^{20}/cc
(*b*)	18	3.47	5.2 x 10^{19}/cc

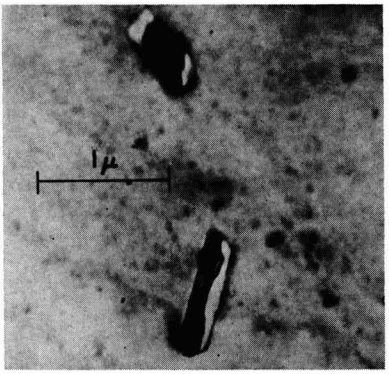

Fig. 2. SiP precipitates in (110) oriented silicon. Transmission electron micrograph.

silicon phosphide (4). SiP is rather resistant to cold dilute acids, whereas its anodization behavior may be expected to be similar to that of (p-type) silicon carbide. Anodization of silicon carbide results in the formation of a dense oxide film, composed presumably entirely of SiO_2 (5).

In order to differentiate between a silicon phosphide phase and elemental phosphorus precipitated at dislocations, the diffused silicon wafers were stripped of the original oxide and were then examined by electron microscopy in transmission.

Electron Microscopic Work

For the examination by direct transmission in the electron microscope, portions of the Si-wafer must be prepared to be transparent to the electron beam (less than 1μ for Si). Small pieces of the Si-wafer were thinned in the central portion by a chemical jet polishing technique (6). By thinning the wafer from one side only, a surface layer approximately 1μ thick can be examined, while carefully timed polishing from the top side and final thinning from the other side allows the examination of layers approximately 1μ thick at any desired distance from the surface (accurate to within $\pm$ 1μ).

The examination of the surface layer of the p-diffused Si-wafers revealed the presence of numerous rod-shapd particles (Fig. 2) oriented along <110> directions, as determined by electron diffraction. Selected area electron diffraction yielded patterns consisting of the reflections from the particle superimposed on that of the <110> pattern of the Si-matrix. The electron diffraction pattern of the particle could be indexed according to structure data reported by Schubert *et al.* (7) for SiAs which is isomorphous with SiP. A detailed report on the structure of SiP and SiAs determined by x-ray diffraction and electron diffraction will be published elsewhere (8), it is briefly summarized here. Contrary to the monoclinic structure of SiAs suggested by Schubert (7) the results of our investigation indicate that SiP has an orthorhombic structure (a = 6.90, b = 9.40, c = 7.68). It precipitates in the Si-matrix with following orientation relationship

$$[010]_{SiP}//[111]_{Si}$$
$$[001]_{SiP}//[110]_{Si}$$

Precipitates, however, could not be detected at other levels below the surface of the Si in accordance with the tracer studies. Thus, the transmission electron microscope observation gives proof of the presence of SiP in the outer regions of the diffused wafer, explaining the anomalous diffusion profile revealed by the tracer experiments. It should be noted that the observations reported here do not exclude the simultaneous presence of phosphorus precipitated in other forms.

Acknowledgment

This work was supported jointly by the Electronics Development Laboratory, Aeronautical Systems Division, Wright-Patterson Air Force Base, Dayton, Ohio, and by Westinghouse Electric Corporation. Thanks are due to Drs. T. W. O'Keeffe and T. J. Phillips for help in the evaluation of the results and to Mr. N. Roney for help with the tracer work.

Manuscript received April 29, 1964.

Any discussion of this paper will appear in a Discussion Section to be published in the June 1965 JOURNAL.

REFERENCES

1. P. F. Schmidt and A. E. Owen, *This Journal*, **111**, 682 (1964).
2. E. Kooi, Recent News Paper, Electrochemical Society Meeting, Pittsburgh, 1963.
3. J. C. Irvin, *Bell System Tech. J.*, **41**, 387 (1962).
4. B. Giessen and R. Vogel, *Z. Metallkunde*, **50**, 274 (1959).
5. P. F. Schmidt, Unpublished data.
6. G. R. Booker and R. Stickler, *British J. Appl. Phys.*, **13**, 446 (1962).
7. K. Schubert, E. Dörre, and E. Günzel, *Naturwissenshaften*, **41**, 448 (1954).
8. T. Phillips and R. Stickler, to be published.

The Effect of Lithium Ion on the Mechanism of the Polarographic Reduction of Benzil in Dimethylformamide

Robert H. Philp, Jr.,[1] Thomas Layloff, and Ralph N. Adams

Department of Chemistry, The University of Kansas, Lawrence, Kansas

The polarographic reduction of benzil in dimethylformamide (DMF) proceeds via a reversible one electron transfer at ca. —1.0v *vs.* SCE followed by an irreversible one electron transfer at ca. —1.6v *vs.* SCE with tetrabutylammonium iodide as the supporting electrolyte (1). The cyclic voltammetry of benzil in DMF with 0.1M tetraethylammonium perchlorate (TEAP) proceeds in a similar fashion at a hanging mercury drop (Fig. 1). The primary reduction wave is found to have $|E_{P\ anodic} - E_{P\ cathodic}| = 59$ mv which is in good agreement with the theoretical value of 58/n mv given by Matsuda and Ayabe for a reversible one electron process (2). An irreversible second reduction wave is observed at —1.6v *vs.* SCE. The one electron transfer step of the primary reduction wave was verified by obtaining the Electron Paramagnetic Resonance (EPR) spectrum of benzil (Fig. 2) by applying a potential just beyond the primary wave employing standard electrochemical *in situ* generation techniques (3). The coupling constants obtained were $a_o = a_p = 1.03$ gauss and $a_m = 0.35$ gauss which is in good agreement with the coupling constants found by

[1] Present address: Department of Chemistry, University of South Carolina, Columbia, South Carolina.

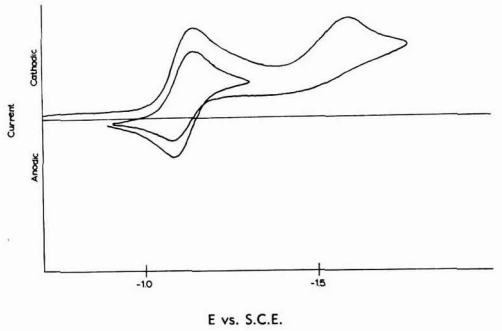

Fig. 1. 10^{-3}M benzil with 0.1 TEAP in DMF

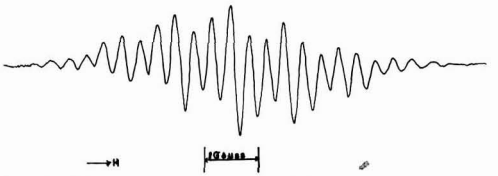

Fig. 2. EPR spectrum of benzil with 0.1M TEAP in DMF. Field increasing toward the right.

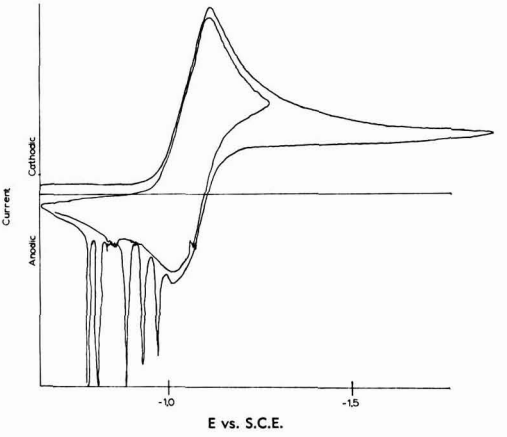

Fig. 3. 10^{-3}M benzil, 0.05M $LiClO_4$, and 0.1M TEAP in DMF

Luckhurst and Orgel via sodium and potassium reduction in tetrahydrofuran (4).

The cyclic polarogram of benzil in the presence of 0.05M lithium perchlorate with 0.1M TEAP in DMF proceeds via a quasi-reversible electrode reaction at a potential corresponding to the primary reduction wave with no lithium ion present. This reduction appears to involve the transfer of two electrons since i_p ($LiClO_4$)/i_p (TEAP) = 2.03 and can proceed either by two consecutive one electron transfers occurring in rapid succession or a one-step two-electron transfer. No EPR spectrum could be obtained with this system by applying a potential just beyond the reduction wave. Thus the EPR experiment did not clarify the electron transfer mechanism of this reaction. In view of the work of Bauld and references therein (5) we suggest the following mechanism

Manuscript received May 18, 1964.

Any discussion of this paper will appear in a Discussion Section to be published in the June 1965 JOURNAL.

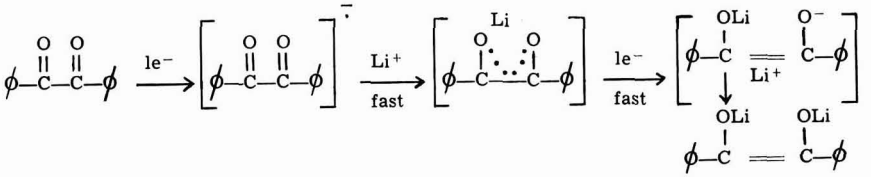

where the follow up reaction of the benzil radical is too fast to obtain its EPR spectrum.

Acknowledgment

This work was supported by the Atomic Energy Commission through contract AT(11-1)-686-40, and this support is gratefully acknowledged.

REFERENCES

1. R. H. Philp, Jr., R. L. Flurry, and R. A. Day, Jr., *This Journal*, **111**, 328 (1964).
2. H. Matsuda and Y. Ayabe, *Z. Electrochem.*, **59**, 494 (1955).
3. L. H. Piette, P. Ludwig, and R. N. Adams, *Anal. Chem.*, **34**, 916 (1962).
4. G. R. Luckhurst and L. E. Orgel, *Mol. Phys.*, **7**, 297 (1964).
5. N. L. Bauld, *J. Am. Chem. Soc.*, **84**, 4345 (1962).

A Correlation of Electrochemical Oxidation Potential of Organic Compounds with Photoionization Potential

W. C. Neikam, Glenn R. Dimeler, and M. M. Desmond

Sun Oil Company, Marcus Hook, Pennsylvania

In studies of electrochemical oxidation of organic substances by polarographic techniques, it has been found in previous work from this laboratory (1) that there is an indication of a linear relation between the half wave potential, $E_{1/2(ox)}$, for oxidation of seven mono- and dinuclear aromatic hydrocarbons, and their ionization potential determined spectroscopically. This relation has been confirmed and extended to include five other hydrocarbon compounds in a more recent paper using photoionization and electron impact ionization potentials (2). Theoretical relations between $E_{1/2(ox)}$ and the energy of the highest occupied molecular orbital have been proposed by Hoijtink (3). The energy factors determining $E_{1/2(ox)}$ for a single electron reaction such as $R \rightarrow O^+ + e_m$ involving a molecule R and its resulting oxidized ionic form O^+ will be given by an equation of the form

$$E_{1/2(ox)} = \alpha I + \Delta E_{solv.} - \beta EA - \frac{T\Delta S^o}{F} - \frac{RT}{F} \ln \frac{f_{o^+} D_R}{f_R D_{o^+}} + C$$

The energy terms are: (i) the ionization potential I modified by a factor α to apply to ionization at the electrode-solution interface, *i.e.*, it corrects I for effects of adsorption on the electrode and the presence of solvent; (ii) the change of heat of solvation $\Delta E_{solv.}$ between R and O^+ expressed as a potential; (iii) the electron affinity EA of the metal m, (*i.e.*, the negative of the relevant work function) modified by a coefficient β to apply to the electrode-solution interface where EA may be perturbed by the effect of the solvent and by oxide film formation; (iv) the term $\Delta S°$ is the sum of entropy changes associated with change of solvation of R to O^+ and effects associated with the temperature dependence of EA due to adsorbed species (mainly solvent) at the metal surface; (v) the logarithmic term involves the activity coefficient f and diffusion coefficient D of reduced and oxidized species in the reaction; (vi) the constant C is determined by the potential of the reference electrode used in the evaluation of $E_{1/2(ox)}$.

In a series of electrochemical oxidations for a range of compounds, changes in the $\Delta S°$ terms and activity coefficient ratio will be expected to be small compared with changes in I. These terms may hence be grouped with C as a combined constant C' and $E_{1/2(ox)}$ may be written

$$E_{1/2(ox)} = \alpha I + \Delta E_{solv.} - \beta EA + C'$$

Hence, for a given electrode metal where βEA may be assumed constant, $E_{1/2(ox)}$ will be proportional to I and will involve any change in solvation energy $\Delta E_{solv.}$ involved in the reaction $R \rightarrow O^+ + e_m$.

In the present paper, the above relations are tested for a series of 23 widely different compounds including both aromatic hydrocarbons and their halogen derivatives, together with olefins. The relation is extended to cover, in addition, $E_{1/2(ox)}$ data for 12 polycyclic hydrocarbons in relation to ionization potential obtained from charge transfer spectra and absorption spectra.

Experimental

The $E_{1/2(ox)}$ data reported here were measured in 0.50*N* $NaClO_4$, 0.10*N* $AgClO_4$.3 CH_3CN (4) acetonitrile solution against a Ag, Ag^+ reference electrode. The anode was a platinum wire, 0.50 cm in length and 0.08 cm in diameter, rotated at 600 rpm. The repeatability of $E_{1/2(ox)}$ values on a Sargent Model XXI polarograph was within 0.02v. Corrections for the resistance of the solution was found to be negligible. The concentration of the organic depolarizer was 1.00 mM in all cases. Further details have been described in a previous article from this laboratory (1) and by Lund (4).

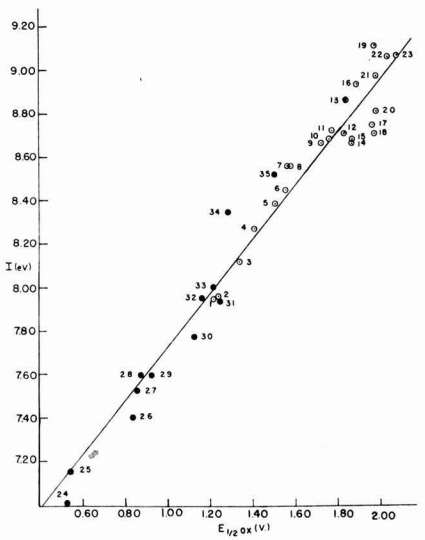

Fig. 1. Plot of photoionization potential (ev) against $E_{1/2(ox)}$ (v) *vs.* the Ag, 0.1*N* Ag^+ reference electrode: ○, ref. (5), (6); ●, ref. (4), (9). Numbers refer to compounds listed in Table I.

Table I. Oxidation potentials and photoionization potentials for organic compounds

No. in Fig. 1	Organic compound	$E_{1/2(ox)}$, v *vs.* Ag, Ag^+	I^e, ev photo-ionization
1	2-Methylnaphthalene	1.22 1.15[a]	7.95
2	1-Methylnaphthalene	1.24 1.13[a]	7.96
3	Naphthalene	1.34 1.24[a] 1.31[b]	8.12
4	1,2,4-Trimethylbenzene	1.41	8.27
5	1,3,5-Trimethylbenzene	1.51 1.50[a]	8.39
6	p-Xylene	1.56 1.47[a]	8.445
7	o-Xylene	1.57 1.59[a]	8.56
8	m-Xylene	1.58 1.61[a]	8.57
9	p-Bromotoluene	1.72	8.67
10	p-Chlorotoluene	1.76	8.69
11	Iodobenzene	1.77	8.73
12	2,3-Dimethyl-1,3-butadiene	1.83	8.72
13	2-Methyl-1,3-butadiene	1.84	8.87
14	t-Butylbenzene	1.87	8.67
15	Isopropylbenzene	1.87	8.69
16	Cyclohexene	1.89	8.94
17	Ethylbenzene	1.96	8.75[d]
18	n-Propylbenzene	1.97	8.72
19	2-Methyl-1-butene	1.97	9.12
20	Toluene	1.98 1.68[a] 1.93[b]	8.82
21	Bromobenzene	1.98	8.98
22	1,3-Butadiene	2.03	9.07
23	Chlorobenzene	2.07	9.07

[a] Data of ref. (2).
[b] Data of ref. (4).
[c] Data of ref. (5).
[d] Data of ref. (6).

Results and Discussion

In Fig. 1 is shown a plot of photoionization potential (5, 6) *vs.* $E_{1/2(ox)}$ for the 23 compounds of Table I[1] (open circles). Also plotted in Fig. 1 (closed circles) is the experimental data from Table II for 12 compounds whose ionization potentials have been de-

[1] The numerical data used in constructing Fig. 1 are recorded in Table I to provide a record for other workers in this field.

Table II. Comparison of I calculated polarographically with I calculated from charge transfer spectra and from absorption spectra

No. of Fig. 1	Organic compound	I, ev charge transfer spectra	I^a, ev, adsorption spectra	I, ev, polarographic	$E_{1/2(ox)}$, v *vs.* Ag, Ag^+
24	Tetracene	6.98[b]	6.94	7.15	0.54[g] 0.47[f]
25	Perylene	7.13[c]	7.10	7.17	0.55[e,f]
26	Anthracene	7.42[b]	7.42	7.52	0.84[g] 0.79[f] 0.83[g]
27	Pyrene	7.50[c]	7.70	7.55	0.86[e,f]
28	1,2-Benzanthracene	7.55[b]	7.52	7.57	0.88[e,f]
29	Coronene	7.63[d]	7.64	7.63	0.93[e,f]
30	Chrysene	7.71[b]	7.82	7.88	1.13[g] 1.05[f] 1.10[g]
31	Hexamethylbenzene	7.95[d]	—	7.92	1.16[g]
32	Phenanthrene	8.11[c]	8.07	8.01	1.23[g] 1.20[f]
33	Triphenylene	7.95[d]	—	8.04	1.25[e,f]
34	1,2,4,5-Tetramethylbenzene	8.35[d]	—	8.09	1.29[g]
35	Styrene	8.53[d]	—	8.34	1.50[g]

[a] From the data of ref. (8).
[b] Average value of the data from ref. (9-11).
[c] Average value of data from ref. (9-12).
[d] Data of ref. (9).
[e] Data of ref. (4). These data and that from this laboratory were used to calculate I.
[f] Data of ref. (2).
[g] Data from this laboratory.

termined from charge transfer spectra. Included in Table I and Table II are the values of $E_{1/2(ox)}$ obtained by Pysh and Yang, and by Lund. The agreement is not as good as is expected considering the precision with which polarograph oxidation potentials can be obtained. The $E_{1/2(ox)}$ values obtained in this laboratory utilized the same reference electrode and electrolyte concentration as was used by Lund. Pysh and Yang used 2M $NaClO_4$ electrolyte solution rather than the 0.5M solution used in this laboratory and by Lund.

However, experiments conducted in this laboratory, in efforts to duplicate Pysh and Yang's work, with 2M $NaClO_4$ but using the Ag, Ag^+ reference gave the same results as in 0.5M $NaClO_4$. The source of discrepancy must be with the reference electrode used. Pysh and Yang used an aqueous calomel electrode with a KCl agar bridge to the electrolyte solution. It has been our experience that this reference causes considerable experimental difficulty in obtaining $E_{1/2(ox)}$ values apparently due to salt precipitation at the agar acetonitrile interface and contamination of the electrolyte solution with water from the agar bridge. The Ag, Ag^+ reference used in this laboratory, and by Lund, avoids difficulties due to junctions or contamination by water. It has the added advantage that it may be made quite large and placed very near the working electrode thus avoiding large corrections for IR drop across the test solution. For these reasons, we believe it is much to be preferred over aqueous references, and we suggest that results obtained with the Ag, Ag^+ reference are more reliable.

The data reported by Pysh and Yang for p-xylene, toluene, and the naphthalenes differ substantially from those from this laboratory and that reported by Lund; we have tried to resolve this difficulty by careful repetition of experiments with American Petroleum Institute standards. We can discover no experimental basis for doubting the validity of our results and the discrepancy must lie in the choice of reference electrode. In this regard, it should be noted, however, that the values obtained by Pysh and Yang for toluene and p-xylene are nearer those expected, from a M.O. consideration of the inductive effect of the methyl group, than are ours.

The least squares equation based on the data represented by the 23 open circles in Fig. 1 is

$$E_{12/(ox)} = 0.827\,I - 5.40\text{v}$$

The values of I predicted by the above equation for the hydrocarbons of Table II are compared with experimental values in Table II; the agreement is good.

The value of the constant 5.40v in the above empirical equation should involve the work function of platinum. The corresponding constant for oxidation at a palladium anode obtained on 16 compounds at this metal is 5.04v. This value differs from that for the platinum electrode by 0.36v which is in good agreement with the difference of the average values of the electron work function for platinum, [5.29 (7)] and palladium [4.82 (7)] *viz.*, 0.47v.

The fact that a very satisfactory straight line is obtained (Fig. 1) must indicate that either (i) the $\Delta E_{solv.} - T\Delta S^\circ_{solv.}$ (*i.e.*, the free energy change in solvation of R as it is oxidized to O^+) term is constant for the whole series of compounds and largely independent of their structure. This implies that ionization produces a localized charge which interacts with solvent with a constant energy independent of the structure of the whole ion, the remainder of which is then solvated with the same energy as that of the neutral reduced form R. In the solvent used this localized charge is probably an ion pair involving interaction with the anion of the electrolyte. The behavior observed indicates that effects associated with delocalization of the charge on the ion (which would be specific for the various molecules involved in the series) are not significant or (ii) the solvation free energy from $\Delta E_{solv.} - T\Delta S^\circ_{solv.}$ changes in proportion to the value of I (2) and is thus included in the value of the proportionality constant 0.827.

As long as a unit electric charge is involved, it does not seem that the latter supposition would be the reason for the behavior observed so that the explanation suggested in (i) must be preferred.

Acknowledgment

The authors are indebted to Dr. Brian Conway for helpful discussions during the course of this research.

Manuscript received March 17, 1964.

Any discussion of this paper will appear in a Discussion Section to be published in the June 1965 JOURNAL.

REFERENCES

1. J. West Loveland and G. R. Dimeler, *J. Anal. Chem.*, **33**, 1196 (1961).
2. E. S. Pysh and N. C. Yang, *J. Am. Chem. Soc.*, **85**, 2124 (1963).
3. G. J. Hoijtink, *Rec. trav. chim.*, **77**, 555 (1958).
4. H. Lund, *Acta Chem. Scand.*, **11**, 1323 (1957).
5. K. Watanabe, *J. Chem. Phys.*, **26**, 542 (1957).
6. W. C. Price, *Chem. Rev.*, 257 (1947).
7. H. B. Michaelson, *J. Appl. Phys.*, **21**, 536 (1950).
8. Haruo Kuroda, *Nature*, **201**, 1214 (1964).
9. C. Briegleb and J. Czekalla, *Z. Elektrochem.*, **63**, 6 (1959).
10. H. Kuroda, K. Yoshihara, and H. Akamatu, *Bull. Chem. Soc. Japan*, **35**, 1604 (1962).
11. M. Kinoshita, *ibid.*, **35**, 1609 (1962).
12. H. Kuroda, M. Kobayashi, M. Kinoshita, and S. Takemoto, *J. Chem. Phys.*, **36**, 457 (1962).

A Technique for Studying Oxygen Diffusion and Locating Oxide Inclusions in Metals by Using the Proton Radioactivation of Oxygen-18

Ralph H. Condit and J. Birch Holt

Lawrence Radiation Laboratory, University of California, Livermore, California

Numerous techniques have been described for the activation analysis of oxygen (1). In view of the importance of oxygen diffusion in many materials and effects of oxygen on the properties of metals, we have been adapting these activation techniques along with autoradiographic methods to locate oxygen, particularly the oxygen-18 tracer. The most generally applicable procedure appears to be that which starts with the proton bombardment of a specimen, wherein the O^{18} (p, n) F^{18} reaction gives fluorine-18. This emits a 0.6 Mev positron and has a half-life of 112 min. Since oxygen-18 is present in 0.2% concentration in normal oxygen, oxide inclusions may be identified in a metallographic section. Also, the use of enriched oxygen-18 together with this activation procedure allows the study of grain boundary and volume diffusion in the

same way as is frequently done using radioactive tracers. Some of the factors of importance in these types of procedures have been discussed in studies of photosynthesis (2) and in the measurement of the thickness of oxide layers on metals (3).

In our procedure we bombard the specimen with 2.7 Mev protons. The reaction is endothermic with a Q of —2.45 Mev (4). Under these conditions, the recoil in most solids will be less than 0.1μ (5). For the purposes of this experiment, therefore, it may be stated that the activity is produced in the same place as the inclusion or the tracer. The neutrons from this reaction will have energies up to 130 kev. Neutrons may also be produced by proton reactions with other elements in a specimen, and these may have higher energies. The additional activation which these neutrons induce in most specimens will be less than a few per cent of the reactions generating them, and the amount of this second-step activation can be minimized by using relatively thin specimens, a few millimeters being a convenient size in many studies. If a specimen is not chemically homogeneous, this activation may not be uniform, and in such cases a control experiment would be required. A zirconium foil partly oxidized in oxygen-18 and placed over the specimen can serve as a convenient neutron source while shielding it from the proton beam.

The protons will activate other elements than the oxygen, but a large fraction of these will yield half-lives short compared with the fluorine-18, and these can be permitted to die out before starting an autoradiograph exposure. Other products will have a sufficiently long half-life that their specific activity will be well below that of the fluorine. In addition, the nuclear coulomb repulsion of an incoming proton increases with atomic number, and the cross section for p,n and p,γ reactions of a 2.7 Mev beam will begin dropping off rapidly above atomic number 40 (6). The degree to which specific elements will obscure the activity due to oxygen activation is currently being investigated. On the basis of literature references [see ref. (3)] and our measurements it is clear that the following elements will cause little if any interference: Be, C, N, F, Mg, Na, Al, Si, P, K, Mn, Co, As, Y, Nb, and those elements above atomic number 50. A few parts per million of oxygen in the presence of these elements or their compounds should be detectable. Others in which some background activity will be generated are: Cr, Fe, Cu, Zr, Rb, and Pd. More serious difficulty will be encountered with Li, B, Ca, Ti, Ni, Ge, Sr, Zn, Cd, Se, and Ag listing them in approximate order of decreasing ease of activation. It might be noted that the energy spread of the available proton beam may vary from one laboratory to another, and the amount of unwanted activation due to the high energy tail on the distribution may differ.

A principal experimental consideration on the use of this technique is the problem of specimen heating in the vacuum of an ion accelerator. For example, a typical 5 μa proton beam put 14w of energy into the sample. It must be ascertained that the diffusion of oxygen during this heating will be negligible. Another difficulty in studies of very small amounts of oxygen in a metal arises from the fact that residual air in the target chamber may react with the hot surface to form a small additional oxide layer.

One reason for using a 2.7 Mev beam is that this energy is low enough to minimize unwanted activation. Another is that while it is only 0.11 Mev above the reaction threshold of 2.59 Mev for the oxygen activation this energy spread includes the first resonance peak at about 2.65 Mev with a cross section of about 40 millibarns (7-8). The essential point is that protons impinging on a typical solid will lose this excess energy after passing about 5μ into it, and the activation will be confined to this surface region. Thus, even though the fluorine-18 positrons might have a range up to 0.1 cm, the surface features of oxygen distribution can be fairly well resolved by autoradiograph film without interference from subsurface activity. In order to take advantage of the fact that this active layer is about 5μ, the film used should have an emulsion of similar thickness, and such stripping films are commercially available.

A diffusion specimen may be beveled in the manner of Kurtz *et al.* (9, 10) before irradiation, and from the distribution of activity along the surface cut at a small angle to the original diffusion interface the oxygen penetration profile may be determined. We are using this procedure to study the grain boundary diffusion of oxygen, and Fig. 1 is an autoradiograph which illustrates the type of result which may be obtained. It was taken on a magnesium oxide bicrystal in which the boundary is roughly a 10° tilt boundary superimposed on a 15° twist. The specimen was annealed in 60% oxygen-18 at 1610°C for 17 hr. The irradiated region is not completely circular, since two collimator shields in the cyclotron beam were not in perfect alignment. The important features of the autoradiograph are the beveled portion in which the grain boundary may be seen, the initial surface below this in the picture and the initial surface in the bottom portion which has a partial cover of platinum. This platinum deposits on the surface during the high-temperature anneal as a result of the usual small amount of vaporization of the platinum crucible in which the specimen was supported. It does not seem to inhibit the exchange of oxygen between the gas and the magnesium oxide. The bevel angle is 0.23° so that on the irradiated spot having a radius of 0.5 cm the new surface at the edge is about 20μ below the original surface. Thermal grooving at the grain boundary which may have occurred during the high-temperature anneal was less than 1μ, so the darkening along it must be due to oxygen diffusion. On the basis of single crystal oxygen exchange measurements (11) the mean penetration of oxygen into the bulk of the specimen should be about 2μ. A microdensitometric inspection of the autoradiograph indicates penetration of oxygen at the grain boundary to the full 20μ depth with the likelihood that it went yet deeper. This activation technique is being applied to further study of diffusion.

Acknowledgment

The authors wish to thank the staff of the 90-in. cyclotron at the Lawrence Radiation Laboratory,

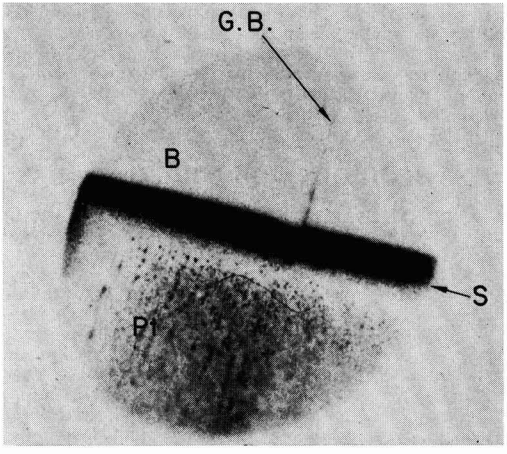

Fig. 1. Autoradiograph of proton irradiated MgO bicrystal: S, initial surface of the specimen; Pt, region of the crystal where surface remained covered with platinum during proton activation; B, beveled region of the crystal, the bevel angle is 0.23°, and the right edge is 20μ below the initial interface; G.B., position of the grain boundary.

Livermore, for their help in carrying out these experiments. Professor C. E. Birchenall of the University of Delaware has also made valuable suggestions in the course of this work. This work was performed under the auspices of the U.S. Atomic Energy Commission.

Manuscript received March 26, 1964.

Any discussion of this paper will appear in a Discussion Section to be published in the June 1965 JOURNAL.

REFERENCES

1. R. C. Koch, "Activation Analysis Handbook," Academic Press, New York (1960).
2. I. Fogelstrom-Fineman, O. Holm-Hansen, B. M. Tolbert, and M. Calvin, *Intern. J. Appl. Radiation and Isotopes*, **2**, 280 (1957).
3. B. A. Thompson, *Anal. Chem.*, **33**, 583 (1961).
4. V. J. Ashby and H. C. Catron, "Tables of Nuclear Reaction Q Values," University California Radiation Laboratory Report No. 5419 (1959).
5. B. G. Harvey, "Annual Review of Nuclear Science," E. Segre, Editor, **10**, 235 (1960).
6. J. Mattauch, "Nuclear Physics Tables," Interscience Publishers, Inc., New York (1946).
7. H. Mark and C. Goodman, *Phys. Rev.*, **101**, 768 (1956).
8. J. M. Blair and J. J. Leigh, *ibid.*, **118**, 495 (1960).
9. A. D. Kurtz, B. L. Averbach, and M. Cohen, *Acta Met.*, **3**, 442 (1955).
10. H. C. Gatos and A. D. Kurtz, *J. Metals*, **6**, 616 (1954).
11. Y. Oishi and W. D. Kingery, *J. Chem. Phys.*, **33**, 905 (1960).

The Phase Diagram of Cobalt Monoxide at High Temperatures

Bertina Fisher and D. S. Tannhauser

Department of Physics, Technion-Israel Institute of Technology, Haifa, Israel

In the course of measuring the electrical properties of CoO, we determined the phase diagram, *i.e.*, the region of existence of the material and the dependence of the ratio Co/O on temperature and pressure, in the range $920 < T < 1350°C$ and the range of pressures $10^{-12} \leq P(O_2) \leq 1$ atm. This was done by a combination of gravimetric and electrical measurements. The results are described by the parameter x in the formula CoO_{1+x}, and appear in Fig. 3 in the form $T = f[P(O_2)]$ at $x =$ constant.

Two samples of cobalt metal sheet (Johnson-Matthey spectrographically standardized, 0.1 mm thick) were suspended in the furnace on platinum wires attached by spotwelding. One sample with four wires was used for electrical measurements, the other one was hung by a single wire from a balance with a sensitivity of about 0.05 mg. The two samples were very close to each other, and a Pt/PtRh thermocouple measured their temperature. A mixture of either O_2 and CO_2 or CO_2 and CO flowed through the furnace, and the partial pressures of oxygen were calculated from the equilibrium constants given by Kassel (1). Oxidation to equilibrium was complete in less than 10 min at 1350°C, and the samples kept their shape. The upper limit of the working range was given by the start of rapid evaporation of both platinum and cobaltmonoxide, and the lower limit by the long time the sample took to reach equilibrium below 900°C. The weight of the metallic cobalt in the weighing sample was determined accurately on a microbalance and was about 1000 mg, so that a change of 3×10^{-4} in x could be detected.

Figure 1 shows the relation between x and the conductance $\Sigma = 1/R$ at various temperatures; it is seen to be linear over most of the range. Since the balance used for weighing in the furnace had a small range and could therefore only measure changes in x, we determined the zero point on the abscissa, *i.e.*, the point of stoichiometric weight, by extrapolating the straight portion of the Σ *vs.* x plot to zero conductance. This zero point was checked independently by the quenching in air of some samples which were oxidized in $P(O_2) = 1$ atm at various temperatures, and by direct weighing on a microbalance of the total oxygen uptake during oxidation. The agreement was better than 5×10^{-4} in x. Values of x in Fig. 1 appear in Fig. 3 as lines of constant composition for $x \geq 2 \cdot 10^{-3}$.

The curves for $x < 2 \cdot 10^{-3}$ were determined as follows: the plot of $\log \Sigma$ *vs.* $\log P(O_2)$ (Fig. 2) gave two distinct regions, region A with slope 1/4 at higher oxygen pressures, corresponding essentially to the range $x > 1 \cdot 10^{-3}$, and region B with slope 1/6 at lower pressures. To explain this behavior we shall assume that the dominant defects in the lattice are metal vacancies which can be singly and doubly ionized. Following the terminology of Kroeger and Vink (2) we can write

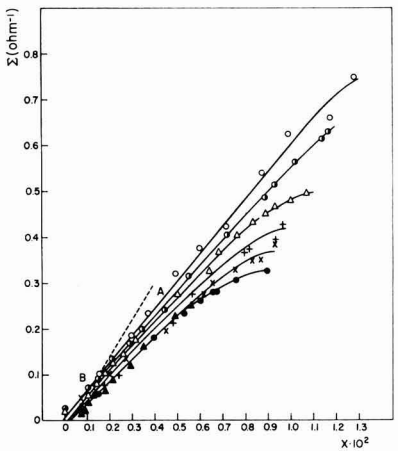

Fig. 1. Conductance *vs.* excess oxygen in cobalt monoxide. x is defined by the formula CoO_{1+x}; A is the region of log Σ = 1/4 [log $P(O_2)$] + const; B is the region of log Σ = 1/6 [log $P(O_2)$] + const (see Fig. 2). Symbols, T, °C: Open circle, 1347; half dark circle, 1285; open triangle, 1191; +, 1129; X, 1094; dark circle, 1035; dark triangle, 986.

$$\frac{[V_M]}{P(O_2)^{1/2}} = K_{xo} \exp\left(-\frac{\Delta H_v}{kT}\right) \equiv K_x \qquad [1]$$

$$\frac{p\,[V_M']}{[V_M]} = K_{10} \exp\left(-\frac{E_1}{kT}\right) \equiv K_1 \qquad [2]$$

$$\frac{p\,[V_M'']}{[V_M']} = K_{20} \exp\left(-\frac{E_2}{kT}\right) \equiv K_2 \qquad [3]$$

$$[V_M'] + 2[V_M''] = p \qquad [4]$$

$$[V_M] + [V_M'] + [V_M''] = x \qquad [5]$$

where $[V_M]$ is the molar fraction of un-ionized vacancies in the lattice, $[V_M']$ is the molar fraction of singly ionized vacancies, $[V_M'']$ is the molar fraction of

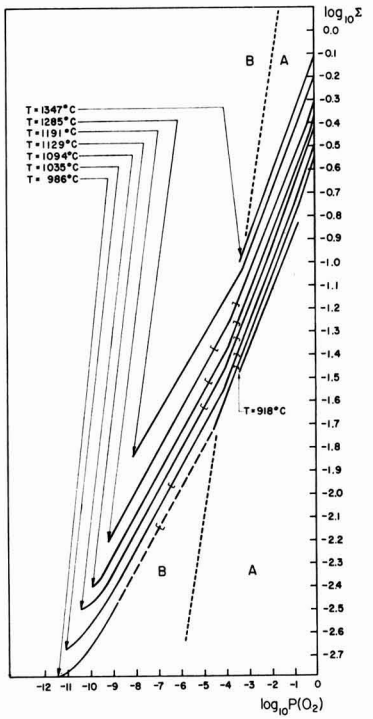

Fig. 2. Logarithm of conductance of cobalt monoxide vs. logarithm of partial pressure of oxygen at various temperatures; the conductance is measured in ohm^{-1} and the pressure in atmospheres. The brackets indicate the range where $P(O_2)$ may contain a large error because of the finite purity of CO_2 and the high mixing ratios in this range.

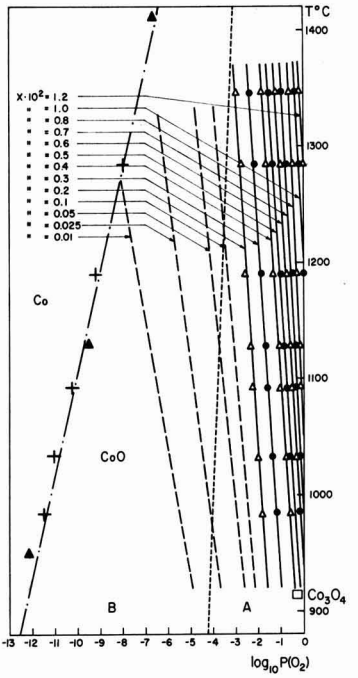

Fig. 3. Phase boundary Co-CoO and lines of constant composition of CoO_{1+x} in the range of temperatures 920°-1350°C. The pressure is measured in atmospheres; +, points on the phase boundary in the present work; ▲, points on the phase boundary given in the literature (4); □, point on the boundary CoO-Co_3O_4; ———, measured compositions; — — —, compositions calculated from conductance measurements; - - - -, boundary between regions A and B (see Fig. 2).

doubly ionized vacancies, p is the molar fraction of free holes and K_x K_1 K_2 are equilibrium constants which depend on the temperature in the manner indicated. Equation [5] is exact only for small molar fractions. These equations give, when $[V_M'] >> [V_M'']$

$$\Sigma = C\mu ep = C\mu e\ (K_xK_1)^{1/2}\ P(O_2)^{1/4} \qquad [6]$$

and when $[V_M''] >> [V_M']$

$$\Sigma = C\mu ep = C\mu e\ (2K_x\,K_1\,K_2)^{1/3}\,P(O_2)^{1/6} \qquad [7]$$

where μ is the mobility, e is the elctronic charge, and the constant C contains the geometry of the sample as well as the conversion factor from molar fraction to the number of charge carriers per cm^3.

When μ is independent of the concentrations we get two linear ranges of $\log \Sigma = f[\log P(O_2)]$ with slopes of 1/4 and 1/6, *i.e.*, the observed behavior.

The linear relation between Σ and x in range A of Fig. 1 shows that $[V_M] << [V_M']$, and therefore according to Eq. [4] and [5] $p = x$ and $\Sigma = C\mu ex$. At the highest values of oxygen pressure x rises faster than Σ, this indicating that we are getting into the range where $[V_M]$ and $[V_M']$ are of the same order of magnitude. In range B the slope of $\Sigma = 2C\mu ex$ *vs.* x should be twice as large as in range A, but this range is so short in terms of x that the difference in slopes is not noticeable.

Figure 1 shows that $C\mu e$, which is given by the slope of Σ *vs.* x, is practically independent of temperature in the range of temperatures studied. Taking an average value of $C\mu e$ we can then calculate p from the curves of Fig. 2, and from that the molar fraction of metal vacancies $x = p$ or $x = \frac{1}{2}p$, respectively. Results appear in Fig. 3 as curves for $x < 2 \cdot 10^{-3}$. It should be noted that we have neglected $[V_M]$ in this range, this being permitted because $[V_M] < p$ already in most of range A, and $[V_M]$ decreases much faster with $P(O_2)$ than p. Naturally the curves for lowest x rely on the assumption that the intrinsic defect structure is negligible, *i.e.*, that no oxygen vacancies appear at these values of x. The analysis of the results assumes that the mobility is independent of charge carrier concentration. This seems to be a reasonable assumption since otherwise the dependence of the conductance on $P(O_2)$ would not give straight lines on a log-log plot.

The results agree with previous measurements of Carter and Richardson (3) at $P(O_2) = 1$ atm and $P(O_2) = 0.005$ atm within their limit of error.

The phase boundary between the CoO and Co phases was determined essentially by the sudden break in the conductance at the boundary. It agrees with results given in "Cobalt monograph" (4). Only one point on the CoO-Co_3O_4 boundary could be determined, since Co_3O_4 is not stable in $P(O_2) < 1$ atm above 920°C. The point agrees with the literature (5).

A full account of the electrical properties of CoO will be published later.

Manuscript received Jan. 27, 1964; revised manuscript received June 15, 1964. This work constitutes part of the thesis to be submitted by one of the authors (B.F.) to the Senate of the Technion in partial fulfillment of the requirements for the D.Sc. degree.

Any discussion of this paper will appear in a Discussion Section to be published in the June 1965 JOURNAL.

REFERENCES
1. L. S. Kassel, *J. Am. Chem. Soc.*, **56**, 1838 (1934).
2. F. A. Kroger and H. J. Vink, "Solid State Physics," Seitz and Turnbull, Editors, Vol. 3, p. 310, Academic Press Inc., New York (1956).
3. R. E. Carter and F. D. Richardson, *Trans. AIME*, **200**, 1244 (1954).
4. "Cobalt Monograph," Edited by Centre d'Information du Cobalt, Brussels, 1960, Table 14, p. 159.
5. C. R. Johns and W. M. Baldwin, *Trans. AIME*, **185**, 720 (1949).

Thin Silicon Film Growth on Polycrystalline Alumina Ceramic

V. Y. Doo

Components Division, International Business Machines Corporation, Poughkeepsie, New York

Epitaxial growth of thin films by vapor deposition on a single crystal substrate of the same material has been carried out on various semiconductor materials, such as germanium, silicon, gallium arsenide, silicon carbide, etc. In those cases where the single crystal substrate material differed from the film material and their physical properties such as the crystal structure, lattice parameter, coefficient of expansion, etc., were compatible, successful epitaxial growth has been reported, *e.g.*, GaAs on Ge and GaP on GaAs (1, 2). However, when the substrates were of polycrystalline material which differed from the film material to be grown and their physical properties were grossly different, it was rather difficult, if not impossible, to grow large crystal films.

Epitaxial growth of silicon on silicon substrate has been in production during the last few years. However, the growth of large crystal silicon film on polycrystalline alumina substrate has involved great difficulties. Rasmanis (3) reported that large-grain silicon films have been grown on alumina substrates which were coated with a glassy layer prior to the film growth. The purpose of this paper is to report a different technique to grow large-grain silicon films on alumina.

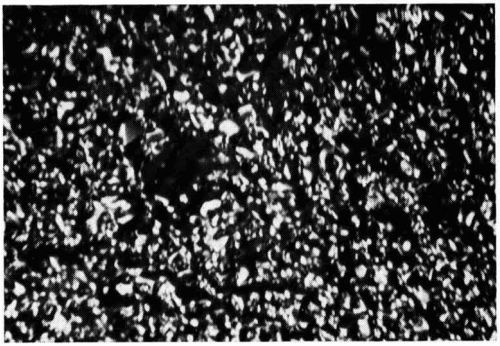

Fig. 1. Polycrystalline silicon film grown on 96% Al_2O_3 ceramic, silicon crystallites of 1-3μ diameter. Magnification 520X.

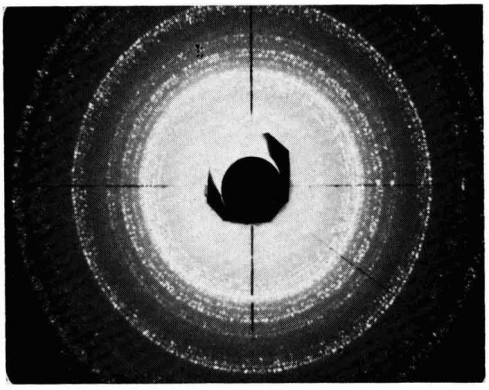

Fig. 2. Laue back-reflection x-ray pattern of polycrystalline silicon film shown in Fig. 1. Crystallites are randomly oriented.

Experiment and Results

The substrate material was mostly of 96% Al_2O_3 and some 99% Al_2O_3 alumina ceramic slides, about ½ x ½ x 40 in./1000 in dimensions. These ceramic slides were rather porous and their grain size was about 1μ in diameter. A thin film of silicon, (approximately 12-15μ thick) was deposited on the substrate by the reduction of silicon tetrachloride by hydrogen at elevated temperature. The as-grown silicon film is shown in Fig. 1. The grain size of the silicon film was about the same as that of the substrate. The x-ray Laue back-reflection pattern showed that the silicon crystals were randomly oriented and their size was quite uniform (Fig. 2).

Annealing at temperatures near the melting point of silicon or at the incipient fusion temperature caused limited grain growth. Figures 3 to 5 show

Fig. 3 Polycrystalline silicon film annealed 30 min at about 5°-10°C below the melting point of silicon. Magnification 520X.

Fig. 4. Same as Fig. 3. except the annealing temperature was very close to, or at, the incipient fusion point. Magnification 520X.

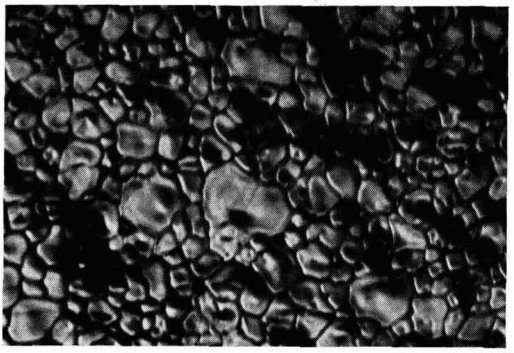

Fig. 5. Same as Fig. 3, except the annealing temperature was at the incipient fusion point. Magnification 520X.

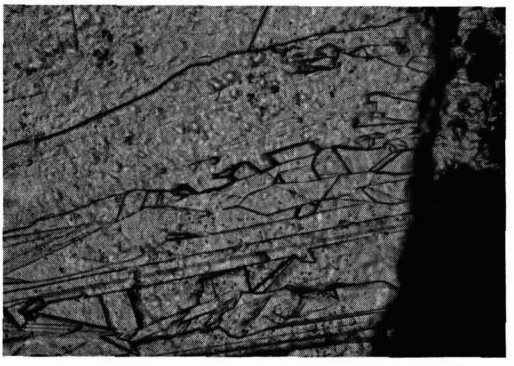

Fig. 6. Film crystals grown by the melt-regrowth method, near the border of molten zone. Magnification 37X.

the silicon film after 30 min annealing at a few degrees below the melting point of silicon, very close to the incipient fusion temperature, and at the incipient fusion temperature, respectively. It is apparent that only the region annealed at the incipient fusion temperature had some degree of growth (from 1μ to about 10-25μ). The region annealed only a few degrees below the melting point of silicon shows very little grain growth. For practical purposes, however, even grains annealed at the incipient fusion temperature are too small to have much value in device application.

A melting and regrowth technique was used to obtain large grain silicon films. A polycrystalline silicon film of about 12-15μ thick was first deposited on the alumina substrate. It was followed by heating to about 5°-15°C above the melting point of silicon until a large part of the silicon film was completely melted. Then the temperature was rapidly lowered to about 30°-50°C below the melting point until the molten silicon film was crystallized, and finally, the sample was slowly brought down to room temperature. Figure 6 shows the regrown silicon crystals near the border of the molten zone. Since the neighboring unmelted crystallites could act as the nuclei in regrowth, some of the grains were relatively small. However, further away from the border, much larger crystals were observed. Figure 7 shows part of a large silicon crystal. Many crystals of about 500μ x 3000μ have been observed. Figure 8 shows the x-ray Laue back-reflection pattern of a large silicon crystal. The orientation of this crystal was [201]. All the silicon films grown on alumina substrate by the melt-regrowth technique were p-type and the resistivity of the film grown on the 96% Al_2O_3 substrate was ranged from 0.0005-0.009 ohm-cm, and that on the 99% Al_2O_3 substrate was about 0.05-0.10 ohm-cm. The samples were then cleaned by light acid etch and subsequently used as the substrate for epitaxial growth. About 5 to 8μ silicon film was grown on the large grain silicon substrate by the conventional vapor growth technique (the reduction of $SiCl_4$ by hydrogen at elevated temperature). No dopant was intentionally added to the epitaxial film. The epitaxial film remained p-type, and the surface resistivity of the films grown on 96% Al_2O_3 ceramic was about 0.03-0.07 ohm-cm and that on 99% Al_2O_3 was about 0.5-1.0 ohm-cm.

A p-n junction was formed in the epitaxial films by phosphorus diffusion. It was followed by masking and mesa etch. Figure 9 shows a single crystal mesa, whose dimension is about 250 x 375μ. Figure 10 shows another mesa, which has a line cutting across the mesa.

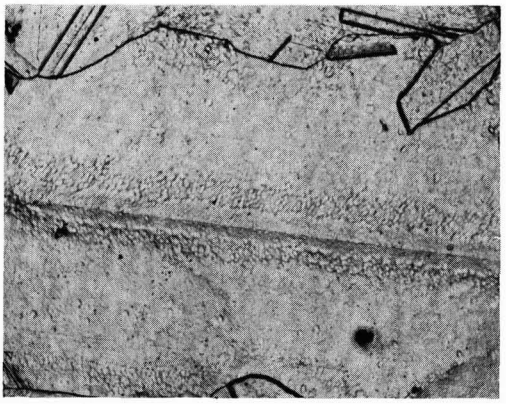

Fig. 7. Same as Fig. 6 except it is about 6-7 mm away from the border of molten zone. Magnification 37X.

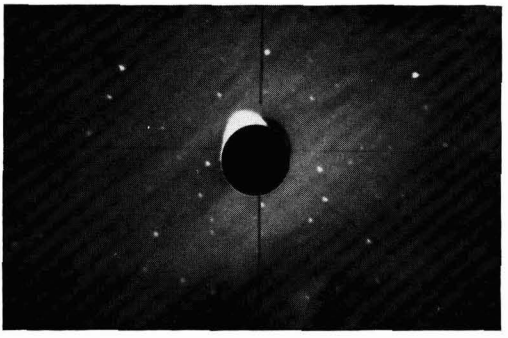

Fig. 8. Laue back-reflection x-ray pattern of a large crystal. Presence of some substructure is indicated and the misorientation is not more than a few minutes.

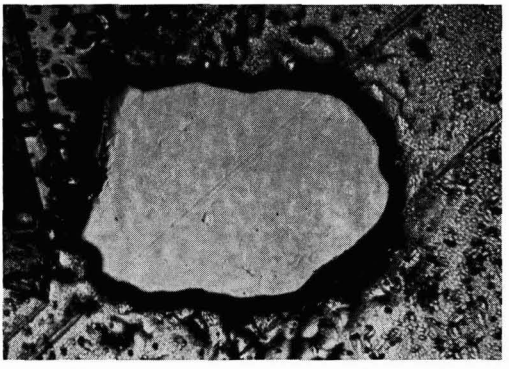

Fig. 9. Single crystal mesa after melt-regrowth, epitaxial growth, phosphorus diffusion, and mesa etch. Magnification 97X.

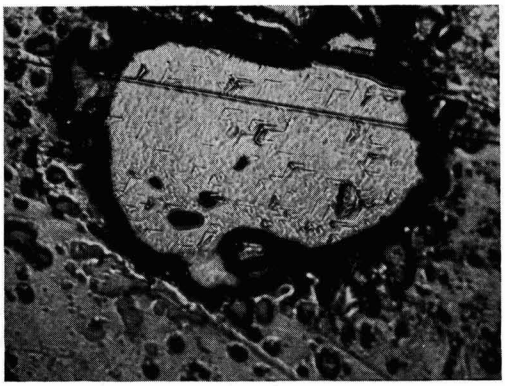

Fig. 10. Same as Fig. 9. The oriented surface defects indicate very small misorientation across the small angle boundary. Magnification 97X.

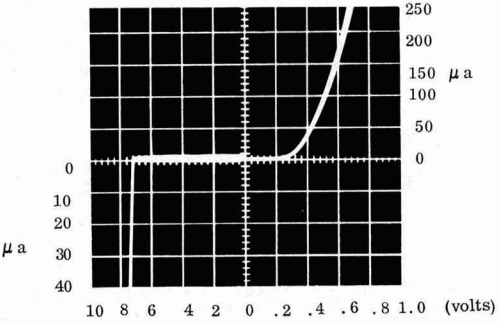

Fig. 11. Forward and reverse bias characteristics of diode made from the silicon film grown on alumina ceramic.

The line appears to be a grain boundary. However, the oriented surface defects observed on both sides of the line indicate that the crystal orientation of one side is not much different from the other. The x-ray pattern shown in Fig. 8 does indicate the presence of some substructures. The misorientation among the substructures is no more than a few minutes.

The electric characteristics of the mesa diodes were measured by point contact-probe which was linked to a micromanipulator. The typical I-V relation of the diodes grown on 96% Al_2O_3 ceramic under both forward and reverse bias is shown in Fig. 11. The high forward-voltage drop is caused primarily by the contact resistance. The reverse bias breakdown voltage is about 7v in Fig. 11. The breakdown voltages of other diodes made on the sample ranged from 6 to 10v. Even though the substrate silicon film was highly contaminated during the melt-regrowth process, the diode made from the epitaxial film grown on it showed sharp breakdown. Also, the current leakage is quite low (in the order of 10^{-8} amp). The breakdown voltage of the diodes made from the epitaxial films grown on the 99% Al_2O_3 ceramic was in the range of 100-150v.

Discussion

As mentioned earlier, the coefficient of expansion of silicon is greatly different from that of alumina, being about a factor of 2.5 smaller than that of alumina. When two different materials in juxtaposition which differ greatly in coefficient of expansion go through large temperature changes severe stress developed at the interface could cause the cracking of the weaker material. However, no cracks have ever been observed on the silicon films grown on alumina substrates. This indicated that between the silicon and alumina, some materials of intermediate coefficient of expansion could be present. At the temperatures above 1400°C, it would not be unexpected that the molten silicon might attack the Al_2O_3 to form a thin film of possibly Al O_x-Si O_y, where x and y are arbitrary constants. This postulation is based on the high electronegativity of silicon over aluminum. This new film situated between Al_2O_3 and silicon might act as a buffer zone which is the analogue of the graded seal in the Pyrex-quartz seal.

The resistivity of the silicon epitaxial films grown on 96% and 99% Al_2O_3 without intentional doping was 0.03-0.07, and 0.5-1.0 ohm-cm (p-type), respectively. It is believed that epitaxial films of various resistivity could be grown on the alumina substrates by adjusting the film thickness and external doping. As has been experienced in growing epitaxial films on heavily doped substrates, the surface resistivity of the film in case of no external doping is a function of the film thickness, *i.e.*, the thicker the film the higher the resistivity. By introducing proper amounts of dopant into the growth chamber, one should be able to compensate or reinforce the impurities from the substrate material.

Manuscript received Feb. 21, 1964.

Any discussion of this paper will appear in a Discussion Section to be published in the June 1965 JOURNAL.

Acknowledgment

The author wishes to thank D. W. Boss and W. H. White for their help in growing film crystals.

REFERENCES

1. N. Holonyak, Jr., D. C. Jillson, and S. F. Bevacque, *AIME Proc. of Tech. Conf.*, **15**, 49 (1961).
2. H. M. Manasevit and W. I. Simpson, "Single Crystal Silicon on a Sapphire Substrate." Late-News Paper Reported at American Physical Society Summer Meeting, August 1962, Edmonton, Ala., Canada.
3. E. Rasmanis, Paper presented at Pittsburgh Meeting of the Electrochemical Society, April 15-18 (1963).

Brief Communication

Radiotracer Studies on the Incorporation of Phosphorus in Epitaxially Grown Silicon

S. Nakanuma

Semiconductor Division, Nippon Electric Company, Kawasaki, Japan

The incorporation of phosphorus into silicon epitaxial films grown by the hydrogen reduction of silicon tetrachloride has been reported by Theuerer (1), Corrigan (2), and Nuttall (3). The radio isotope tracer technique was applied to obtain information about the transfer of phosphorus from gas phase to solid phase and the ratio of Hall mobility to conductivity mobility, μ_H/μ_c, which is an important parameter in the determination of impurity concentrations in semiconductors from the Hall coefficient R_H. That is

$$R_H = -\left(\frac{\mu_H}{\mu_c}\right)\frac{1}{ne}$$

but little experimental data exist for this ratio for phosphorus in silicon.

The radioactive phosphorus trichloride used as the dopant in this experiment was synthesized by the carbon reduction of phosphoric acid, which contained β-emitting phosphorus P^{32}, to yellow phosphorus in a nitrogen stream, followed by chlorination and reduction to phosphorus trichloride. Using silicon tetrachloride doped with the radioactive phosphorus trichloride, silicon epitaxial films were grown at 1250°C with a hydrogen flow of 1 l/min at a mole fraction of 0.02. The films were about 30μ thick.

Phosphorus concentrations in the films were determined from the measurements of volume, and activity by a gas flow counter, which gives a high geometrical efficiency. The self-absorption effect was neglected in these experiments, because the energy of β particles from P^{32} is high enough to penetrate through the epitaxial films. Phosphorus concentration in the gas phase was calculated from Raoult's law and the preliminary determination of phosphorus concentration in the silicon tetrachloride solutions. Hall samples were prepared by the evaporation of Au containing Sb for ohmic contacts and mesa-etch as shown in Fig. 1. The

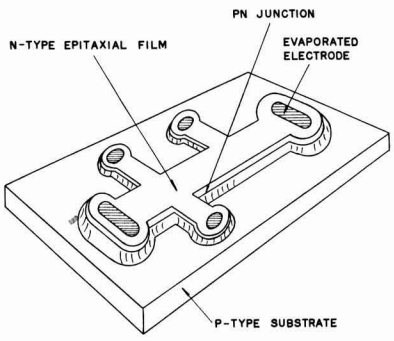

Fig. 1. Hall sample

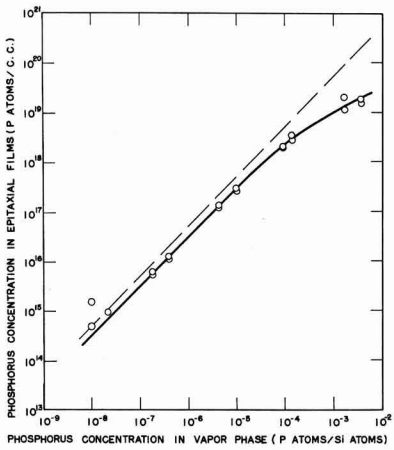

Fig. 2. Phosphorus transfer from vapor phase to films

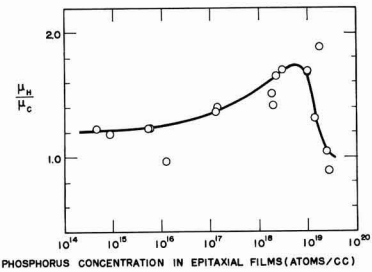

Fig. 3. The ratio of Hall mobility to conductivity mobility

measurements of Hall coefficient and conductivity were made over a temperature range from 77° and 300°K under a magnetic field of 5350 gauss.

Figure 2 shows the phosphorus concentration in the epitaxially grown silicon films as a function of that in gas phase. The dashed line is the curve calculated assuming a transfer ratio of unity as defined by the following formula

$$\text{transfer ratio} = \frac{(\text{P atoms/Si atoms})_{\text{in solid}}}{(\text{P atoms/Si atoms})_{\text{in gas}}}$$

The transfer ratio remains constant at about 0.8 over the range of phosphorus-silicon atom ratio in the gas phase between 10^{-8}-10^{-4}, but a relatively large de-

crease in this ratio is observed at higher concentrations. This might be due to the effect of repulsive forces between phosphorus in the gas phase and that adsorbed on the growing surface, or the effect of having reached the solubility limit of phosphorus in silicon.

Figure 3 shows the ratio of Hall mobility to conductivity mobility as a function of phosphorus concentration at 300°K. The theoretical treatment of this ratio in semiconductors has been discussed by several authors (4) and gives a ratio greater than unity in the nondegenerate case and a ratio of unity in the degenerate case. This is in good agreement with the present results. The Hall mobilities observed are close to the values reported by Morin and Maita (5). It is concluded from these results that the phosphorus atoms in silicon epitaxial films grown by the hydrogen reduction of silicon tetrachloride doped with phosphorus trichloride are incorporated substitutionally in the silicon lattice in spite of much lower growth temperature than from a melt; that is, there is no existence of electrically inactive phosphorus atoms in these films up to phosphorus concentrations of 3×10^{19} at./cc.

Acknowledgment

The author wishes to extend his appreciation to Mr. K. Ohta for laboratory assistance, Mr. S. Ohtani for isotope handling guidance, and Dr. H. Osafune and Y. Matsukura for helpful discussions.

Manuscript received May 18, 1964; revised manuscript received July 2, 1964.

Any discussion of this paper will appear in a Discussion Section to be published in the June 1965 JOURNAL.

REFERENCES

1. H. C. Theuerer, *This Journal*, **108**, 649 (1961).
2. W. J. Corrigan, *Metallurgy of Semiconductor Materials*, **15**, 103 (1962).
3. R. Nuttall, *This Journal*, **111**, 317 (1964).
4. F. J. Blatt, *Phys. Rev.*, **105**, 1203 (1957).
5. F. J. Morin and J. P. Maita, *ibid.*, **96**, 28 (1954).

FUTURE MEETINGS OF
The Electrochemical Society

★ ★ ★

Washington, D. C., October 11, 12, 13, 14, and 15, 1964

Headquarters at the Sheraton-Park Hotel

Sessions will be scheduled on Batteries (including Round Table Discussion on Sealed Storage Batteries and, also, a Joint Symposium on Fuel Cells), Corrosion (including Symposia on Properties of Oxide Corrosion Products and, also, Metallurgical Factors Affecting the Corrosion Processes), Electrodeposition (including a Joint Symposium with Theoretical Electrochemistry Division on Mechanisms of Electrodeposition), Electronics (including Semiconductors), and Electrothermics and Metallurgy (including Symposium on Liquid Metal Corrosion and Phenomena jointly with the Corrosion Division and a symposium on Electron Microprobe)

★ ★ ★

San Francisco, Calif., May 9, 10, 11, 12, and 13, 1965

Headquarters at the Sheraton Palace

Sessions probably will be scheduled on Electric Insulation, Electronics (including Luminescence and Semiconductors and a Symposium on Optical Masers), Electro-Organic (including a Symposium on Industrial Organic Chemistry and a Symposium on Elucidation of Electro-Organic Electrode Processes jointly with the Theoretical Electrochemistry Division), Electrothermics and Metallurgy (including joint Symposium on Molten Salts jointly with the Theoretical Electrochemistry Division and, also, a Symposium on Strengthening Mechanisms in Nonmetallics), Industrial Electrolytic (including a Symposium on Electrolytic Diaphragms and Battery Separators jointly with the Battery Division and, also, a Symposium on the Production of Chlorine without Caustics)

★ ★ ★

Buffalo, N. Y., October 10, 11, 12, 13, and 14, 1965

Headquarters at the Statler-Hilton Hotel

★ ★ ★

Cleveland, Ohio, May 1, 2, 3, 4, and 5, 1966

Headquarters at the Sheraton-Cleveland Hotel

★ ★ ★

Papers are now being solicited for the meeting to be held in San Francisco, Calif., May 9, 10, 11, 12, and 13, 1965. **Triplicate copies of the usual 75-word abstract, as well as of an extended abstract of 500-1000 words** (see notice on page 242C of this issue), are due at Society Headquarters, 30 East 42 St., New York, N. Y., 10017, *not later than December 15, 1964 in order to be included in the program. Please indicate on 75-word abstract for which Division's symposium the paper is to be scheduled, and underline the name of the author who will present the paper.* No paper will be placed on the program unless one of the authors, or a qualified person designated by the authors, has agreed to present it in person. Clearance for presentation of a paper at the meeting should be obtained before the abstract is submitted. An author who wishes his paper considered for publication in the JOURNAL or ELECTROCHEMICAL TECHNOLOGY should send triplicate copies of the manuscript to the Managing Editor of the appropriate publication, 30 East 42 St., New York, N. Y., 10017. Concerning papers to be published in the JOURNAL, see notice on per page charge on page 247C of this issue.

Presentation of a paper at a technical meeting of the Society does not guarantee publication in the JOURNAL or in ELECTROCHEMICAL TECHNOLOGY. However, all papers so presented become the property of The Electrochemical Society, and may not be published elsewhere, either in whole or in part, unless permission for release is requested of and granted by the Editor. Papers already published elsewhere, or submitted for publication elsewhere, are not acceptable for oral presentation except on invitation by a Divisional program Chairman.

Extended Abstract Book Publication Program for the Society's 1965 Spring Meeting in San Francisco, Calif.

The Board of Directors has provided that the National Office shall assist Divisions with the mechanics of publishing Extended Abstracts for sessions involving 15 or more papers at our National Meetings.

The Divisions will handle the technical editing of the abstracts following which the Society Office will arrange for the printing and distribution of the books, thus relieving Division representatives of this responsibility. Each Division program will be the subject of a separate Extended Abstract Book.

This means that each author who submits a paper for presentation at our meeting should do three things:

1—Submit *three* copies of the usual 75-word abstract of the paper for publication in the printed program of the meeting;

2—Simultaneously submit *three* copies of an extended abstract of the paper of 500-1000 words; and

3—Send the 75-word abstract and the 500-1000-word extended abstract to Society Headquarters, 30 East 42 St., New York, N. Y., 10017, *not later than December 15, 1964.*

The Extended Abstract Books will be published by photo-offset reproduction *from typewritten copy submitted by the author.* Special care should therefore be given to the following typing instructions so as to establish uniformity in printing:

1—Abstracts are to be 500-1000 words in length.

2—Use white bond paper, size 8½ x 11 inches.

3—Abstracts should be typed SINGLE space.

4—Use 1¼ inch margins at the top and bottom and at the sides of each page.

5—All copy, including figures, symbols, and corrections, should be in black ink.

6—Figures should be pasted in within the typing dimensions indicated. Captions should be typed not wider than figure dimensions and pasted in proper place in the abstract. Figure captions should appear at bottom of figure. Table titles should appear at top of tables.

7—Wherever possible, avoid use of halftones.

8—Title of paper should be in capital letters. Author(s) name and affiliation should be typed immediately below. It is not necessary in the heading or body to designate paper as "Extended Abstract," or quote the Divisional Symposium involved.

9—Mail to Society Headquarters *unfolded.*

Members and JOURNAL subscribers will receive notice of Extended Abstracts Books to be scheduled for publication. The notices will be accompanied by order blanks for the copies desired. Orders should be submitted with remittance. The advance orders will be necessary for estimating numbers of books to be printed and will be mailed to purchasers prior to the San Francisco meeting. Some extra copies will be available at the meeting but the advance-paid order is the only way to be assured of getting copies.

Candidates for ECS Offices

. . . Nominated as Officers for 1965

Here are brief biographical sketches and photographs of the candidates recommended for the 1965 national election of the Society.

Ballots will be mailed from the office of the Executive Secretary in October 1964.

Offices not affected by this election are those of the two other Vice-Presidents, Harold J. Read and Harry C. Gatos, and Treasurer, Ralph A. Schaefer.

Ernest B. Yeager

Presidential Candidate

Ernest B. Yeager, professor of chemistry at Western Reserve University, Cleveland, was born in Orange, N. J., in 1924. He received his B.A. degree (*summa cum laude*) from New Jersey State College at Montclair in 1945, his M.S. from Western Reserve University in 1946, and his Ph.D. in Physical Chemistry from the same University in 1948. While a graduate student at Western Reserve University, he held a Coffin Fellowship (General Electric).

After receiving his Ph.D. degree, Dr. Yeager stayed on as an instructor in the Dept. of Chemistry at Western Reserve. He became an assistant professor in 1951, an associate professor in 1953, and a professor in 1957. During the 1964-1965 academic year Dr. Yeager is serving as Chairman of the Dept. of Chemistry at Western Reserve. Dr. Yeager is also director of the Ultrasonics Research Lab. and chairman of the Frontiers in Chemistry lecture series at the University.

His research interests include the properties of electrolytes, electrode kinetics, applications for ultrasonic techniques in physical chemistry, and emission spectroscopy. He and his graduate students at the University are credited with the initial development of the sodium amalgam-oxygen fuel cell. In addition to many published articles in electrochemistry and ultrasonics, Dr. Yeager is editor of The Electrochemical Society Monograph on "Electrode Processes" (John Wiley & Sons, Inc., 1961).

In 1954, Dr. Yeager received the Technical Award of the Cleveland Technical Societies Council, in 1956 the Biennial Award of the Acoustical Society of America for his research on ultrasonics, and in 1959 the Annual Award of the Chemical Professions in Cleveland.

Dr. Yeager has been active as a member of The Electrochemical Society since 1949. He served as Vice-Chairman of the Theoretical Electrochemistry Division from 1953 to 1954, and Chairman from 1955 to 1957. In addition, Dr. Yeager was Vice-Chairman of the Cleveland Section of the Society from 1953 to 1954, and Chairman from 1954 to 1955. He was elected Vice-President of the Society in 1962.

Other societies in which Dr. Yeager has been active include the Acoustical Society of America, of which he is a Fellow and Council Member, Sigma Xi, the Optical Society of America, the Society for Applied Spectroscopy (past chairman of the Cleveland Section), the American Chemical Society, and the American Association of University Professors. He has presented lectures before 45 local sections of the American Chemical Society. Dr. Yeager also has been active on various Government committees, including the Committee on Undersea Warfare and the Primary Battery Panel of the National Academy of Sciences.

Ivor E. Campbell

Vice-Presidential Candidate

Ivor E. Campbell is President of the United Metallurgical Corp. at Berkeley, Calif. He was born in Kenton, Ohio, in 1919, and received his undergraduate training in chemistry and mathematics at Evansville College in Evansville, Ind., and his graduate training at the Ohio State University, from which he received his Ph.D. degree in Organic Chemistry in 1943. In 1963 he was awarded an honorary Dr. of Science degree by Evansville College.

Dr. Campbell joined the staff of the Battelle Memorial Institute in 1943 as a research chemist, became assistant supervisor of the Division of Nonferrous Metallurgy and from 1950 to 1959 was chief of the Division of Inorganic Chemistry and Chemical Engineering at Battelle. In 1959 Dr. Campbell left Battelle to become director of research and development of the National Steel Corp. at Weirton, W. Va., which position he held until assuming his present position in 1963.

He is the author of over 40 papers in various scientific and trade journals. His papers deal principally with physical chemistry, vapor plating, preparation of high-purity metals, and super refractories. He is co-author of The Electrochemical Society's monograph "Vapor Plating" published in 1955, and editor of "High Temperature Technology" published in 1956.

Dr. Campbell joined The Electrochemical Society in 1944. He served as Secretary-Treasurer of the Electrothermics Metallurgy Division from 1949 to 1953, Chairman of the Division from 1953 to 1955, and as a member of the Executive Committee of the Division from 1955 to 1957. He was Chairman of the By-laws Committee of the Society in 1954 and 1955, and Chairman of the Becket Memorial Award Committee in 1956.

Dr. Campbell has been Secretary of The Electrochemical Society since January of 1959.

Paul Delahay

Vice-Presidential Candidate

Paul Delahay was born in the Netherlands and received his education in Belgium and in the United States. He holds a B.S. degree in engineering (Brussels), M.S. degrees in electrical engineering and chemistry (Liège, Brussels) and a Ph.D. degree in chemistry from the University of Oregon. He was an instructor in chemistry at the University of Brussels in 1945-1946. He came to the United States in 1946 and remained at the University of Oregon until 1949 at which time he joined Louisiana

State University as assistant professor. He has been Boyd Professor at this institution since 1956.

Paul Delahay is the author of three books and more than 100 research papers in the field of electrochemistry. Translations of his books have appeared in Russian, Japanese, Korean, Spanish, and Italian. His last book, "Double Layer and Electrode Kinetics," is now in press. He is coeditor of the "Advances in Electrochemistry and Electrochemical Engineering" with Professor C. W. Tobias of the University of California, Berkeley.

His work was recognized by the Turner Prize of The Electrochemical Society (1951), the Award in Pure Chemistry of the American Chemical Society (1955), the Southwest Award of the American Chemical Society (1959), and the University Medal of the University of Brussels (1963). He was a Guggenheim Fellow at Cambridge University in 1955 and Fulbright Professor at the University of Paris during 1962-63.

Dr. Delahay is a member of the editorial board of *The Journal of the American Chemical Society* and the *Journal of Electroanalytical Chemistry*. He is a member of the Analytical Chemistry Division of the International Union of Pure and Applied Chemistry and a past president of the Commission on Electrochemical Data of that organization. He is at present a member of the Analytical Chemistry Committee of the National Research Council. He has been active in The Electrochemical Society and particularly in the Theoretical Electrochemistry Division as Secretary, Vice-Chairman, and Chairman of the Division. In the latter capacity, he organized the highly successful symposium on electrode processes at the 1959 Philadelphia meeting of the Society. He has been a frequent lecturer at American and European universities and international conferences (IUPAC, CITCE, *etc.*). He was a national lecturer for the Society of Sigma XI in 1958.

Charles W. Tobias

Vice-Presidential Candidate

Charles W. Tobias, professor of Chemical Engineering at the University of California in Berkeley, was born in Hungary in 1920. Following high school and graduation from the Municipal Conservatory of Music, he received his Chemical Engineer's Diploma from the University of Technical Sciences (Müegyetem) in Budapest. Interrupted by one year of military service with the Army Engineers, he was employed by the radio tube division of the United Incandescent Lamp and Electrical Co., Ltd., between 1942-1947, and held a demonstrator's appointment in the Institute of Physical Chemistry under Professor Náray-Szabo during 1945-1946. After obtaining the doctoral degree (major subject: Physical Chemistry) in 1946, he came to the United States in mid-1947 on a fellowship appointment. From July 1947 to the present he has been a member of the faculty of the College of Chemistry in Berkeley, where he was appointed to full professorship in 1960. While on leave during the year 1958-1959, he was a professor in the Miller Institute for Basic Research. Since 1955 he has been a member of the staff of the Lawrence Radiation Laboratory, and affiliated with its Inorganic Materials Research Div. since 1962.

Dr. Tobias' early research interest in electrodeposition and electrophoresis were broadened to the general area of scale dependent processes associated with electrode systems. His publications are concerned primarily with ionic transport by diffusion, migration and convection, exact solutions of potential and current distribution problems, conductance in heterogeneous media, quantitative description of processes in porous electrodes. In more recent years he and his coworkers have undertaken the exploration of electrochemical properties of certain nonaqueous solvents, including carbonate esters and liquid ammonia. Dr. Tobias teaches undergraduate courses in Thermodynamics, Unit Operations, and he developed a graduate course treating the design and scale up of electrochemical processes.

Dr. Tobias joined The Electrochemical Society in 1948, a year in which he participated in the founding of the San Francisco Section. He served as Vice-Chairman and Chairman of this Section in 1953-56. He was a member of the Executive Committee, Vice-Chairman and Chairman of the Theoretical Division of the Society in 1955-1961. Over the past decade he served on the following committees: Ways and Means, Nominations, Honors and Awards, Summer Session Award, and Palladium Medal Award.

Since 1954 Dr. Tobias has served as Theoretical Divisional Editor for the JOURNAL OF THE ELECTROCHEMICAL SOCIETY.

With Dr. Paul Delahay, Dr. Tobias is coeditor of the "Advances in Electrochemistry and Electrochemical Engineering" series, in which volumes IV and V are at present under preparation.

Dr. Tobias organized the Symposium on Electrochemical Engineering, Electrochemical Society (Chicago, May 1960) and a similar symposium sponsored by the AIChE (San Francisco, 1959). He served as chairman and keynote speaker on many other occasions.

Dr. Tobias is a member of the ACS, AIChE, CITCE, Sigma Xi, and Alpha Chi Sigma. He is a member of the advisory board of Stiles Hall, the University YMCA in Berkeley.

Richard F. Bechtold

Secretarial Candidate

Richard F. Bechtold was born in Roslyn, Wash., in 1923. He was educated at the University of Washington in Seattle, graduating in 1945 with a B.S. degree in Chemical Engineering.

Mr. Bechtold's present position is that of manager of inorganic chemicals products in the Chemicals Dept. of the Dow Chemical Co. In this capacity, he works with the production, research, development, and sales groups on all inorganic products, which include all of Dow's electrochemical products. He began his professional career, following graduation, at Dow's Pittsburg, Calif., plant in 1945. His initial position was that of technical assistant in the Electrochemical Production area. Subsequently, he became assistant superintendent in 1951 and superintendent in 1953. His work was concerned with all of the various areas of activity connected with the production of chlorine, caustic soda, caustic potash, and ammonia. He was directly involved in the research and development activities concerning electrochemistry. In 1961, he transferred to Midland, Mich., to assume his present position.

Mr. Bechtold's activities in The Electrochemical Society began in 1948 at the time the San Francisco Section was formed. He served for several years as the original Secretary-Treasurer of the Section and, subsequently became Vice-Chairman and Chairman and Representative to the Council of Local Sections. He is, at present, Representative of the Council of Local Sections for the Midland Section of the Society. He was General Chairman of the San Francisco Meeting of the Society held in 1956. Mr. Bechtold has served as Secretary-Treasurer, Vice Chairman, and Chairman of the Industrial Electrolytic Division. On the Council of Local Sections, he has been Secretary, Vice-Chairman, and Chairman, and is currently a representative on the Board of Directors for this group. He has also served on the Finance Committee for the Society and is at present on the Ways and Means Committee.

F. G. Will to Receive Battery Division Research Award for 1963-1964

The Battery Division has selected Dr. Fritz G. Will of the Research Lab., General Electric Co., Schenectady, N. Y., to receive its Research Award for 1964. The selection of Dr. Will was based on the pair of papers entitled "Electrochemical Oxidation of Hydrogen on Partially Immersed Platinum Electrodes, I. Experiments and Interpretation and II. Theoretical Treatment," which appeared in the February 1963 JOURNAL, pp. 145-160. The award will be presented to Dr. Will at the Battery Division luncheon and biennial business meeting to be held on Tuesday October 13, 1964, during the Fall Meeting of the Society in Washington, D. C.

Dr. Will was born in Breslau, Germany in 1931. He received his B.S. degree in 1953, M.S. degree in Physics in 1957, and his Ph.D. degree in Electrochemistry in 1959, all from the Institute of Technology, Munich, Germany. His Ph.D. thesis was entitled "Investigation of Adsorption Phenomena on Noble Metal Electrodes by a New Nonstationary Method." While with the Electrochemistry Dept. of the Institute of Technology, Dr. Will worked on projects supported by the Badische Soda & Anilin Fabrik and the Deutsche Forschungs Gemeinshaft, a national institute devoted to the support of university research, and for the U.S. Air Force Research and Development Center (Brussels). The work included the design and set up of electronic instrumentation and electrochemical investigations, including the study of hydrogen and oxygen adsorption on noble metal surfaces by a new method.

Dr. Will came to the United States in September of 1959 and became a research scientist in the Electrical Engineering Dept. of the U.S. Army Engineer Research and Development Labs. at Fort Belvoir, Virginia, where he reviewed and evaluated proposals and reports of contracts on fuel cell research. In May 1960, he joined the Research Lab. of General Electric Co. as a physical chemist and is at present working on the effects of surface structure on chemisorption, mechanisms of gas diffusion electrodes, and solions.

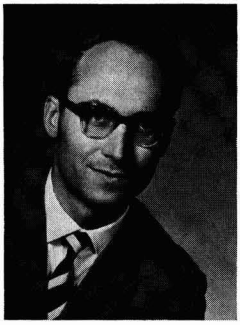

Fritz G. Will

Dr. Will is the author or coauthor of about a dozen papers, mainly dealing with modern instrumentation and methods for studying and interpreting electrode reactions and with the mechanisms of gas diffusion electrodes. The papers have been published in the *Zeitschrift fuer Elektrochemie* or its successor, the *Berichte der Bunsengesellschaft für Physikalische Chemie* and the *Journal of the Electrochemical Society*. Dr. Will has been a member of The Electrochemical Society since 1961 and is a member of the Deutsche Bunsengesellschaft für Elektrochemie.

He is married to the former Hertha M. Dirkl and they have three children, one son and two daughters.

The Research Award of the Battery Division was established in 1958 for the purpose of stimulating battery research and encouraging the preparation of high-quality papers for the *Journal of The Electrochemical Society* and now extended to include *Electrochemical Technology*. It is expected that a selection will be made every two years of an author, or authors, of a paper relating to electrochemical cells or batteries which has been published in either of the Society's journals. The paper is selected primarily on the basis of scientific merit and importance, the originality of concept and experimental approach, thoroughness of experiments, logic of conclusions, and clarity of presentation. The Research Award consists of a scroll to the author of the chosen paper, along with a check which may be used by the recipient to prepay his membership in the Society and subscription to the JOURNAL for life. Joint authors of a selected paper each receive a scroll and a check for $100.

A Research Award winner is chosen by a committee appointed by the Battery Division Chairman. The selection is approved by the Battery Division Executive Committee and the recommendation is submitted to the Society's Board of Directors for final approval. The Award Committee who selected the fourth recipient of the Battery Division Research Award consisted of J. J. Coleman, A. G. Hellfritsch, P. C. Milner, W. C. Vosburgh, and E. J. Ritchie, Chairman.

Division News

Electrodeposition Division

The following candidates are slated for the fall election to be voted on at the Washington Meeting of the Society.

Chairman—Dan Trivich, 16204 Northlawn, Detroit 21, Mich.

Vice-Chairman—E. J. Smith, Coated Products, National Steel Corp., Weirton, W. Va.

Secretary-Treasurer—J. Petrocelli, Engineering Dept., Ford Motor Co., Detroit, Mich.

Members at Large—Fielding Ogburn, National Bureau of Standards, Connecticut and Van Ness, Washington, D. C.; I. W. Wolf, Ampex Corp., 401 Broadway, Redwood City, Calif.

D. Gardner Foulke, *Chairman*
Nominating Committee

Notice to DBG Subscribers

The Society has been informed by the Deutsche Bunsen-Gesellschaft Society (DBG) that the subscription price to members and subscribers receiving their Journal will be increased to $15.00 effective January 1, 1965.

Personals

William E. Blodgett was appointed manager, materials and process development, at the Louisville, Ky., laboratories of the Plumbing and Heating Division of American-Standard, it was announced.

Richard E. Grace has been appointed to the position of interim head of the School of Metallurgical Engineering at Purdue University.

John M. Robertson has been appointed chief ceramic engineer at the Louisville, Ky., laboratories of the Plumbing and Heating Division of American-Standard, it has been announced recently.

Notice to Journal Subscribers

Your subscription to the JOURNAL of The Electrochemical Society will expire on *December 31, 1964.* Avoid missing any issue. Send us your remittance in the amount of $24.00 immediately upon receipt of your subscription renewal bill to insure proper handling of your subscription. (Subscribers located outside the Continental United States must add $1.50 to the subscription price for postage ($25.50), and payment must be made by Money Order or New York draft, not local check.) A subscription renewal bill has been mailed to all subscribers.

Because of the increasing number of pages published each year, the Bound Volume of the 1965 JOURNAL will be bound in two parts: Part One, January-June; Part Two, July-December. The two parts of the volume will *not* be sold separately. The bound volume can be obtained at the prepublication price of $12.00 by adding this amount to your remittance. No orders will be accepted at this rate after *December 1, 1964,* when the price will be increased to $18.00 subject to prior acceptance. The bound volume is *not* offered independently of your JOURNAL subscription.

Worden Waring, formerly manager of the Chemistry Dept. at Fairchild Semiconductor's Research and Development Labs., has joined the Attending Staff Association at Rancho Los Amigos Hospital in Downey, Calif. Dr. Waring is director of a project on the use of the electrical activity of muscles as control signals for powered devices to aid disabled patients.

John H. Zauner has been elected vice-president of the Perkin-Elmer Corp., Norwalk, Conn., and head of its Instrument Group. Mr. Zauner will be responsible for the company's domestic and international commercial analytical instrument operations.

Obituary

Frederick F. Schuetz

Frederick F. Schuetz of 525 Prospect St., Maplewood, N. J., a retired

Electrochemical Symposium

The Industrial Electrolytic and Battery Divisions of the Society are jointly sponsoring a symposium on "Electrolytic Diaphragms and Battery Separators" for the 1965 Spring Meeting to be held in San Francisco, May 9-13, 1965.

Communications and inquiries regarding this symposium should be addressed to: Dr. Robert E. Meredith, Department of Chemical Engineering, Oregon State University, Corvallis, Oregon.

Electroorganic Symposia

The Electro-Organic Division is planning two symposia for the 1965 Spring Meeting of the Society in San Francisco. One of these on "Elucidation of Organic Electrode Processes" is jointly sponsored with the Theoretical Electrochemistry Division. All papers will be given by invited speakers and the program will be announced later. Dr. Philip Elving, University of Michigan, Ann Arbor, Mich. is Chairman of the symposium.

The second is entitled "Industrial Electroorganic Chemistry" and the Chairman is Dr. Manuel M. Baizer, Monsanto Chemical Co., 800 N. Lindbergh Boulevard, St. Louis, Mo., 63166. Speakers have been invited but others interested in participation should contact Dr. Baizer.

Papers Solicited for Symposium on Molten Salts for Spring 1965 Meeting

A Symposium on Molten Salts is being organized jointly by the Electrothermics and Metallurgy Division and the Theoretical Electrochemistry Division. The symposium will be a part of the Spring Meeting of The Electrochemical Society to be held in San Francisco, Calif.

Papers are solicited from research workers active in various phases of molten salt chemistry. It is hoped that research in both the fundamental and applied aspects will be discussed at the symposium. Questions concerning the symposium and the appropriateness of a particular paper should be addressed to D. Cubicciotti, Stanford Research Institute, Menlo Park, Calif.

Three copies of the usual 75-word abstract and three copies of an extended 500-1000 word abstract are due at Society Headquarters, 30 East 42 St., New York, N. Y. 10017, not later than December 15, 1964. (See general notice 242C in this issue concerning Extended Abstract Book Publication Program.)

Symposium on Production of Chlorine without Caustic for Spring 1965 Meeting

A Symposium in the Production of Chlorine without Caustic is being organized by the Industrial Electrolytic Division. This symposium will be part of the Spring Meeting of the Society to be held in San Francisco, Calif., May 9-13, 1965.

Papers are solicited from research, development, engineering, and production workers active on the general area of direct and indirect electrolysis of hydrochloric acid and chemical processes producing chlorine without caustic. It is hoped that papers on theoretical and practical aspects will be presented at the symposium. Questions concerning the symposium and appropriateness of a particular paper should be addressed to Dr. Morris P. Grotheer, Hooker Chemical Corp., P.O. Box 344, Niagara Falls, N. Y. 14302.

Three copies of the usual 75-word abstract and three copies of an extended 500-1000 word abstract are due at The Electrochemical Society, Inc., 30 East 42 St., New York, N. Y. 10017, *not later than December 15, 1964.* (See general notice on page 242C of this issue concerning Extended Abstract Program.)

patent attorney, died at his home on July 19, 1964. He was 82.

He had been a patent attorney since 1906 maintaining an office in the Woolworth Bldg. in New York for the last 20 years. He retired from business last year.

He was a member of The Electrochemical Society, the New York Patent Lawyers Association, the American Association for the Advancement of Science, the American Society of Mechanical Engineers, and was an associate member of the American Institute of Electrical Engineers.

Book Reviews

"Compound Semiconductors. Vol. I. Preparation of III-V Compounds," Edited by R. D. Willardson and H. L. Goering. Published by Reinhold Publishing Corp., N. Y., 1962, 533 pages; $25.00.

This work is an excellent source and reference book for those who have been engaged in research and development in this field. It is also a very useful introductory book, providing a general background to engineers and scientists with no previous experience in III-V compound semiconductor material technology. The authors have approached the subject with the idea of enabling the reader to perform purifications, syntheses, and single-crystal growth of these materials. The emphasis is on the experimental aspect, discussing the design, construction, and use of the system appropriate to his problem. However, there are chapters devoted to the discussion of basic theory pertinent particularly to III-V compound semiconductors such as chemical bonding and surface structures.

This book, by covering the various material technological and scientific aspects of III-V compound semiconductors, tries to present an integral picture. Section I discusses crystal structure and bonding, including a chapter on cleavage studies which has not received its share of attention in most material publications. Section II deals with purification of the elements. A minor problem here is the missing information on purity of some of the elements. Section III is a review of techniques useful for the detection of trace impurities, implying that the importance of both chemical and electrical (more or less empirical) methods for the determination of purity level. Section IV describes extensively preparative methods for known III-V compound semiconductors. The presentation varies because technology associated with a certain number of these compounds has lagged behind, due to lack of practical interest. In several chapters, single-crystal growth techniques were briefly described. Here, some discussion on the tolerable degree of stoichiometry achieved is desirable. Section V presents single crystal growth techniques with emphasis on growth from melt. Section VI discusses thin film formation techniques. In these two sections, somehow, epitaxial film growth from the vapor phase by transfer has not been mentioned, except in the brief introductory comment. This is an area of interest, particularly in growth of epitaxial films, on foreign substrates and growth of films of mixtures of III-V semiconductors. Sections VII and VIII give some insight of solid state diffusion and impurity segregation in these materials. Section IX is a thorough and authoritative presentation of surface problems and phenomena on typical III-V semiconducting compounds. Section X is a discussion of experimental techniques and results on thermodynamic properties of these materials obtained by means of phase diagram, mass spectrometric, and calorimetric investigations. An extensive bibliography of publications in this area up to 1960 concludes the book. More recent references (up to 1961) in the footnotes provide additional source of information. Lacking here is a discussion of structural perfection of single crystals of these compounds and means for observation and measurements of these defects. Hopefully, these will be included in the subsequent volumes of this work.

This massive and comprehensive volume is undoubtedly of compelling interest to any one engaged in work in this field and is a necessary addition to the library of engineering schools and many industries. The need for such a book is apparent because of the enormous amount of work which has been done in the

Notice to ECT Subscribers

Nonmember subscriptions to ELECTROCHEMICAL TECHNOLOGY will expire on *December 31, 1964.* Avoid missing any issue. Send us your remittance in the amount of $15.00 immediately upon receipt of your ECT subscription renewal bill to insure proper handling of your subscription. (Subscribers outside of the Continental United States must add $1.00 to the subscription price for postage.)

The 1965 bound volumes of ELECTROCHEMICAL TECHNOLOGY can be obtained at the prepublication price of $4.00 by adding this amount to your remittance. However, no orders will be accepted at this rate after *December 1, 1964,* when the price will be increased to $6.00 subject to prior acceptance. Bound volumes are *not* offered independently of your ECT subscription.

Page Charge Adopted for the JOURNAL

Increased costs of publication have made it necessary for The Electrochemical Society to institute a per page charge for publication in the JOURNAL.

At the Meeting of the Board of Directors held in New York on September 29, 1963 a charge of $35.00 per printed page was established by the Board of Directors, on recommendation of the Publication and Finance Committees, for papers published in the JOURNAL. This action becomes effective for papers received after February 1, 1964.

A 10% reduction in the page charge will apply to papers authored by one or more members of The Electrochemical Society and/or by one or more employees of Patron or Sustaining Members of the Society.

Papers are accepted for publication on the basis of merit by established practices of review. Acceptance of future papers for publication will not be dependent on payment of this invoice. Where funds are not available for payment of this charge it will be waived by The Electrochemical Society.

Notice to Members

Re Voting Ballot

You will soon receive your official voting ballot from Society Headquarters. Please return it by *December 15* so that your vote can be included in the final election count.

Symposium on Strengthening Mechanisms in Nonmetallics Planned for Spring 1965 Meeting

Announcement is made by Chairman William E. Kuhn, of the Electrothermics and Metallurgy Division, that symposia plans for the Society's San Francisco, Calif., Meeting to be held May 9-13, 1965 include Strengthening Mechanisms in Nonmetallics.

Papers are now solicited for presentation at this symposium. Materials of interest should include intermetallic compounds, oxides, carbides, nitrides, silicides, and the like. Strengthening mechanisms may be dispersed phases, porosity control, grain size control, thermal treatments, short fiber reinforcement, anisotropic effects, surface effects, and nonstoichiometry. Papers concerning both low and high temperature studies are invited.

Three copies of a 75-word abstract, as well as of an extended abstract of 500-1000 words are due at The Electrochemical Society, 30 East 42 St., New York, N. Y., 10017 *not later than December 15, 1965.* (See notice on page 242C of this issue.)

Inquiries and suggestions should be sent to Symposium Chairman, James H. Healy, Spindletop Research, Inc., Ironwork Pike, Lexington, Ky. 40505. If you are considering submitting a paper for this symposium, it would be helpful if you notify him as soon as possible.

last few years and the increasing importance of these compounds. It is a timely publication. However, by its own nature, in a few years, it will be superseded or perhaps better still, augmented by similar works or a new edition.

Pei Wang
Sylvania Electric Products

"Modern Polarographic Methods," by Helmuth Schmidt and Mark von Stackelberg. Translated from the German by R. E. W. Maddison. Published by Academic Press, New York and London, 1963. 93 pages; $5.50.

This book is a lucid introduction into the recently developed instrumental methods related to conventional polarography. Without overloading the reader with mathematics the writers succeed in clearly explaining the underlying principles, the potentialities, and practical limitations of the various methods.

The treatment includes: differential (page 2), derivative (page 5), and strobe (page 4) polarography; oscillographic polarography with either controlled current (page 9) or potential (page 12); ac (page 22) and ac bridge (page 5), polarography; square wave (page 7), pulse (page 8), and radiofrequency polarography (page 10).

As one rarely completely agrees with all the statements in a text, I would like to make a few minor criticisms which however, do not detract anything from the overall impression of the book.

It is stated several times (pages 13, 17, 18, and 25) that in conventional polarography the mean current only is measured, which means that heavy damping is applied. This is unnecessary and actually very disadvantageous. In fact, the use of maximally undamped polarograms, in conjunction with some means of mechanical drop detachment, has all the advantages of strobe polarography (plus a few more: adsorption waves *e.g.*, can easily be distinguished from the shape of the current-voltage curve of a single drop) and does not necessitate the rather elaborate equipment of strobe polarograph.

The analytical difficulties and inadequacy of ac polarography are very well explained (although there is a confusing error on page 36, line 8 from the top, where "peak" should be replaced by "wave"). However, I regret the statement (page 51) that "there is a wide field of application in the investigation of electrode reactions." In this respect I think the method is even less satisfactory and cannot compete with impedance measurements.

In the section on ac bridge polarography a recent phase-sensitive detector circuit is explained at length. Unfortunately no mention is made of

the Cambridge Univector, which however is erroneously cited as being an ordinary ac polarograph (page 57). Although this attachment unit presumably is not quite as satisfactory as the bridge technique, it lacks the major disadvantages of ac polarography, was developed much earlier, can be used in conjunction with any conventional polarograph and has been on the European market for years.

It is a pity that the terms "reversible" and "irreversible" are used freely without any definition of their notion in the context (with the exception of page 38, where an incorrect one is given). This may be a little confusing since the time scales of the various methods are not the same at all, consequently a reaction which behaves "reversibly" with a slow method may behave quite "irreversibly" with a fast one.

There are many enjoyable features in the book: the emphasis is on main principles, the reasoning in general is very clear, a consistent distinction is made between accuracy, sensitivity, resolvability, and separability. Simple diagrams illustrate the working principles. Much of the information given in the book could before only be found, at the cost of much time, scattered all over literature.

The translation is good; the German origin of the book only shows in the symbols used in the figures and formulae, as they sometimes follow German usage, sometimes English, *e.g.*, U, V, and E are used indiscriminately for potential. The literature is covered up to about 1960.

This is a highly recommended book, which gives a concise, readable, and critical treatment of the subject matter.

R. de Levie
Louisiana State University

Announcements from Publishers

"Corrosion of Refractories by Lithium," Report ORNL-3551,* $2.00.
"Salt Fog Tests of Magnesium Alloys," Report AD 600 029,* $1.00.
"Recent Soviet Studies in Corrosion," Report AD 600 784,* $5.00.
"Literature Search on Fretting Corrosion," Report AD 430 908,* $2.25.
"Thermal Energy Storage," Report AD 431 201,* $3.00.
"Cell Equalization Techniques," Report AD 427 070,* $1.00.
"Alkaline Battery Evaluation," Report AD 429 135,* $5.00.
"Silver Transport Mechanism," Report AD 421 049,* $1.50.
"A Silver-Zinc Secondary Battery Study," Report AD 422 077,* $2.25.
"Mercury Cell Battery Investigation," Report AD 430 404,* $1.75.
"Thin Film Gallium Arsenide Study," Report AD 428 634,* $1.75.
"Dendritic Silicon Solar Cell Panel," Report AD 429 136,* $2.25.
"Cadmium-Sulfide Front Wall Solar Cell," Report AD 423 684,* $1.75.
"Additives for Nickel Plating Solutions," Report AD 424 466,* 75 cents.
"Thermocouples for Measuring Boiling Surface Temperatures," Report IS 810,* $1.50.
"New Oxidants and Their Mechanisms," Report AD 431 871,* 75 cents.
"Diaphragms for Sulphate Cycle Electrolytic Cells," Report AD 421 167,* 50 cents.
"Hydrogen Sources for Fuel Cells," Report AD 424 580,* 75 cents.
"Ultrasonic Wave Propagation Models," Report HW-78701,* $1.25.
"Cadmium Oxides as Coatings," Report AD 423 682,* 50 cents.
"Control of Stress Corrosion Cracking," Report AD 432 320,* 50 cents.
"A Stannate-Pyrophosphate Solution," Report AD 427 131,* 50 cents.

* Order from Office of Technical Services, Business and Defense Services Administration, U. S. Dept. of Commerce, Washington 25, D. C.

Advertiser's Index

The Electrochemical Society

INSTRUCTIONS TO AUTHORS OF PAPERS

(Revised as of 4/1/64)

Address all correspondence to the Editor, JOURNAL OF THE ELECTROCHEMICAL SOCIETY, 30 East 42 St., New York, N. Y., 10017

GENERAL

Manuscripts must be submitted in triplicate to expedite review. They should be typewritten, double-spaced, with 2½-4 cm margins.

Title should be brief, followed by the author's name and professional connection. Authors should be as brief as is consistent with clarity and should omit introductory or explanatory material which may be regarded as familiar to specialists in the particular field. Proprietary and trade names should be avoided if possible; if used, they should be capitalized to protect the owners' rights.

Authors may suggest qualified reviewers for their papers, but the JOURNAL reserves the right of final choice.

TYPES OF ARTICLES

Technical Articles must describe original research of basic nature and must have adequate scientific depth. Articles of wide diversity of interest are appropriate, but subjects primarily covered in other specialized journals (*e.g.,* analytical or nuclear chemistry) are not considered appropriate. An ***Abstract*** of about 100 words should state the scope of the paper and summarize its results. Suitable headings and subheadings should be included, but sections should not be numbered. Articles in recent issues of the JOURNAL should be consulted for current style.

Technical Notes are used for reporting briefer research, developmental work, process technology; new or improved devices, materials, techniques, or processes which do not involve more extensive basic scientific study. No abstract is required.

Brief Communications are used only to report new information of scientific or technological importance which warrants rapid dissemination.

ILLUSTRATIONS

Drawings and ***Graphs*** ordinarily will be reduced to column width, 8.3 cm, and after such reduction should have lettering no less than 0.15 cm high. Lettering must be of letter-guide quality. India ink on tracing cloth or paper is preferred, but India ink on coordinate paper with blue ruling is acceptable. The sample graph shown on the reverse page conforms to suggestions of the American Standards Association (ASA Report Y15.1-1959).

Photographs should be used sparingly, must be glossy prints, and should be mailed with protection against folding. ***Micrographs*** should have a labeled length unit drawn or pasted on the picture.

Captions for figures (including photographs) must be included on a separate sheet. Captions and figure numbers must *not* appear in the body of the figure; they will be removed if they do.

Numerical Data should not be duplicated in tables and figures.

EQUATIONS

Mathematical Equations should be written on a single line if possible, and parentheses, brackets, the solidus (/), negative exponents, etc., may be used freely for this purpose. Authors are urged to consult Chapter VI of the "Style Manual" of the American Institute of Physics (available for $1.00 at American Institute of Physics, 57 East 55 St., New York, N. Y., 10022) and to follow the patterns described there.

SYMBOLS

If more than a few ***Symbols*** are used, they should be defined in a list at the end of the paper, with units given. For example:

$a, b \ldots =$ empirical constants of Brown equation

$\mathring{f}_i =$ fugacity of pure ith component, atm

$D_v =$ volume diffusion coefficient, cm^2/sec

ABBREVIATIONS UNITS

The AIP "Style Manual" referred to here gives a suitable list of common ***Abbreviations.*** Units usually will be abbreviated without periods throughout the text, as sec, min, hr, cm, mm, etc. **Metric Units** should be used throughout, unless English units are clearly more appropriate in the area of discussion.

POTENTIAL SIGNS

Electrode Potentials: Authors are urged to state and make use of the polarity of test electrodes with respect to the reference electrode used, *i.e.*, Zn is normally negative, Cu normally positive with respect to the standard hydrogen electrode. The sign for the emf of a cell should conform to the free energy change of the chemical reaction as written or implied, in accordance with the definition $\Delta G = -nFE$. These suggestions agree with the IUPAC conventions adopted in 1953. If any other convention is used, it should be stated clearly and used consistently throughout the manuscript.

REFERENCES

Literature References should be listed on a separate sheet at the end of the paper in the order in which they are cited in the text. Authors' initials must be given, and the style and abbreviations adopted by *Chemical Abstracts* should be used. Any recent issue of the JOURNAL may be consulted.

PUBLICATION CHARGE

A charge of $35 per printed page is made for publication of technical material in THIS JOURNAL. A 10% reduction is allowed if at least one author of an article is an ECS member or an employee of a Patron or Sustaining Member firm. However, acceptance of a manuscript is in no way dependent on such payment, and the charge may be waived in individual cases.

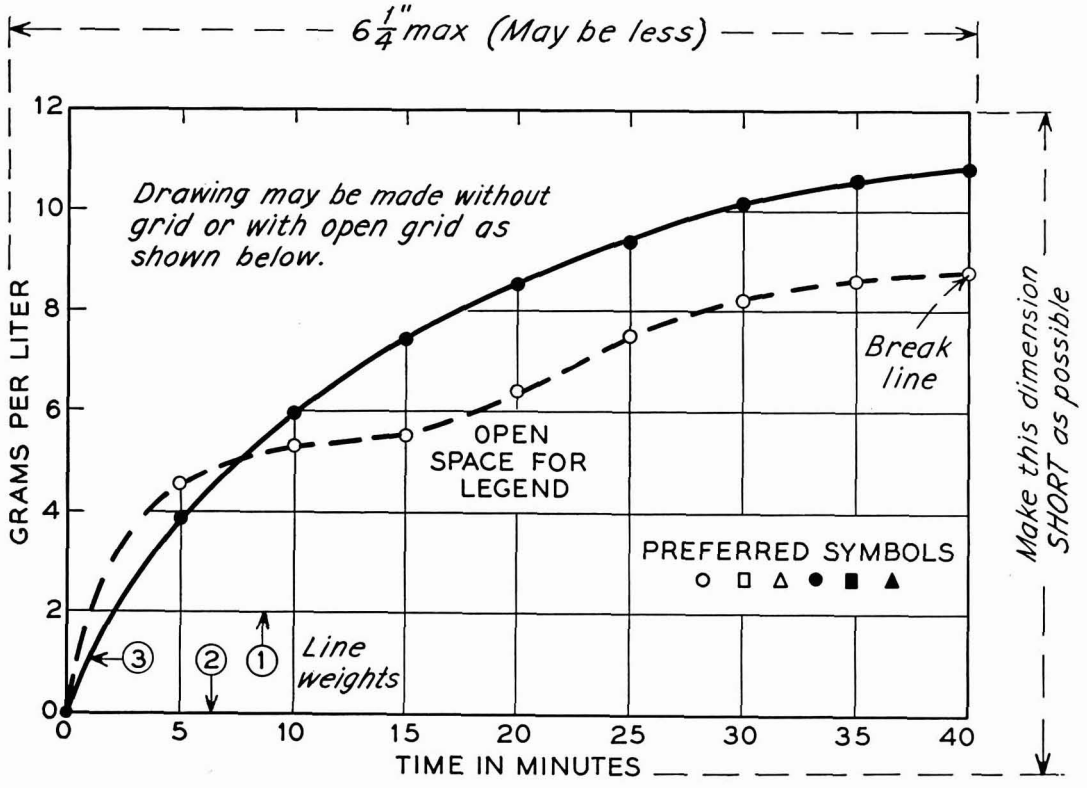

Remarks: Line weight 2 is used for borders and zero lines. When several curves are shown, each may be numbered and described in the caption. Lettering shown is approximately ⅛ in. In plotting current or potential as ordinate, increasing negative values should go down.

SAMPLE CURVE DRAWING FOR REDUCTION TO $\frac{1}{2}$ SIZE

The Electrochemical Society

Patron Members

Aluminum Co. of Canada, Ltd., Montreal, Que., Canada
International Nickel Co., Inc., New York, N. Y.
General Electric Co.
Capacitor Dept., Hudson Falls, N. Y.
Chemical Laboratory, Knolls Atomic Power Laboratory, Schenectady, N. Y.
Chemical and Materials Engineering Laboratory, Advanced Technology Laboratories, Schenectady, N. Y.
Chemistry Research Dept., Schenectady, N. Y.
Direct Energy Conversion Operation, West Lynn, Mass.
Lamp Division, Cleveland, Ohio
Materials & Processes Laboratory, Large Steam Turbine-Generator Dept., Schenectady, N. Y.
Metallurgy and Ceramics Research Dept., Schenectady, N. Y.
Olin Mathieson Chemical Corp.,
Chemicals Div., Research Dept., New Haven, Conn.
Union Carbide Corp.
Divisions:
Carbon Products Div., New York, N. Y.
Consumer Products Div., New York, N. Y.
Westinghouse Electric Corp., Pittsburgh, Pa.

Sustaining Members

Air Reduction Co., Inc., New York, N. Y.
Allen-Bradley Co., Milwaukee, Wis.
Allied Chemical Corp.
General Chemical Div., Morristown, N. J.
Alloy Steel Products Co., Inc., Linden, N. J.
Aluminum Co. of America, New Kensington, Pa.
American Metal Climax, Inc., New York, N. Y.
American Potash & Chemical Corp., Los Angeles, Calif.
American Smelting and Refining Co., South Plainfield, N. J.
American Zinc Co. of Illinois, East St. Louis, Ill.
American Zinc, Lead & Smelting Co., St. Louis, Mo.
M. Ames Chemical Works, Inc., Glens Falls, N. Y.
Ampex Corp., Redwood City, Calif.
Armco Steel Corp., Middletown, Ohio
Basic Inc., Bettsville, Ohio
Bell Telephone Laboratories, Inc., New York, N. Y. (2 memberships)
Bethlehem Steel Co., Bethlehem, Pa. (2 memberships)
Boeing Co., Seattle, Wash.
Burgess Battery Co., Freeport, Ill. (2 memberships)
Burndy Corp., Norwalk, Conn.
Canadian Industries Ltd., Montreal, Que., Canada
Carborundum Co., Niagara Falls, N. Y.
Chrysler Corp., Detroit, Mich.
Consolidated Mining & Smelting Co. of Canada, Ltd., Trail, B. C., Canada (2 memberships)
Continental Can Co., Inc., Chicago, Ill.
Cooper Metallurgical Associates, Cleveland, Ohio
Corning Glass Works, Corning, N. Y.
Diamond Alkali Co., Painesville, Ohio
Dow Chemical Co., Midland, Mich.
Wilbur B. Driver Co., Newark, N. J. (2 memberships)
E. I. du Pont de Nemours & Co., Inc., Wilmington, Del.
Eagle-Picher Co., Chemical and Metals Div., Joplin, Mo.
Eastman Kodak Co., Rochester, N. Y.
Thomas A. Edison Research Laboratory, Div. of McGraw-Edison Co., West Orange, N. J.
Eltra Corp.,
Prestolite Div., Toledo, Ohio
C&D Batteries, Conshohocken, Pa.
Electric Storage Battery Co., Yardley, Pa.
Engelhard Industries, Inc., Newark, N. J. (2 memberships)
The Eppley Laboratory, Inc., Newport, R. I. (2 memberships)
Exmet Corp., Bridgeport, Conn.
Fairchild Semiconductor Corp., Palo Alto, Calif.
FMC Corp.
Inorganic Chemical Div., Buffalo, N. Y.
Chlor-Alkali Div., South Charleston, W. Va.
Foote Mineral Co., Exton, Pa.
Ford Motor Co., Dearborn, Mich.
General Motors Corp.
Allison Div., Indianapolis, Ind.
Delco-Remy Div., Anderson, Ind.
Research Laboratories Div., Warren, Mich.
General Telephone & Electronics Laboratories Inc., Bayside, N. Y. (2 memberships)
Globe-Union, Inc., Milwaukee, Wis.
B. F. Goodrich Chemical Co., Cleveland, Ohio
Gould-National Batteries, Inc., Minneapolis, Minn.
Great Lakes Carbon Corp., New York, N. Y.

(Sustaining Members cont'd)

Hanson-Van Winkle-Munning Co., Matawan, N. J. (2 memberships)
Harshaw Chemical Co., Cleveland, Ohio (2 memberships)
Hercules Powder Co., Wilmington, Del.
Hill Cross Co., Inc., West New York, N. J.
Hoffman Electronics Corp., Semiconductor Div., El Monte, Calif.
Hooker Chemical Corp., Niagara Falls, N. Y. (3 memberships)
HP Associates, Palo Alto, Calif.
Hughes Research Laboratories, Div. of Hughes Aircraft Co., Malibu, Calif.
International Business Machines Corp., New York, N. Y.
International Minerals & Chemical Corp., Skokie, Ill.
International Resistance Co., Philadelphia, Pa.
ITT Federal Laboratories, Div. of International Telephone & Telegraph Corp., Nutley, N. J.
Jones & Laughlin Steel Corp., Pittsburgh, Pa.
K. W. Battery Co., Skokie, Ill.
Kaiser Aluminum & Chemical Corp.
Div. of Chemical Research, Permanente, Calif.
Div. of Metallurgical Research, Spokane, Wash.
Kawecki Chemical Co., Boyertown, Pa.
Kennecott Copper Corp., New York, N. Y.
Leesona Moos Laboratories, Div. of Leesona Corp., Jamaica, N. Y.
Arthur D. Little, Inc., Cambridge, Mass.
Lockheed Aircraft Corp., Missiles & Space Div., Sunnyvale, Calif.
Mallinckrodt Chemical Works, St. Louis, Mo.
P. R. Mallory & Co., Indianapolis, Ind.
Melpar, Inc., Falls Church, Va.
Miles Chemical Co., Div. of Miles Laboratories, Inc., Elkhart, Ind.
Minneapolis-Honeywell Regulator Co., Minneapolis, Minn.
Monsanto Chemical Co., St. Louis, Mo.
M&T Chemicals Inc., Detroit, Mich.
National Cash Register Co., Dayton, Ohio
National Lead Co., New York, N. Y.
National Research Corp., Cambridge, Mass.
National Steel Corp., Weirton, W. Va.
North American Aviation, Inc., El Segundo, Calif.
Northern Electric Co., Montreal, Que., Canada
Norton Co., Worcester, Mass.
Owens-Illinois Glass Co., Toledo, Ohio
Pennsalt Chemicals Corp., Philadelphia, Pa.
Phelps Dodge Refining Corp., Maspeth, N. Y.
Philco Corp., Research Div., Blue Bell, Pa.
Philips Laboratories, Inc., Briarcliff Manor, N. Y.
Pittsburgh Plate Glass Co., Chemical Div., Pittsburgh, Pa.
Potash Co. of America, Carlsbad, N. Mex.
Radio Corp. of America
Electronic Components and Devices, Lancaster, Pa.
Tube Div., Harrison, N. J.
RCA Victor Record Div., Indianapolis, Ind.
Ray-O-Vac Co., Madison, Wis.
Raytheon Co., Waltham, Mass.
Reynolds Metals Co., Richmond, Va.
Shawinigan Chemicals Ltd., Montreal, Que., Canada
Socony Mobil Oil Co., Inc., Dallas, Texas
Speer Carbon Co.
International Graphite & Electrode Div., St. Marys, Pa.
Sprague Electric Co., North Adams, Mass.
Stackpole Carbon Co., St. Marys, Pa.
Stauffer Chemical Co., New York, N. Y.
Texas Instruments, Inc., Dallas, Texas
Metals and Controls Corp., Attleboro, Mass.
3M Company, St. Paul, Minn.
Titanium Metals Corp. of America, Henderson, Nev.
Udylite Corp., Detroit, Mich. (4 memberships)
United States Borax & Chemical Corp., Los Angeles, Calif.
United States Steel Corp., Pittsburgh, Pa.
Univac, Div. of Sperry Rand Corp., New York, N. Y.
Universal-Cyclops Steel Corp., Bridgeville, Pa.
Upjohn Co., Kalamazoo, Mich.
Western Electric Co., Inc., Chicago, Ill.
Wyandotte Chemicals Corp., Wyandotte, Mich.
Yardney Electric Corp., New York, N. Y.